



**OPTIMISING THE QUANTITATIVE
ANALYSIS IN FUNCTIONAL PET
BRAIN IMAGING**

Yasser Zamil Alzamil

Thesis submitted on 29th March 2019 at Cardiff
University for the award of Doctor of Philosophy

Table of Contents

TABLE OF CONTENTS.....	II
ACKNOWLEDGEMENTS.....	VI
SUMMARY	VII
LIST OF FIGURES	IX
LIST OF TABLES	XII
1 INTRODUCTION.....	1
1.1 Background and overview.....	1
1.2 Research problem and motivation	3
1.3 Research objectives	4
1.4 Thesis structure (outline)	5
2 MEDICAL AND PHYSICAL BACKGROUND.....	6
2.1 Overview.....	6
Basic positron physics.....	7
2.2.....	7
2.3 PET instrumentation	8
2.3.1 PET camera overview	8
2.3.2 PET scintillation detectors	9
2.3.3 Attenuation correction.....	10
2.3.4 System sensitivity.....	11
2.4 PET image acquisition and processing.....	12
2.5 Combination PET/CT imaging.....	13
2.6 Full-body PET scanner	13
2.7 Radiopharmaceuticals: Fluorine-18	14
2.8 Biodistribution and metabolism of ¹⁸ F-DOPA in neurology and oncology	16
2.9 PET's advantages in neuroimaging.....	17
2.10 Dopaminergic areas in the brain	18
2.11 Dopamine receptors	19

2.12	PET tracers in the dopaminergic system	20
2.13	Basics and concepts of PET tracer kinetic modelling	21
2.13.1	Overview.....	21
2.13.2	Dynamic PET scan	23
2.13.3	PET image quantitation.....	23
2.13.4	TKM in PET.....	24
2.13.5	Modelling process.....	24
2.13.6	Types of tracers and models	25
2.13.7	Input-function methods.....	33
2.13.8	Standards and recommendations for PET quantification.....	34
3	LITERATURE REVIEW.....	36
3.1	Introduction	36
3.2	Background information.....	38
3.2.1	Principles of Patlak analysis	39
3.2.2	Making plots with Patlak equations	41
3.3	Sources of errors in PET quantitative analysis	43
3.3.1	Acquisition protocol design	44
3.3.2	Physical aspects data errors	45
3.3.3	PET data errors	46
3.4	Sources of errors in Patlak analysis.....	49
3.5	PET imaging quantification methods in PD with 18F-FDOPA tracer	51
3.6	Conclusion.....	58
4	METHODOLOGY.....	60
4.1	Materials and methods	60
4.1.1	Scanner and reconstruction parameters.....	60
4.1.2	Simulation parameters of dPETSTEP	61
4.1.3	PMOD software.....	63
4.1.4	Thesis strategy.....	66
4.2	GDNF analysis and chapter 8's materials and methods.....	68
4.2.1	Study design and subjects.....	68
4.2.2	Scanner and reconstruction parameters.....	69
4.2.3	Protocol scan	70
4.2.4	Image reconstruction and data transfer.....	71
4.2.5	Regional and sub regional analysis.....	72
4.3	Conclusion.....	75
5	IMPACT OF NOISE ON QUANTITATIVE 18F-FDOPA IMAGES IN PHANTOM DYNAMIC PET DATA	76
5.1	Introduction	76
5.2	Theory	78
5.2.1	FDOPA kinetic analysis method	78
5.3	Bias and Statistical Noise-Reduction Methods	80
5.3.1	Ordinary least squares.....	80

5.3.2	Generalized linear least squares.....	83
5.3.3	Robust fitting regression.....	86
5.3.4	Total least squares.....	88
5.4	Results.....	89
5.4.1	Normal simulated Ki values.....	89
5.4.2	Averaged Ki values (normal and abnormal).....	94
5.5	Discussion.....	96
5.6	Conclusion.....	97
6	NOISE REDUCTION TECHNIQUES IN SIMULATED ¹⁸F- FDOPA DYNAMIC PET DATA.....	99
6.1	Introduction.....	99
6.2	Theory.....	101
6.2.1	Gradient anisotropic diffusion filter.....	101
6.2.2	Curvature anisotropic diffusion filter.....	104
6.2.3	Wavelets.....	105
6.3	Results.....	109
6.3.1	GADF result.....	109
6.3.2	CADF result.....	111
6.3.3	DW analysis.....	113
6.3.4	BLW analysis.....	115
6.4	Discussion.....	118
6.4.1	GADF analysis.....	118
6.4.2	CADF analysis.....	119
6.4.3	DW analysis.....	120
6.4.4	BLW analysis.....	121
6.5	Conclusion.....	122
7	NOISE REDUCTION IN SIMULATED PET DATA IN PATLAK ANALYSIS.....	123
7.1	Introduction.....	123
7.2	Theory.....	125
7.2.1	Moving average filtering.....	125
7.2.2	Savitzky-Golay filtering.....	126
7.2.3	Curve fitting.....	130
7.2.4	Median filtering.....	133
7.3	Results.....	135
7.3.1	MAF results.....	135
7.3.2	SGF results.....	137
7.3.3	PCF results.....	139
7.3.4	MF results.....	142
7.4	Discussion.....	145
7.4.1	MAF analysis.....	145
7.4.2	SGF Analysis.....	147
7.4.3	PCF analysis.....	147
7.4.4	MF analysis.....	148

7.5 Conclusion.....	149
8 IMPROVING THE QUANTITATIVE ¹⁸F-FDOPA IMAGES IN HUMAN DYNAMIC PET DATA FOR PARKINSON’S DISEASE PATIENTS.....	150
8.1 Introduction	150
8.2 Results	152
8.2.1 Regional and Sub-Regional Outcomes and Analysis	153
8.2.2 Regional and Sub-Regional Analysis with optimised methods	159
8.3 Discussion	164
8.4 Conclusion.....	167
9 CONCLUSION AND FUTURE WORK	169
9.1 Summary and Conclusions	169
9.2 Summary of significant findings.....	171
9.3 Future Work and directions.....	172
APPENDICES	174
REFERENCES.....	196
GLOSSARY	209
SOFTWARE AND ANALYSIS TOOLS WEBSITE.....	211

Acknowledgements

The accomplishment of this research project was made possible by the financial help of University of Hail (UOH), and Saudi Arabian Ministry of Education (MOE), which is represented by Saudi Arabian Cultural Bureau (SACB) in the UK, I am very grateful to their staff for their generosity and support during this project.

I would like to dedicate this thesis to Zamil & Haya my loving parents and to my lovely wife Abeer, the most wonderful people I have ever known. I am forever grateful to them for always being at my side and for reassure me throughout writing this thesis and my life in general.

I would like to express my sincere gratitude to my main supervisor Prof. Christopher Marshall and co-supervisor Dr. Yulia Hicks for the continuous support during my PhD program, for their patience, motivation, and for putting so much faith in my work. Their guidance helped me in all the time of research and writing of this thesis. I could not have imagined having better supervisors, advisors and mentors for my PhD study.

My sincere thanks also goes to Dr. Emiliano Spezi, who performed the annual review, for insightful comments and his encouragement, which guided me to widen my research from various perspectives. Also I thank Dr. Chris Yang for helping me in designing the training program during the four years.

I thank my colleagues in research rooms in PETIC and ENGIN School for the stimulating discussions. Also I thank my friends Fahad, Eissa, Sambu, Saad, Nassir and Yasir for all the fun we have had. A very special gratitude goes out to my neighbour Mazin and his wife for helping us in school dropping off and picking up for my kids.

And finally, last but by no means least, also to my other family members and my friends in Hail who have supported me along the way.

Thanks for all your encouragement!

Summary

Patlak analysis techniques based on linear regression are often applied to positron emission tomography (PET) images to estimate a number of physiological parameters. The Patlak equation forms the basis for most extension works regarding graphical analysis of many tracers in quantitative PET measurements. Patlak analysis is primarily used to obtain the rate constant K_i , which represents the tracer transfer rate from plasma to the targeted tissue. One of the most common issues associated with Patlak analysis is the introduction of statistical noise, adopted originally from the images, that affects the slope of the graphical plot, leading to bias, and causes errors in the calculation of the rate constant K_i . In this thesis, several statistical and noise reduction methods for 2 and 3 dimensional data are proposed and applied to simulated ^{18}F -FDOPA brain images generated from a PET imaging simulator. The methods were applied to investigate whether their utilisation could reduce the bias and error caused by noisy images and improve the accuracy of quantitative measurements. Then, validation step extended to ^{18}F -FDOPA PET images obtained from a clinical trial for Parkinson's disease. The minimum averaged SE, SSE and the highest averaged reduction of noisy K_i values were found with the feasible generalised least squares (FGLS) model. Battle-Lemarie wavelet (BLW) showed significant change in data for the 3D PET images. Savitzky-Golay filtering (SGF) demonstrated significant change for most of the noise levels applied to 2D data. In clinical ^{18}F -FDOPA images, the mean and standard deviation of standard error (SE) and sum-squared error (SSE) were significantly reduced in both baseline and after therapy groups. This work has the potential to be extended to other graphical analysis in quantitative PET data measurements.

Statements and Declaration

Statement 1

This thesis is being submitted in partial fulfillment of the requirements for the degree of PhD.

Signed _____

Date _____

Statement 2

This work has not been submitted in substance for any other degree or award at this or any other university or place of learning, nor is being submitted concurrently for any other degree or award (outside of any formal collaboration agreement between the University and a partner organisation)

Signed _____

Date _____

Statement 3

I hereby give consent for my thesis, if accepted, to be available in the University's Open Access repository (or, where approved, to be available in the University's library and for inter-library loan), and for the title and summary to be made available to outside organisations, subject to the expiry of a University-approved bar on access if applicable.

Signed _____

Date _____

Declaration

This thesis is the result of my own independent work, except where otherwise stated, other sources are acknowledged by explicit references. The thesis has not been edited by a third party beyond what is permitted by Cardiff University's Use of Third Party Editors by Research Degree Students Procedure.

Signed _____

Date _____

WORD COUNT _____

(Excluding summary, acknowledgements, declarations, contents pages, appendices, tables, diagrams and figures, references, bibliography, footnotes and endnotes)

List of Figures

Figure 2-1. Positron decay. A positron (β^+) is emitted and interacts with an electron (β^-) to form an annihilation reaction that results in the emission of two 511-keV photons (gamma rays) roughly 180° apart (Mettler and Guiberteau 2011).....	8
Figure 2-2. A multiple full-ring system of PET cameras, with each ring consisting of multiple blocks.	10
Figure 2-3. A PET scintillation block detector.	10
Figure 2-4. A PET/CT scanner.....	13
Figure 2-5. The EXPLORER (EXtreme performance Long REsearch scanner) PET scanner.	14
Figure 2-6. FDOPA decarboxylation.	16
Figure 2-7. Steps for developing a model.	24
Figure 2-8. Tracer delivery, uptake, binding, and clearance in the ROI tissue.	25
Figure 2-9. Common quantification methods in PET image analysis.	27
Figure 3-1. Summary of graphical analysis characteristics and tracer behaviour options.	38
Figure 3-2. (A) Example of the irreversible compartment where the tracer is trapped in the ROI. (B) Two compartmental models, including both reversible and irreversible compartments.	40
Figure 3-3. (A) Example of data represented by points on the plot (B) Shows the best fitting line (regression line).....	42
Figure 3-4. The compartmental model suggested by Gjedde et al. (1991) and applied in Dhawan et al. (1996) study shows FDOPA and its metabolites.	53
Figure 3-5. ADD (summed) and net influx rate constant (K_i) maps of single slices from a healthy subject (top) and a subject with PD (bottom). The subject with PD shows reduced uptake in the caudate and putamen, which is greater on the right-hand side (Whone et al. 2004).....	56
Figure 5-1. Two-tissue compartmental model where $C_p(t)$ is the plasma tracer concentration at time (t). C_1 is the free tracer concentration in tissue and C_2 is the trapped tracer concentration. K_1 , k_2 , and k_3 are unidirectional rate constants of the tracer between plasma and tissues.	78
Figure 5-2. PET activity measured from ROI is divided by the reference tissue activity that represents y-axis, and plotted against the integral of the reference TAC from the injection time divided by the reference activity, which represents x-axis. The model plot resulted in a straight line after $t^* = 30$ min in this analysis.	79
Figure 5-3. An example showing how the OLS method is used to construct the regression line from PET dynamic data; y-axis represents the amount of radioactivity (kBq/cc) and x-axis represents time points in minutes when the radioactivity was recorded.	81
Figure 5-4. Ordinary least squares (A) and total least squares (B) fit of the set of $m = 20$ data points in the plane. (ϕ ---) data points, $[a_i b_i]$, x-approximations $[\hat{a}_i \hat{b}_i]$, solid line (—) fitting model $\hat{a}\hat{x} = \hat{b}$, dashed lines (- -) approximation errors.	89

Figure 5-5. TACs for the reference tissue (cerebellum) and ROI (left striatum) that were obtained from the first simulation data without noise are plotted as an example.	91
Figure 5-6. OLS regression method used for kinetic Patlak analysis on all simulation data and Ki values illustrated within 10 noise levels.	91
Figure 5-7. FGLS regression method used for kinetic Patlak analysis on all simulation data and Ki values illustrated within 10 noise levels.	91
Figure 5-8. TLS regression method used for kinetic Patlak analysis on all simulation data and Ki values illustrated within 10 noise levels.	92
Figure 5-9. RFR regression method used for kinetic Patlak analysis on all simulation data and Ki values illustrated within 10 noise levels.	92
Figure 6-1. Effect of the gradient anisotropic diffusion image filter on a slice from an image of the brain (right); noise reduction can be seen compared to the noisy image (left).	104
Figure 6-2. The first row shows images with noise levels of 10%, 20%, and 40% Gaussian with mean=0; and the second row shows the same images after applying GADF with 10 iterations.	119
Figure 6-3. The first row shows images with noise levels 10%, 20%, and 40% Gaussian with mean=0; the second row shows the same images after applying CADF with 3 iterations.	120
Figure 6-4. The first row shows images with noise levels of 10%, 20%, and 40% Gaussian with mean=0; the second row shows the same images after applying the DW technique.	121
Figure 7-1. In plot (a), the first data point is not smoothed, as a span cannot be constructed. In plot (b), the second data point is smoothed using a span of three. Plots (c) and (d) show that a span of five is used to calculate the smoothed value.	126
Figure 7-4. In the first plot (left), there is a slight reduction in noise at the beginning and at the end of the noise levels, but significant noise in the intervening levels. The centre plot illustrates the reduction in SE values, and the third plot shows the SSE values. Both have a significant reduction of noisy Ki values after applying MAF.	137
Figure 7-5. In the first plot (left), a slight reduction in Ki value at the beginning is shown, while it is more substantial in the other levels. The second plot in the middle illustrates the reduction in SE values, and the third plot shows the SSE values; both have a significant reduction of noisy Ki values and are more stabilised after applying SGF.	139
Figure 7-6. Curves for Ki values in simulation 1 before and after applying different degrees of PCF starts from 1 st to 9 th order. In the middle of the graph, the black line represents the Ki value (0.0140 min ⁻¹) without noise for comparison to other curves.	141
Figure 7-7. Curves for Ki values in simulation 1 before and after applying different orders of MF up to 4 th order. In the middle of the graph, the black line represents the original Ki value (0.0140 min ⁻¹) without noise for comparison to other curves.	143
Figure 7-8. Comparison between original Ki values and noisy, same, and double spans. This shows that double-span MAF brings much better results compared to other values.	146
Figure 8-1. Chart (A) shows a comparison between the whole striatum (R and L) in baseline (BL) vs. after treatment (AT) in placebo group. Chart (B), shows the same group after organise the Ki values ascending and show the trend lines.	155

Figure 8-2. Chart (A) shows a comparison between the whole striatum (R and L) in baseline (BL) vs. after treatment (AT) in GDNF group. Chart (B), shows the same group after showing the trend lines of the Ki values ascending.155

Figure 8-3. Boxes of plot represent GDNF and placebo groups with assign the Ki change as a y-axis shows the differences in mean and outliers.156

Figure 8-4. Chart 1 (left) shows a comparison between the whole striatum (R and L) in baseline vs. week 40 in placebo group after applying optimised methods. Chart 2 (right), shows the same group after organise the Ki values ascending and show the trend lines.160

Figure 8-5. Chart 1 (left) shows a comparison between the whole striatum (R and L) in baseline vs. week 40 in GDNF group. Chart 2 (right), shows the same group after showing the trend lines of the Ki values ascending. ...160

Figure 8-6. Boxes of plot represent GDNF and placebo groups after optimisation with assigning the striatum Ki change as a y-axis, the differences in mean and outliers are shown.161

List of Tables

Table 2-1. Laplace transform properties.	32
Table 4-1. PET/CT scanner parameters for FDOPA imaging.....	60
Table 5-2. SE, SSE, and fold change values for each method applied to simulation data.	94
Table 5-4. SE, SSE, and fold change values for each method applied to average 2D simulation data.	95
Table 5-5. A one-way repeated measured analysis of variance (ANOVA) result to average 3D simulation data.	95
Table 5-6. SE, SSE, and fold change values for each method applied to average 3D simulation data.	96
Table 6-2. A one-way repeated measured analysis of variance (ANOVA) result for SE values in simulations before and after applying GADF at 5 and 10 iterations.	110
Table 6-3. A one-way repeated measured analysis of variance (RM-ANOVA) result for SSE values in simulations before and after applying GADF at 5 and 10 iterations.	111
Table 6-5. A one-way repeated measured analysis of variance (ANOVA) result for SE values in simulations before and after applying CADF at 1, 2, and 3 iterations.	112
Table 6-6. A one-way repeated measured analysis of variance (ANOVA) result for SSE values in simulations before and after applying CADF at 1, 2, and 3 iterations.	113
Table 6-7. A one-way repeated measured analysis of variance (ANOVA) result for Ki values in simulations before and after applying DW with 20% coefficients to keep.	114
Table 6-8. A one-way repeated measured analysis of variance (ANOVA) result for SE values in simulations before and after applying DW with 20% coefficients to keep.	114
Table 6-9. A one-way repeated measured analysis of variance (ANOVA) result for SSE values in simulations before and after applying DW with 20% coefficients to keep.	114
Table 6-10. A one-way repeated measured analysis of variance (ANOVA) result for Ki values in simulations before and after applying BLW with 20% coefficients to keep.	115
Table 6-11. A one-way repeated measured analysis of variance (ANOVA) result for SE values in simulations before and after applying BLW with 20% coefficients to keep.	116
Table 6-12. A one-way repeated measured analysis of variance (ANOVA) result for SSE values in simulations before and after applying BLW with 20% coefficients to keep.	116
Table 6-13. A comparison between reductions in Ki, SE, and SSE values for all methods used with simulated data before and after denoising processes.	117
Table 7-1. ANOVA results for Ki values in simulations before and after applying MAF.	136
Table 7-2. ANOVA results for SE values in simulations before and after applying MAF.	136

Table 7-3. ANOVA result for SSE values in simulations before and after applying MAF.	136
Table 7-4. ANOVA results for Ki values in simulations before and after applying SGF.	138
Table 7-5. ANOVA results for SE values in simulations before and after applying SGF.	138
Table 7-6. ANOVA results for SSE values in simulations before and after applying SGF.	138
Table 7-8. ANOVA results for Ki values in simulations before and after applying PCF.	141
Table 7-9. ANOVA results for SE values in simulations before and after applying PCF.	142
Table 7-10. ANOVA results for SSE values in simulations before and after applying PCF.	142
Table 7-11. Result for Ki values in simulation 1 before and after applying different degrees of MF starts from 1 st to 4 th order.	143
Table 7-12. ANOVA results for Ki values in simulations before and after applying MF.	143
Table 7-13. ANOVA result for SE values in simulations before and after applying MF.	144
Table 7-14. ANOVA result for SSE values in simulations before and after applying MF.	144
Table 7-15. A comparison of reductions in Ki, SE, and SSE values for all methods used with simulated data before and after the denoising process.	145
Table 7-16. Difference in Ki values of the first simulation in noisy, same span value, and double span value for reference tissue TAC.	146
Table 8-1. Mean Ki values \pm SD are obtained from patients' FDOPA images baseline and after treatment (40 weeks) scans of left and right side of brain by Patlak analysis included both GDNF and placebo groups.	156
Table 8-2. ANCOVA model result, SE and SSE means are obtained from patients' FDOPA images baseline and after treatment scans by Patlak analysis including both GDNF and placebo groups.	158
Table 8-3. RM-ANOVA model is applied for SE and SSE means in baseline vs. week 40 group and presented in the table below with significant change.	158
Table 8-4. Mean Ki values \pm SD are obtained, after applying optimised methods suggested, from patients' FDOPA images baseline and after treatment (40 weeks) scans of left and right side of brain by Patlak analysis included both GDNF and placebo groups.	162
Table 8-6. RM-ANOVA model is applied for SE and SSE means in baseline vs. week 40 group after applying optimised methods for PET data and presented in the table below with no significant change.	163
Table 8-7. RM-ANOVA model is applied for SE and SSE means in baseline vs. week 40 group after applying optimised methods for PET data and presented in the table below with no significant change.	164

1 Introduction

1.1 Background and overview

Positron emission tomography (PET) is considered one of the most powerful diagnostic tools in various applications of clinical imaging. For instance, PET plays a major role in the progress of functional brain imaging and research. With a PET scanner, the brain mapping of in vivo functions can be studied and evaluated; metabolism, receptor binding, and density in neurons can all be analysed via PET images. A PET scanner measures and detects the emission of radioactive isotopes (that produce gamma rays), which usually have a short half-life of between two minutes and two hours. For a typical PET scan, a tracer labelled with a radioisotope is administered to the patient, usually intravenously (Turkheimer et al. 2014).

PET allows for the study of the molecular function of tissue via the tracer's emission recorded with the scanner. With it, one can reconstruct three-dimensional (3D) images for the region of interest (ROI). Therefore, the cross-section images of the human body can be viewed as a single plane or a 3D volume. Physiological and pathological information or parameters can be obtained, which are valuable for the diagnosis and evaluation of diseases. PET was recently combined with an X-ray computed tomography (CT) or Magnetic resonance imaging (MRI) scanners so the necessary images can be obtained in the same session. This process allows for the more precise alignment and correlation of the body's activity and the anatomical region. This combination of functional and anatomical images has influenced many diagnostic procedures recently in neurology, oncology, radiation therapy, and cancer staging (Salomaki et al. 2017).

PET was the first imaging tool that allowed for direct measurement of dopamine-system (DA) mechanisms in the living human brain (Hou et al. 2012). In functional brain studies, the radiotracer crosses the blood-brain barrier (BBB) and might be metabolized or bind to neuroreceptors, or it might be stored in the vesicles in neurons. With the emission data obtained over the duration of the scan, images of the radiotracer distribution in the tissue of interest can be reconstructed, and appropriate algorithms, including physical corrections, such as scatter and attenuation, can be used to quantitatively obtain the distribution of radiotracer activity in the ROI tissue.

The primary objective of my PhD project is to improve the quantitative analysis of ^{18}F -FDOPA dynamic images to enable greater sensitivity and accuracy in the detection of changes in sequential ^{18}F -FDOPA images, which are obtained from positron emission tomography/computed tomography (PET/CT) imaging modality. The optimization process will be applied to images obtained from a clinical trial with the aim of assessing the safety and efficacy of intermittent, bilateral, and intraputamenal glial cell line-derived neurotrophic factor (GDNF) infusions administered via convection-enhanced delivery (CED) in subjects with Parkinson's disease (PD). The clinical trial is a placebo-controlled, randomised, double-blind study that will include baseline and post-therapy scans. PET ligands can demonstrate dopamine terminal dysfunction that relates to PD, which is a chronic and progressive degenerative neurological disorder and could affect other central neurotransmitter systems (Brooks and Pavese 2011). A comprehensive model that represents tracer distribution (^{18}F -FDOPA) in the brain and ROIs will be selected and modified to be compliant with and suitable for available analytical tools. ^{18}F -FDOPA as a PET tracer is used to image the presynaptic side in the dopaminergic system and can assess the uptake of radiolabelled dopamine. Therefore, during the progression of PD, the level of FDOPA declines, thereby reflecting the level of L-dopa and dopamine in ROIs (Sioka et al. 2010). ^{18}F -FDOPA is the tracer that can

most frequently be used to investigate dopamine synthesis (Hou et al. 2012). A validation step using a simulation of the phantom process should also be performed for the suggested model before applying it to PET data. Additional programs will be developed to process the phantom's output data and to perform the kinetic analysis. Several quantification approaches will be used to analyse the PET data, including mathematical expressions and graphical analysis. In addition, Patlak analysis, which is based on regression analysis, will be selected to investigate PET data in this research. All data should be obtained from dynamic and possibly static images.

1.2 Research problem and motivation

^{18}F -FDOPA tracer is considered irreversible (trapped in tissue), and due to the lack of arterial blood sampling in a GDNF clinical trial, images are used as an input function for the analysis. Various quantification methods have been introduced to provide more accurate results and parameters that allow us to understand the distribution of labelled compounds inside the body. In this case, Patlak graphical analysis is the best option as a quantitative technique to use for ^{18}F -FDOPA brain images. The Patlak equation is based on linear regression to analyse activity in the ROI and requires an input function (blood samples or reference tissue images) and dynamic images to obtain diagnostic parameters.

Graphical analysis methods are independent of any particular model structure and are considered to be simple for PET analysis. They could be used for a wide range of tracers without complicated mathematical compartmental modelling. However, this type of analysis can lead to issues. One is the bias or variance introduced, which stems from the sensitivity to statistical noise of outlier data. This limitation usually affects the parameter estimates' accuracy when one uses the ordinary least squares method in regression analysis. In some images' voxels, outliers are likely to exist in the regression

analyses and could cause higher false negative rates or higher false positive rates, ultimately affecting the diagnosis decision. The effect of outliers is particularly problematic, as a simple correction is not available. One could reduce this issue by applying other regression methods and reducing noise in PET dynamic images prior to the quantification process. Improved methods that optimise the statistical process in the Patlak equation and that reduce the noise in images are developed in this thesis and implemented on all PET data obtained from the simulated phantom and the GDNF clinical trial. The accuracy of the estimates is improved where bias in estimates is reduced without a significant rise in variance.

1.3 Research objectives

The research methodology in this thesis can be summarised as follows. The first step is to generate simulated PET data from the simulated phantom similar to data generated from the PET scanner. The features and settings of the scanner, scan protocol, and reconstruction algorithms are all considered to obtain dynamic images. Then, improved statistical and denoising methods are applied to the simulated PET data. The most successful methods are applied again to clinical PET data obtained from the patients. These two major steps can be broken down into smaller steps as follows:

- Using the setting parameters of the PET scanner in PETIC as input for the simulated phantom. The values of the time activity curves are simulated to generate PET data (chapter5).
- A Noise is applied to all groups first only for time activity curves (TACs) extracted from images (reference tissue and ROI) and then for all dynamic images (chapter 5 and 6).
- The Patlak equation with improved statistical models is applied to quantify and analyse PET data from the phantom and the clinical trials (chapter 5, 6, 7 and 8).

- PET denoising methods are applied using MATLAB codes and specific image processing software. 2D and 3D data-denoising methods are used to reduce bias introduced within the data of simulated and clinical PET data (chapter 6 and 7).

1.4 Thesis structure (outline)

The rest of this thesis is structured as follows: Chapter 2 provides the medical and physical backgrounds of the PET scanner as well as its specifications and applications. In addition, the basic concepts of the PET quantification methods are available to obtain physiological parameters and evaluate biological systems in the human body. Chapter 3 first presents the methodology and application of tracer kinetic modelling in PET data, and describes the requirements for quantifying images. The second section describes the sources of errors in kinetic modelling and the impact on quantitative measurements. The third part covers the application of ^{18}F -FDOPA in neurology, including the review of previous studies and analysis methods used to monitor and diagnose PD. Chapter 4 describes all of the methods and materials used and proposed to generate and analyse the PET data, including mathematical expressions, functions, and equations applied to the data. Chapter 5 reveals all of the results obtained from statistical models implemented in the experiments, followed by a discussion and analysis. Chapter 6 describes methods used to reduce noise in PET dynamic images followed by results and discussion. In Chapter 7, approaches were applied to reduce noise in 2D data (TACs) are shown and discussed. Successful methods that are approved by simulated data applied on clinical FDOPA images in chapter 8 for extra validation. Chapter 9 includes a conclusion of all of the results and contributions followed by research directions for future work resulting from this thesis.

2 Medical and Physical Background

2.1 Overview

PET, which involves the labelling of positron-emitting radionuclides, has evolved over the past 35 years to become a routine clinical imaging modality. PET allows for the in vivo imaging of physiologically and pathologically important molecules such as those that contain essential organic elements (e.g. carbon, hydrogen, and oxygen). PET data provide relevant molecular and/or metabolic information, which is valuable in providing accurate diagnoses and disease evaluations (Mettler and Guiberteau 2011). Labelled substances have several advantages, including the high specificity of molecular targeting, the ability to use biologically active materials without changing their behaviour, and the success of the tracer principle (Ziegler 2005). Unlike X-ray, CT or MRI scans, which usually provide anatomical information, PET also gives information about the chemical activity in normal and abnormal tissue; various radiotracers are available for neurologic, cardiologic, and oncologic applications and for both clinical and research purposes (Christian and Waterstram-Rich 2013; Ziegler 2005). This chapter provides an overview of PET imaging, as well as discussions of the basic concepts of tracer kinetic modelling (TKM) and PET quantification methods.

2.2 Basic positron physics

Positrons (positive electrons) are subatomic particles that have a positive charge and the same mass and charge magnitude as electrons (which are negatively charged); in other words, the positron is the antiparticle of the electron. Positron-emitting radionuclides are usually produced when a stable element is bombarded with protons, deuterons, or helium nuclei, typically in a cyclotron. The product has an excess of protons, which decay by emitting positrons. The five positron-emitting isotopes that are most commonly used in PET imaging are carbon-11 (C-11), nitrogen-13 (N-13), oxygen-15 (O-15), fluorine-18 (F-18), and rubidium-82 (Rb-82) (Mettler and Guiberteau 2011). The positron travels from its site of origin, loses its kinetic energy, and then reacts with a resident electron in an annihilation reaction that generates two gamma photons (511 keV), which are emitted in opposite directions (Fig. 2-1). This annihilation defines a line, and the PET scanner records the interaction so that the data about the event can be reconstructed and displayed (Christian and Waterstram-Rich 2013; Mettler and Guiberteau 2011). The production of PET tracers requires very expensive equipment (e.g., a cyclotron, an automated synthesis module, and a hot cell) to ensure radiopharmaceutical quality control (QC) and prepare the precursor (Christian and Waterstram-Rich 2013). The radioisotopes used in PET scanning usually have short half-lives: C-11, 20.4 min; N-13, 9.97 min; O-15, 2.2 min; F-18, 110 min. and Rb-82, 0.75 min (Jadvar and Parker 2006).

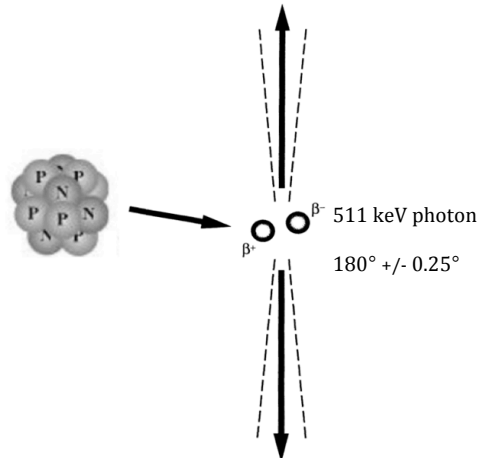


Figure 2-1. Positron decay. A positron (β^+) is emitted and interacts with an electron (β^-) to form an annihilation reaction that results in the emission of two 511-keV photons (gamma rays) roughly 180° apart (Mettler and Guiberteau 2011).

2.3 PET instrumentation

2.3.1 PET camera overview

A PET camera consists of multiple rings of detectors that contain scintillation crystals; these crystals are linked to photomultiplier tubes (PMTs). The ring design helps detect the two photons that emerge in opposite directions from a single annihilation event. The simultaneous detection provides localization information, as the event can be assumed to have happened on a line between the two detectors. This line is called the line of response (LOR), and it helps researchers construct raw data sets to represent the projections of the positron tracers that are distributed in the body being scanned. A cross-sectional image can be produced using a reconstruction process that is based on several algorithms. For a photon to be accepted and used in imaging, it must be recorded at a specific energy (about 511 keV) and paired with another photon that reaches an opposing detector within a short time window (typically 6 to 12 nanoseconds, though it varies from one camera to another). These events are used in constructing valuable PET images (Mettler and Guiberteau 2011). Scattered photons, which have lost most of their energy during Compton scattering before reaching the

detectors, are excluded using an energy window-based methods; photons with specific energies that are indicative of random events are excluded, in addition to calculation-based methods including a single scatter simulation (SSS) technique (Ibaraki et al. 2016). This imaging method is 3D (i.e. volume-based), which is required so as to significantly increase the sensitivity of the camera and compensate for the increase in scatter rates (Hogg and Testanera 2010).

2.3.2 PET scintillation detectors

Scintillation is the most common principle in PET scanning; it is used in all positron systems. In this method, a flash of light is produced when photons interact with crystals that are coupled with PMTs. Current PET scanners are full-ring (360-degree) multidetector systems that surround the patient. The crystals are grouped together in 6×6 or 8×8 blocks (i.e., 36 or 64 crystals/block) that are each coupled to about four PMTs (Figs. 2-2, 2-3); there are 200–400 blocks per PET camera scanner. Ideal crystals should have the following: (1) high stopping power for photons with 511-keV energy, thus providing high efficiency and high spatial resolution; (2) low system dead time via the rapid decay of intense output light; and (3) accurate scatter rejection due to good energy resolution. The dead time is the period when the crystal and PMT are busy producing and detecting an event, thus causing a slight delay before another event can be detected. All the events that occur during this dead time are lost and cannot be recorded. Decreasing dead time is highly important, particularly in 3D acquisitions and for short-lived radionuclides (e.g. oxygen-15) (Mettler and Guiberteau 2011). Silicon photomultipliers (SiPMs) are an alternative to PMTs; they offer good timing, spatial resolution and energy SiPMs can be integrated into PET or MRI scanners because of their robustness to magnetic fields. Both types of SiPMs analogue (A-SiPM) and digital (D-SiPM) are used in PET applications (Wehner et al. 2014; Xu et al. 2013). New

combination PET and CT systems with SiPMs outperform standard scanners in terms of image quality; adding the use of time of flight (TOF) could also be advantageous in detecting small tumorous lesions, which can lead to more precise disease staging. A SiPM array provides close-to-ideal time resolution, and its measured spatial resolution is much better than that of currently available scanners (Berg and Cherry 2018; Park et al. 2017).

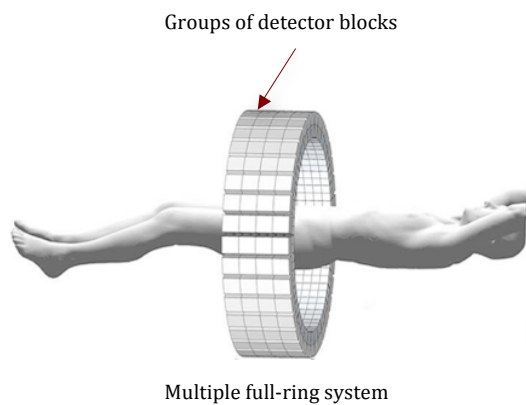


Figure 2-2. A multiple full-ring system of PET cameras, with each ring consisting of multiple blocks.

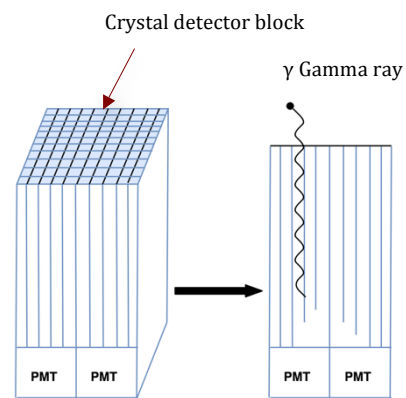


Figure 2-3. A PET scintillation block detector.

2.3.3 Attenuation correction

Attenuation the loss of true events due to absorption by the body or scattering out of the detector's field of view (FOV) is usually worse in PET imaging than in other types of imaging. In PET, the attenuation likelihood is high because both photons in a pair must escape the patient to be detected; PET attenuation could reach as high 95%, which means that PET produces more noise, artefacts, and distortion than other imaging modalities. Thus, attenuation correction (AC) is necessary; more accurate qualitative assessments and more precise quantitative measurements can be performed based on the tracer's uptake. The tracer's delivery, retention, and clearance determine its uptake in a specific tissue. Two methods of correction are commonly used in PET imaging. The first is calculated correction, which assumes uniform attenuation and is typically applied

to the head or brain. The second method, measured correction, uses authentic measurements of transmission data and is applied when attenuation is variable; in this method, a map of body density is used to correct for the attenuation in various tissues. In combination PET and CT scans, X-rays can be used for attenuation correction, as this is faster than using radionuclide transmission data and provides an accurate alignment of the PET data with the X-ray's high-resolution anatomical information. Two steps are mandatory after obtaining the transmission images but before applying the reconstruction algorithms to the PET data, Firstly, as the X-ray's energy must be lower than 511 keV, all transmission data must be adjusted to construct a suitable attenuation map for the annihilation photons. Secondly, image segmentation must be used to reduce pixel noise in the images. This process involves selecting image regions for several types of identified tissues. All regions with the same tissue type are identified, and the pixel values are replaced with new values that represent the known linear-attenuation coefficients for that type of tissue (Christian and Waterstram-Rich 2013; Mettler and Guiberteau 2011).

2.3.4 System sensitivity

A PET camera's sensitivity is defined as the number of true events recorded divided by the activity concentration; multiple factors including scanner geometry, crystal efficiency, and photon attenuation in tissue can influence this measure (Christian and Waterstram-Rich 2013; Mettler and Guiberteau 2011). The detectors' stopping efficiency for 511-keV particles also affects the system's sensitivity. The scintillation detectors provide the highest stopping power of any detector type and also have good energy resolution. A highly sensitive scanner records a high number of coincidental

events in a fixed amount of time and has a fixed radioactivity amount in its FOV; such scanners have a strong signal-to-noise ratio (SNR) (Bailey et al. 2005a).

2.4 PET image acquisition and processing

A common mode in PET imaging is to scan the whole-body by moving the table in steps to obtain segmental views, which can then be used to construct contiguous images. The scan usually extends from the base of the brain to the mid-thigh area. For low-scatter scans such as those in brain studies, 3D imaging is routinely used. The data are then processed and converted to images using either filtered back projection (FBP) or iterative reconstruction. The FBP method is simple and fast; the iterative algorithms are used due to the complexity of the 3D data (Tong et al. 2010). The iterative methods are used to refine the pixel-estimation values and thus obtain more accurate reconstructions of the tracers' distribution in the body. The iterative process starts with a guess about the radioactivity distribution. The data are then forward-projected based on the scanner's geometry, and the results of these projections are compared to the measured raw data; error-projection is then used to correct the estimate. The new estimate is then forward-projected again, and the same process of comparison and correction is repeated to produce a new estimate. These steps are continued until statistical agreement between the estimated and measured data is reached (Ziegler 2005). Iterative reconstruction is common because it produces higher image quality than the FBP method. However, iteration reduces the images' SNR. The most common types of iteration are the maximum likelihood expectation maximization (MLEM) and ordered subset expectation maximization (OSEM) methods (Alessio and Kinahan 2006). Increasing the number of iterations also increases the likelihood that the estimated image (representing

the radiotracer distribution within the patient) is accurate. The process of estimating the distribution is known as convergence (Zaidi 2006).

2.5 Combination PET/CT imaging

Determining the anatomic location of an event in a PET scan is quite difficult due to increased uptake in some areas. Knowing the exact location of the uptake is essential when considering normality and abnormality, so it is best to perform PET and CT scans sequentially, CT then PET and from the same position; this eliminates the need to fuse separate scanned images. The advantages of using PET and CT in combination include accurate AC, short imaging time, accurate anatomic localization for detecting lesions, equivocal interpretation reduction, and simultaneous anatomic and physiologic information. A modern PET/CT combination scanner appears to be a single machine but actually comprises a CT and a PET together in one scanner (Fig. 2-4). The CT data are also used to provide precise anatomic localization in the AC of the PET data. The combination CT and PET imaging is used to progressively strengthen the metabolic and anatomic information, which can then be used in diagnosis, staging, and therapy (Pinilla et al. 2011; Vaidya et al. 2012).

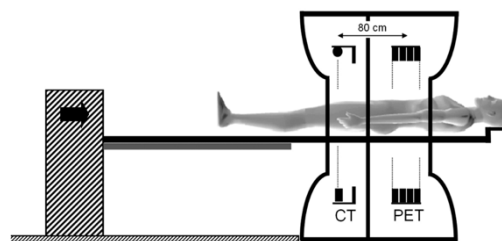


Figure 2-4. A PET/CT scanner.

2.6 Full-body PET scanner

The EXPLORER (EXtreme performance Long REsearch scanner) scanner is a 2-meter-long total-body PET system that is meant to overcome the limitations of current

PET scanners (Fig. 2-5). The FOV of a current clinical PET scanner is between 15 and 25 cm, which limits coverage of the body. Moreover, the EXPLORER system offers 30 or more times better efficiency than current scanners; as a result, the radiation activity for EXPLORER can be as low as 10 MBq, as opposed to the 200-500 MBq required in current PET scanners. Consequently, PET can be allowed for paediatric and adolescent populations, which will help in the study and monitoring of many chronic diseases (Xuezhu et al. 2017).

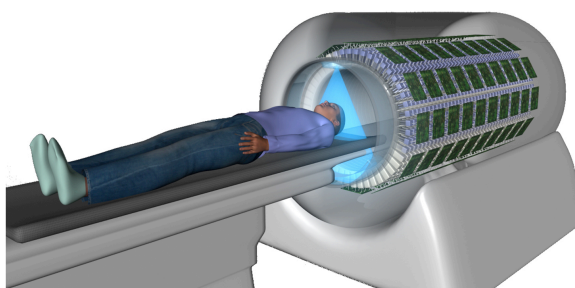


Figure 2-5. The EXPLORER (EXtreme performance Long REsearch scanneR) PET scanner.

2.7 Radiopharmaceuticals: Fluorine-18

Fluorine-18 is a common radioisotope that is commonly used in PET. It has a half-life of 109.7 minutes and can be produced using a nuclear reaction with either $^{18}\text{O}(p,n)$ or $^{20}\text{Ne}(d,a)$. The preferred method is to use ^{18}O -labelled water targets, as this produces ^{18}F in yields greater than 74 GBq. However, this process has high costs and low availability of materials. One of the most common PET tracer labels involving ^{18}F is 2-deoxy-2- ^{18}F fluor-D-glucose (FDG) (Bailey et al. 2005b). The use of ^{18}O gas produces $^{18}\text{F}_2$, which allows for efficient production of another tracer, such as ^{18}F -FDOPA (6- ^{18}F fluoro-L3,4-dihydroxyphenylalanine). The $^{18}\text{O}_2$ double-shoot radionuclide production approach yields more ^{18}F F_2 but less carrier F_2 than the ^{20}Ne production method, which yields a low specific activity of ^{18}F -FDOPA. The $^{18}\text{O}_2$ double-shoot radionuclide production method also leads to higher amounts of FDOPA and a higher

specific activity (Luurtsema et al. 2017). ^{18}F -FDOPA is used in the imaging of brain dopamine neurons. As an investigational diagnostic PET pharmaceutical, ^{18}F -FDOPA is approved for clinical use in the United Kingdom. The normal biodistribution for ^{18}F -FDOPA is also the normal distribution of L-DOPA (Heiko Schöder 2013); ^{18}F -FDOPA is also known as

- L-3,4-Dihydroxy-6- ^{18}F fluorophenylalanine,
- Fluorodopa F18,
- ^{18}F Fluorodopa,
- ^{18}F -6-L-fluorodopa,
- ^{18}F -fluoro-L-DOPA,
- L-6- ^{18}F fluoro-3, 4- dihydroxyphenylalanine, and
- 6- ^{18}F Fluoro-L-DOPA.

The common abbreviations for this substance are FDOPA, ^{18}F FDOPA, ^{18}F -FDOPA, and ^{18}F -DOPA. In neuroimaging, the most common targets for ^{18}F -DOPA are the dopamine receptors in the brain; in oncology, the tracers' targets are amino acid transporters and overexpressed DOPA decarboxylase. The image processing is usually focused on the regional distribution of neurotransmitter dopamine in the brain and on the amino acid uptake and metabolism in tumours (Heiko Schöder 2013; Leung 2011). The main clinical applications of PET/CT imaging with ^{18}F -DOPA are assessments of the striatum, brain tumours, neuroendocrine tumours (NETs), and congenital hyperinsulinemic hypoglycaemia (Chondrogiannis et al. 2013). The positron-emitting fluorinated L-DOPA analogue is 6- ^{18}F -fluoro-L-3,4-dihydroxyphenylalanine (Fig. 2-6). Dopamine is unable to cross the BBB, but ^{18}F -FDOPA, which is the analogue of L-DOPA, can cross the BBB; once in the brain, it is converted to 6- ^{18}F -fluorodopamine through decarboxylation (Fig. 2-6) .

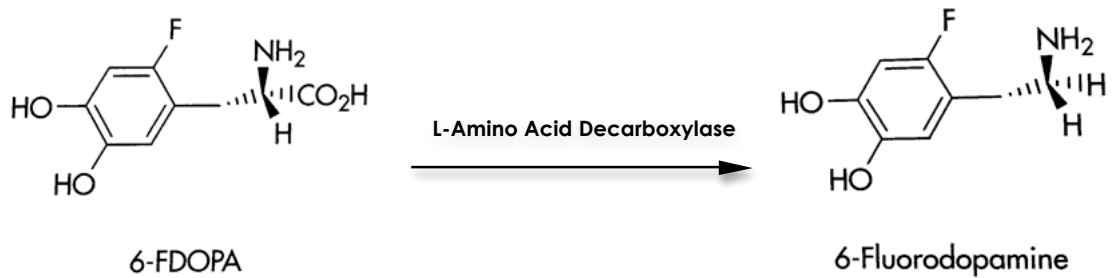


Figure 2-6. FDOPA decarboxylation.

2.8 Biodistribution and metabolism of ^{18}F -DOPA in neurology and oncology

Because ^{18}F -FDOPA can cross the BBB, where it is converted in the striatum by dopa decarboxylase (the enzyme used is amino acid decarboxylase, or AADC) into ^{18}F -fluorodopamine (FDA) and then stored in intraneuronal (presynaptic) vesicles. Next, when the neuron activation triggers the presynaptic vesicles, ^{18}F -fluorodopamine releases and binds to the dopamine receptors. Catechol-O-methyl transferase (COMT), which is distributed uniformly throughout the brain, converts ^{18}F -FDOPA to 3-O-methyl-6-fluoro-L-DOPA (3-OMFD). The administration of carbidopa and entacapone inhibits dopa decarboxylase and COMT, respectively, and can enhance the availability of FDOPA in the brain. Entacapone enhances the metabolism of plasma FDOPA from 16% to about 50% at 80 minutes after the injection (Ruottinen et al. 1995). The non-dopaminergic brain regions have limited metabolic processes (Heiko Schöder 2013). In neurology, ^{18}F -FDOPA is used for the study of presynaptic striatal dopaminergic function in neurologic disorders. Several psychiatric syndromes have been associated with abnormalities in dopamine synthesis or storage, as well as with dopamine-receptor expression, density, and activation (Leung 2011; Patel et al. 2010). PET imaging could be helpful for Parkinson's disease evaluation and for the differential diagnosis of various related syndromes (Sioka et al. 2010). In oncology, ^{18}F -FDOPA is an excellent tracer for imaging NETs, including pheochromocytomas, extra-adrenal paragangliomas,

medullary thyroid carcinomas, and gastro-entero-pancreatic tumours (Balogova et al. 2013). Researchers have also used ^{18}F -FDOPA to image brain tumours. This tracer accumulates in both high-grade and low-grade gliomas. In addition, based on limited data, the uptake of ^{18}F -FDOPA in radionecrosis is lower than in recurrent brain tumours (Chen et al. 2006). The intensity of tumour uptake may correlate with the tumour's grade and cellularity (Pafundi et al. 2013). Changes in ^{18}F -FDOPA uptake in brain tumours may be useful in the creation of early-response assessments (Harris et al. 2012).

2.9 PET's advantages in neuroimaging

Neuroimaging has been used to image the brain non-invasively and to provide both structural and functional information. PET is steadily progressing and expanding understanding regarding the pathophysiological mechanisms of neurological and psychiatric diseases; it is also useful in the clinical management of patients. PET allows for in vivo, non-invasive, 3D imaging of functional disorders. In recent years, the non-invasive tomographic imaging of the brain with PET has improved through the use of dedicated instrumentation and advancements in radiopharmaceutical synthesis. The major advantage of PET is its ability to provide an absolute measure of regional cerebral blood flow; this measure is significant in cognition studies. Another major strength of PET is its ability to map the distribution of particular receptors in the brain using appropriate radioligands (i.e. radioactive chemicals that are lodged in the receptors and that behave like neurotransmitters). Furthermore, this method allows for the imaging and mapping of receptor regions (Kosslyn et al. 2001).

2.10 Dopaminergic areas in the brain

Dopamine plays important roles inside the brain, including in motor control, motivation, arousal, cognition, and reward. There are relatively few dopaminergic neurons (i.e. those neurons that have dopamine as a primary neurotransmitter)—about 400,000 in the human brain—and their cell bodies are confined to seven relatively small brain regions (Schultz 2007). These regions are assigned labels that start with the letter *A* (for *aminergic*). The regions A8 through A14 are the dopamine neurotransmitters (the regions A1 through A7 contain norepinephrine neurotransmitters) (Ferry et al. 2014). The dopaminergic regions are the substantia nigra, ventral tegmental area (VTA), posterior hypothalamus, arcuate nucleus, periventricular nucleus, and zona incerta. The substantia nigra is a small midbrain region that is part of the basal ganglia. In this region, the dopamine neurons are found mainly in a section called the pars compacta (cell group A8)—or nearby (group A9) (Björklund and Dunnett 2007). The dopamine is transmitted from the substantia nigra pars compacta to the dorsal striatum (specifically, the caudate nucleus and putamen). Parkinsonian syndrome results when a large fraction of neurons in this area have died (Christine and Aminoff 2004).

The VTA cell group (A10) is the largest group of dopaminergic cells in the human brain. The nucleus accumbens and prefrontal cortex (among other areas) receive projections from these dopaminergic neurons (Björklund and Dunnett 2007). Neurons in this area play a main role in reward and other motivational aspects. The striatum is involved in the highest levels of motor control, including motivation and decision-making; the nucleus accumbens is the limbic part of the striatum. Thus, the VTA's role in motivation and decision-making is structurally analogous to the substantia nigra's role in low-level motor control (DeLong and Wichmann 2010). The dopaminergic cells of the posterior hypothalamus (group A11) project to the spinal cord, but their function

is not well-established. There is some evidence that pathology in this area plays a role in restless-legs syndrome (Paulus and Schomburg 2006). Dopamine in the cells of the hypothalamus' arcuate nucleus (cell group A12) and periventricular nucleus (cell group A14) influences the pituitary gland's secretion of the hormone prolactin (Ben-Jonathan and Hnasko 2001). The zona incerta cells (group A13) project to several areas of the hypothalamus; these cells influence the gonadotropin-releasing hormones, which are necessary for activating the development of reproductive systems during puberty in both males and females (Ben-Jonathan and Hnasko 2001).

2.11 Dopamine receptors

Dopamine receptors are G-protein-coupled receptors that are commonly found in the central nervous system. Dopamine is the primary endogenous ligand for dopamine receptors. Dopamine receptors are involved in many neurological procedures, including motivation, pleasure, cognition, memory, learning, and fine motor control, as well as the modulation of neuroendocrine signalling. Abnormal dopamine receptor signalling or dopaminergic nerve function cause several neuropsychiatric disorders (Lalchandani et al. 2013). There are five subtypes of dopamine receptors: D1, D2, D3, D4, and D5. Another categorization has been suggested in which there are two families of receptors: the D1-like family (D1 and D5), and the D2-like family (D2, D3, and D4). The D1 receptors have extensive expression throughout the brain, and the D1 and D2 receptor subtypes are found at 10–100 times the levels of the D3, D4, and D5 subtypes (Ellenbroek et al. 2014; Hurley and Jenner 2006). The D2 gene product permits a short form (D2S) and a long form (D2L), the latter of which includes an additional 29 amino acids. The D1 and D2 receptors comprise the majority of dopamine receptors in the striatum (Cumming 2009). The D1-like family receptors couple to the Gs protein and activate adenylyl cyclase, whereas the D2-like family receptors are prototypical of the

G-protein-coupled receptors, which inhibit adenylyl cyclase and activate K⁺ channels (Missale et al. 1998).

2.12 PET tracers in the dopaminergic system

The dopaminergic system has been implicated in several neurological and psychiatric disorders. The evaluation of altered dopamine synthesis and receptor densities is essential in determining the mechanisms that underlie the pathogenesis of these diseases and of developing therapies for them. Various suitable radiopharmaceuticals are used in combination with PET to investigate these factors in vivo, including ¹⁸F-FDOPA, ¹⁸F-FMT, ¹¹C-dihydrotrabenzazine, ¹¹C-nomifensine, and various radiolabelled cocaine derivatives. These tracers can be used to measure dopamine synthesis and transport; such measurements are required to investigate presynaptic functions. In addition, [¹¹C/¹⁸F]-labelled tropane analogues are clinically used. Postsynaptically, the five subtypes of the dopamine-receptor family (D1 through D5) require the investigation of high-affinity PET radioligands. The tracers for the D1 receptor subtype are ¹¹C-SCH 23390 and ¹¹C-NNC 112, whereas ¹¹C-raclopride, ¹¹C-CMNPA, and ¹⁸F-DMFP are the usual tracers for the D2 and D3 subtypes (Sioka et al. 2010). For extrapyramidal D2-receptors, ¹⁸F-Fallypride and ¹¹C-FLB-457 are suitable PET tracers (Cervenka 2018; Elsinga et al. 2006). The [¹¹C/¹⁸F]*N*-methylspiperone radioligand shows a high affinity for the D4 receptor (Mach and Luedtke 2018). However, there is no suitable radioligand for PET imaging of the D4 receptor in vivo. Various promising clinical trial studies (both in vitro and ex vivo) could lead to a suitable D4-selective PET radioligand, however. The D5 receptor subtype is closely related to the D1 subtype, as the ligands for D5 also show high affinity for D1 as well. An issue related to imaging D5 in brain is that its density is quite low compared with that of the D1 subtype; as a result, no successful PET ligand for D5 has yet been reported (Prante et al. 2013).

2.13 Basics and concepts of PET tracer kinetic modelling

2.13.1 Overview

Quantitative radioactivity measurements are produced from a ROI, tissue, or organ. With respect to the appropriate selection of tracer and imaging conditions, the physiological characteristics of the ROI (blood flow, receptor concentration, etc.) significantly influence the measured activity values. TKM is meant to describe, in detail, the relationship between the measurements and the ROI's physiological or biochemical parameters while considering all of the biological factors that contribute to the tissue's radioactivity. Two factors contribute significantly to the radioactivity concentration in any ROI tissue. Firstly, the most important factor is the tissue's physiology or biochemistry (e.g. its blood flow or metabolism); the next most important factor is the input function, which controls the delivery of the tracer to the target tissue or organ. This is represented by a time course (which shows the varying activity over time following the administration) for the tracer's concentration in the blood or plasma. The relationships between these factors and radioactivity concentration in tissue can be described using mathematical equations; together, these equations comprise a model. The model is considered to be full if the prediction of the radioactivity concentration's time course is known; this information is usually extracted from the tissue's physiological or biochemical variables and from the input function. A simpler model could be used to predict only certain aspects, such as the initial slope, the area under the curve, and the activity concentration of both the ROI and a reference region from the tissue-concentration curve (Carson 2005).

There are no absolute rules regarding the essential components in designing a model, which can make the process very complex. A successful method for developing a model must consider limitations related to instrumental availability, statistics, and patient

logistics. Compromises must be made to establish a useful model; any model with 100% accuracy is likely to be impractical. Thus, a simpler model with less accuracy is often more useful. In model-based methods, knowing the tracer's behaviour and the study's conditions (e.g. the tracer administration, the scheme, the methods for scanning the blood, and the data collection and processing methods) can help in defining the physiological parameters (Carson 2005). Study conditions are used to create a dynamic data-acquisition protocol, in which multiple scans are performed after the tracer administration so as to provide functional information. Dynamic data acquisitions are used to extract physiological or biochemical parameters through the use of mathematical tools; this step is known as kinetic analysis. Dynamic data can be used to produce time-activity curves (TACs), which illustrate the change in the activity concentration over time for various ROIs, volumes of interest (VOIs), or voxels (Erlandsson 2011).

TKM analysis is based on a compartmental model of tracer behaviour and consists of a series of compartments. These compartments show the tracer concentrations in various regions, as well as the rate constants that govern the transfer of the tracer between these compartments. The model parameters can be determined using information about the tracer's delivery (as an input function); this information is represented by the time course of the tracer's concentration in the arterial blood or plasma. Scholars in various clinical areas (e.g. cardiology, oncology, and neurology) have found kinetic analysis to be very useful for quantification as part of diagnoses (Erlandsson 2011). The basic mathematical tools and concepts used in TKM are discussed later in this chapter.

2.13.2 Dynamic PET scan

The rate of metabolism which can be calculated by applying a pharmacokinetic model to dynamic PET data is the gold standard of PET quantification. This method requires at least 60 minutes; in addition, when used with a CT study, this method for example will cover field of view (FOV) around 70 cm × 15 cm in brain studies. One advantage of this method is that has high validity because it is a simplified quantitative method (Boellaard 2009).

2.13.3 PET image quantitation

Visual inspection of PET images is still the main interpretive tool for many diseases. This method is satisfactory, but in some cases, visual interpretations are challenging, which can affect the results. Thus, various quantification methods have been introduced to provide more accurate and less observer-dependent evaluations for clinical cases (Boellaard 2009). Quantitative techniques are important. Firstly, they ensure the accuracy of the interpretations as long as there are no physical artefacts. Secondly, they enable the use of the TKM methodology to model the distribution of a labelled compound in the body based on the tracer's time variance; this model subsequently can be used to estimate other physiological parameters (Meikle and Badawi 2005). During image reconstruction, the images' intensity should be proportional to the ROI activity concentration. This is preferable for comparison with different activity distributions in different regions, as it creates distinctions between normal and diseased tissue; this method is essential to dynamic and metabolic studies.

The image's voxel intensity is also proportional to the radioactivity in the voxel. It is often helpful to calculate the amount of radioactivity in a voxel or other volume in the ROI, which is known as PET image quantification (Cherry et al. 2012). There are

several methods for quantifying tissue radioactivity and uptake, and each is discussed below either briefly or in detail, as they relate to this research.

2.13.4 TKM in PET

A tracer's uptake represents its concentration during the acquisition and is dependent on the tracer's kinetics in a specific tissue. Kinetics require a characterization process that provides improved information from the biological data and images. TKM is meant to describe the relationship between the physiological parameters and the measurable data with regard to the uptake and tracer metabolism. TKM is based on mathematical concepts that can be applied to the tissue. The advantages and disadvantages of TKM are discussed in depth in the next chapter, as are the ways of developing such models. Many researchers have successfully applied TKM models in their analyses.

2.13.5 Modelling process

After selecting the radioactive tracer, several steps must be considered to ensure that the model is useful. These steps are illustrated in Figure 2-7 (Carson 2005).

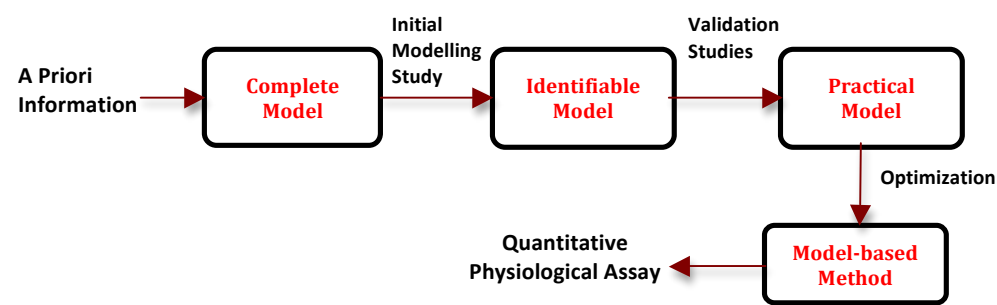


Figure 2-7. Steps for developing a model.

A priori information about in vivo tracer behaviour is essential to overcome statistical noise when specifying a complete model that involves many parameters. An initial modelling study is performed to design a simple model and to determine which parameters can be identified and developed. A validation step must then be performed to improve the model and to prove that its assumptions and physiological parameters are

accurate. After that, a simpler protocol can be applied for routine patient use. This step may involve limited blood measurements and simple data analysis. The optimization process follows; it involves determining the sources of error and reducing them so as to finalize the development of a model-based method for producing reliable physiological measurements. The characteristics of the instrumentation used in scans are important, as they affect the form of the model; the measurements' reconstruction algorithms, accuracy, and noise level could also affect the number of parameters that can be estimated (Carson 2005).

2.13.6 Types of tracers and models

Tracers are present in tissue at negligible mass concentrations, so they cause little or no change in the saturation of enzymes or receptors. Figure 2-8 shows the paths of a tracer after intravenous injection.

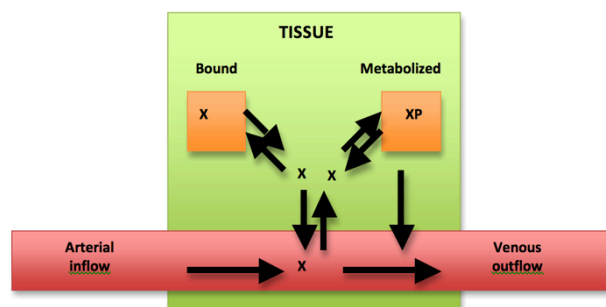


Figure 2-8. Tracer delivery, uptake, binding, and clearance in the ROI tissue.

The tracer in this example is delivered to the ROI tissue through arterial inflow and then carried away through venous outflow; the transfer occurs when it crosses the capillary membrane. In the tissue, the tracer may bind (irreversibly or reversibly) to intra- or extracellular sites; it can also be metabolized (XP in Fig. 2-8) into another chemical form and thus move out of the tissue and into the blood. Each tracer is designed to provide information about a specific function of the ROI, such as blood flow or metabolic processes. Although the physiological process under study is the primary factor in the control of tracer uptake and distribution, other factors also slightly affect

the concentration, distribution, and kinetics of receptor-binding radiotracers; these include regional blood flow, plasma–protein binding, capillary permeability, non-specific tissue binding, receptor association and dissociation rates, free-receptor concentration, the tracer’s clearance from the blood, the tracer’s metabolism, and the regional uptake of the radioactive metabolites. These factors have only a minor net effect if the tracer is well-designed, however. A tracer can be a direct radiolabelled version of a natural compound, an analogue of a natural compound, or a unique radiolabelled drug. The chemical features of the analogue compound differ significantly from the original compound, so the measured kinetics are different from that of the natural element; this needs to be corrected. Firstly, the relationship between the radiolabelled analogue material and the natural compound must be determined, and then the relationship must be assessed under various pathological conditions (e.g. the lumped constant in FDG) (Carson 2005).

Several approaches have been suggested for extracting useful physiological information from tissue radioactivity in PET images. All these approaches share basic assumptions, particularly the principle of mass conservation. The stochastic or non-compartmental approach requires minimal assumptions regarding the underlying physiology of the uptake and metabolism. These methods’ measurements do not require explicit details for all the specific pools or compartments that a tracer can enter. In contrast to the stochastic model, the distributed model provides a full description of the radiotracer, including its physical locations, biochemical forms, and concentration gradients within various physiological domains. Scholars have developed many distributed models for capillary–tissue exchange, which is noteworthy, as this exchange is usually the first step in the uptake of any tracer. Another approach, compartmental modelling (CM), is meant to reduce the complexities found in the stochastic and distributed models. Compartmental models provide some details about the underlying physiology but do

not include the concentration gradients. One of the most common applications of CM is for the mathematical description of a tracer's distribution in the body. The main principle of this type of modelling involves assigning organs or tissues (or groups of them) to individual compartments, after which the kinetics are defined both within and outside of each compartment. This is very useful when the TAC of blood or urine is the primary measurable data. In a compartmental model, if the tracer both enters and leaves the ROI through the blood, there is no need to consider other bodily regions when evaluating the ROI's physiological features (Carson 2005). Scholars have introduced several quantification models to provide more accurate results and more parameters; this allows for more knowledge regarding the distribution of labelled compounds inside the body. Figure 2-9 shows an example of the most common methods in PET imaging analysis, which are usually categorized as semi-quantitative and quantitative methods. Semi-quantitative methods include the standardized uptake value (SUV) and the ratio of tissue to normal (reference) tissue (T/N). These types of analysis do not require an input function or a dynamic image acquisition. The quantitative methods include fractional uptake rate (FUR), graphical analysis (GA), and CM; each of these requires an input function and dynamic images to ensure that the quantification analysis is complete (Turkheimer et al. 2014).

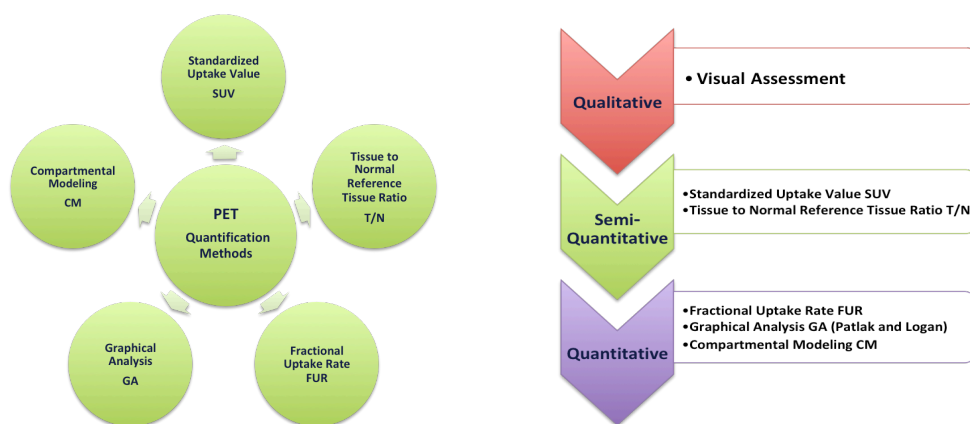


Figure 2-9. Common quantification methods in PET image analysis.

2.13.6.1 Standardized uptake value

SUV is one of the most commonly used methods in PET imaging quantification. Accurate SUVs are usually calculated from images of the targeted organ or ROI that have undergone physical corrections including AC, scatter, decay, deadtime and partial volume corrections. These images are created using special software that extracts pixel values from the images' uptake regions at any time but usually 1 hour or 90 min after injection is preferable where the tracer distribution is stable; there is some evidence suggesting that 2 hours may be a more appropriate waiting period for certain types of tumours (Mettler and Guiberteau 2011). SUV is defined by Eq. 2-1 below:

$$\text{SUV} = \frac{\text{Mean ROI activity (mCi/mL)}}{\text{Administered activity (mCi/body weight (g))}} = \text{grams/mL} \quad \text{Eq. 2-1}$$

SUV represents the PET tracer's uptake within the ROI, as measured at a certain interval after the tracer's injection and normalized to the dose criteria (e.g. body weight); Eq. 2-1 shows how to normalize SUV to body weight. The mean ROI activity represents the average activity concentration in the specified volume of interest or the maximum value. The administered activity is the dose of tracer that is administered after correcting for physical decay (Boellaard 2009).

2.13.6.2 Ratio of tissue to normal (reference) tissue

The T/N ratio does not demand cross-calibration of the PET scanner and the dose calibrator, and the PET data do not need to be corrected for physical decay. Thus, the T/N ratio is considered more robust than the SUV. The T/N technique is often the first option for brain-receptor studies, and it can be used before validating any model. In receptor studies, a reference tissue such as the cerebellum must be established; in diagnostic brain studies, the other hemisphere can be used to calculate an asymmetry index. For tumours, healthy tissue can be used as a reference when calculating the T/N

ratio. The limitations of this technique include the difficulty of finding ideal reference tissue and the significant noise in the data obtained from the tissue due to the low tracer uptake (Ciarmiello and Mansi 2016; Kostakoglu and Valk 2006).

2.13.6.3 Fractional uptake rate

FUR is a measurement of the rate of a tracer's movement from the blood into various organs. It is simply the fraction of the tracer that organs have taken up from the blood (per unit time). FUR is calculated as a ratio of tissue activity at time T to the integral of the plasma activity from time 0 to time T; it can be expressed as in Eq. 2-2:

$$FUR = \frac{C_{tissue}(T)}{\int_0^T C_{plasma}(t) dt} \quad \text{Eq. 2-2}$$

The unit of FUR is min^{-1} , and blood sampling is required from the injection until the end of scan. SUV can be calculated from the late PET scan. In this calculation, plasma TAC is integrated from the beginning of the injection time (0) to the midpoint of the PET time frame, either for each time (if the PET scan involves several frames) or for the middle time of the PET scan (if the scan has a single frame). The FUR value is obtained by dividing the mean tissue concentration by the integral of the plasma activity (Kotasidis et al. 2014; Rutland et al. 2000).

2.13.6.4 Graphical analysis

Another approach involves the integration of the differential equations that describe the kinetic models. This method can produce other equations and yield data that can be plotted in a graph. A straight line is then fitted to the points, and the slope and intercept of this line indicate various characteristics of the tracer. This approach is also termed *linearization* because it involves converting nonlinear parameters into estimated linear ones. This method is useful in voxel-based analysis as well (Erlandsson 2011). A method known as Logan GA (Logan et al. 1990) is used for reversible tracer's

behaviour; another method, Patlak plot analysis (Patlak and Blasberg 1985) is used for irreversible tracers. The selection of the quantification method includes trade-offs regarding bias, variance, and practicality. To increase the validity and accuracy of a chosen model, various iterations can be used a simplified model and a complex one, for example so as to compare the estimated outcome measures (Erlandsson 2011). More discussion of Patlak GA and the methods for selecting the appropriate model are covered in the following chapter.

2.13.6.5 Compartmental modelling

Serious assumptions are required in TKM. Firstly, the physiological processes that affect the measurements must remain in a static state. Secondly, the administered radioligands (tracers) must not affect the physiological or biochemical processes being investigated. Thirdly, the tracer concentration must be homogeneous within each compartment. Scholars have often used compartmental models to describe physiological or biochemical systems. In these systems, the tracer is transported between compartments, which are represented by separate regions in the body (e.g. vascular, interstitial, and intracellular space). The transfer rate from one compartment to another is proportional to the original compartment's concentration and the first-order rate constant. A differential equation system is applied to describe the compartmental model; in this system, each equation relates to the sum of all transfer rates (both to and from any specific compartment, i), thus forming the following equation (Erlandsson 2011):

$$\frac{d}{dt}C_i = \sum_{\substack{j=1,..,N \\ j \neq i}} (k_{ij}C_j(t) - k_{ji}C_i(t)); i = 1,..,N \quad \text{Eq. 2-3}$$

In this equation, $C_i(t)$ is the tracer concentration in compartment i , N is the number of compartments in the model, and k_{ij} is the constant rate of transfer of the tracer from

compartment j to compartment i . Compartmental models can be categorized as reversible or irreversible. In the latter type, at least one compartment does not have an outflow. A tracer's rate constants are usually termed as K_1 (capitalized) when the transfer is from the blood to the tissue and as k_2 (lowercase) when the transfer is from the tissue to the blood. Any additional rate constants in the model are referred to as k_3 , k_4 , and so on. K_1 corresponds to a clearance term and has a similar unit to that of blood flow: mL/min/mL or mL/min/g (i.e. mL of blood or plasma per minute per mL or g of tissue). On the other hand, k_i must be greater than or equal to 2 and is expressed in min^{-1} (Erlandsson 2011). This inverse time unit reflects the fraction of tracer molecules in a specific compartment that will move to another compartment each minute. The tracer's movement-rate constants are defined based on physiological interpretations of the source and destination compartments; this allows for the quantitative estimates or indices of the physiological parameters to be obtained. Estimation of one or more of these rate constants based on the tissue's radioactive measurements is the underlying goal of all modelling methods (Carson 2005). Figure 2-10 shows examples of various compartmental models in which the compartments are represented by rectangular boxes. The rate constants are labels on the arrows between compartments; the arrows also show the tracer's movement direction. The blood is usually considered a compartment and is accounted for with a primary data set, which is used to estimate the rate constants for the model. Blood measurements are sometimes treated as known values rather than as concentration values that the model needs to predict (i.e. the blood is not counted as a compartment) (Carson 2005).

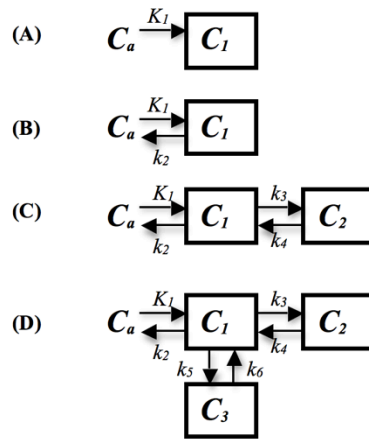


Figure 2-10. Examples of compartmental models. C_a is the tracer concentration in arterial blood, and C_1 , C_2 , and C_3 are the concentrations in compartments 1, 2, and 3, respectively. K_1 is the rate constant for transfer from the blood to the tissue, and k_2 , k_3 , and so on are the rate constants of the tracer movements between compartments. **(A)** is the simplest compartmental model; it shows only one tissue compartment, with irreversible uptake. This is used for radioactive microspheres or for tracers that are trapped in tissue. **(B)** shows one tissue compartment that exhibits reversible tracer uptake, which is common in tracer measures of local blood flow. **(C)** includes two tissue compartments, which is usually used when the tracer is either metabolized into another form (such as deoxyglucose) or returned to the blood. **(D)** is a three-tissue compartmental model, which usually represents a receptor-binding ligand; the compartments represent a free tracer, a tracer specifically bound to a receptor, and a tracer non-specifically bound to other tissue elements (Carson 2005).

The interpretation of the compartmental models starts by solving Eq. 2-3 with the Laplace transform tool. The resulting equation is commonly used in solving linear, first-order differential equations such as Eq. 2-3, and it can be defined as:

$$F(s) = \int_0^{\infty} e^{-st} f(t) dt \quad \text{Eq. 2-4}$$

In this equation, s is a complex Laplace-space variable. Complex compartmental systems can be solved and translated using the properties illustrated in Table 2-1 (Erlandsson 2011).

Table 2-1. Laplace transform properties.

Time domain	Laplace domain
$f(t)$	$F(s)$
k	k/s
e^{kt}	$1/(s - k)$
$ag(t)+bh(t)$	$aG(s)+bH(s)$
$g'(t)$	$sG(s) - g(0)$
$g(t) \otimes h(t)$	$G(s)H(s)$

In this table, k , a , and b are constants; t and s are variables; $g(t)$, $G(s)$, $h(t)$ and $H(s)$ are all derivation functions; and \otimes is the convolution operation.

The solution of a biological systems model is usually expressed as:

$$C_T(t) = H_N(t) \otimes C_a(t) \quad \text{Eq. 2-5}$$

Here, $C_a(t)$ is the input function, and $C_T(t)$ is the output function; \otimes represents the convolution operation, and $H_N(t)$ is the model-impulse response function. $H_N(t)$ has the following general form (Erlandsson 2011):

$$H_N(t) = \sum_{i=1}^N \phi_i e^{\theta_i t} \quad \text{Eq. 2-6}$$

Here, ϕ_i and θ_i are rate constants functions of the model, and N is the number of compartments. The number of model-tissue compartments is equal to the number of terms in the impulse equation. After this impulse function is determined, the rate constants and individual parameters can be estimated (Erlandsson 2011).

2.13.7 Input-function methods

The distribution of the tracer in the body during PET imaging is represented as a function of time and the ROI; it can be observed in the vascular system. The measured signal in the PET image can be produced from the labelled molecules as administered (as with the free radiotracer); accumulated and transformed within the cells (as in metabolism); rejected to the blood (as with metabolites); or excreted from cells, at which point the kidneys filter them out or they re-enter the cells (as in recirculation). The factors that affect the PET data include the administered tracer dose, the duration of tracer administration, the tracer's behaviour in tissue, and the data-collection time. The process of delivering the tracer to the tissue is a function of time, and it represents the

input (also known as the excitation); the data measured with a PET camera is the output (also known as the response). The input function is defined as the radiotracer's concentration in the blood, which is also called the blood curve or the plasma curve (Bentourkia 2011).

Many equations need to be applied to the input function in order to produce the output PET data. The input function is essential to any PET quantification process, but the importance of the measurement and analysis protocols also must be stated. The measured data is reconstructed in various time frames; in order to observe the uptake of the radiotracer, the first frame must be narrow (especially for a bolus injection). Errors in the shape and amplitude of the input function lead to inaccurate tissue data and biased constant rate values. For image-based TKM, several techniques can be used, including manual sampling, automatic sampling, and image-based input functions (Bentourkia 2011). The manual and automatic sampling techniques are based on blood samples collected during the scan. Due to that procedure's difficulty for the patients, we instead used the image-based technique to obtain the input function for our quantification project.

In the image-based technique, there is no need for blood sampling or for measurement or calibration procedures. There also is no or a little mathematical delay or dispersion in the input function; in addition, the limitation in PET's spatial resolution has a considerable affect. The image-based input function takes the same unit of the same tissue's TAC, which is expressed as the count per voxel per second or as Becquerels per voxel (Bentourkia 2011).

2.13.8 Standards and recommendations for PET quantification

The standards of the National Electrical Manufacturers Association (NEMA), number 2 (NU2) standardized the basic characteristics of a PET, or PET/CT, scanner. These standards allow for the evaluation of many features, including sensitivity, spatial

resolution, noise-equivalent count-rate curve, scatter fraction, counting-rate linearity, and image quality. This protocol standardizes the outcome of PET scans, but the differences between scans are still considerable due to variance in the patient-preparation methods, the acquisition settings, the reconstruction algorithms, and the data-analysis software. This explains why it is difficult to produce the same SUV across PET centres. The NEMA's NU2 recommendations for PET quantification reflect the chronological order of PET imaging scans, which is as follows: patient preparation, procedures and interventions, dose administration, PET acquisition, analysis of image quality and SNR, image reconstruction, clinical-image resolution, data analysis and SUV normalization, and QC of the instrumentation and personnel (Boellaard 2009).

Cardiff University's PET/CT systems follow the QC standards that the Institute of Physics and Engineering in Medicine (IPEM) established. These standards were published mainly to provide quality assurance programs and support for clinical PET/CT services and research. The standards describe the minimum recommended QC for PET and PET/CT, and they are based on consultations with relevant specialists as well as on a review of present practices. Report 108 is a useful reference for scientists in the PET services field; this report covers various aspects, including acquisition techniques, clinical applications, acceptance testing, requirements for QC testing, PET data management, image display, and additional equipment that is relevant to PET/CT scanning (Morgan 2012).

3 Literature Review

3.1 Introduction

Tracer kinetic modelling (TKM) and other PET quantification procedures, helps to represent acquired dynamic images in ROI tissue based on the molecular interactions of the radiotracer in this tissue. PET quantification refers to expressing images as an amount or number in addition to measuring or estimating the quantity of radioactivity from the images. In this thesis, the term is usually used to refer to the process of analysing dynamic images numerically to extract physiological parameters that are clinically beneficial in diagnosis or for monitoring diseases (Erlandsson 2011). Nuclear medicine imaging including PET and SPECT is a successful sensitive imaging modality that can provides in vivo assessment of pathophysiology and quantification measurements (Dickson et al. 2019). TKM can be applied either to a homogeneous ROI or to individual voxels if the noise in these voxels is within acceptable range. The parameters produced from a single voxel are averaged due to inhomogeneity of the cells. More precise kinetic parameters can be obtained if the voxels represent a homogeneous tissue (Bentourkia 2011). Several factors can affect the calculation of parameter values, including the imaging protocol, the kinetic model choice, and the choice of input function for the model (Lammertsma 2014).

In chapter 2, several quantification approaches to parameter estimation from the data were discussed, including model-based techniques, spectral analysis, and graphical analysis. Model-based kinetic modelling techniques (compartment models) have been validated by different approaches, such as biopsies, autoradiography, biochemical analysis, and in vitro experiments (Turkheimer et al. 2014). Compartment models allow isolated components of the signal measured to be reconstructed through applying

mathematical equations suited to the tracer behaviour in the targeted tissue. The images, which will be used for PET quantification, must be dynamic and start from the tracer injection time. The time frame should be optimal for both collecting enough photons to measure the physiological and/or pathological changes and for obtaining precise PET data. Spectral and graphical analysis are widely used due to their ease of use and rely on calculating statistical parameters (slopes and intercepts), which sometimes need to be rearranged to correspond to standardized parameters (Bentourkia 2011).

In this chapter, background information about the Patlak principle and sources of errors in PET quantification will firstly be described generally; then, errors in graphical analysis specifically will be discussed. Different methods and strategies proposed earlier by literature to improve parameter estimation and reduce bias and noise are reviewed as well. In addition, clinical studies using the Patlak technique in brain studies are also reviewed, focusing on PD studies that use ^{18}F -DOPA as a tracer along with blood sampling as a general input function, specifically with reference tissue. A review of clinical studies adds better understanding of image-processing strategies applied for diagnosing and evaluating disease progression. This literature review will close with a conclusion and recommendations as a consequence of the discussion and clarify how the research will proceed.

3.2 Background information

Graphical analysis (GA) or multigraphical analysis (MTGA) is a technique used for quantifying dynamic PET data that includes studying a tracer over time during its accumulation in tissue. The main assumption is that the tracer will accumulate in a specific anatomic region. If this accumulation continues, and there is never a net egress of tracer, then the tracer is known as an irreversibly bound tracer, and a **Patlak analysis** is suitable. If tracer accumulation washes out after a certain time period, the tracer is considered a reversibly bound tracer, and a **Logan analysis** is more appropriate (Logan et al. 1990; Patlak and Blasberg 1985). Figure 3-1 shows a summary of the graphical analysis options.

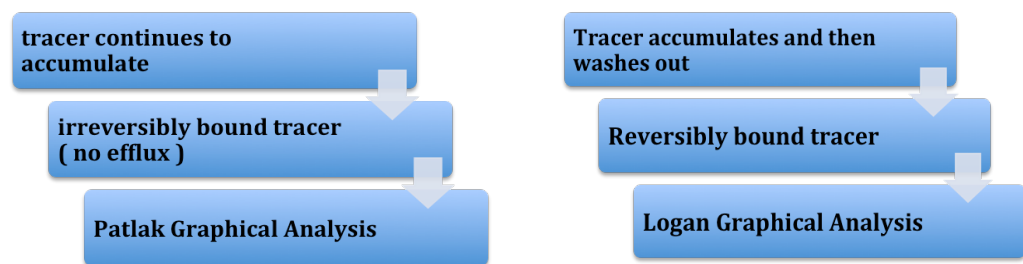


Figure 3-1. Summary of graphical analysis characteristics and tracer behaviour options.

The input data required for GA include a dynamic series of tomographic PET data (images) and an input function or time-activity curve (TAC) of the tracer concentration in the blood. This technique has been used for many neurotransmitters (^{18}F -F-DOPA, ^{18}F -FMT, ^{11}C -raclopride, etc.), metabolism markers (^{18}F -FDG), and even cardiac applications. The underlying goal of this type of GA is to reduce a series of observations to a single value that can be compared across subjects (Patlak and Blasberg 1985). Since the concentration of most PET tracers in tissue changes over time, a single high-statistic image is not appropriate. On the other hand, an image acquired over a short time period with minimal change in tracer concentration will have relatively poor

signal, or low noise qualities. Thus, various graphical approaches have been developed to use short time frames with acceptable temporal resolution, while still effectively using all of the events counted over an extended period of time (Logan 2003).

GA is based on combining the tissue region of interest and arterial plasma tracer concentration curves into a single curve that approaches linearity when certain conditions are reached. With traditional regression methods, the data can be plotted in a graph, and the line can be fitted to the linear phase. The slope of the fitted line represents the net uptake rate of the tracer or the volume of distribution (Patlak and Blasberg 1985; Patlak et al. 1983).

In some instances, the arterial plasma input can be replaced by a reference region curve. One feature of GA is the independence of any particular model structure, although the slope can be interpreted as a combination of model parameters for some model structure. Munk (Munk 2012) recommends using *vi*-plots to study at which time point the quasi-steady state is reached, allowing Logan or Patlak linear fitting plots. The *vi*-plot shows the time course of the instantaneous distribution volume and the instantaneous influx rate, plus visualises physiological information that facilitates model selection. Direct physiological interpretation appears on both axes of the *vi*-plot and shows kinetic parameter in close agreement with non-linear kinetic modelling estimates. The Patlak option is a graphical method that can analyse irreversible tracer ^{18}F -FDOPA images and is used to diagnose and monitor PD.

3.2.1 Principles of Patlak analysis

Patlak analysis does not depend on any specific compartmental model configuration for the tracer used. The minimal assumption is that the tracer's behaviour can be approximated by two compartments: a "central" (or reversible) compartment, which is in rapid equilibrium with plasma and must remain stable, and a "peripheral" (or

irreversible) compartment, where tracer enters without leaving during the measurements (Patlak and Blasberg 1985; Patlak et al. 1983).

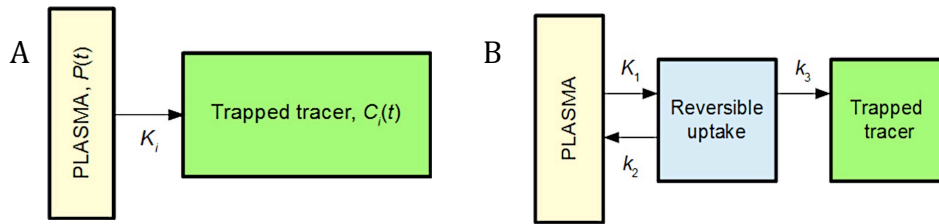


Figure 3-2. (A) Example of the irreversible compartment where the tracer is trapped in the ROI. (B) Two compartmental models, including both reversible and irreversible compartments.

This tracer movement can happen after the initial sharp concentration changes, when the plasma curve (input function) falls slowly enough for the tissue compartments to follow. Any number of reversible compartments can exist, where the tracer can come and go. After some time, the tracer concentrations in these compartments will start to follow the tracer concentration changes in plasma (the ratio does not change). Then, any change in the total tissue concentration (measured by PET) per plasma concentration represents the change in irreversible compartment(s) (Lammertsma 2014). The amount of tracer in the ROI accumulates according to the Patlak equation (Patlak and Blasberg 1985):

$$R(t) = K \int_0^t C_p(\tau) d\tau + V_0 C_p(t) \quad \text{Eq. 3-1}$$

t : time after tracer injection.

$R(t)$: amount of tracer in the region of interest

$C_p(\tau)$: the concentration of tracer in plasma or blood during the scan time.

K : the clearance determining the rate of entry into the irreversible compartment, represented by K_i as well (influx rate).

V_0 : the distribution volume of the tracer in the central compartment.

The first term of the right-hand side represents the tracer in the peripheral compartment, and the second term is the tracer in the central compartment. Dividing both sides by $C_p(t)$ obtains:

$$\frac{R(t)}{C_p(t)} = K \frac{\int_0^t C_p(\tau) d\tau}{C_p(t)} + V_0 \quad \text{Eq. 3-2}$$

The unknown constants K and V_0 can be obtained by linear regression from a graph of:

$$\frac{R(t)}{C_p(t)} \quad \text{and} \quad \frac{\int_0^t C_p(\tau) d\tau}{C_p(t)}$$

3.2.2 Making plots with Patlak equations

In statistics, linear regression is an approach for modelling the relationship between a scalar dependent variable y (criterion variable) and one or more explanatory variables (or the independent variable the predictor variable) denoted as x . When there is only one predictor variable, the prediction method is called simple regression. In simple linear regression, the predictions of y when plotted as a function of x form points. Linear regression consists of finding the best-fitting straight line through the points (see Figure 3-3 (A)). The best-fitting line is called a regression line. The black diagonal line in Figure 3-3 (B) is the regression line and consists of the predicted score for y for each possible value of x . The vertical lines from the points to the regression line represent the prediction errors (Montgomery et al. 2012).

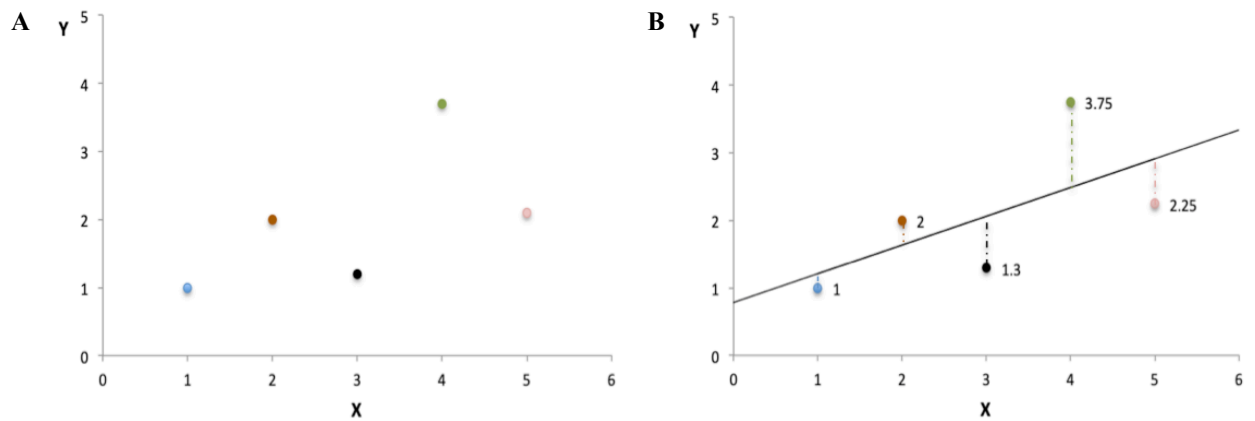


Figure 3-3. (A) Example of data represented by points on the plot (B) Shows the best fitting line (regression line) between plotted data.

The first two points in Figure 3-3 (B) is very near the regression line, so their prediction errors are small. The green point is much further away from the regression line; therefore, its prediction error is large. The Patlak plot becomes linear during the equilibrium in tracer concentration between the plasma and reversible compartment. The slope of the linear phase represents the net transfer rate K_i (influx constant) and represents the amount of accumulated tracer in relation to the tracer in plasma. The y-axis of the plot contains the ratio of tracer concentrations in tissue to that in plasma (distribution volumes). On the x-axis is the ratio of the integral of the plasma concentration to the plasma concentration. It may be possible to use a reference region instead of a plasma concentration curve (ex. the cerebellum in FDOPA studies) (Gunn et al. 1997; Lammertsma et al. 1996). The reference region contains only reversible compartments and must be in equilibrium with the plasma. The reference region can be included in the model, and the plasma curve is cancelled out (Patlak and Blasberg 1985). In practice, the only difference in the calculation using plasma input is that the plasma curve is replaced with a reference region curve.

Several conditions exist when choosing the reference region tissue to use as an input function in PET quantification: the reference region has no specific uptake of the radioligand, the uptake must not be affected by disease processes or treatment, and the

non-specific binding must be similar for both the reference region and regions of interest. The reference region chosen should be near the tissue of interest so it will be available in the same PET images. The ratios of the reference tissue and plasma input curves must be in equilibrium, called steady state or quasi-steady state; at this time point, linear fitting can be allowed for Patlak plots (Munk 2012). This approach is still a preferred analysis method due to its ease (it is non-invasive) and low labour cost, which makes it possible to use in small PET centres. In chapter 4, these methods of quantification will be discussed in steps, with ^{18}F -FDOPA selected as the tracer for our clinical trial and quantification research project.

3.3 Sources of errors in PET quantitative analysis

GA involves converting equations into linear plots, and the slope of the resulting fitted line represents the tracer binding measurements. The slope is related to the model parameters after making assumptions about the structure for that model (Logan 2000). Despite the ease of GA, however, some problems are encountered in GA that could affect its accuracy. These problems include separating the tracer activity between delivering and binding (Logan 2000); limitations to reference tissue options, as they are available for only a few brain receptor tracers; and the spillover or scatter of radioactivity from adjacent tissues (Carson 2005). Another issue that produces negative bias in GA is that the noise level of the tissue tracer concentration may affect the model's parameter estimation (Kimura et al. 2007; Zhou et al. 2010). Several approaches have been proposed to remove or reduce the bias caused by noise in PET data, which are all applicable to input functions obtained by blood sampling from reference tissue (Ichise et al. 2002; Joshi et al. 2008; Logan et al. 2001; Varga and Szabo 2002). However, the proposed methods remove only part of the bias or removed bias at the expense of precision, and were validated only in Logan plots, without application in Patlak analysis. Errors in GA can come from three sources: design of

acquisition protocols, physical aspect errors, and data analysis errors. Sources of error in PET quantification in general will be discussed in detail in the following sections of this chapter. Then, errors and limitations related to the Patlak method will be reviewed in another section.

3.3.1 Acquisition protocol design

The half-life, amount, and injection duration of the tracer all affect the images. The half-life should be enough to produce images with contrast. With no deadtime issues and after applying the appropriate corrections, the measured signal is proportional to the amount of the injected dose, considering the saturation in receptors or transporters and the demand limitations (Carson 2005). The duration of PET data collection must be optimal. The first frame of dynamic imaging should be shorter than later frames to give a better explanation of the tracer uptake (tissue perfusion; K_1 rate constant). Later frames usually take a longer time because the radiopharmaceutical reach the optimal distribution in tissue and allows better temporal resolution and SNR, and they allow for more variations in the signal intensity as well, so the optimal duration of the scan must be considered (Bentourkia 2011). Patient preparation has an essential role in obtaining accurate PET data. The subjects sometimes need to be fast, cease medication before the study, and should sit comfortably on the scanner bed without moving until the scan's completion. A patient moving during the scan could easily degrade the data, neck and leg support is always recommended. Explaining the scan procedure and the patient emptying his or her bladder could facilitate the scan procedure and help to gain precise data. Patients who have claustrophobia or issues with blood samples being drawn are usually excluded from quantitative studies (Boellaard et al. 2015). Parameters/settings and the methods used during PET acquisition, image reconstruction, and data analysis play main roles in the quantification of PET studies (Hogg and Testanera 2010).

3.3.2 Physical aspects data errors

PET imaging playing an important role in the diagnosis and monitoring response to treatment. Significant improvements have been achieved to meet the challenge of improving the PET modality performance. using quality assurance (QA) programmes when using PET/CT systems, including quality control (QC) procedures is a legal requirement and must be followed. The subsequent QA programme includes periodic service visits, regular calibration for PMTs, a timing calibration for coincident events, and detector normalization (Hogg and Testanera 2010). Daily QC should be performed before starting the scan to ensure there are no errors that could produce inaccurate data. Applying QA and QC programmes successfully will reduce the likelihood of scanning patients with malfunctioning equipment, which will reduce image artefacts (Hogg and Testanera 2010). Accurate transmission measurement is essential for attenuation and scatter corrections, as pitfalls in transmission measurement will lead to less accurate image . AC based on CT and the scatter will produce substantial changes in TAC and provoke the smoothing of neighbouring voxels. The accuracy of the emission sites' positioning could be affected by nonlinear photon emissions (diverging from 180°) and positron displacement (1 mm or less), with effects including marginal uncertainty. Using a cylinder phantom filled by a uniform concentration of radioactivity will help to verify the operational integrity of the PET system, maintain consistent and high image quality and minimize chances for artefacts (Bentourkia 2011; Boellaard et al. 2015; Daube-Witherspoon et al. 2002).

3.3.3 PET data errors

PET data errors can be categorised into data processing and data analysis errors related to quantitative PET measurements (Lammertsma 2019). Data-processing corrections can be performed before or after image reconstruction. Before image reconstruction and at the level of grouping sinograms or projections, a balance should be performed between the image statistical quality and the spatial resolution, as they have an inverse relationship. Another compromise during the reconstruction is to sort high-resolution images with noise to one side and low-noise smooth images on the other side. Smoothing images with less noise allows a suitable fit for the PET data in kinetic modelling while minimizing variation in the parameter values at the same time (Bentourkia 2011). The variation directly affects the value of K_i , which is inversely proportional to the integration of the input function and proportional to the signal rise in tissue TAC, and could cause errors to other values (Selivanov et al. 2001).

Organ or patient motion could introduce uncertainty into parameter estimation as well as heterogeneous voxels due to tissue motion. Homogeneous tissue is a requirement to obtain accurate TAC in a quantitative process. The aim of applying kinetic modelling to the images is to appropriately fit the parameters to the PET data. Thus, decay correction and delineation of tissue on images to be modelled must be considered to prevent errors in TAC (Bentourkia 2011).

Other corrections that should be performed during PET image reconstruction include detector efficiency (normalization), system dead time, random coincidences, scatter, attenuation, and sampling non-uniformity (Boellaard 2009; Delbeke et al. 2006). PET data correction is mandatory to achieve high quantitative accuracy. Factors like detector dead time, variable detector efficiencies, scatter and random coincidence events, and limited image resolution can significantly undermine quantitative accuracy and possibly result in failing to resolve small tissue regions accurately (Markiewicz et al. 2018;

Meikle and Badawi 2005). Additional corrections emphasized by Vaquero and Kinahan (2015) include, in rough order of effect size, patient movement, geometry-based variations in efficiency, signal gain, energy resolution, and event positioning.

The data-analysis stage starts by defining the ROI and input function data (blood or reference tissue activity), to be able to extract the quantitative measurements. Several methods are available to draw the ROI, including manually drawing contours and semi-automated and fully automated methods based on PET and/or MRI templates that are usually provided by recent processing software. A special PET template for a specific tracer can also be generated for clinical and research purposes. It should be considered that different ROI methods can lead to different quantitative outcomes (Boellaard et al. 2004). A consistent ROI methodology should be used for images during a longitudinal study to avoid differences in measurement outcomes (Shankar et al. 2006).

Dynamic PET images require blood samples for quantitative analysis to define the radiotracer blood clearance and specific biological analyses (e.g. glucose concentration in FDG studies) and to determine radiotracer metabolites. An automated blood sampling system can perform this process, in which blood is collected by vascular access and counted in an external activity-counting system. The blood counter system must be calibrated with the scanner to relate the resulting activity information to the image data. A phantom measured using a dose calibrator (with known activity) is imaged in the PET scanner, with several samples from the phantom counted in the blood system counter.

The values obtained from all counting sources are used to calculate the standard units of activity concentration, such as kBq/ml (Muzi et al. 2012). Counting the blood activity provides a direct measure of tracer clearance and availability for tissue uptake. Samples are collected usually about 20–30 times from the arterial vessel, for routine quantitative analysis of a dynamic PET image immediately after bolus injection of the radiotracer. Blood sample measurements are used as an input function and must be robust and

reproducible, as any failure or change in these measurements will lead to failed data analysis for the experiment (Turkheimer et al. 2014).

Replacing the arterial input function with a tissue concentration has been validated and can be used in certain conditions, as mentioned earlier. Sometimes called a reference tissue or image-derived input function (IDIF), it is an alternative to arterial blood sampling, but the method must be validated with the arterial input function before being used clinically (Christensen et al. 2014). However, some limitations with this method include the availability of few radiotracers and sometimes requiring blood samples to be collected unless a form of calibration is performed (Zanotti-Fregonara et al. 2011; Zanotti-Fregonara et al. 2014).

Another issue resulting from using image-based input functions is the partial volume effect (PVE), which is caused by image-sampling factors, where the image voxel might contain only part of the ROI tissue. The PVE is also caused by low scanner spatial resolution and can lead to blurred images. PVE can severely compromise both visual and quantitative PET and reduce the ability to map underlying physiological processes accurately (Dickson et al. 2015). Tumour and brain studies usually have this effect as a spill-out of radioactivity from a hot region into adjacent tissues, causes underestimation of tracer uptake, and spill-over (spill-in) into VOI in other studies, leading to overestimation of the uptake (Aston et al. 2002). A study of the PVE's impact on ^{18}F -FDOPA brain imaging shows that PVE leads to severe underestimation of K_i in certain brain structures (Rousset et al. 2000). With PVE, hot lesions sometimes appear to have reduced activity (less aggressive) and to be more spread out and larger in images than in actuality. Due to the negative impact of the PVE on images, partial volume correction (PVC) becomes necessary for accurate quantitative measurements. PVC is critically important for aging studies, where apparent reduction in metabolic activity usually disappears after applying PVC (Giovacchini et al. 2004). PVC can improve quantitative

accuracy and provides better differentiation between normal and abnormal studies (Dickson et al. 2015).

When the point-spread function (PSF) is known for the scanner, more corrections can be achieved. Clinical studies have used PSF in the image-reconstruction process as an alternative to PVC but with possible serious image artefacts (Munk et al. 2017). Two approaches can be implemented to perform PVC. The first method is called geometric transfer matrix (GTM), introduced by Rousset et al. (2008) and Rousset et al. (1998). This correction assumes that the volume of images is separated into homogeneous uptake VOIs and that by knowing the PET scanner resolution, the contaminated mutual signals in these VOIs can be calculated and corrected. Information derived from high-definition morphologic images could be used to improve the PET images' quality. Structures can be much better delineated in MRI-guided PET PVC for real brain data. In addition, MRI-guided PET image filtering can produce less noise in images and less bias; plus, it can reduce the coefficient of variation (Yan et al. 2015). The second approach is to use MRI in addition to PET images. It is assumed that white matter (WM) and grey matter (GM) in an MRI brain image have homogeneous uptake levels. All image pixels are categorized into WM or GM segments; then, the spill-out from WM to GM and from GM into surrounding tissues can be estimated based on these segments and the PET scanner resolution (Giovacchini et al. 2004; Müller-Gärtner et al. 1992).

3.4 Sources of errors in Patlak analysis

The main limit of Patlak analysis is the bias introduced in the parameter estimations obtained from the images. This bias is caused by statistical noise during the regression analysis plus the noise in the images themselves. Also, noise can introduce bias into the distribution volume, which is the slope of the graphical analysis of reversible tracers. For irreversible tracers, if the Patlak model does not fit properly the data, bias can be

introduced into the output parameters. Bias is introduced into linearized equations from noisy data because the error term exists at any given time point (Abi-Dargham et al. 2000). The graphical method, on average, will underestimate the GA parameters, and the effect on any data set will depend upon the nature of the noise. When one particular data set diverges in a non-random way from the original data, the analysis methods will show an obvious bias.

Another issue with GA is the difficulty of obtaining true estimates of the tracer with slow kinetics that have a short half-life, such as C^{11} (Logan et al. 2001). Simulated noise with zero mean, which is similar to the noise within PET data, causes the graphic technique to underestimate the outcome measure slope systematically, and the amount of underestimation increases proportionally as the standard deviation of the noise increases (Slifstein and Laruelle 2000). Estimates using ordinary regression line estimation (OLE) will be correlated with the activity rate from blood to tissue. With a low amount of activity moving to the ROI, the estimates will be lower, and the noise level will become larger, which will lead to underestimating the GA parameters (Kimura et al. 2007). The introduced bias is caused mainly by the statistical noise in the ROI activity concentration involved in the GA equations, and the determination of t^* , which is the equilibration time where activity ratio between ROI and reference become constant, also affects the estimates' accuracy (Ikoma et al. 2008). The underestimation induced in GA analysis can reduce contrasts in the binding potential (BP) estimates among ROIs and reduce the statistical power of discrimination of populations of interest by a specific tissue BP (Zhou et al. 2008; Zhou et al. 2010).

PVE influences Patlak analysis negatively on the slopes due to the loss in counts produced by the blurring of counts from the ROIs. Freedman et al. (2003) found a disagreement between their clinical data and the tumour sizes, suggesting that the

blurring of counts in the tumour ROI is time dependent, consequently affecting the Ki value of Patlak analysis.

3.5 PET imaging quantification methods in PD with 18F-FDOPA tracer

FDOPA has been used for brain imaging for many years. The first PET study to use FDOPA in brain imaging was conducted in 1983 (Garnett et al. 1983). The study showed a localized tracer in the striatum and that only 1% of tracer entered the brain. FDOPA is used extensively in diagnosing Parkinson's disease (PD), addiction, schizophrenia, and attention deficit hyperactivity disorder (ADHD). PD is a common progressive neurodegenerative disorder characterized by progressive damage of the dopaminergic neurons in the brain striatum (Leung 2011). Tremor, rigidity, and bradykinesia are the clinical symptoms of PD. When at least 50% of the dopaminergic cells are lost, some or all of these symptoms occur. Two of these syndromes being present will confirm a diagnosis of PD. The loss of dopaminergic cells is associated with exhaustion of striatal dopaminergic transporter (DAT) (Gerasimou 2006). In patients with bilateral PD, FDOPA showed bilateral reductions of the influx constant in the caudate and putamen compared to normal subjects (Vingerhoets et al. 1994). FDOPA allows the monitoring of PD progression, progression and the evaluation of neuroprotection therapies, and of early diagnosis (Leung 2011). In this section, studies about FDOPA quantification in brain imaging with patients with PD will be reviewed, and the quantification approaches used will be discussed.

Using the keywords “¹⁸F-FDOPA” (in all chemical name forms) and “quantification” in the PUBMED database shows few articles about quantification methods used for FDOPA images. FDOPA has been used as an investigation tracer for many years in neuroimaging, but few methods of quantification have been suggested. Among the conducted studies, few models have been suggested and developed to quantify the

images. The differences between these models are usually based on the assumptions made and parameters that are estimated (Dhawan et al. 1996).

Wahl et al. (1996) proposed a mathematical approach that includes designing a two-compartment, three-parameter model relating the radioactivity in blood to the radioactivity in the brain, and Patlak plots are used as well. The compartmental model had better data fit than Patlak plots. The models used were usually categorized into graphical analyses or compartmental analyses. A number of investigators have used graphical techniques to answer clinical questions (Brooks et al. 1990; Chan et al. 1992; Eidelberg et al. 1993; Martin et al. 1989). The main purpose of Wahl et al.'s study was to investigate the simplest compartmental model that would fit the measured time course of radioactivity in the striatum after F-DOPA injection. In total, 28 subjects between the ages of 21 and 70 volunteered in this study. Six subjects were normal, while 20 subjects were diagnosed for idiopathic Parkinson's disease for 3–5 years. Two subjects fulfilled DSM III (Diagnostic and Statistical Manual for Mental Disorders) criteria for schizophrenia. Blood samples were collected during each scan after a bolus injection of F-DOPA at different time frames. Each scan lasted 2.5 hrs, and radioactivity in plasma was counted and corrected for the time of injection. The ROIs were placed to the right and left of the striatum, and the time course of activity was expressed in counts per second per pixel for each region. All counts were corrected for injected dose and were expressed in the same units used for the plasma counts. Additional rate constants or compartments did not significantly improve the fit to the measured data. The influx constants of the compartmental and graphical methods showed excellent agreement and good correlation (Wahl and Nahmias 1996). Their study yields useful mathematical approaches and results about quantifying the FDOPA using compartmental modelling and/or graphical analysis. However, the data will only support a two-compartment, three-parameter model for the striatum; plus, the study

could reveal more accurate results if the FDOPA model is only applied on Parkinson's and normal patients. Moreover, recent studies suggest using entacapone and carbidopa to inhibit causes of metabolite products (Heiko Schöder 2013), which have not been used. The study analyses the arterial blood sampling method only and does not include image-based input functions.

Dhawan et al. (1996) studied three normal volunteer subjects and five classical Parkinson's disease patients (mild/moderate) without dementia. The study was based on a model suggested by Kuwabara et al. (Gjedde et al. 1991). The aim of the study was to address the issue of FDOPA metabolites by performing two scans for each patient, with ^{18}F -FDOPA and then 3OMFD. Before the FDOPA scan (1.5 hr) the subjects had received 200 mg carbidopa. Arterial blood sampling and plasma centrifugation were applied with each subject in the study. The kinetic measures were obtained by applied graphical analysis and tissue to reference tissue ratio methods. From a practical standpoint, the authors suggested using GA to calculate K_i in the striatum rather than calculate it from the compartmental model. Complete pharmacological suppression of 3OMFD formation by tolcapone was suggested to simplify the FDOPA quantification analysis model. The study illustrated that increasing the parameters number will rarely improve the curve fit; in contrast, the number should be reduced by further assumptions.

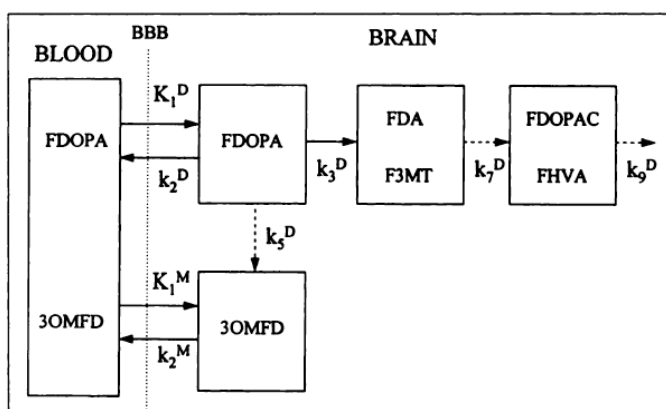


Figure 3-4. The compartmental model suggested by Gjedde et al. (1991) and applied in Dhawan et al. (1996) study shows FDOPA and its metabolites.

Ruottinen et al. (1995) studied entacapone use in advanced Parkinsonian patients and healthy controls using a FDOPA tracer. All subjects in the study received carbidopa (150 mg) and had two PET scans performed, with and without (baseline) entacapone. Arterial blood samples were collected for further analysis during the PET scan. ROIs were drawn on the head of the caudate, the putamen, and the occipital region (grey and white matter) as reference regions due to the lack of dopaminergic neurons. This reference region activity was considered non-specific uptake and was assumed to be equal to the striatum non-specific activity. The striatal structures represent the activity concentration 20-90 minutes after FDOPA injection. The average concentration for each ROI was calculated and averaged before statistical analysis. Based on other studies (Leenders et al. 1986; Martin et al. 1986; Melega et al. 1991), the authors considered the radioactivity concentration in the striatal structures to consist of FDOPA and FDOPA metabolites. Patlak GA was used to calculate the metabolic rate of FDOPA in striatal regions, using the occipital region as a reference (input function).

Dhawan et al. (2002) compared the ratio method to the GA for FDOPA uptake in striatal structures. They investigated 21 patients with moderate PD and performed a dynamic scan for 100 min after injection. All of the frames were realigned to the images at 55 min using the Statistical Parametric Mapping software (SPM99). Images taken between 40 and 100 min were averaged. The values of the right and left sides of the reference (occipital region) were averaged to reduce the noise. The TACs of the caudate, putamen, and occipital regions were computed by using single-slice PET images, and striatal-to-occipital ratio (SOR) values were also generated for each region. The SOR was calculated every 10 min for frames 65–95 min after injection. Graphical analysis over 40–100 min was performed to calculate K_i . Data from the PD patients were compared to data from the healthy group using discriminant function analysis (F-test). SOR versus K_i values was correlated at late images between 65 and 95 min, and

the highest was correlation was at 95 min. Both parameters can be discriminated between PD from the healthy subjects in both sides of the striatal structures. The study recommends performing SOR and Ki analysis separately for the anterior and posterior parts of the putamen. The SOR is used as index with which to map the changes in FDOPA uptake after therapeutic treatment (Nakamura et al. 2001). For the PD subjects, it was difficult to decide which side of the brain was more affected. The correlation between SOR and Ki suggested that these parameters can reflect PD progression in similar quantitative manners, which has been validated before (Vingerhoets et al. 1996).

In another study performed by Whone et al. (2004) on a data set obtained from six PET centres worldwide to analyse the FDOPA scans, images were analysed after a randomized controlled clinical trial in those centres, to compare ropinirole to the L-DOPA treatment (Whone et al. 2003). The group size was 186, and the analyses were conducted at a single site. The aim was to provide further details about centralized PET analysis. A standard method was used to assess the FDOPA uptake, by assuming only mono-directional uptake via the exchangeable pool from the blood into the basal ganglia. The influx rate constant (K_i), which measures the radiotracer accumulation rate, was obtained by applying the Patlak technique. FDOPA PET was performed between 4 weeks and 3 months after starting the medication. The mean percentage reduction in the side-to-side averaged putamen FDOPA influx constant (K_i) between both scans (baseline and follow up) was the primary outcome (Whone et al. 2004). All data were in 3D, and dynamic data were obtained from the start of injection; the entire time series lasted at least 90 min. At each centre, the standard manufacturer-supplied 3D reconstruction programme provided with the camera was used for image reconstruction. Each site selected their preferred method from the options supplied with their programme. The fully 3D filtered back projection algorithm was used in all centres for the reconstruction procedure. Specific FDOPA influx constants (K_i) were created

for the whole brain on a voxel-wise basis as parametric images, and the input function was obtained from the occipital cortex as the reference region. IDL software (Interactive DATA Language; Research Systems International) was used to form the parametric images, which was validated in another study (Rakshi et al. 1996). For each pixel individually, the net influx rate constant (K_i) was calculated within the range 30–90 min. The outputs of this program were a parametric whole brain volume showing the net influx rate constant (K_i) and an image of the integrated FDOPA signal from 30 to 90 min (ADD or summed image), both represented in Figure 3–5 (Whone et al. 2004).

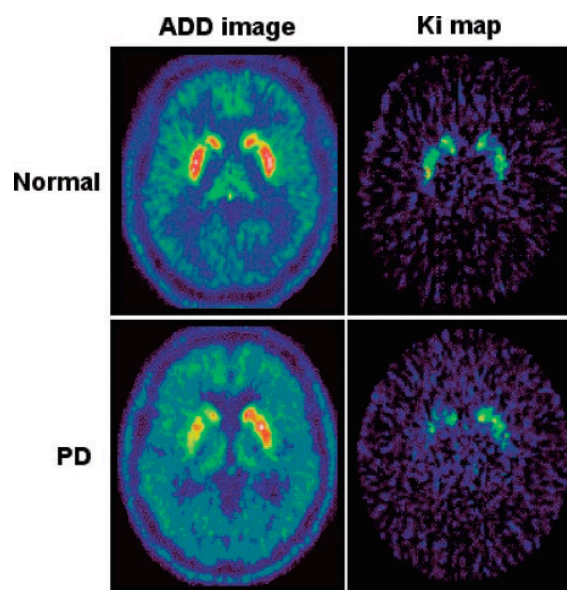


Figure 3-5. ADD (summed) and net influx rate constant (K_i) maps of single slices from a healthy subject (top) and a subject with PD (bottom). The subject with PD shows reduced uptake in the caudate and putamen, which is greater on the right-hand side (Whone et al. 2004).

In terms of reducing the variations in this study, standards were establishing for ROIs to be applied to the data sets. A single template of predefined volumes of interest was used and applied to each spatially transformed parametric image. SPM99 software (Veltman and Hutton 2001) was used for spatial normalization by applying the software’s algorithm to transform each individual K_i image to the Montreal Neurological Institute (MNI) space, similar to the MRI template space in SPM99. This normalization process allowed the same ROIs to be assessed between pairs of scans. The K_i maps were also analysed using SPM software to localize significant mean differences between the

baseline and follow-up scans by investigating the whole brain imaging volume for each subject in the two groups based on the type of medication (L-DOPA or ropinirole). The putamen FDOPA signal decline was significantly (one third) slower in the ropinirole group compared to the L-DOPA group.

Bruck et al. (2009) studied the progression of striatal dopaminergic function among 16 subjects with PD who underwent three FDOPA scans over a follow-up time of 5 years. The smallest uptake values were found in the dorso-caudal part. The rate of decline in the contralateral putamen was faster and significantly changed in the early stage of the disease, with annual decline in K_i of $0.5 (x 10^{-3} \text{ min}^{-1})$, on average, during the first 2 years and $0.2 (x 10^{-3} \text{ min}^{-1})$ during the subsequent 3 years. In the caudate, the rate of decline was slower than in the putamen and did not change significantly during the follow-up time. The annual decline in the contralateral caudate was $0.1 (x 10^{-3} \text{ min}^{-1})$ between the baseline and 2 years and $0.3 (x 10^{-3} \text{ min}^{-1})$ between 2 and 5 years. All subjects were given 150 mg carbidopa to exclude structural abnormalities; for co-registration purposes, all subjects underwent MRI scans. A voxel-based statistical analysis was performed using SPM and Matlab. Parametric images were calculated with the Patlak GA method. ROIs were defined on the co-registered MR image, which was in the same standard space as the subjects' PET images. Putamen and caudate nucleus ROIs were defined bilaterally, and the putamen was divided into the following sub-regions: the dorsal part of the rostral putamen, ventral part of the rostral putamen, dorsal part of the caudal putamen, and ventral part of the caudal putamen. The head of the caudate nucleus was divided into the dorsal and ventral caudate. The K_i in the time range from 15 to 90 min following the injection was calculated using the occipital cortex as the reference region. In contrast, a similar longitudinal study conducted by Gallagher et al. (2011) in PD subjects and healthy controls over 4.5 years showed that

the slope of decline did not differ between sub-regions among the PD subjects. These two studies found that the decline rates were greater at earlier time stages.

Akamatsu et al. (2017) used a newer high-resolution PET/CT scanner with ^{18}F -FDOPA synthesized from $^{18}\text{F}\text{-F}_2^-$ rather than $^{18}\text{F}\text{-F}_2$, which has a low specific activity, in order to re-evaluate this technique on normal subjects and patients with PD, together with D_2 receptor imaging with ^{11}C -raclopride (RAC). The image-reconstruction parameters were optimized with phantom and Patlak analysis, and the ratio method was performed for the late-phase images to quantify the striatal uptakes. Appropriate reconstruction parameters were empirically determined to obtain high-resolution images with enough quantitative accuracy. Both ^{18}F -FDOPA (4000 MBq/nmol-specific activity) and ^{11}C -RAC PET showed higher uptake values than in previous studies. The quantified ratio values were correlated with the graphical values for both tracers, and FDOPA uptake in the substantia nigra was clearly observed in most of the subjects.

Glaab et al. (2019) used machine-learning techniques to investigate whether the joint data analysis of blood metabolomics and PET data would provide improved diagnostic discrimination and further pathophysiological insights. The data sets were analysed using two machine learning approaches: linear support vector machines and random forests. The diagnostic predictive performance (DPP) was highest when combining imaging features with metabolomics data and lower with only PET attributes or only metabolomics signatures.

3.6 Conclusion

PET quantification measurements can help with obtaining further physiological information, to diagnose diseases and evaluate therapeutic procedures. Sources of error that can affect the calculation of quantitative parameter values were discussed, including the imaging protocol, the kinetic model choice, and the input function chosen for the

model. Clinical brain studies using the Patlak technique were also reviewed, specifically PD studies that used ^{18}F -F-DOPA as the tracer. In the following four chapters, methods and strategies will be proposed to improve parameter estimation and to reduce bias and noise in the Patlak model, dynamic images, and TAC data required for plots. The next chapter will describe the methodology used in the experiments, immediately followed by three technical chapters that show the experimental work on simulation. Finally, successful methods will be applied to clinical PET data obtained from the GDNF trial.

4 Methodology

4.1 Materials and methods

4.1.1 Scanner and reconstruction parameters

The scanner available in the PET Imaging Centre at the University Hospital of Wales is a GE Discovery 690 PET/CT (General Electric Healthcare), and it is made for clinical and research use. The reconstruction method used with FDOPA imaging is a maximum likelihood ordered subset estimation maximisation (ML OSEM) using a Vue Point FX algorithm with time of flight (TOF) correction. The scanner is illustrated in Figure 4-3, and the reconstruction parameters are summarised in Table 4-1.

Table 4-1. PET/CT scanner parameters for FDOPA imaging

Reconstruction Parameter	Value	Reconstruction Parameter	Value
Reconstruction algorithm	Vue Point FX TOF-corrected	PET 3D sensitivity	7 cps/kBq
Algorithm settings	3D ML OSEM - 24 subsets - 2 iterations cut-off with PSF	Scatter fraction	0.37 - 0.3436
Field of view	700 mm×153 mm	Random fraction	0.07
Bed position and scan duration	A single position dynamic PET scan over 94.5 min	Scale factor to multiply the input function with concentration	1 Kbq/ml
Time frames	26 time frames; (1×30 sec, 4×1 min, 3×2 min, 3×3 min, and 15×5 min)	Half-life of nuclide (¹⁸ F)	6.5863e + 3 sec
Post-processing filter cut-off	6.4 mm	Convolution time step	0.5 sec
CT-based attenuation correction	Yes	Diameter of the scanner ring	810 mm
Scatter correction	Yes	Set's initial projection data size	288 mm
Dead time correction	Yes	Maximum allowed ring difference	11 mm
Detector normalisation	Yes	PSF for the system	4.3 (FWHM)
Matrix size CT	512×512×47 (voxels)	Correction	4.3 (FWHM)
Matrix size PET	256×256×47 (voxels)	Size of dynamic image FOV	157 mm
Voxel size CT	1.37×1.37×3.75 mm	Matrix size of reconstructed image	256,256,47,26 (mm, mm, slices, frames)
Voxel size PET	2.73×2.73×3.27 mm	Post-recon Z-axis filter 3-point smoothing	None

4.1.2 Simulation parameters of dPETSTEP

The dynamic PET simulator dPETSTEP can generate PET brain images and allows full simulation of kinetic modelling (Haggstrom et al. 2016). The dynamic PET data can then be model-fitted to produce physiological parameter estimates. In addition, dPETSTEP uses the MATLAB platform and works as an extension of the PETSTEP application, and they share some commands. In PETSTEP, PET images can be simulated with a full simulation of a user defined activity distributions or insertion of realistic user defined tumours into existing patient's images. This simulator is written in Matlab and designed as a plugin for CERR (Computational Environment for Radiological Research) and the input and output files must be in DICOM format (Berthon et al. 2015). This application is considered as a faster and more accessible alternative tool to Monte Carlo (MC) simulation particularly for studies assessing image features and segmentation techniques methods. The 3D PET images can be generated in PETSTEP from PET/CT data or synthetic CT and PET maps in short time (4-6 min), with adding user-drawn lesions, acquisition and user sets reconstruction parameters.

The dPETSTEP is a fast, simple tool and can be used as well as an alternative to MC simulation to produce dynamic PET data, as it is 8000 times faster than MC. In terms of kinetic analysis, dPETSTEP is helpful for the evaluation of different processing choices with dynamic and parametric images that usually require a long time for image analysis where each pixel is analysed. To generate the dynamic data, the simulation settings must first be adjusted to be consistent with the PET scanner features that are targeted by the analysis or evaluation. TACs are generated for each voxel, and imaging effects, such as blurring, counting noise, scatter, randoms, and attenuation, are simulated for all frames. Each frame is then reconstructed into images according to user specified methods, settings, and corrections. This application useful for educational, research purposes as it allows evaluation of the effects of the clinical environment, plus the post-

processing choices. It provide the researchers a better understand of the bias and uncertainty trade-offs through simulating and evaluating several choices, such as reconstruction parameters, post-filtering, and parameter fitting models. Finally, dPETSTEP will help to obtain reliable and actionable kinetic parameters and possibly have better knowledge about sources and magnitude of bias and uncertainty associated with selected parameters. In addition, this tool could provide more understanding how these parameters are affected by the acquisition environment and reconstruction parameter choices (Haggstrom et al. 2016). Both applications are open source and available on the GitHub© website.

Table 4-1 shows all required simulation settings to generate simulated dynamic PET data for ^{18}F -FDOPA images performed for a PD patient. The simulated dynamic PET scan is acquired as 26 time frames over 94.5 min (1×30 sec, 4×1 min, 3×2 min, 3×3 min, and 15×5 min) with a dose of 111 MBq. The cerebellum region from each time frame is used as the reference region tissue (input function) for the quantitative analysis. The output after running the simulator is a 4D matrix with reconstructed dynamic images based on OSEM with point spread function (PSF) correction, which is similar in features to the dynamic PET data produced by the real scanner. The noise level of the 4D matrix is kept at a minimum in its sonogram. The entire volume of images is separated into single slices as 2D images (Figure 4-1), and these are saved to a MATLAB version 4 file (MAT-file), which allows them to be loaded in any MATLAB version with 2D double, character, and sparse arrays without compression. In this version, each variable has a maximum size of 100 million elements per array and 2^{31} bytes per variable, which allows all data information to be kept without losing any details. Scatter and decay correction is applied during the reconstruction process by setting the parameters file within the simulation codes. All slices introduced by the 4D

matrix are exported to PMOD 3.4 software to perform further analysis in kinetic modelling with specific ROI.

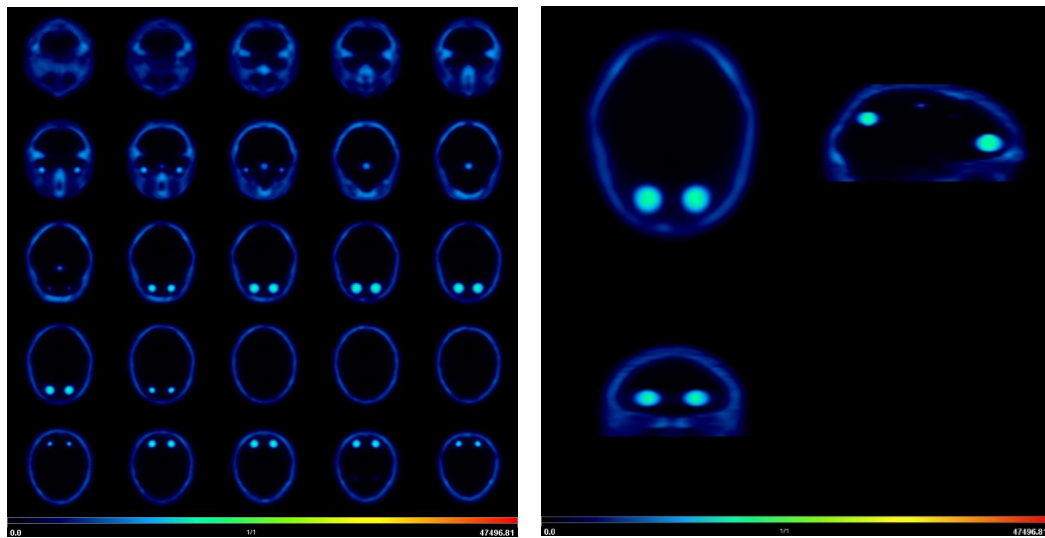


Figure 4- 1. (Left) The entire volume of images is separated into single slices as 2D images, which are saved to a MATLAB version 4 (MAT-file), which allows them to be loaded to PMOD software (Right).

4.1.3 PMOD software

PMOD software is designed for researchers in the molecular imaging field and provides suitable tools for all quantitative data processing steps. This allows researchers to pay more attention to content and clinical data rather than programming new tools from scratch. PMOD can process various types of images, such, as CT, MR, and SPECT, in many imaging formats, from simple processing tasks to sophisticated protocols and analysis. It is validated and referred to in more than 1000 peer-reviewed publications on kinetic modelling and biomedical research (PMOD 2017).

In this experiment, two applications are used for the analysis: PBAS and PKIN, which permit the importation of simulated dynamic PET images and application of kinetic analysis, respectively. PBAS is the main tool in PMOD and can receive images in various formats, including v4 MAT-files, which should be imported to PBAS in a double SE data form. The images imported must be in Bq/cc units, and the images

orientation should be corrected if it looks different from the original position. The simulator makes all corrections, so PMOD should do nothing in terms of corrections. Firstly, all slices are merged into frames again, and the times for each frame are consistent with the protocol used with the simulator. Secondly, all frames are saved in the Digital Imaging and Communications in Medicine (DICOM) standard format. This format is data rich, and the header information includes attenuation, scatter and decay correction, normalisation, frame timing, and reconstruction parameters, as well as the standard required details of matrix dimensions and pixel size.

PBAS was used to draw and analyse the VOIs (left striatum) and reference tissue (cerebellum). The left striatum was chosen because it is assumed that in simulated images, the left and right sides will have the same amount of radioactivity. The net influx rate constant (K_i) is usually calculated over a range of 30–90 minutes for dynamic images, so all frames between 30 and 90 minutes were averaged into slices, and the ROIs were drawn on all slices to show them. Two volumes of interest (VOIs) at minimum must be created: one ROI for the cerebellum represents the reversible region, and another one for the left striatum represents the irreversible region. For regional analysis, within each ROI the ROIs were drawn freehand as complete contours (Figure 4-2).

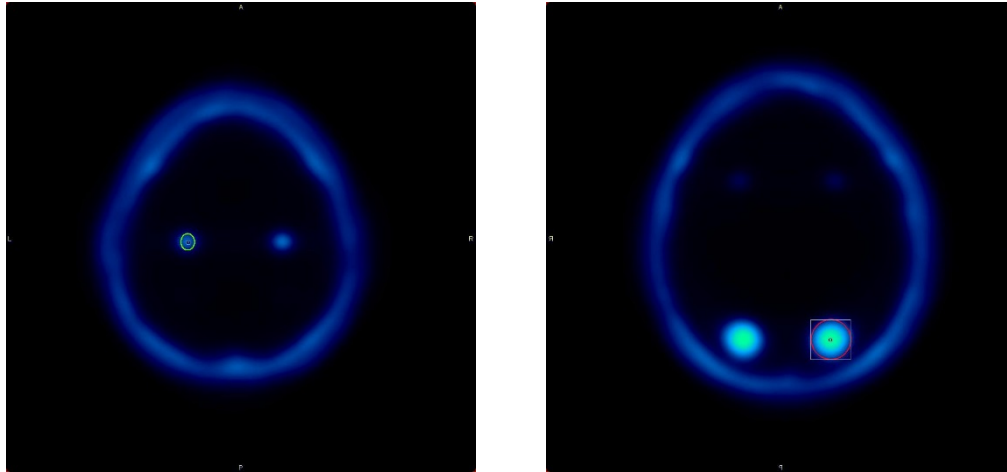


Figure 4- 2. For regional analysis, the ROI is drawn as one complete contour. The ROI objects were drawn freehand: simulated striatum (Left) and part of simulated cerebellum (Right).

Each VOI included contours that were drawn over the simulated anatomical region required for the analysis, and all VOIs were saved in a single file to be used again as a template. In fact, even the ROIs' contours were drawn on the averaged dynamic frames; however, the TACs then will be obtained from the original dynamic PET volume. Thus, the images were averaged to guide the drawing on all slices that show ROIs. Then, the TACs were generated from the contours of regions required for the analysis. TACs for all regions must be checked, and the tracer in the reversible curve should show a clear washout. PMOD uses an algorithm to determine the best time for t^* . In this experiment, the Patlak reference tissue analysis was based on $t^* = 30$ min. This is important for slope calculations (K_i value). For regional analysis, the result will be (K_i) value, which is the slope. For each specific ROI made, the intercepts that represent (V), standard errors (SE), and Chi-square are calculated within the analysis.

4.1.4 Thesis strategy

In Chapter 5, for the first data group, the simulation of the FDOPA dynamic PET data was repeated 10 times and simulated different K_i values within normal healthy subjects, which are between 0.0122 and 0.014 according to the literature (Akamatsu et al. 2017; Jokinen et al. 2009; Laakso et al. 2002), considering that the imaging protocol of FDOPA for scanning patients is based on giving both carbidopa and entacapone. These simulated images were generated by dPETSTEP, then these volumes of images were exported to PMOD to further processing with PBAS tool and extract TACs. PKIN tool is receiving directly TACs required to run the kinetic analysis and apply Patlak model. After finishing the kinetic modelling analysis, Gaussian noise with a zero mean was applied in 10 levels (5, 10, 15, 20, 25, 30, 35, 40, 45 and 50%) for the reference and targeted tissue TACs. These steps are repeated for the second and third data categories, however K_i values include normal and abnormal data in these groups, and each point of the K_i was repeated 10 times and averaged. The K_i values simulated are six points: 0.0122 and 0.014 represent healthy subjects, whereas 0.010, 0.0075, 0.0050, and 0.0025 represent diseased subjects. The difference between the second and third data categories is the implementation of noise, which is applied to the second group for the TACs required for regression analysis and the third group, noise was added on dynamic images. All TACs were exported to MATLAB for additional analysis and to evaluate our suggested statistical calculation methods: ordinary least squares (OLS), feasible generalised least squares (FGLS), total least squares (TLS) and robust fitting regression (RFR). Codes were written in MATLAB software with using statistical tool to analyse all TACs obtained from the simulated images processed by PMOD, and the K_i results were saved to Excel sheets. The results section in chapter 5 illustrates the results for the

simulated data, including statistics, which were calculated to evaluate how the methods affected the estimate of the final K_i values.

In chapter 6, simulated FDOPA dynamic PET data was produced for a range of different K_i values corresponding to normal and abnormal subjects ($0.014 - 0.0025 \text{ min}^{-1}$) according to the literature (Cropley et al. 2008; Moore et al. 2003; Whone et al. 2004) using an the imaging protocol based on administering both carbidopa and entacapone. After generating the dynamic images, Gaussian noise with a zero mean was applied in 10 levels between 5 and 50% to the all frames of simulated FDOPA. The K_i values simulated are six points: 0.0122 and 0.014 min^{-1} represent healthy subjects, whereas 0.010 , 0.0075 , 0.0050 , and 0.0025 min^{-1} represent diseased subjects. Noise reduction methods suggested were applied on 4D images and then Patlak regression analysis performed to investigate the impact of those methods quantitatively. Methods were used including anisotropic diffusion (Gradient and curvature) and wavelets (Daubechies and Battle-Lemarie). The results section in the chapter illustrates the output for the simulated data, including statistics, which were calculated to evaluate how the methods affected the estimate of the final K_i values.

In chapter 7, several data smoothing algorithms and filters are discussed and applied to our simulated 2D PET data set (TACs) that are required for Patlak analysis. The aim is to remove or reduce included noise and improve the accuracy of final results with lower fitting standard errors. These methods include the moving averaging filter, *Savitzky-Golay*, *polynomial curve fitting*, and the *median filtering* method. Each chapter discusses the theory behind each method, followed by the result of the experiment performed.

4.2 GDNF analysis and chapter 8's materials and methods

4.2.1 Study design and subjects

A placebo double-blind randomized controlled clinical trial was completed at a single site at the Wales Research and Diagnostic PET Imaging Centre (PETIC), Cardiff, UK. This study aims to assess the efficacy of a novel drug using intermittent bilateral intraputamenal glial cell line-derived neurotrophic factor (GDNF) for PD patients. The trial's main objective is to test whether GDNF administration achieves neurorestoration and causes significant clinical benefit (Whone et al. 2019).

The treatment infusions were administered via convection enhanced delivery (CED). Thirty-five subjects were involved in the primary stage of this trial (N=35; female=17, male=18). All were randomised (1:1 ratio) and assigned to two groups. The GDNF group received the treatment and placebo, and both groups received artificial cerebral spinal fluid (aCSF). GDNF, placebo, and aCSF were visually identical. Patients and investigators were blinded to treatment and placebo groups to avoid bias. Each subject received two scans (baseline and after treatment). Patients involved in this study were aged 35 to 75 years, diagnosed with bilateral idiopathic PD according to UK Brain Bank criteria, and underwent full assessment. See appendix D (Figure D-2) for the CONSORT (Consolidated Standards of Reporting Trials) flow diagram followed in designing the clinical trial. All subjects had been treated with an anti-Parkinson's drug for longer than 6 weeks and had motor symptoms associated with moderate severity of the disease for 5 years or longer.

A T1-weighted MRI scan was performed after CED implementation for each subject to assess the CED infusion system and for later use for PET co-registration. The therapy plan lasted 40 weeks, and all subjects received a FDOPA PET tracer to image the brain before and after treatment. A low dose CT scan was performed for each subject prior to

the PET scan at the same position and used during the quantification analysis for AC for PET dynamic images. Parkinson's medication was not ceased during the study, and modification were allowed to control symptoms. Another T1-weighted MRI was performed for each subject at the end of treatment (Week 40) to determine maintenance of CED system. This study followed a previous randomised controlled pilot stage (N=6). FDOPA PET and T1-weighted MRIs were co-registered and quantified by applying VOIs on ROIs (striatum, caudate nucleus, and putamen). Patlak graphical analysis was the standard method used for assessment. This type of analysis is based on the assumption of the unidirectional uptake from the blood into the midbrain and basal ganglia, particularly in striatum, after the tracer injection. The main parameter is K_i , which measures the rate of tracer accumulation in the targeted ROI. The mean percentage change in the side-to-side averaged striatum (caudate and putamen) K_i between the baseline and after therapy scans is the main output. This analysis was repeated after applying our suggested methods, statistical models, and noise reduction to FDOPA images. Appendix D (Figure D-2) shows the GDNF clinical trial outline followed in PETIC department in the University Hospital of Wales.

4.2.2 Scanner and reconstruction parameters

All baseline and after therapy scans were obtained from the same scanner, a GE Discovery 690 PET/CT available in PETIC (Figure 4-1). Acquiring images from the same scanner helps to avoid bias that could be caused by using different tomographs. All subjects followed the same protocol designed by the PETIC department. Image acquisition settings and parameters are mentioned earlier in Table 4-1.



Figure 4- 3. GE Discovery 690 PET/CT scanner available in PETIC and used for clinical and research studies obtained from GE Healthcare (2019).

4.2.3 Protocol scan

The Administration of Radioactive Substances Advisory Committee (ARSAC) certified approved the protocol scan, and Cardiff University was responsible for supplying the radiopharmaceuticals. All radiographer and operators were trained and qualified to perform PET/CT imaging of subjects and familiar with the FDOPA GDNF trial procedures. For scan preparation, subjects received 150 mg of carbidopa and 400 mg of entacapone. After 1 hour, a low dose CT scan was acquired including vertex to C1. Thereafter, a dynamic PET scan was acquired as 26 time frames over 94.5 min (1 × 30 sec, 4 × 1 min, 3 × 2 min, 3 × 3 min, and 15 × 5 min). ^{18}F -FDOPA administered in normal saline immediately after the scan commences with a dose of 111 MBq through a long connecting tube as a bolus injection. The cerebellum region from each time frame was used as reference region tissue (input function) for quantitative analysis. Both scans (baseline and after therapy) were acquired, reconstructed, and attenuated using the same PET scanner in PETIC, and blinded investigators were assigned to the therapy group to obtain all scans.

4.2.4 Image reconstruction and data transfer

The computer used for reconstruction images is a 2.7 GHz quad-core Intel Core i5. The computer used for quantifying the FDOPA phantom images has a 3.20 GHz Intel ® Core™ i7 CPU running the Windows 7 Enterprise 64-bit OS and 32 GB RAM. PMOD version 3.409 and MATLAB version R2016a software were used to quantify dynamic FDOPA images. Image reconstruction was performed using the standard manufacturer-supplied 3D reconstruction program provided with the PET cameras. Various choices can be made within this reconstruction program (e.g. filter window, zoom factor, whether to decay correct). AC for baseline and follow-up images using a CT scan is performed before PET dynamic acquisition. The reconstruction method used with FDOPA imaging is ML OSEM for 3D imaging using the Vue Point FX algorithm with TOF correction. Scatter correction was applied during the reconstruction process, and detector normalization and geometric corrections were applied using the scanner manufacturer's standard methods. The image files were all formatted using the DICOM standard. This format is data rich, and the header information includes attenuation, scatter and decay correction, normalization, frame timing, and reconstruction parameters, as well as the standard required details of matrix dimensions and pixel size. When dynamic files reconstruction was complete, data were copied to CD-ROM to allow transfer to the research office where the image analysis is performed using PMOD and MATLAB. Images were uploaded to the TeleHERMES™ system and PETDATA folder and made available for viewing at any time. Two pilot baseline and follow-up scans were sent before transferring all studies to verify compatibility of reconstructed images with our software for analysis and to ensure that all corrections required for quantification process were performed. A further inspection step was taken to verify that all time frames were present and that the duration was 94.5 min.

4.2.5 Regional and sub regional analysis

The PMOD software, and specifically its PVIEW and PKIN tools, is used to draw and analyse ROIs and reference tissue. K_i is usually calculated over the range 30–94.5 min for dynamic images. Three VOIs at minimum must be created: one VOI for reversible regions, representing the cerebellum, and two VOIs for the right and left striatum. For regional analysis, VOI are drawn as one complete contour including the striatum (caudate and putamen) for each side of the brain, whereas in sub regional analysis, each side of the striatum is divided into two regions (caudate and putamen). The putamen is then divided into three parts (Figure 4-4: A, B, & C). Each VOI includes contours that are drawn over the anatomical region required for the analysis, and VOIs are saved as a template in a single file to be used again for the follow-up scan analysis. Then, the TACs are generated from the contours of ROIs required for the Patlak analysis (Figure 4-5: Top). TACs for all regions must be inspected, and the tracer in reversible curve (cerebellum TAC) should show a clear washout to confirm the absence of specific binding. PMOD has an algorithm to determine the best time for t^* , and because frames from 30–94.5 min will be analysed, the Patlak equation begins calculations at $t^* = 30$ min. For regional and sub-regional analysis, the result will be the mean (K_i) value, the slope (Figure (4-5: Bottom)), and the intercept that represents V for each specific ROI made. Standard error (SE), sum squared error (SSE) and Chi-square are calculated within the analysis. An image of integrated FDOPA signals from 30–94.5 min (summed or ADD image) (Figure 4-6: Left) is created for use when applying ROIs contours to individual FDOPA dynamic images. Where a single template of predefined volumes of interest including all ROIs contours is prepared by the PVIEW tool, these are then applied to each subject PET dynamic image. The SPM software was used to perform spatial normalization, image smoothing (8-mm FWHM smoothness parameter), and co-registration processes in which each PET image registered into the MRI scan is taken

from the same patient (Figure 4-6: Right). This allows the drawing of VOI templates (objects maps) accurately on MRIs. Using the PVIEW tool, a template can be applied immediately to the PET images. The object map defines both putamen (left and right), putamen parts, and heads of caudate nuclei. ROI objects were drawn freehand on the single-subject MRI. Comparisons were made to localize significant mean (Ki) differences between baseline and follow-up scans in ROIs.

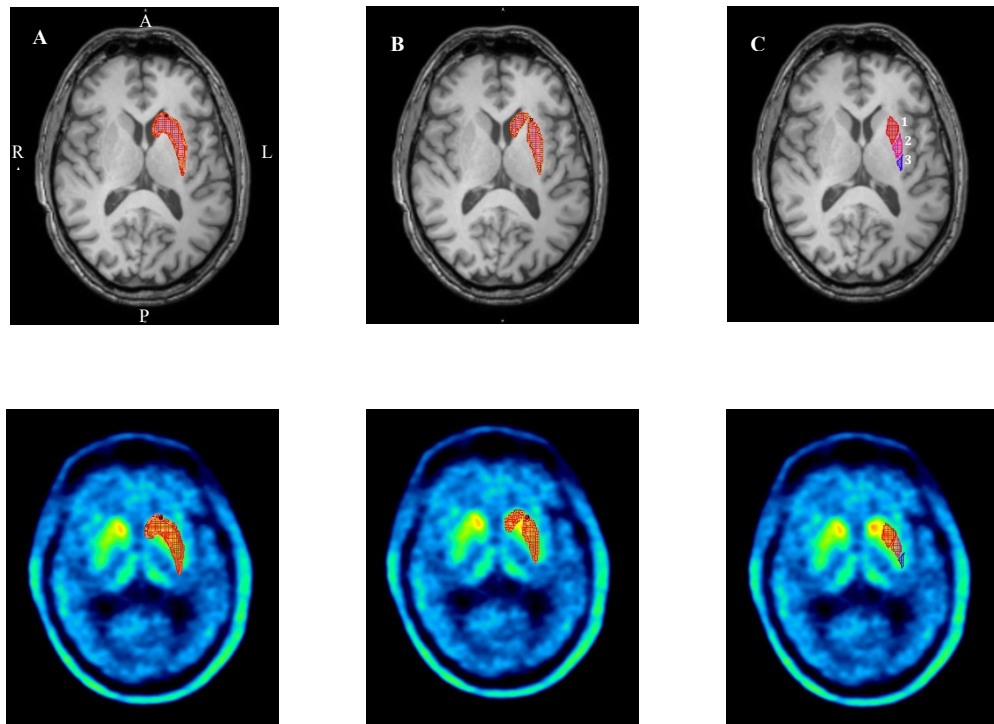


Figure 4- 4. Example of drawing contours on ROIs. The first row shows MRI images (A) in which the ROI left striatum is drawn in one complete contour. (B) ROIs in sub-regional analysis are divided into two regions: caudate and putamen. (C) The putamen as an ROI in sub-regional analysis is divided into three parts: 1 (Anterior), 2 (Central), and 3 (Posterior). The second row illustrates PET images where contours are copied from MRIs to generate TACs.

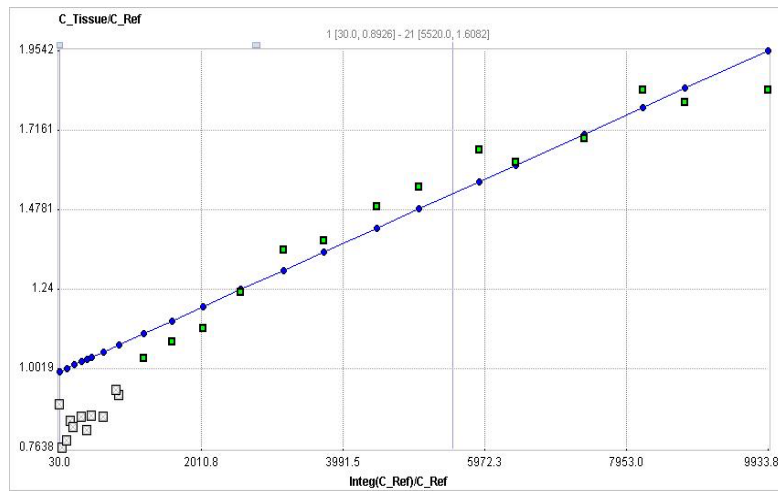
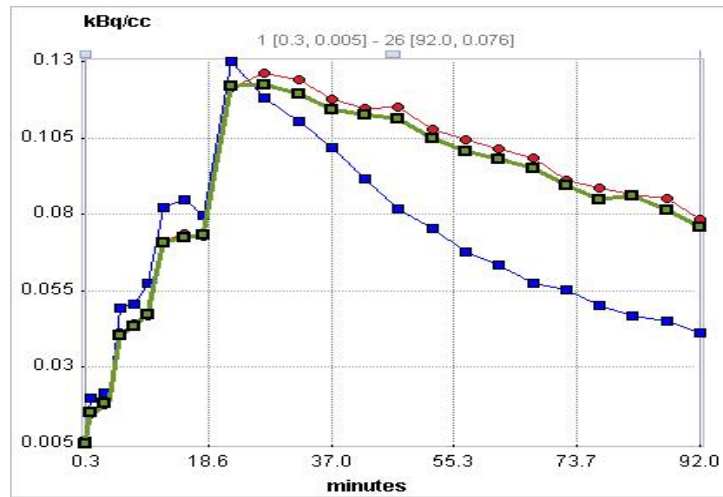


Figure 4- 5. (Top) The TACs from the contours of regions (right, left striatum, and cerebellum) that are required for the Patlak analysis. Cerebellum TAC (blue line) shows a clear washout, and it is the reference input function for the analysis as an alternative to blood input data. (Bottom) The Patlak regression model results in straight line after applying the equation; (K_i) is equal to the slope value.

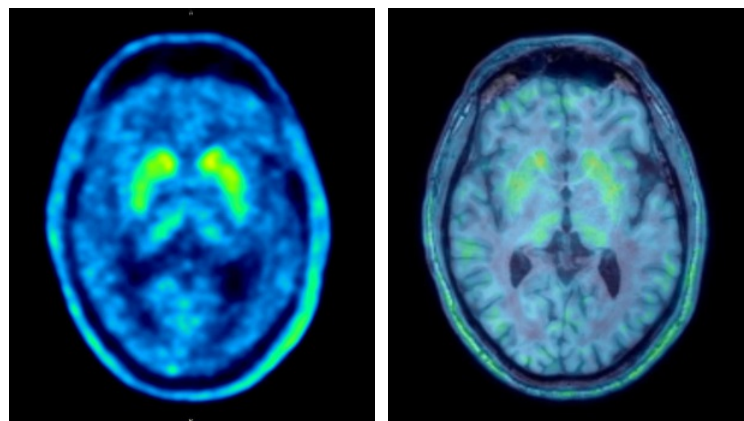


Figure 4- 6. The summed (ADD) image on the left was obtained from a single slice of FDOPA scan (30–94.5 min) from a PD subject. Fused PET-MRI images were used to prepare the VOIs template for analysis.

4.3 Conclusion

The experimental work in this thesis will first generate simulated PET data that mimics the FDOPA images obtained by the scanner available in the PETIC department. In this step, dPETSTEP will be used as a dynamic PET simulator for brain images that allows full simulation of kinetic modelling. After generating the simulated data, various statistical and mathematical methods will be applied to the data generated to reduce or remove noise and bias introduced in quantitative analysis. MATLAB and PMOD will be used as a platform and a tool to apply and evaluate suggested methods, respectively. Successful approaches will then be applied to the FDOPA clinical images for further validation and evaluation following procedures and steps validated in the published literature. The next chapter covers the experiments dealing with statistical noise in PET data and focus on statistical models used to remove or reduce the noise.

5 Impact of Noise on Quantitative ^{18}F -FDOPA Images in Phantom Dynamic PET Data

5.1 Introduction

This chapter describes our first experiment in the optimization process for ^{18}F -FDOPA quantification in Parkinson's disease (PD) images. Patlak graphical analysis, using the various statistical methods, was first applied to the simulated positron emission tomography (PET) data in order to investigate their ability to reduce the effects of bias and noise as well as to maintain the accuracy of the result. The calculation of goodness of fit of the slope and the SEs of the regression line (RL) are the reference for the evaluation of the performance of each statistical method. Graphical techniques are considered simple for the PET data analysis, as it could be used for a wide range of tracers without complicated mathematical compartmental modelling. One issue usually associated with graphical techniques is the introduction of bias, which is caused by the sensitivity of the method to statistical noise and data outliers (Logan 2003) that affect the result accuracy using the ordinary least squares (OLS) method. In some voxels, outliers are likely to exist in the regression analysis and will cause errors in the calculated values, which could result in higher false negative rates (FNRs) or higher false positive rates (FPRs) and affect the diagnosis decision (Wager et al. 2005). This unpredictability of the effects of outliers is particularly problematic, as a simple correction (e.g. an alpha or p value correction) is not available.

The errors and bias associated with the OLS method could be overcome by selecting and applying several other methods. Examples of other methods include the following:

1. Feasible generalized linear least squares (FGLS),
2. Total least square (TLS), and

3. Robust fitting regression (RFR).

In this chapter, these methods will be applied to Patlak equation with simulated phantom PET data generated from the dPETSTEP simulation tool (Haggstrom et al. 2016) in the first instance to see how they affect the result of image analysis and how they perform with increasing levels of noise. The simulated PET data are categorised into three groups, and the first group represents 10 normal K_i values with added noise calculated from TACs obtained from simulated PET images. With this group, statistical models suggested before were used in Patlak analysis and comparison performed for them.

In second group, these various statistical methods again applied to a set of simulated PET images containing both normal and abnormal K_i values not only normal K_i values like in first group. As with the first set of data, increased levels of noise will be applied as well to the same TACs data previously involved in the Patlak regression only. Finally, for the last group of analysis, we investigated the various methods on the simulated PET images of normal and abnormal K_i values and the noise this time is applied to the images before extracting the data required for regression analysis. Thus, for the first two groups noise was added to TACs required to Patlak analysis and for the third group noise added on the simulated images. The equations, materials, algorithms, and tools used in the experiment will be described, and the results will be discussed and evaluated in the rest of the chapter.

5.2 Theory

5.2.1 FDOPA kinetic analysis method

The main feature distinguishing reversible from irreversible tracers is the experiment's length; in other words, a tracer can be reversible over a long period, but it can be irreversible during the experiment or scanning time (Logan 2000). For irreversible tracers, the Patlak reference model is used to calculate the tracer uptake in a ROI using the blood data as an input function. For ^{18}F -FDOPA, the Patlak reference model is used, and it is possible to replace the blood activity using a reference region to generate a time activity curve (TAC). The reference region must be devoid of targeted receptors (Patlak and Blasberg 1985; Patlak et al. 1983). The Patlak method can be modelled as two-tissue compartments (Figure 5-1).

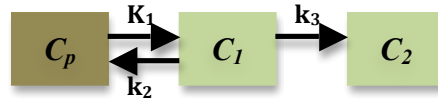


Figure 5-1. Two-tissue compartmental model where $C_p(t)$ is the plasma tracer concentration at time (t), C_1 is the free tracer concentration in tissue and C_2 is the trapped tracer concentration. K_1 , k_2 , and k_3 are unidirectional rate constants of the tracer between plasma and tissues.

With FDOPA, the regions used to generate Patlak parameters include one reversible region (cerebellum) and one irreversible region (striatum). In this instance, the TACs of the cerebellum are used, instead of directly measuring blood plasma, as an input function for Patlak analysis. The Patlak equations with reference tissue as an input function can be described by

$$\frac{C_T(t)}{C_{T_r}(t)} = K \frac{\int_0^t C_{T_r}(\tau) d\tau}{C_{T_r}(t)} + V \quad \text{Eq. 5-1}$$

where $K = slope = \frac{K_2 K_3}{(K_2 + K_3)}$, $C_T(t)$ is the TAC values of the ROI tissue (striatum),

and $C_{T_r}(t)$ is the TAC values of the reference tissue (cerebellum) at time (t). The equation works for $t > t^*$, where t^* is the equilibration time where the radioactivity ratio

between reference and ROI tissue becomes reasonably constant (Ikoma et al. 2008). K represents the tracer net uptake calculated from the regression slope, and V is the intercept, which is equal to the volume fraction of blood in ROI tissue at time 0 .

This means the activity in the striatal VOI is divided by the reference tissue activity (cerebellum), representing the y-axis, and plotted against the integral of the reference tissue activity from the injection time divided by the reference tissue activity, representing the x-axis. As ^{18}F -FDOPA is a tracer that targets brain receptors in the striatum, the model plot will result in a straight line (Figure 5-2) after t^* (Patlak and Blasberg 1985).

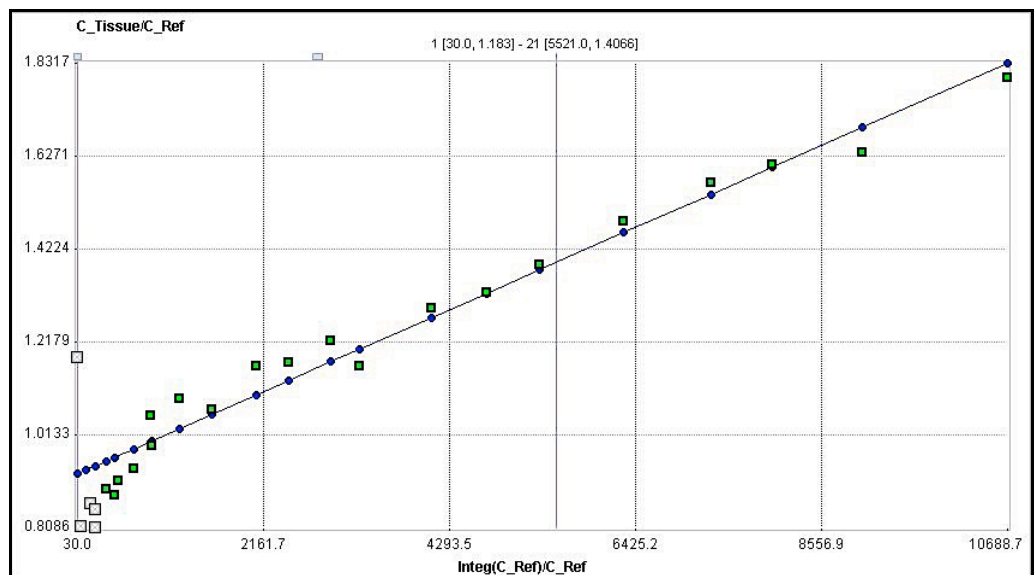


Figure 5-2. PET activity measured from ROI is divided by the reference tissue activity that represents y-axis, and plotted against the integral of the reference TAC from the injection time divided by the reference activity, which represents x-axis. The model plot resulted in a straight line after $t^* = 30$ min in this analysis.

Graphical analysis is based on regression, so in many cases, it cannot fit all data accurately generated from reference tissue or striatal VOI, where outliers exist in some voxels of brain images. When this happens, a bias can be introduced into the parameters (Logan et al. 2001). In the Patlak equation, this bias is usually introduced in the tracer net uptake. Also, bias is present due to errors within the linearized equations during all the time points (Feng et al. 1996; Feng et al. 1993). The effect of bias depends on the

type of noise present. Most of the analysis introduces bias and can usually be addressed by reducing the source of noise in the data or averaging the dataset (Logan et al. 2001).

5.3 Bias and Statistical Noise-Reduction Methods

5.3.1 Ordinary least squares

OLS is one of the simplest methods of linear regression, and it is frequently used to analyse both experimental and observational data. It aims to closely “fit” a function to the data by minimizing the sum of squared differences between the observed responses in the given dataset and those predicted by a linear function. On a plotted graph, this is seen as the sum of the squared vertical distances between each data point in the set and the corresponding point on the regression line (RL) (Figure 5-3). When the differences are smaller, the model of the data has a better fit (Hayashi 2000). In the case of a model with p explanatory variables, the OLS regression model is expressed as the following:

$$Y = \beta_0 + \sum_{j=1}^p \beta_j X_j + \varepsilon \quad \text{Eq. 5-2}$$

where Y is the dependent variable, β_0 is the intercept of the model, X_j corresponds to the j^{th} explanatory variable of the model ($j=1$ to p), and ε is the random error with expectation 0 and variance σ^2 . With n observations, the estimation of the predicted value of the dependent variable Y for the i^{th} observation is given by

$$y_i = \beta_0 + \sum_{j=1}^p \beta_j X_{ij} \quad \text{Eq. 5-3}$$

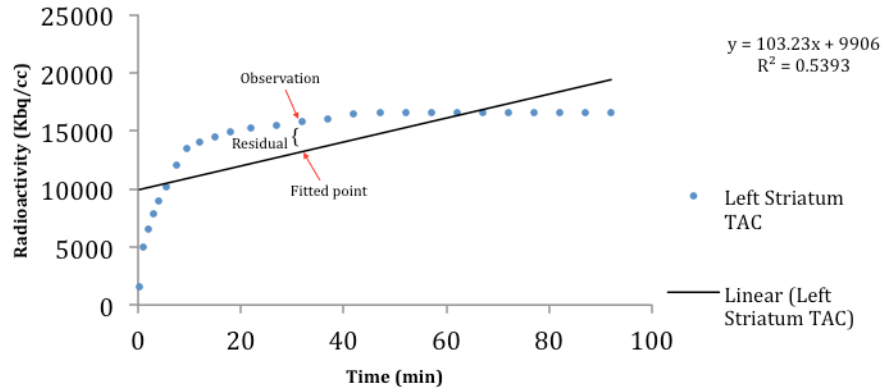


Figure 5-3. An example showing how the OLS method is used to construct the regression line from PET dynamic data; y-axis represents the amount of radioactivity (kBq/cc) and x-axis represents time points in minutes when the radioactivity was recorded.

The OLS method corresponds to minimizing the sum of squared differences between the observed and predicted values of a dataset. In a model, this leads to the following estimators of the parameters:

$$y = X(X'DX)^{-1} X'Dy \sigma^2 = 1 / (w - p^*) \sum_{i=j}^n = 1..nw_i(y_i - y_i) \quad \text{Eq. 5-4}$$

where β is the vector of the estimators of the β_i parameters, X is the matrix of the explanatory variables preceded by a vector of 1, y is the vector of n observed values of the dependent variable, p^* is the number of explanatory variables to which we add 1 if the intercept is not fixed, w_i is the weight of the i^{th} observation, w is the sum of the w_i weights, and D is a matrix with the w_i weights on its diagonal. The vector of the predicted values can be written as follows (Freedman 2009):

$$y = X(X'DX)^{-1} X'Dy \quad \text{Eq. 5-5}$$

The OLS estimation tool has assumptions in linear regression to provide the best possible estimates; in a model, the result could be doubted if these assumptions are violated and other estimation methods are suggested to be used. In contrast, unbiased coefficient estimates can be generated when the linear regression analysis satisfies the OLS assumptions. In this case, coefficients become somewhat close to the minimum

variance level that represents the true population values (Frost 2018). Because the population value's error term is unknown, residuals of the observational sample (fitted points) are the best option to estimate the error. The OLS assumptions are six assumptions, and some reviews make them seven. All of them are summarized as follows (de Souza and Junqueira 2005; Frost 2018; Lewis-Beck and Lewis-Beck 2015): The first assumption indicates the existence of linearity in the functional form of the model, coefficients, and error term. The second assumption is with regards to the error term, where the average value must have a population mean equal to zero. The third assumption addresses the independent variables, as they must be uncorrelated with the error term that is related to the dependent variables. Observations of the error terms should not correlate to each other, so one observational error is assumed not to predict the next one, and this is the fourth assumption that must be considered. Assumption five states that the homoscedasticity is the case of the error term variance for the observations where the variance is considered to be constant. The sixth assumption concerns the independent variables, as each variable must not act as a linear function for another one, so the change in any independent variable should not change another by a fixed proportion; this issue is usually referred to as a multicollinearity condition. The last assumption, which is the normality of error distribution, is not compulsory for the quality of OLS estimates; however, it is very useful in the statistics to select the suitable hypothesis test.

Although OLS is commonly used for its simplicity, there are some problems and pitfalls that can be introduced within data using OLS analysis. Outliers, which refer to the large or small data points compared to the rest of dataset, can affect not only the final resulting constants of the analysis but even all data points. Large or small outliers have effects on other types of regression (linear or nonlinear) and could result in largely excessive regression constants. In some cases, it is difficult to know exactly what the

best error measurement to minimize, and that leads to trying other methods of least squares though some choices that could be better than others. For that reason, applying other least squares methods such as generalized linear least squares (GLLS), RFR, and TLS could provide fewer error measurements for our dataset.

5.3.2 Generalized linear least squares

GLLS was originally developed by Feng et al. (1993) and has been applied in various PET quantitative model equations (Logan et al. 2001) to remove bias. GLLS is used for estimating the unknown parameters in models based on a linear regression when calculated data show a certain degree of correlation in the residuals. Based on this correlation, calculated data are categorized into two parts: for times 0 to T1 and from T1 to the end time, and then another estimation is calculated. The parameters generated a curve used as input to the linear regression analysis (Logan et al. 2001). The two types of GLLS are called weighted least squares (WLS) and feasible generalized least squares (FGLS). WLS can be applied when all the off-diagonal entries of the covariance error matrix (W) are 0. In FGLS, the opposite occurs when the covariance of errors is unknown (Strutz 2010). With FGLS, the calculation progresses through two steps: Firstly, the residuals are obtained by using OLS to establish the errors covariance matrix that shows a consistency in estimation. The second step is the implementation of GLLS, which is to divide the given data into two parts. The part that has the low variance is given more weight than the other parts to generate a more accurate fitted line. With finite samples, an estimator's accuracy with FGLS can be improved by an iterative process where residuals are used to update the errors covariance estimator, and, consequently, the FGLS estimation is updated (Freedman 2008; Gujarati 2009; Long and Trivedi 1992). The FGLS estimator may or may not be unbiased in small samples, but if \hat{W} is a consistent estimator of W , the FGLS estimator is asymptotically unbiased,

efficient, and consistent. Monte Carlo (MC) studies have shown that the FGLS estimator generally yields better estimates than the OLS estimator (Kennedy 2008).

The general linear regression model is defined by the following set of assumptions:

- Linearity in parameters is the functional form

$$y = X\beta + \mu \quad \text{Eq. 5-6}$$

- Error term has a mean of zero

$$E(\mu) = 0 \quad \text{Eq. 5-7}$$

- Errors are non-spherical

$$\text{Cov}(\mu) = E(\mu\mu^T) = W \quad \text{Eq. 5-8}$$

where W is any non-singular $T \times T$ variance–covariance matrix of disturbances.

- Error term has a normal distribution

$$\mu \sim N$$

- Error term is uncorrelated with each independent variable

$$\text{Cov}(\mu, X) = 0 \quad \text{Eq. 5-9}$$

There are two types of non-spherical errors: Firstly, when an error term does not have constant variance, this is called heteroscedasticity. In this type of error, the disturbances are drawn from probability distributions that have different variances, and the error term has non-constant variance; the variance–covariance matrix of disturbances is not given by a constant multiplied by the identity matrix (i.e. $W \neq \sigma^2 I$). Secondly, the errors are correlated, which is called autocorrelation or serial correlation, where disturbances are correlated with one another. This occurs when using time-series data. When the disturbances are correlated, the variance–covariance matrix of disturbances is not given by a constant multiplied by the identity matrix (i.e. $W \neq \sigma^2 I$). This is because the elements of the principal diagonal of W , which are the covariance of the disturbances, are non-zero numbers (Granger 1994).

In a general linear regression model stated in matrix format, the sample of T multivariate observations $(Y_t, X_{t1}, X_{t2}, \dots, X_{tk})$ is generated by a process explained below:

$$y = X\beta + \mu, \quad \mu \sim N(0, W) \quad \text{Eq. 5-10}$$

or

$$y \sim N(X\beta, W)$$

An FGLS estimator uses the sample of data to obtain an estimate of W , where the true W is replaced with its estimate \hat{W} . The FGLS estimator is given by the following rule:

$$\hat{\beta}^{FGLS} = (X^T \hat{W}^{-1} X)^{-1} X^T \hat{W}^{-1} y \quad \text{Eq. 5-11}$$

The variance covariance matrix of estimates for the GLS estimator is

$$Cov(\hat{\beta}) = (X^T \hat{W}^{-1} X)^{-1} \quad \text{Eq. 5-12}$$

The FGLS estimator is also a WLS estimator. The WLS estimator is derived as follows. Find a $T \times T$ transformation matrix P , such that $\mu^* = P\mu$, where μ^* has the variance-covariance matrix $Cov(\mu^*) = E(\mu^* \mu^{*T}) = \sigma^2 I$. This transforms the original error term μ that is non-spherical into a new error term that is spherical. Use the matrix P to derive a transformed model (Granger 1994; Kennedy 2008):

$$Py = PX\beta + P\mu \quad \text{Eq. 5-13}$$

or

$$y^* = X^* \beta + \mu^* \quad \text{Eq. 5-14}$$

where $y^* = Py$, $X^* = PX$, and $\mu^* = P\mu$. The FGLS estimator is the OLS estimator applied to the transformed model, which is considered a computational device only to obtain efficient estimates of the parameters and SEs of the original model of interest.

5.3.3 Robust fitting regression

Robustness denotes the solidity of conclusions and how their differences from assumptions are assigned to a certain model. This means that small changes in the data distribution do not cause large changes in the variance of the estimates (Western 1995). RFR provides an alternative to OLS when the underlying assumptions are invalid within the model. RFR provides much improved regression coefficient estimates when data noise or outliers are present. The influence of outliers is down-weighted by making the outlying residuals larger and simpler to detect, plus performing an iterative procedure to identify outliers and to reduce the impact on the coefficient estimates. Robust regression implements its own residual analysis and reduces or completely removes numerous data points, so a decision should be made as to whether these observations are essential in the analysis (Hintze 2001; Kutner et al. 2004). The most common general method of robust regression is a class of techniques called *M*-estimators that discount the impact of outlying observations (Fox 2002) introduced by Huber (1964). Consider the linear model

$$y_i = \alpha + \beta_1 x_{i1} + \beta_2 x_{i2} + \dots + \beta_k x_{ik} + \varepsilon_i = x'_i \beta + \varepsilon_i \quad \text{Eq. 5-15}$$

The fitted model for the *i*th of *n* observations is

$$y_i = \alpha + \beta_1 x_{i1} + \beta_2 x_{i2} + \dots + \beta_k x_{ik} + e_i = x'_i b + e_i \quad \text{Eq. 5-16}$$

The general *M*-estimator minimizes the objective function

$$\sum_{i=1}^n p(e_i) = \sum_{i=1}^n p(y_i - x'_i b) \quad \text{Eq. 5-17}$$

The function ρ gives the contribution of each residual to the objective function and should have the following properties:

- $\rho(e) \geq 0$
- $\rho(0) = 0$
- $\rho(e) = \rho(-e)$
- $\rho(e_i) \geq \rho(e_i')$ for $|e_i| > |e_i'|$

For least squares estimation, $\rho(e_i) = e_i^2$, let $\psi = \rho'$ be the derivative of ρ , differentiating the objective function while considering the coefficients b , and assume the partial derivatives to be 0, which enervates a system of $k+1$ estimating equations for the coefficients:

$$\sum_{i=1}^n \psi(y_i - x_i' b) x_i' = 0 \quad \text{Eq. 5-18}$$

Assume the weight function $w(e) = \psi(e)/e$, and let $w_i = w(e_i)$, so that the estimating equations can be written as

$$\sum_{i=1}^n w_i (y_i - x_i' b) x_i' = 0 \quad \text{Eq. 5-19}$$

An iterative solution called iteratively reweighted least squares (IRLS) is required due to the dependency between weights, residuals, and estimated coefficients. The iteration is performed by following these steps:

1. Select initial estimates $b(0)$; for example, the least squares estimates.
2. At each iteration t , calculate residuals $e_i^{(t-1)}$ and related weights $w_i^{(t-1)} = w[e_i^{(t-1)}]$ from the previous iteration.
3. Apply for new weighted least squares estimates.

$$b(t) = [X' W^{(t-1)} X]^{-1} X' W^{(t-1)} y \quad \text{Eq. 5-20}$$

X is the model matrix, with x_i' as its i th row, and $w_i^{(t-1)} = \text{diag} \{w_i^{(t-1)}\}$ is the current weight matrix. These steps are repeated until the estimated coefficients converge and the covariance matrix of b is

$$Vb = \frac{E(\psi^2)}{[E(\psi')]^2} (X'X)^{-1} \quad \text{Eq. 5-21}$$

Using $\sum[\psi(e_i)]^2$ to estimate $E(\psi^2)$ and $[\sum\psi'(e_i)/n]^2$ to estimate $\sum[E\psi']^2$ produces the estimated covariance matrix $\hat{V}(b)$.

5.3.4 Total least squares

The TLS method, also known as the error-in-variables method or orthogonal regression method, is a general approach that can be used in n -dimensional space (Petras and Podlubny 2010). Many areas of application use the TLS method such as signal processing, image processing, and economics. The orthogonal distance (i.e. distance between the data point and fitted line) is the main category of TLS, as illustrated in Figure 5-4, and it can be mathematically expressed by the following relation (Petráš and Bednárová 2010):

$$R = \sum_{i=1}^n |d_i| \quad \text{Eq. 5-22}$$

d is the orthogonal distance, and the target is to find a minimum of R ; the TLS approach minimizes the sum of the squared d from the data points to the fitting line. With the TLS method, the well-known mathematical tools are usually used.

For the linear regression model of the expression,

$$y = bx + a \quad \text{Eq. 5-23}$$

The coefficients a and b can be derived from the following relations:

$$a = \frac{\sum_{i=1}^n y_i - b \sum_{i=1}^n x_i}{n} = \bar{y} - b\bar{x} \quad \text{Eq. 5-24}$$

$$B = \frac{1}{2} \frac{(\sum_{i=1}^n y_i^2 - n\bar{y}^2) - (\sum_{i=1}^n x_i^2 - n\bar{x}^2)}{n\bar{x}\bar{y} - \sum_{i=1}^n x_i y_i} \quad \text{Eq. 5-25}$$

where $b = -B \pm \sqrt{B^2 + 1}$ can be obtained from correlation coefficient r .

The OLS and TLS methods assess the fitting accuracy in various ways: the OLS method minimizes the sum of the squared vertical distances from the data points to the fitting line, whereas the TLS method minimizes the sum of the squared d from the data points to the fitting line. Figure 5-4 shows OLS and TLS fitting lines as well as the data approximation. In the least squares case, the data approximation is obtained by correcting the second coordinate only. In TLS, the data approximation is obtained by correcting both coordinates (Markovsky and Van Huffel 2007). This method takes into account the noise in the independent and dependent variables (Varga and Szabo 2002).

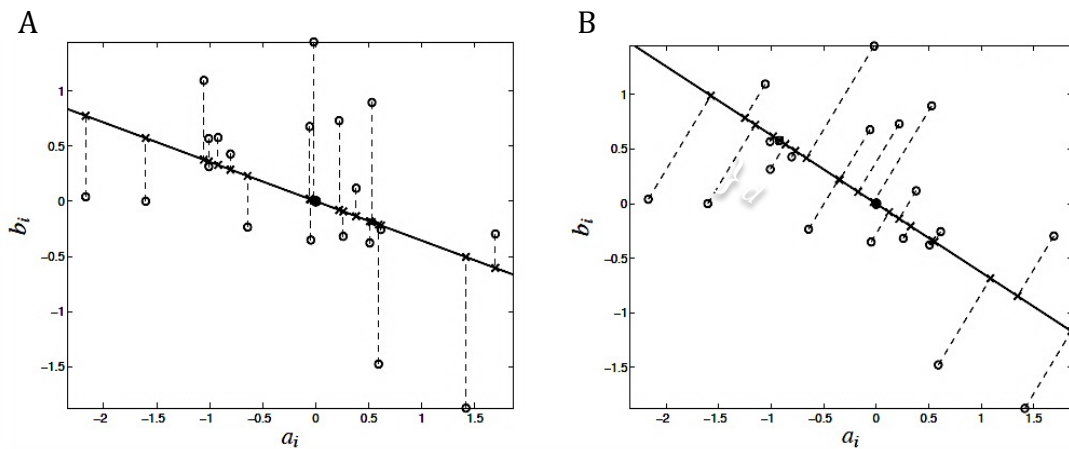


Figure 5-4. Ordinary least squares (A) and total least squares (B) fit of the set of $m = 20$ data points in the plane. (○---) data points, $[a_i b_i]$, x- approximations $[\hat{a}_i \hat{b}_i]$, solid line (—) fitting model $\hat{a}\hat{x} = \hat{b}$, dashed lines (---) approximation errors.

5.4 Results

5.4.1 Normal simulated Ki values

TACs for reference tissue (cerebellum) and ROI (left striatum) that were obtained from the first simulation data without noise are plotted as an example in Figure 5-5. The

curves show that activity in the cerebellum starts to increase significantly, reaching 12000 kBq/cc, and then decreases (washout) to around 4000 kBq/cc, as well as starts what is known as the equilibration stage, which is the time point most preferable for Patlak analysis. The activity washout confirms the reversibility of the cerebellum region. In contrast, the left striatum TAC increased until it reached a stable level for the remainder of the scan, which confirms the irreversibility. The (Ki) results from all simulated data are presented in figure 5-6, 5-7, 5-8 and 5-9 and in Appendix A: Tables A-1, A-2, A-3, and A-4 for OLS, FGLS, TLS, and RFR calculation, respectively; the results include noisy and non-noisy data. After fitting the data into the statistical models, two numerical methods used to evaluate the goodness of fit for all linear regression analyses were included: the sum of squares due to error (SSE) and the standard error (SE), known as the root mean squared error (RMSE) as well. The numerical measures are more closely concentrated on a specific aspect of the data and often try to compress that information into a single number. SSE measures the total deviation of the response values from the fit, where a value closer to 0 indicates a smaller random error component within the model selected, and the fit will be more useful for prediction. It is also known as the summed square of residuals.

$$SSE = \sum_{i=1}^n (y_i - \hat{y}_i)^2 \quad \text{Eq. 5-26}$$

SE is an estimate of the standard deviation of the random components in the data and is similar to the SSE. An SE value closer to 0 indicates a fit that is more useful for estimation. SE is described as

$$SE = \sqrt{MSE} \quad \text{Eq. 5-27}$$

$$MSE = \frac{SSE}{v} \quad \text{Eq. 5-28}$$

$$v = n - m \quad \text{Eq. 5-29}$$

where MSE is the mean square error or the residual mean square, and ν indicates the number of independent pieces of information involving the n data points that are required to calculate the sum of squares, calculated as the number of response values n minus the number of fitted coefficients m estimated from the response values.

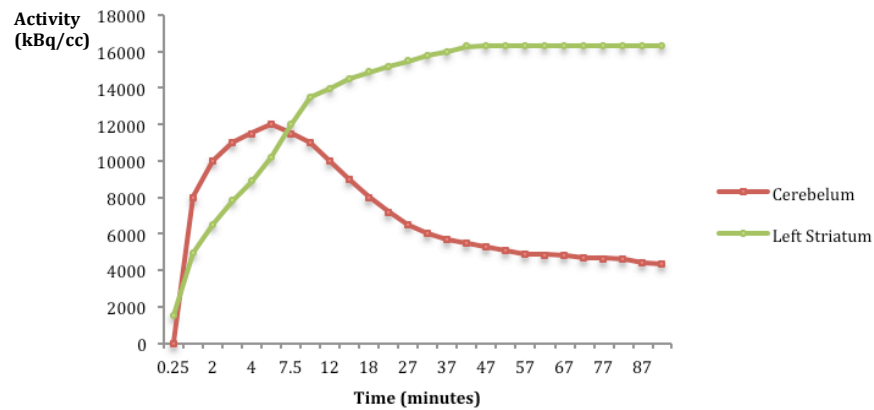


Figure 5-5. TACs for the reference tissue (cerebellum) and ROI (left striatum) that were obtained from the first simulation data without noise are plotted as an example.

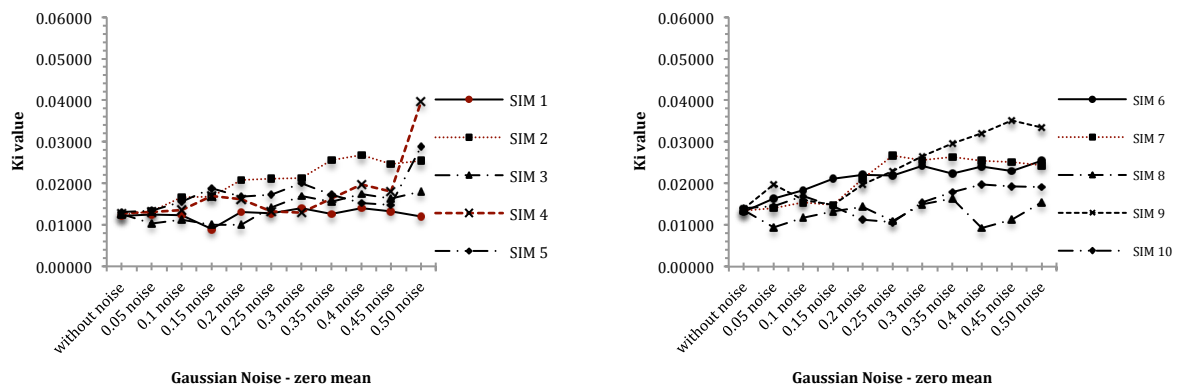


Figure 5-6. OLS regression method used for kinetic Patlak analysis on all simulation data and K_i values illustrated within 10 noise levels.

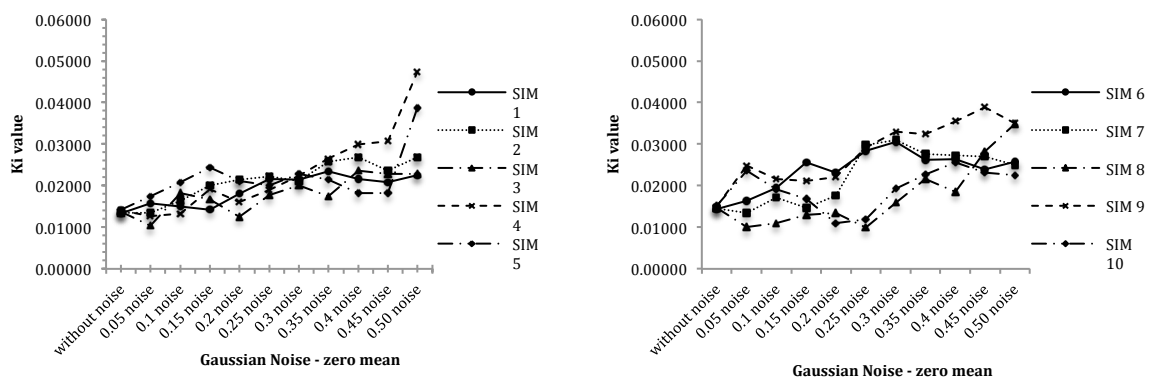


Figure 5-7. FGLS regression method used for kinetic Patlak analysis on all simulation data and K_i values illustrated within 10 noise levels.

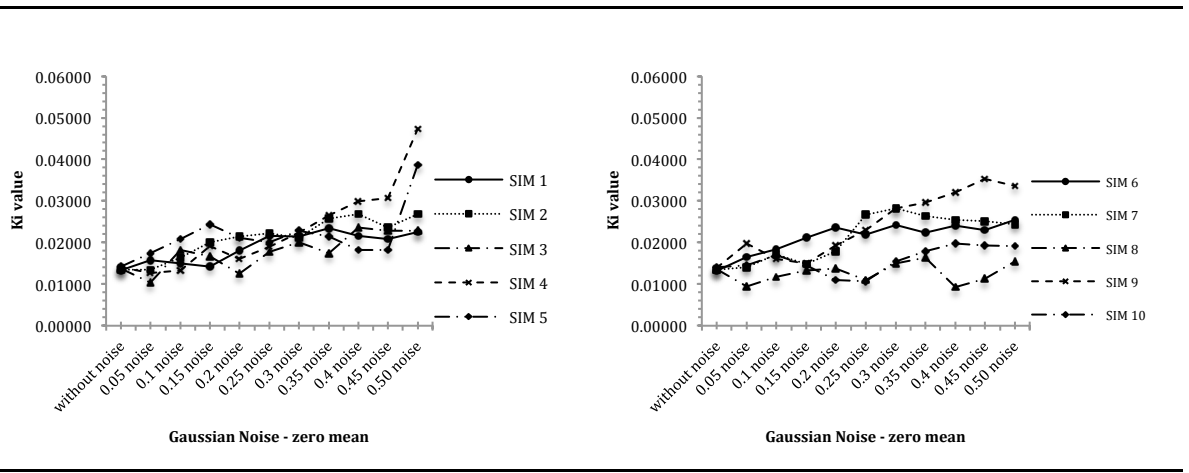


Figure 5-8. TLS regression method used for kinetic Patlak analysis on all simulation data and K_i values illustrated within 10 noise levels.

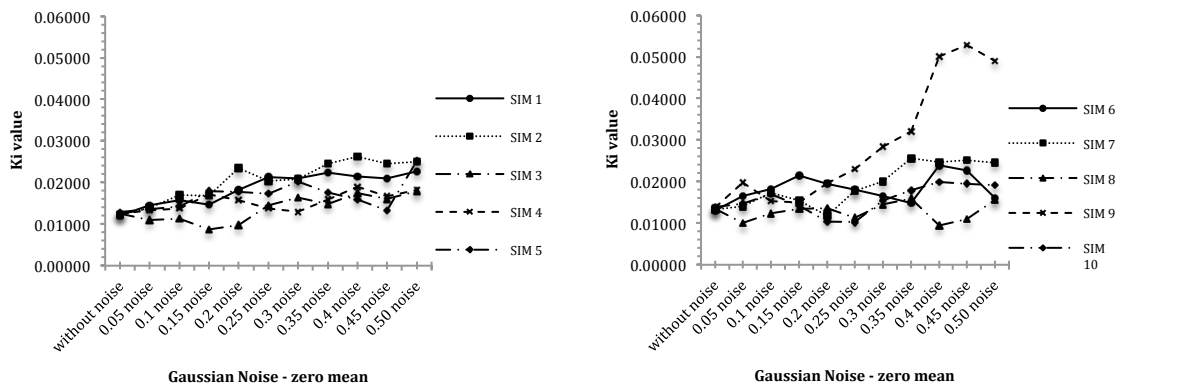


Figure 5-9. RFR regression method used for kinetic Patlak analysis on all simulation data and K_i values illustrated within 10 noise levels.

A one-way repeated measured analysis of variance (ANOVA) was conducted to evaluate the null hypothesis that there is no change in the simulations' K_i value when calculated with various statistical regression models in all four groups ($N = 10$). The results are summarized in Table 5-1. The ANOVA test results indicated a significant effect, Wilks' Lambda = .001, $F(3, 7) = 41.17$, $p < 0.01$, $\eta^2 = .75$. Thus, there is significant evidence to reject the null hypothesis. Follow-up comparisons indicated that each pairwise difference was significant, $p < 0.01$, except between OLS and TLS, where $p = 0.09$. There was a significant difference between the statistical models used, suggesting that using a different linear regression model reveals a different K_i value, which is the main parameter used in diagnosis. A repeated measured ANOVA is performed when the samples are considered to be related (dependent) and more than

two groups. The measurements of SE, SSE, and fold changes are summarized in Table 5-2. With the OLS method, the min SE in all simulations, including noisy data, was 0.057, and the max was 1.01070; the average SE was 0.236. For SSE, the min was 0.0003, the max was 0.093, and the average was 0.007. The fold change range was between 0.0004 and 2.097. FGLS calculations with the data showed that the SE min was 0.0012, the max was 0.0106, and the average was 0.0042. The SSE min was 1×10^{-7} , the max was 1×10^{-5} , and the average was 2×10^{-6} , with a general fold change range of 0.003-2.381. For TLS analysis, the min SE was 0.0697, the max was 1.3071, and the average SE in all data calculations was 0.4505. The SSE min was 0.0004, the max was 0.1553, and the average was 0.0237. The fold change range was 0.005-2.096. The min SE in the RFR analysis was 0.070, the max was 0.922, and the average was 0.379. The SSE min was 0.0005, the max was 0.077, and the average was 0.0180, with a fold change range of 0.008-2.838.

Table 5-1. A one-way repeated measured analysis of variance (ANOVA) result.

Test	Wilks' Lambda	F(3, 7)	p -value
ANOVA (N=10)	.001	41.17	p < 0.01
	pairwise difference	OLS and TLS, pairwise	η^2
	p < 0.01	p = 0.09	.75

Table 5-2. SE, SSE, and fold change values for each method applied to simulation data.

Stat. Model		SE	SSE	fold change
OLS	Min	0.0568	0.0003	0.0004
	Max	1.0107	0.0929	2.0956
	Avg.	0.2355	0.0074	0.4290
FGLS	Min	0.0012	0.1 E-06	0.0032
	Max	0.0106	10.2 E-06	2.3815
	Avg.	0.0042	2.0 E-06	0.5842
TLS	Min	0.0697	0.0004	0.0051
	Max	1.3071	0.1553	2.0957
	Avg.	0.4505	0.0237	0.4820
RFR	Min	0.0703	0.0005	0.0075
	Max	0.9216	0.0772	2.83823
	Avg.	0.3795	0.0180	0.4728

5.4.2 Averaged Ki values (normal and abnormal)

5.4.2.1 2D data analysis (Curve data)

An ANOVA was conducted to evaluate the null hypothesis that there is no change in the simulations' Ki value when calculated with various statistical regression models in all four groups and each group contains six simulations of Ki values ($N = 6$). The results are summarized in Table 5-3. The ANOVA test results indicated a significant effect, Wilks' Lambda = .068, $F(3, 3) = 13.743$, $p < 0.05$, $\eta^2 = .932$. Thus, there is significant evidence to reject the null hypothesis. Follow-up comparisons indicated that each pairwise difference was not significant, $p > 0.05$, $p=1$. There was a significant difference between the statistical models used, suggesting that using a different linear regression model reveals a different Ki value, which is the main parameter of diagnosis.

The measurements of SE, SSE, and fold changes are summarized in Table 5-4.

Table 5-3. A one-way repeated measured analysis of variance (ANOVA) result to average 2D simulation data.

Test	Wilks' Lambda	F(3, 3)	p -value
ANOVA (N=6)	.068	13.743	p < 0.05 p=0.029
	pairwise difference between stat. models		η^2
	p > 0.05 p = 1		.932

Table 5-4. SE, SSE, and fold change values for each method applied to average 2D simulation data.

Stat. Model		SE	SSE	fold change
OLS	Min	0.0354	0.0001	0.0916
	Max	1.1634	0.1231	2.0716
	Avg.	0.3893	0.0180	0.7560
FGLS	Min	0.0004	1.16E-08	0.1613
	Max	0.0282	7.22E-05	2.9431
	Avg.	0.0059	4.89E-06	1.0210
TLS	Min	0.0259	6.10E-05	0.0915
	Max	1.0646	0.1030	2.0770
	Avg.	0.3078	0.0122	0.7711
RFR	Min	0.0238	5.15E-05	0.0162
	Max	0.9610	0.0838	2.0702
	Avg.	0.2704	0.0097	0.6382

5.4.2.2 *Dynamic images (3D data analysis)*

An ANOVA was conducted to evaluate the null hypothesis that there is no change in the simulations' Ki value when calculated with various statistical regression models in all four groups ($N = 6$). The results are summarized in Table 5-5. The ANOVA test results indicated a significant effect, Wilks' Lambda = .099, $F(3, 3) = 9.079$, $p < 0.05$, $\eta^2 = .901$. Thus, there is significant evidence to reject the null hypothesis. Follow-up comparisons indicated that each pairwise difference was not significant, $p > 0.05$. There was a significant difference between the statistical models used, suggesting that using a different linear regression model reveals a different Ki value, which is the main parameter of diagnosis. The measurements of SE, SSE, and fold changes are summarized in Table 5-6.

Table 5-5. A one-way repeated measured analysis of variance (ANOVA) result to average 3D simulation data.

Test	Wilks' Lambda	F(3, 3)	p -value
ANOVA (N=6)	.099	9.079	p = 0.05
	pairwise difference between stat. models		η^2
	p > 0.05		.901

Table 5-6. SE, SSE, and fold change values for each method applied to average 3D simulation data.

Stat. Model		SE	SSE	fold change
OLS	Min	0.0274	6.81E-05	0.0040
	Max	1.1881	0.1283	0.7924
	Avg.	0.3331	0.0109	0.0998
FGLS	Min	0.0005	2.51E-08	0.0029
	Max	0.0361	0.0001	1.9704
	Avg.	0.0040	2.39E-06	0.2083
TLS	Min	0.0342	0.0001	0.0050
	Max	2.9391	0.7853	0.7967
	Avg.	0.1526	0.0047	0.0943
RFR	Min	0.0369	0.0001	2.77E-05
	Max	0.9945	0.0899	0.3334
	Avg.	0.1189	0.0019	0.0883

5.5 Discussion

For most of the K_i values, they increase in proportion to the level of noise. SE and SSE also increase with a higher noise level. In all data groups, repeated measures ANOVA tests indicated that there is significant evidence to reject the null hypothesis $p < 0.01$ in the first group and $p \leq 0.05$ in the 2nd and 3rd groups. This confirms that those statistical models reveal different results for the final K_i value for both 2D and 3D data sources. Each statistical regression model dealt with the simulation data in a different way, and based on the goodness of fit evaluations, the regression model with the best fit can be chosen. In the first group of data, in simulations 1-5, the data behaved quite similarly with the noise effect compared to simulations 6-10, which had more scattering, and increasing the K_i amount for the data without noise could have caused this. Follow-up comparisons indicated that each pairwise difference was significant, $p < 0.01$, except between OLS and TLS, where $p = 0.09$. The p value between OLS and TLS confirms the similarity between these two calculations. The second and third datasets show a p value higher than 0.05, $p > 0.05$, indicating that there is no significant differences between each individual statistical model used in the last two experiments.

There was a significant difference between the statistical models used, suggesting that using a different linear regression model reveals a different K_i value, which is the main parameter of PD diagnosis. The min SE and SSE were found with FGLS, and this suggests that FGLS is the best of these models to fit the noisy data. RFR had the lowest fold change rate among all results, this can be noticed when measure the change difference from the noisy K_i value from values without noise, then the absolute amounts in percentages are obtained. This indicates more resistance to the noise effect than the other methods. The big difference within the SE from one noise level to another indicates the high sensitivity to noise in linear regression analysis, which confirms the previous results in the published literature review. The experiment has contributed to the knowledge in the field by suggesting the use of FGLS as a linear regression method for Patlak graphical analysis in clinical data that are assumed to have low noise. From the above results, using FGLS could provide better data fitting with low SE and SEE. In the case where PET data may include a high level of noise, the RFR statistical model would be better in achieving high accuracy than FGLS, but this might generate high SE and SSE records. Repeating the experiment with various equivalent time (t^*) points could reveal more details and alter the accuracy of those methods. It would be useful to apply those models on clinical data obtained from patient dynamic images and compare the results to the outcome of this experiment.

5.6 Conclusion

Graphical techniques in PET data analysis from reference tissue are considered simple means of analysis to obtain physiological parameters. Patlak equations for irreversible tracers were used to measure the K_i rate constant, which is used to diagnose and evaluate FDOPA PD images. One issue usually generated with this type of analysis is the introduction of bias, caused by the sensitivity to statistical noise that is usually

present when using the OLS method. The study shows that selecting and applying other statistical methods could reduce bias and sensitivity to noise. The min SE and SSE were found with FGLS, and this suggests that FGLS is the best of these models to fit the noisy data. The simulated phantom PET data generated from the dPETSTEP simulation tool illustrated how various statistical methods can affect the image analysis result and how they behave with various levels of noise. There was a significant difference between the statistical models used, suggesting that using a different linear regression model reveals a different K_i value. Analysing the PET data with various statistical regression approaches and evaluating each approach graphically and numerically could improve the final result for more accurate diagnosis.

6 Noise Reduction Techniques in Simulated ^{18}F -FDOPA Dynamic PET Data

6.1 Introduction

PET is a medical imaging modality that allows researchers and clinicians to noninvasively image and evaluate physiological and functional processes that are valuable in patient diagnosis, monitoring, and therapy outcomes. The quantification of PET data in conjunction with CT or MRI data provides additional information alongside visual inspection of the images. One of the confounding factors that affects the quantification of PET images is noise in the images. In fact, PET images have increased noise levels compared to other imaging modalities such as CT, MRI, or US (Teymurazyan et al. 2013). In recent years, new image processing methods and techniques have been introduced in imaging equipment of different modalities. Some of these methods were introduced to reduce the effect of noise, although understanding and categorising PET imaging noise is challenging. Positron decay events from a radioactive tracer have a Poisson distribution, and the scanner's components add noise to that characteristic distribution, which is further altered during image reconstruction and the application of corrections (Teymurazyan et al. 2013). The reduction of noise in PET images can be performed by applying post-process quantification. The noise model found in PET images is usually characterized as Gaussian (Boyat and Joshi 2015; Coxson et al. 1995; Ollinger and Fessler 1997). Post-processing techniques are an alternative way to increase the signal to noise ratio rather than increasing the injected dose, which is considered unethical and increases the risk of harm to the patient.

^{18}F -FDOPA is used to scan and quantify the function of dopaminergic receptors in the brain. It is assumed to be an irreversible tracer and can be analysed using Patlak graphical analysis. This type of model is very sensitive to the noise in PET images due to several factors, including nonspecific binding in tissue or plasma proteins, model linearity introducing bias from early time points, and dependency on regression estimation analysis (Logan 2003; Varga and Szabo 2002). Some physiological parameters, such as influx rate (K_i), that are obtained by quantification models sometimes become meaningless and include errors due to the amplification of noise during the analysis (Axelsson and Sørensen 2013). This could lead to a false positive and/or negative result, which consequently affects diagnosis and treatment decisions.

In this chapter, we have identified several methods of noise reduction, including anisotropic diffusion (gradient and curvature) and wavelet (Daubechies and Battle-Lemarie wavelets) and applied them to simulated PET dynamic images to evaluate the effects of these methods. Simulated PET data used in the studies mimics the ^{18}F -FDOPA tracer brain images. The dose, scan protocol, scanner characteristics, reconstruction algorithm, and all physical corrections have been simulated using dPETSTEP (Haggstrom et al. 2016). The K_i values used in the experiment represent both normal and abnormal subjects, and Patlak analysis was performed based on reference tissue as an input function, so no blood time activity curve was required. The aim of this study was to optimise the quantification of PET analysis by identifying the most suitable method of noise reduction whilst preserving the pixel and voxel quantitative values. The theory and equations behind each method are illustrated in the following theory section.

6.2 Theory

Several noise reduction methods applicable to 3D images are used in this study, and the theory behind these methods will be explained in the following section. Each method was applied on noisy simulated PET data for 0.014, 0.012, 0.010, 0.0075, 0.0050 and 0.0025; various K_i values represent normal and abnormal influx rates and each K_i value was exposed to ten levels (between 5% and 50%) of Gaussian noise with mean=0. After performing Patlak graphical analysis on the appropriate statistics, standard errors (SEs) and sum-squared errors (SSEs) were presented for evaluation. The SE of the regression or estimate is the average distance between observational points and the regression line and evaluates how the regression model is wrong using the units of response variable. SEs were used to measure the accuracy of the predictions; a smaller value indicates better accuracy and closer observations to the fitting line. SSE refers to the sum of the squared differences between the prediction of each observation and its group mean. A small SSE value indicates a tight fit of the model to the data and can be used as a measurement of variation within a data group (Lewis-Beck and Lewis-Beck 2015; Montgomery et al. 2012).

6.2.1 Gradient anisotropic diffusion filter

Anisotropic diffusion, also known as the Perona-Malik (Perona and Malik 1990) diffusion method, was originally introduced as an alternative to the linear-filtering method, which tends to blur sharp boundaries and makes separating the anatomical structures in the images more difficult. A gradient anisotropic diffusion filter (GADF) aims to reduce the noise whilst preserving the image contents that are essential for interpretation (Sapiro 2006). In this approach, groups of successively blurred parameterized images are generated based on the diffusion process, then each image within this group is given as a convolution to a 2D isotropic Gaussian filter. The width

of this filter is increased proportionally to the parameter. Thus, each resultant image is a combination of the original image (based on its content) and a filter. As a consequence, anisotropic diffusion is a non-linear and space variant transformation of an original image, considering that the diffusion process is a linear and space-invariant transformation (Guidotti 2009; Méndez-Rial and Martín-Herrero 2018). This can be described using a mathematical expression:

$$\frac{\partial g(x,y,t)}{\partial t} = \nabla \cdot \nabla g(x,y,t) \quad \text{Eq. 6-1}$$

The input image is $g(x,y,t)$, $g(x,y,t) = G(\sqrt{2t}) \otimes f(x,y)$, and $G(\sigma)$ is a Gaussian filter with standard deviation σ ; x and y make up the coordinate system used to locate the image's pixels (line, column), and t refers to time or iteration steps in a discrete case. The variable conductance term is included within anisotropic diffusion. It depends on the differential structure of the image, can be devised to constrain the smoothing at the “edges”, and is measured by a high gradient magnitude (Johnson et al. 2017);

$$g_t = \nabla \cdot c(|\nabla g|) \nabla g \quad \text{Eq. 6-2}$$

$$c(|\nabla g|) = e^{-\frac{|\nabla g|^2}{2k^2}} \quad \text{Eq. 6-3}$$

The diffusion coefficient c controls the rate of diffusion and the conductance term introduces a free parameter k (Eq. 6-3) to be quite effective; the conductance parameter k controls the sensitivity of the procedure to the contrast of the image's edge. Thus, anisotropic diffusion demands two free parameters: k and t , the conductance parameter and the time parameter, respectively, that correspond to σ . When using Gaussian kernels, it is the effective width of the filter. The smoothed image can only be acquired by an iterative process without a convolution or non-stationary linear filter. Equation 6-2 can be solved on a discrete grid using finite forward differences where it is a nonlinear

partial differential equation. Thus, few iterations are required for practical results and this technique can be applied effectively to 3D images at the cost of more processing time (Johnson et al. 2017).

Gradient anisotropic diffusion applies an N -dimensional version of the standard Perona-Malik anisotropic diffusion calculation for scalar-valued images, where at each point of the image, a conductance term for this operation is selected as a function of the gradient magnitude, and the strength of the diffusion at the edge pixels is reduced (Perona and Malik 1990).

$$C(x) = e^{-\left(\frac{\|\nabla U(x)\|}{K}\right)^2} \quad \text{Eq. 6-4}$$

$U(x)$ is an image and K is the constant that controls the sensitivity to edges, it is usually selected as a function of noise in the image or experimentally. Gradient magnitude estimation is a more robust technique with more generalization to N dimensions. Three parameters are usually required to start this method: iteration number, the time step, and the conductance level. A time step equal to 0.125 in 3D images is highly recommended, and the number of iterations is usually set to 5, as increasing it leads to more image smoothing and costs more time and the conductance level is set to 1 (Johnson et al. 2017). Figure 6-1 illustrates the effect of this filter on a simulated ^{18}F -FDOPA image of the brain, where the gradient anisotropic diffusion filter was run with a time step of 0.125 and conductance = 1 for 5 iterations. The figure shows how the image is smoothed, noise reduced and edges are more preserved.

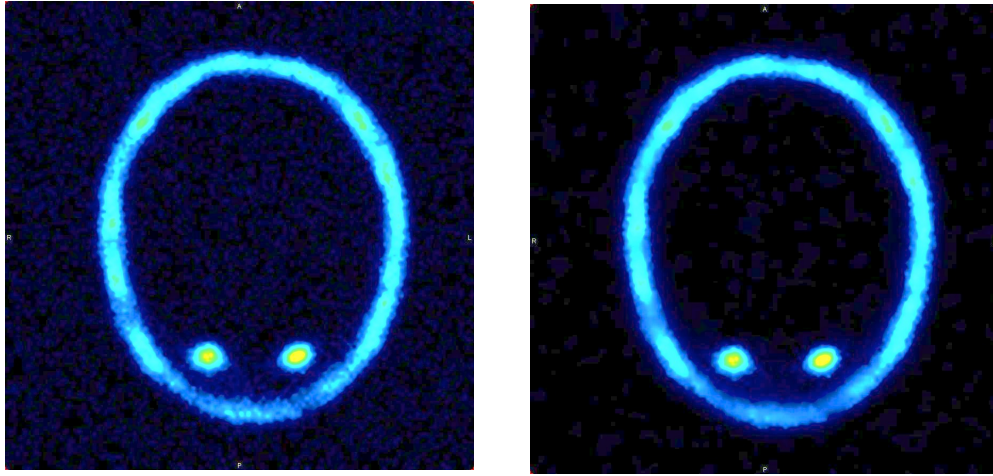


Figure 6-1. Effect of the gradient anisotropic diffusion image filter on a slice from an image of the brain (right); noise reduction can be seen compared to the noisy image (left).

6.2.2 Curvature anisotropic diffusion filter

The curvature anisotropic diffusion filter (CADF) uses a modified curvature diffusion equation (MCDE) to perform anisotropic diffusion on images without exhibiting the edge-enhancing properties of classic anisotropic diffusion, which undergoes a “negative” diffusion that can enhance the contrast of edges. The conductance term in CADF is the only parameter that plays a role in varying the strength of diffusion. For visual assessment, CADF performs very well in comparison to the other non-linear diffusion techniques. It has lower sensitivity to contrast than the original Perona-Malik diffusion technique and provides superior preservation of detailed structures in images. There is a potential speed trade-off for using this function in place of GADF, as a low number of iterations may be required to reach an acceptable solution (Johnson et al. 2017).

The MCDE equation can be written as

$$f_t = |\nabla f| \nabla \cdot c(|\nabla f|) \frac{\nabla f}{|\nabla f|} \quad \text{Eq. 6-5}$$

and the conductance modified curvature term is

$$\nabla \cdot \frac{\nabla f}{|\nabla f|}$$

Similar to GADF, this technique requires three parameters: iteration numbers, time steps used in the computation, and the value of conductance. Parameter values of a time step of 0.0625 and conductance of 3 were recommended by (Johnson et al. 2017) when using this method on 3D images. In our experiment, we varied the number of iterations from 1 to 3. Increasing the number of iterations increases the processing time as well, further smoothing the image.

6.2.3 Wavelets

A wavelet is a wave-like oscillation with amplitude that begins at zero, increases, and then decreases back to zero. Wavelets were originally designed to produce useful characterisations of signals in signal and imaging processing fields. The aim of a wavelet is to merge with known parts of the signal and provide details about unknown parts of the signal using several convolutional techniques, such as shifting, reversing, and integrating signals. There are different types of wavelets, and each type has applications in many fields. Generally, the full data set is analysed using a set of wavelets by cutting the original signal into various components based on frequency. Then, the original signal is recovered with minimal information loss depending on compression and decompression algorithms. In general, wavelets under certain mathematical conditions are used to represent original data sets or functions after resolving missing parts, gaps, or overlap at different scales within the signal. These advantages of wavelets make them desirable in many applications instead of the classical Fourier methods, particularly in fields in which the signal includes sharp spikes or discontinuities (Chui 2016; Graps 1995).

Briefly, a wavelet-based denoising algorithm usually has these steps:

- (1) A wavelet is applied to transform the noisy data.
- (2) Soft thresholding is performed on the wavelet coefficients to establish the noise variance.
- (3) Coefficients obtained from step 2 are then padded with zeros to produce a matrix.
- (4) The signal estimation is obtained later by inverting the matrix.

Wavelet transforms can be categorised into three types: continuous, discrete, and multi-resolution basis. Daubechies' and Battle-Lemarie wavelets are two varieties that have been widely applied in medical image processing for noise reduction. In this section, these two techniques will be discussed theoretically and applied to our PET data set to evaluate their impact on quantification analysis.

6.2.3.1 Daubechies' wavelet

Daubechies' wavelet (DW) is frequently used in smoothing and denoising 2D and 3D images. Due to the limitations of imaging equipment and reconstruction algorithms, pre- and post-processing filtering methods are desirable for many radiologists. The ultimate aim of applying DW to our data is to extract the quantity value from the 3D volume's voxels and remove or at least reduce the noise. Wavelet methodology has been used in many studies to remove noise from medical images and signals in general (Jansen 2012; Nowak 1999; Pizurica et al. 2003). The main assumption in this analysis is that the added noise has different frequencies than the useful data (Wang 2001). When the wavelet technique is applied to the raw imaging data, many of the artefacts caused by interfering signals and/or waves picked up by the scanner are disregarded. This could improve the signal to noise ratio for the data and is applicable in all medical imaging modalities (Singh and Urooj 2015).

The DW method was originally developed to overcome the limitations of discontinuous step functions, such as Haar's wavelet technique (Stanković and Falkowski 2003). Medical images regularly contain smooth regions and thus are not suitable for Haar's

wavelet base functions or other discontinuous step functions, and analysing smoothing with continuous derivative construction could introduce unsatisfactory analysis results. Haar's orthogonal wavelet bases (Wang 2001) are defined on $[0,1]$, namely $h_0(x), h_1(x), \dots, h_n(x)$ and for any continuous function $f(x)$ on $[0,1]$, the series can be expressed as

$$\sum_{j=1}^{\infty} \langle f, h_j \rangle h_j(x) \quad \text{Eq. 6-6}$$

Uniformly on $[0,1]$, this converges to $f(x)$;

$$\langle u, v \rangle = \int_0^1 u(x) \overline{v(x)} dx \quad \text{Eq. 6-7}$$

$\langle u, v \rangle$ denotes the inner product of u and v , where \bar{v} is the complex conjugate of v and they are equal in the case of real-valued function. An example of Haar's structure (Porwik and Lisowska 2004) can be written as

$$h(x) = \begin{cases} 1, x \in [0, 0.5) \\ -1, x \in [0.5, 1) \\ 0, elsewhere \end{cases} \quad \text{Eq. 6-8}$$

$$h_n(x) = 2^{j/2} h(2^j x - k) \quad \text{Eq. 6-9}$$

where $n = 2^j + k, k \in [0, 2^j), x \in [k2^{-j}, (k+1)2^{-j})$.

In DW, the orthonormal basis for $L^2(\mathbf{R})$ for each integer r is defined as

$\phi_{r,j,k}(x) = 2^{j/2} \phi_r(2^j x - k), j, k \in \mathbf{Z}$	Eq. 6-10
--	-----------------

r, j , and k are the filtering, scaling, and shifting indexes, respectively, and f_j at scale

2^{-j} in the function $f \in L^2(\mathbf{R})$ can be expressed as

$$f_j(x) = \sum_k \langle f, \phi_{r,j,k} \rangle \phi_{r,j,k}(x) \quad \text{Eq. 6-11}$$

The fluctuations' function (details) can be defined as

$$d_j(x) = f_{j+1}(x) - f_j(x) \quad \text{Eq. 6-12}$$

These details can be analysed on a certain scale by giving the properties of $\phi_r(x)$ to another orthonormal basis noted as $\psi_r(x)$; $\phi_r(x)$ and $\psi_r(x)$ are usually called the father wavelet and the mother wavelet, respectively, and they are both required for the rest of the DW analysis. The properties of this method can be summarized as follows (Singh and Urooj 2015; Wang 2001);

- $\psi_r(x)$ has the compact support interval $[0, 2r+1]$
- $\psi_r(x)$ has about $r/5$ continuous derivatives
- $\int_{-\infty}^{\infty} \psi_r(x) dx = \dots = \int_{-\infty}^{\infty} x^r \psi_r(x) dx = 0$

Due to these characteristics, DWs can deliver exceptional results in image processing. The detail analysis of a function can be implemented by convolving it with low- and high-pass filters.

6.2.3.2 Battle-Lemarie wavelet

The Battle-Lemarie wavelet (BLW) family is one of the common classical orthonormal wavelets constructed using spline functions. Using cardinal B-splines, BLW bases can be constructed with unique characteristics such as symmetry and exponential decay (Xiao et al. 2003). BLW shifts from orthonormal bases of the spline-wavelet spaces and the shapes of its magnitude spectra tend to be rectangular as the order of spline function increases (Averbuch et al. 2015).

The B-spline function has simple, clear formulas in the time-domain and the frequency-domain of degree m , N_m , and generally, the time-domain form of the cardinal B-spline of degree m can be given by

$$\hat{N}_m(\omega) = \left(\frac{\sin \omega / 2}{\omega / 2} \right)^{m+1} \cdot e^{-i\lambda\omega/2} \quad m = 0, 1, 2\Lambda \quad \text{Eq. 6-13}$$

where $\lambda=0$, $N_m(t)$ is symmetrical around $t=0$ if m is odd, $\lambda=1$; $N_m(t)$ is symmetrical around $t=1/2$ if m is even.

The ϕ_{Haar} (Haar scaling function), $m(t)$, and the $\{N_m(-k): k \in Z\}$, $m \geq 1$ are not orthonormal, with the exception of $N_0(t)$ or the cardinal B-spline of degree zero. Orthonormalization deception is applied to the $N_m(t)$, and (orthonormal) BL scaling function ϕ_{BL} , $m(t)$ can be obtained and the function of the resultant filter can be written as

$$H_{BL,m}(\omega) = \frac{1}{2^m} \frac{\sqrt{\sum_{2^m}(\omega)}}{\sum_{2^m}(\omega)} e^{-i\lambda\omega/2} = \sum_{k \in Z} h_k e^{-ik\omega} \quad \text{Eq. 6-14}$$

$\Sigma_m(\omega) = \sum_{k \in Z} 1/(\omega + 2k\pi)^m$, $h_{BL,m} = \{h_k: k \in Z\}$ is the Fourier series coefficient set of $H_{BL,m}(\omega)$, and it is called the scaling filter coefficient or sometimes the mask of $\phi_{BL,m}$.

$H_{BL,m}(\omega)$ filter function has a concise expression. An example of the lower order case:

$$H_{BL,0}(\omega) = \frac{1}{2} + \frac{1}{2} e^{-i\omega} = H_{Haar}(\omega) \quad \text{Eq. 6-15}$$

6.3 Results

6.3.1 GADF result

A one-way repeated measured analysis of variance (ANOVA) was conducted to evaluate the null hypothesis that there would be no change in the simulations' Ki, SE, and SSE values when calculated with the GADF in all groups of 5 and 10 iterations ($N = 6$). The results are summarized in Tables 6-1, 6-2, and 6-3. The ANOVA test results indicated no significant effect of GADF in noisy images for all noise levels, Wilks' lambda > 0.005 , and $p > 0.05$. Thus, there is no significant evidence to reject the null hypothesis for GADF (5 and 10 iterations). A repeated-measures ANOVA was

performed when the samples were considered related (dependent) and in more than two groups. The average reduction in Ki mean values for 5 and 10 iterations was -2% and -1%; for SE, +9.7% and 0%; and for SSE, +23% and -4%, respectively. Note the increasing percentage in the mean values in SE and SSE for the 5-iteration process. More details and comparisons of results are presented in Table 6-13 for GADF and all remaining methods at the end of the result section.

Table 6-1. A one-way repeated measured analysis of variance (ANOVA) result for Ki values in simulations before and after applying GADF at 5 and 10 iterations.

Test (Ki)	Statistics	Noise levels										
		0.05	0.1	0.15	0.2	0.25	0.3	0.35	0.4	0.45	0.5	
RM-ANOVA (n=6)	p-value	0.62	0.259	0.683	0.541	0.407	0.825	0.388	0.334	0.317	0.246	
	Wilks' lambda	0.79	0.509	0.826	0.735	0.638	0.908	0.623	0.422	0.563	0.496	
	η^2	0.21	0.491	0.174	0.265	0.362	0.092	0.377	0.578	0.437	0.504	
	SD	Sim	0.0045	0.0050	0.0048	0.0058	0.0051	0.0052	0.0047	0.0051	0.0043	0.0055
		GADF 5	0.0044	0.0048	0.0053	0.0047	0.0047	0.0054	0.0049	0.0053	0.0043	0.0056
		GADF10	0.0042	0.0048	0.0047	0.0056	0.0050	0.0052	0.0052	0.0057	.00440	0.0060
	μ	Sim	.0089	0.0095	0.0094	0.0098	0.0092	0.0096	0.0093	0.0097	0.0083	0.0010
		GADF 5	.0088	0.0093	0.0096	0.0090	0.0092	0.0097	0.0084	0.0098	0.0084	0.0010
		GADF10	.0086	0.0093	0.0093	0.0096	0.0094	0.0096	0.0087	0.0100	0.0086	0.0010

Table 6-2. A one-way repeated measured analysis of variance (ANOVA) result for SE values in simulations before and after applying GADF at 5 and 10 iterations.

Test (SE)	Statistics	Noise levels										
		0.05	0.1	0.15	0.2	0.25	0.3	0.35	0.4	0.45	0.5	
RM-ANOVA (n=6)	p-value	.556	.933	.550	.578	.585	.591	.412	.248	.636	.411	
	Wilks' lambda	.745	.966	.742	.760	.765	.769	.642	.498	.798	.641	
	η^2	.255	.034	.258	.240	.235	.231	.358	.502	.202	.359	
	SD	Sim	.0387	.0561	.0490	.0414	.0347	.0545	.0444	.0582	.2413	.0590
		GADF5	.0445	.0587	.0663	.2526	.0978	.1039	.1704	.0393	.2216	.0685
		GADF10	.0425	.0574	.0464	.0491	.0313	.0333	.1430	.0345	.1659	.0709
	μ	Sim	.3014	.2864	.2939	.2922	.3076	.3239	.3140	.3230	.4130	.2925
		GADF5	.3127	.2872	.3109	.3884	.3432	.3625	.3766	.3163	.4044	.2941
		GADF10	.3071	.2869	.2924	.2806	.2941	.3115	.3558	.3070	.3782	.2874

Table 6-3. A one-way repeated measured analysis of variance (RM-ANOVA) result for SSE values in simulations before and after applying GADF at 5 and 10 iterations.

Test (SSE)	Statistics	Noise levels										
		0.05	0.1	0.15	0.2	0.25	0.3	0.35	0.4	0.45	0.5	
RM-ANOVA (n=6)	p-value	.510	.832	.574	.604	.586	.575	.444	.255	.650	.398	
	Wilks' Lambda	.714	.912	.758	.777	.765	.638	.666	.505	.806	.631	
	η^2	.286	.088	.242	.223	.235	.242	.334	.495	.194	.369	
	SD	Sim	.0022	.0028	.0025	.0022	.0020	.0034	.0026	.0035	.0258	.0030
		GADF 5	.0025	.0030	.0038	.0268	.0073	.0081	.0156	.0022	.0230	.0035
		GADF10	.0024	.0029	.0024	.0026	.0017	.0019	.0118	.0019	.0151	.0036
	μ	Sim	.0084	.0077	.0080	.0079	.0087	.0098	.0091	.0097	.0199	.0080
		GADF 5	.0090	.0078	.0091	.0185	.0114	.0128	.0151	.0092	.0186	.0082
		GADF10	.0087	.0077	.0079	.0073	.0079	.0089	.0131	.0087	.0151	.0079

6.3.2 CADF result

The results of multiple one-way RM-ANOVAs were used to evaluate the CADF effect on removing noise from simulated data. Ki values of three levels of CADF iterations were compared during all ten noise stages (5%-50%). The null hypothesis was that there would be no change in the simulations' Ki, SE, and SSE values when calculated with CADF. The results are summarized in Tables 6-4, 6-5, and 6-6 and comparisons made for Ki, SE, and SSE, respectively. Sample size is $N = 6$ for all analyses; for Ki, the statistical test results indicated that in most of the noise levels (6 of 10), CADF had no significant filtering effect for noisy images, $p > 0.05$, and Wilks' lambda > 0.05 in all data analysis; p -values at noise levels of 10%, 30%, 35%, and 45% were all significantly affected by CADF where $p < 0.05$. Thus, as most of the noisy data showed no significant difference, there was not enough evidence to reject the null hypothesis for CADF's effect on noise reduction in data. The average reduction in Ki mean value for CADF 1, 2, and 3 iterations was -1.32%, -1.12%, and -1.02%; for mean SE, -1.55%, -2.46, and -3.27%; for mean SSE, -3.54%, 1.52%, and -7.34%, respectively. More details and comparisons of results are presented in Table 6-13 for CADF and all remaining methods.

Table 6-4. A one-way repeated measured analysis of variance (ANOVA) result for Ki values in simulations before and after applying CADF at 1, 2, and 3 iterations.

Test (Ki)	Statistics	Noise levels										
		0.05	0.1	0.15	0.2	0.25	0.3	0.35	0.4	0.45	0.5	
RM-ANOVA (n=6)	p-value	.081	.039	.562	.084	.156	.039	.046	.707	.017	.055	
	Wilks' lambda	.136	.082	.549	.139	.214	.081	.091	.665	.047	.104	
	η^2	.864	.918	.451	.861	.786	.919	.909	.335	.953	.896	
	SD	Sim	.0045	.0050	.0048	.0058	.0054	.0053	.0055	.0055	.0064	.0056
		CADF1	.0044	.0050	.0048	.0056	.0053	.0047	.0051	.0051	.0060	.0055
		CADF2	.0044	.0050	.0048	.0054	.0052	.0048	.0048	.0050	.0057	.0056
		CADF3	.0043	.0048	.0047	.0054	.0051	.0047	.0047	.0049	.0056	.0055
	μ	Sim	.0089	.0095	.0094	.0102	.0099	.0098	.0099	.0099	.0108	.0102
		CADF1	.0089	.0095	.0094	.0101	.0098	.0094	.0097	.0097	.0105	.0102
		CADF2	.0089	.0096	.0095	.0100	.0097	.0096	.0097	.0098	.0103	.0103
		CADF3	.0090	.0095	.0096	.0100	.0098	.0096	.0096	.0098	.0103	.0103

Another RM-ANOVA was made to compare the SE between data groups after applying CADF for all iterations. Table 6-5 illustrates these results, which indicate that there was no significant difference for any level in most groups of noise. The exceptions were at stages 10% and 20%, which showed significant effects of CADF on SE values. P-values equalled 0.005 and 0.05 for the two noise levels, respectively. The majority of non-significant effects suggest accepting the null hypothesis that no change would occur in population. SD and the μ were reduced with more in SD in all iterations; the reduction percentages in SD were -8%, -13.1%, and -17.1% for CADF 1, 2, and 3, respectively.

Table 6-5. A one-way repeated measured analysis of variance (ANOVA) result for SE values in simulations before and after applying CADF at 1, 2, and 3 iterations.

Test (SE)	Statistics	Noise levels										
		0.05	0.1	0.15	0.2	0.25	0.3	0.35	0.4	0.45	0.5	
RM-ANOVA (n=6)	p-value	.753	.005	.098	.049	.059	.633	.245	.326	.733	.206	
	Wilks' lambda	.705	.021	.154	.096	.109	.606	.294	.361	.687	.260	
	η^2	.295	.979	.846	.904	.891	.394	.706	.639	.313	.740	
	SD	Sim	.0398	.0560	.0490	.0452	.0389	.0658	.0535	.0814	.0737	.0603
		CADF1	.0405	.0539	.0490	.0512	.0371	.0517	.0459	.0644	.0564	.0683
		CADF2	.0403	.0531	.0474	.0504	.0343	.0472	.0450	.0555	.0492	.0676
		CADF3	.0395	.0530	.0465	.0490	.0325	.0424	.0468	.0495	.0418	.0661
	μ	Sim	.3002	.2866	.2939	.2730	.2857	.3108	.2978	.2850	.2802	.2853
		CADF1	.2978	.2794	.2831	.2678	.2786	.3011	.2917	.2853	.2863	.2826
		CADF2	.2954	.2765	.2786	.2680	.2785	.2962	.2863	.2823	.2883	.2770
		CADF3	.2932	.2761	.2759	.2634	.2761	.2935	.2844	.2793	.2885	.2734

Table 6-6 illustrates the comparison SSE result for CADF and p-values in all analyses > 0.05, clearly indicating the non-significant effect of CADF on SSE. Thus, the null hypothesis is accepted; the minimum Wilks' lambda was 0.123, and the SD showed more reduction in data than those in Ki and SE. The percentages of reduction were -9.5%, -14.2%, and -21.4% for CADF 1, 2, and 3, respectively. The averaged μ showed reduction in CADF 1 and 3 only, whereas in CADF 2, there was a small increase in the mean.

Table 6-6. A one-way repeated measured analysis of variance (ANOVA) result for SSE values in simulations before and after applying CADF at 1, 2, and 3 iterations.

Test (SSE)	Statistics	Noise levels										
		0.05	0.1	0.15	0.2	0.25	0.3	0.35	0.4	0.45	0.5	
RM-ANOVA (n=6)	p-value	.070	.109	.170	.072	.287	.172	.076	.133	.754	.225	
	Wilks' Lambda	.123	.166	.227	.125	.330	.229	.129	.190	.705	.277	
	η^2	.877	.834	.773	.875	.670	.771	.871	.810	.295	.723	
	SD	Sim	.0022	.0028	.0025	.0023	.0019	.0039	.0030	.0043	.0035	.0031
		CADF1	.0023	.0027	.0024	.0026	.0019	.0029	.0023	.0033	.0028	.0035
		CADF2	.0024	.0029	.0026	.0028	.0020	.0026	.0023	.0023	.0018	.0036
		CADF3	.0021	.0026	.0022	.0024	.0016	.0022	.0023	.0025	.0021	.0032
	μ	Sim	.0083	.0077	.0080	.0069	.0075	.0091	.0083	.0079	.0076	.0077
		CADF1	.0082	.0073	.0075	.0067	.0072	.0084	.0079	.0077	.0077	.0076
		CADF2	.0084	.0076	.0078	.0074	.0078	.0086	.0077	.0085	.0087	.0077
		CADF3	.0079	.0071	.0071	.0065	.0070	.0080	.0075	.0073	.0077	.0071

6.3.3 DW analysis

In Table 6-7, the result of the RM-ANOVA is summarised and shows no significant in all data analysed with DW. P-values during all noise levels was > 0.05 for Ki values. Wilks' lambda was > 0.440, η^2 was > 0.250 in all stages, and SD showed reduction in all new Ki points after applying the DW technique and μ ; there was also a slight reduction in all levels. The reduction percentage for the averaged Ki was -3.55%, and for SD, it was equal to -6%. In SD, the reduction started from -2% at low noise levels and reached -14% at high levels of noise. Similarly, reduction in the μ started from -1% at 5% noise and reached -7% at 45% and 50% noise points. The technique was applied to the 3D PET images, maintaining the time and the coefficients at 20%.

The coefficients to keep determine the level of smoothing: the lower the % value entered, the smoother the image.

Tables 6-8 and 6-9 illustrate the results of SE and SSE analyses where there was no significant change, at $p\text{-value} > 0.05$ and Wilks' $\lambda > 0.537$ at all noise levels. SD increased in SE and SSE with 6% and 12%, respectively, and μ showed a slight reduction with -1.17% and -1.77%, respectively.

Table 6-7. A one-way repeated measured analysis of variance (ANOVA) result for Ki values in simulations before and after applying DW with 20% coefficients to keep.

Test (Ki)	Statistics	Noise levels										
		0.05	0.1	0.15	0.2	0.25	0.3	0.35	0.4	0.45	0.5	
RM-ANOVA (n=6)	p-value	.193	.203	.053	.110	.177	.253	.120	.148	.099	.088	
	Wilks' lambda	.689	.700	.440	.570	.670	.750	.588	.632	.549	.528	
	η^2	.311	.300	.560	.430	.330	.250	.412	.368	.451	.472	
	SD	Sim	.0046	.0050	.0048	.0058	.0054	.0053	.0055	.0055	.0064	.0056
		DW 20%	.0045	.0047	.0047	.0055	.0053	.0052	.0052	.0052	.0055	.0049
	μ	Sim	.0090	.0094	.0094	.0102	.0099	.0098	.0099	.0099	.0108	.0102
		DW 20%	.0089	.0092	.0092	.0098	.0096	.0096	.0095	.0096	.0100	.0096

Table 6-8. A one-way repeated measured analysis of variance (ANOVA) result for SE values in simulations before and after applying DW with 20% coefficients to keep.

Test (SE)	Statistics	Noise levels										
		0.05	0.1	0.15	0.2	0.25	0.3	0.35	0.4	0.45	0.5	
RM-ANOVA (n=6)	p-value	.408	.092	.117	.699	.961	.445	.285	.519	.325	.694	
	Wilks' lambda	.860	.537	.583	.968	.999	.879	.777	.912	.808	.966	
	η^2	.140	.463	.417	.032	.001	.121	.223	.088	.192	.034	
	SD	Sim	.0398	.0560	.0489	.0452	.0389	.0658	.0535	.0814	.0737	.0603
		DW 20%	.1257	.0567	.0423	.0463	.0320	.0749	.0388	.0779	.0787	.0552
	μ	Sim	.3002	.2866	.2938	.2730	.2857	.3108	.2978	.2850	.2802	.2853
		DW 20%	.2573	.2907	.2990	.2745	.2855	.3056	.2791	.2919	.2937	.2873

Table 6-9. A one-way repeated measured analysis of variance (ANOVA) result for SSE values in simulations before and after applying DW with 20% coefficients to keep.

Test (SSE)	Statistics	Noise levels										
		0.05	0.1	0.15	0.2	0.25	0.3	0.35	0.4	0.45	0.5	
RM-ANOVA (n=6)	p-value	.448	.116	.602	.654	.830	.612	.306	.458	.357	.773	
	Wilks' lambda	.881	.582	.942	.957	.990	.945	.793	.885	.830	.982	
	η^2	.119	.418	.058	.043	.010	.055	.207	.115	.170	.018	
	SD	Sim	.0022	.0028	.0025	.0023	.0019	.0039	.0030	.0043	.0035	.0031
		DW 20%	.0041	.0028	.0023	.0023	.0016	.0045	.0020	.0044	.0044	.0029
	μ	Sim	.0083	.0077	.0080	.0069	.0075	.0091	.0083	.0079	.0076	.0077
		DW 20%	.0072	.0079	.0077	.0070	.0075	.0089	.0072	.0082	.0083	.0077

6.3.4 BLW analysis

In contrast to previous methods, BLW results showed significant differences in all Ki values in RM-ANOVA. The p-value was ≤ 0.05 for all noise levels, Wilks' lambda < 0.450 , and $\eta^2 < 0.673$. SD and μ were reduced, with average percentages of -8% and -6.38%, respectively. This reduction was evident at all 10 stages. Table 6-10 summarises the result of Ki analysis after applying the BLW method. SE and SSE both showed insignificant effects for all analyses and p-values > 0.05 except at noise levels 10% and 45%, where it was < 0.05 . Generally, the majority of results did not significantly change in SE and SSE values. In SE, the SD and μ both increased 9% on average, while in SSE, they grew 22% and 19%, respectively. Tables 6-11 and 6-12 illustrate the summary of the RM-ANOVA and descriptive statistics. The coefficient to keep with BLW methods is 20%, and 3D volume is considered in implementation.

Table 6-10. A one-way repeated measured analysis of variance (ANOVA) result for Ki values in simulations before and after applying BLW with 20% coefficients to keep.

Test (Ki)	Statistics	Noise levels										
		0.05	0.1	0.15	0.2	0.25	0.3	0.35	0.4	0.45	0.5	
RM-ANOVA (n=6)	p-value	.047	.042	.042	.047	.024	.044	.031	.054	.051	.051	
	Wilks' lambda	.422	.405	.405	.420	.327	.411	.362	.444	.432	.435	
	η^2	.578	.595	.595	.580	.673	.589	.638	.556	.568	.565	
	SD	Sim	.0047	.0050	.0048	.0058	.0054	.0053	.0055	.0055	.0064	.0056
		BLW 20%	.0046	.0047	.0046	.0056	.0053	.0049	.0048	.0047	.0053	.0051
	μ	Sim	.0092	.0094	.0094	.0102	.0099	.0098	.0099	.0099	.0108	.0102
		BLW 20%	.0089	.0091	.0090	.0098	.0096	.0091	.0089	.0089	.0096	.0095

Table 6-11. A one-way repeated measured analysis of variance (ANOVA) result for SE values in simulations before and after applying BLW with 20% coefficients to keep.

Test (SE)	Statistics	Noise levels										
		0.05	0.1	0.15	0.2	0.25	0.3	0.35	0.4	0.45	0.5	
RM-ANOVA (n=6)	p-value	.213	.007	.137	.223	.208	.154	.535	.208	.025	.169	
	Wilks' lambda	.711	.203	.614	.721	.705	.639	.919	.705	.331	.659	
	η^2	.289	.797	.386	.279	.295	.361	.081	.295	.669	.341	
	SD	Sim	.0421	.0560	.0489	.0452	.0389	.0658	.0535	.0814	.0737	.0603
		BLW 20%	.0610	.0579	.0508	.0702	.0576	.0597	.0393	.0531	.0690	.0679
	μ	Sim	.2960	.2866	.2938	.2730	.2857	.3108	.2978	.2850	.2802	.2853
		BLW 20%	.3349	.2961	.3244	.3092	.3216	.3529	.3065	.3053	.3118	.2969

Table 6-12. A one-way repeated measured analysis of variance (ANOVA) result for SSE values in simulations before and after applying BLW with 20% coefficients to keep.

Test (SSE)	Statistics	Noise levels										
		0.05	0.1	0.15	0.2	0.25	0.3	0.35	0.4	0.45	0.5	
RM-ANOVA (n=6)	p-value	.280	.014	.135	.248	.225	.166	.650	.239	.034	.159	
	Wilks' lambda	.773	.267	.612	.745	.723	.656	.956	.737	.376	.647	
	η^2	.227	.733	.388	.255	.277	.344	.044	.263	.624	.353	
	SD	Sim	.0022	.0028	.0025	.0023	.0019	.0039	.0030	.0043	.0035	.0031
		BLW 20%	.0039	.0030	.0027	.0042	.0035	.0038	.0022	.0030	.0039	.0035
	μ	Sim	.0083	.0077	.0080	.0069	.0075	.0091	.0083	.0079	.0076	.0077
		BLW 20%	.0105	.0082	.0098	.0091	.0097	.0116	.0087	.0087	.0092	.0084

Table 6-13 summarises the change and reduction in percentage for K_i , SE, and SSE values for all methods used with simulated data before and after denoising processes. The first section represents the mean K_i values; the BLW method has the highest reduction value with -6.38%, and the lowest is from the GADF method at -0.70%. The highest reduction in SE was -3.27%, obtained by CADF (3), and there was an increase of 9.7% in GADF (5). In SSE, the highest reduction was found in CADF (3) with -7.34%, and there was an increase in GADF (5) with 23%.

Table 6-13. A comparison between reductions in Ki, SE, and SSE values for all methods used with simulated data before and after denoising processes.

Mean Ki values ($\times 10^{-2}$)					
Denoising method	Type (iterations, coefficients)	Simulated noisy data	After denoising process	Change	Fold change %
GADF	5	0.8471 \pm 0.4988	0.832 \pm 0.4945	-0.0151	-1.78%
	10		0.8412 \pm 0.5068	-0.0059	-0.70%
CADF	1	0.985 \pm 0.538	0.972 \pm 0.515	-0.013	-1.32%
	2		0.974 \pm 0.507	-0.011	-1.12%
	3		0.975 \pm 0.497	-0.01	-1.02%
DW	20%	0.985 \pm 0.539	0.950 \pm 0.507	-0.035	-3.55%
BLW	20%	0.987 \pm 0.54	0.924 \pm 0.496	-0.063	-6.38%
Mean SE values (%)					
Denoising method	Type (iterations, coefficients)	Simulated noisy data	After denoising process	Change	Fold change
GADF	5	31% \pm 7%	34% \pm 11%	3%	9.7%
	10		31% \pm 7%	0%	0%
CADF	1	28.99% \pm 5.6%	28.54% \pm 5.2%	-0.45%	-1.55%
	2		28.27% \pm 4.9%	-0.71%	-2.46%
	3		28.04% \pm 4.7%	-0.95%	-3.27%
DW	20%	28.98% \pm 5.6%	28.65% \pm 6.3%	-0.338%	-1.17%
BLW	20%	28.94% \pm 5.7%	31.60% \pm 5.9%	2.65%	9.17%
Mean ($\mu \pm$ SD) SSE values ($\times 10^{-2}$)					
Denoising method	Type (iterations, coefficients)	Simulated noisy data	After denoising process	Change	Fold change
GADF	5	0.972 \pm 0.500	1.197 \pm 0.958	0.225	23%
	10		0.932 \pm 0.463	-0.04	-4%
CADF	1	0.790 \pm 0.295	0.762 \pm 0.267	-0.028	-3.54%
	2		0.802 \pm 0.253	0.012	1.52%
	3		0.732 \pm 0.232	-0.058	-7.34%
DW	20%	0.790 \pm 0.295	0.776 \pm 0.313	-0.014	-1.77%
BLW	20%	0.790 \pm 0.295	0.939 \pm 0.337	0.149	19%

6.4 Discussion

6.4.1 GADF analysis

The intention was to define to what extent GADF is capable of removing noise while preserving the tracer quantity in each voxel. Synthetic PET brain images were generated with dPETSTEP with a simulated ^{18}F -FDOPA tracer in a PD patient, and variable noise levels were applied to answer the question. Does GADF have the ability to remove the noise from the simulated dynamic images with no influence on the authentic tracer quantity in voxels?

The non-significant p-value for all comparison results indicates that the difference between the mean of data groups might not be observable and/or significant in the population, which is represented by the sample. As seen in appendix B, Figure B-1, in most simulations, K_i values increased with noise levels, and applying GADF with 10 iterations showed lower K_i values than the others. This could suggest a call for a new study with an increased number of iterations for GADF and a sample size (n) appropriate for verification. For all induced noise levels, the visual appearance after applying GADF was well preserved, and impulse noise in images was mostly removed. Unlike the quantification analysis, GADF is promising regarding visual assessment, qualitatively more than quantitatively. Figure 6-2 shows images before and after applying the filter, and it is clear that the anatomical regions were preserved at the cost of increasing the blur in the images. With low levels of noise (between 5% and 20%), GADF can preserve the sharpness of images and remove noise; high-noise images are clearly very blurry in relation to the amount of noise.

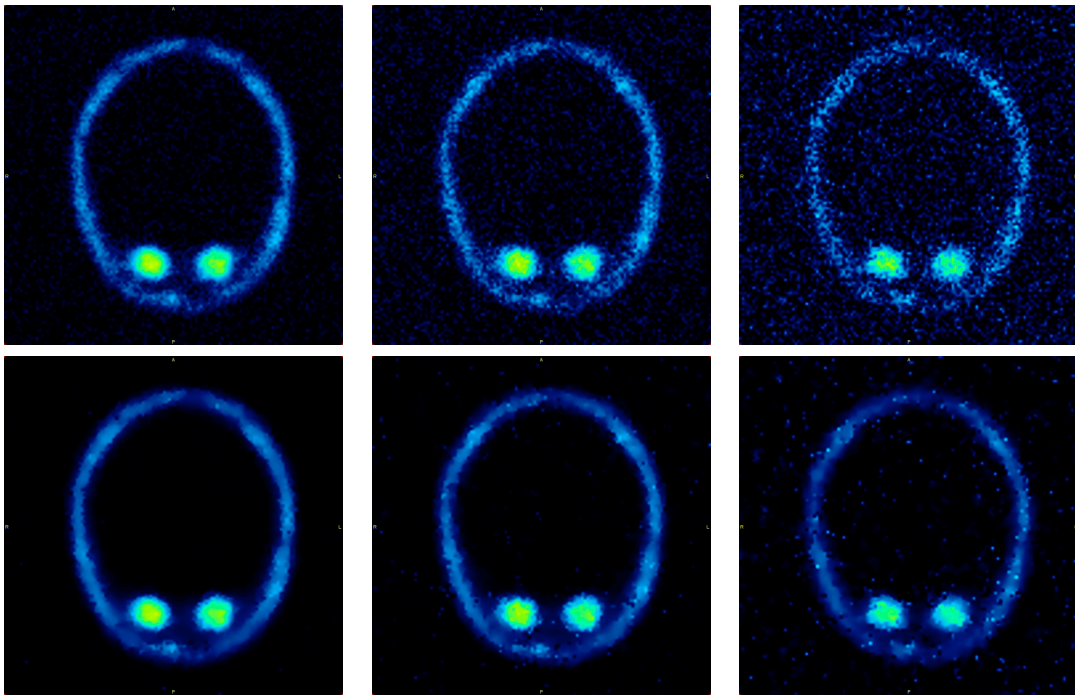


Figure 6-2. The first row shows images with noise levels of 10%, 20%, and 40% Gaussian with mean=0; and the second row shows the same images after applying GADF with 10 iterations.

6.4.2 CADF analysis

This type of filter did not show an obvious noise reduction in noisy PET data. Though four points in Ki values were considered significant effects and mostly found at high level of noise. This could suggest that CADF effectively acts with very noisy images than lower one. The majority of the data group did not show notable levels of affected or removed noise. The small reduction in SD and μ could be used as evidence that this method does not affect the quantitative analysis negatively. Thus, this technique is useful for enhancing the anatomical appearance with no effect on the image's pixel quantity. The p-value and Wilks' lambda levels in Ki analysis suggest accepting the null hypothesis that there would be no change between noisy simulation data groups and CADF 1, 2, and 3 groups. Regarding SE values, in a comparison study of 8 out of 10 noise level data groups, the p-value showed non-significant changes in all CADF iteration stages. Similarly, SSE analysis results showed non-significant changes; both indicate goodness of fit. SD and μ were reduced in proportion to the number of

iterations except for CADF2 where there is a slight increasing in values, this can be an effect of applying low iteration numbers. However, this could be subjective to this study and not objective for the population group. This means that the CADF technique also has no effect on the linear regression calculation in the population parameters. Figure 6-3 illustrates different noisy images before and after applying the CADF technique. A quick look after applying the GADF and CADF methods shows that CADF provided more noise removal with less blurring, suggesting that the curvature has more advantages than gradient anisotropic.

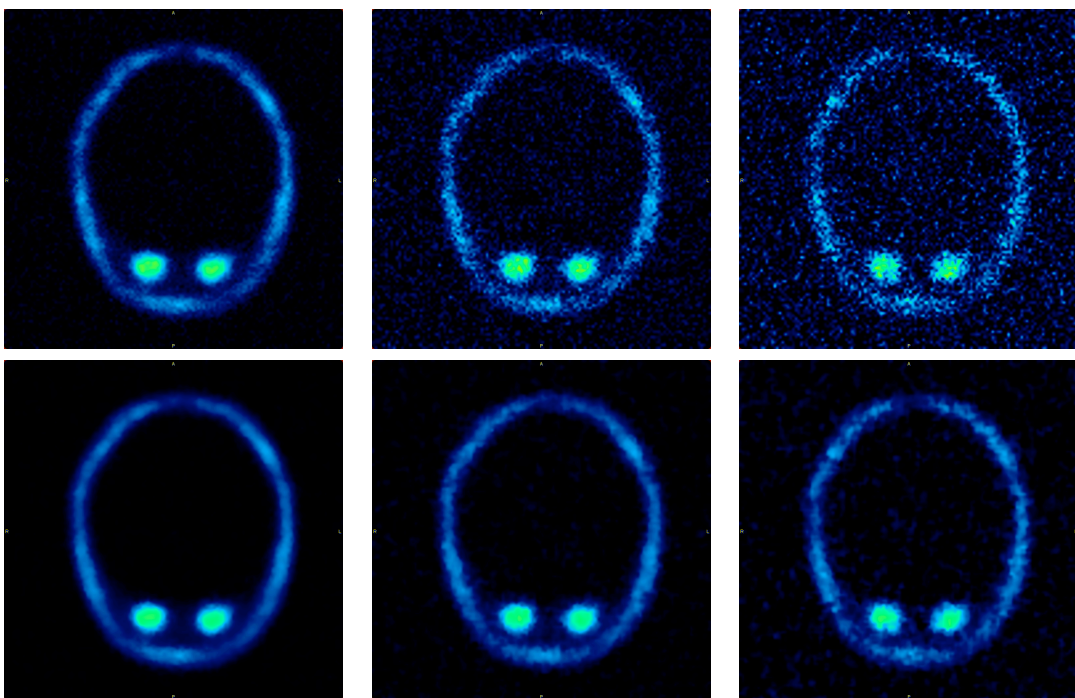


Figure 6-3. The first row shows images with noise levels 10%, 20%, and 40% Gaussian with mean=0; the second row shows the same images after applying CADF with 3 iterations.

6.4.3 DW analysis

The p-value in all results indicated acceptance of the null hypothesis; it cannot be rejected where there is no significant effect or change in Ki levels before and after applying the DW technique. There was no observable trend in p-values at any noise level, and similarity can be found at low and high levels. The reduction in SD and μ in Ki values might suggest that DW analysis tends to reduce the impact of noise as the fold

change is lower after applying DW method. Ki values increased in proportion to the noise, and the DW method's reduction was in proportion to the noise stages. This may indicate the ability of this technique to detect and remove noise. In contrast, SD of SE and SSE analysis shows an increasing percentage, indicating a reduction in the goodness of fit. However, this is still a negligible level and cannot be considered a serious issue, as there is no significant effect in the quantification analysis. Observing the images before and after the technique is applied, there is no obvious noise removal effect. Three images in Figure 6-4 (first row) show noise levels of 10%, 20%, and 40% Gaussian with mean=0 before applying the DW code; the second row shows the same images after applying DW with 20% coefficients. Compared to all previous methods, this technique had the least effect on dynamic images qualitatively and quantitatively.

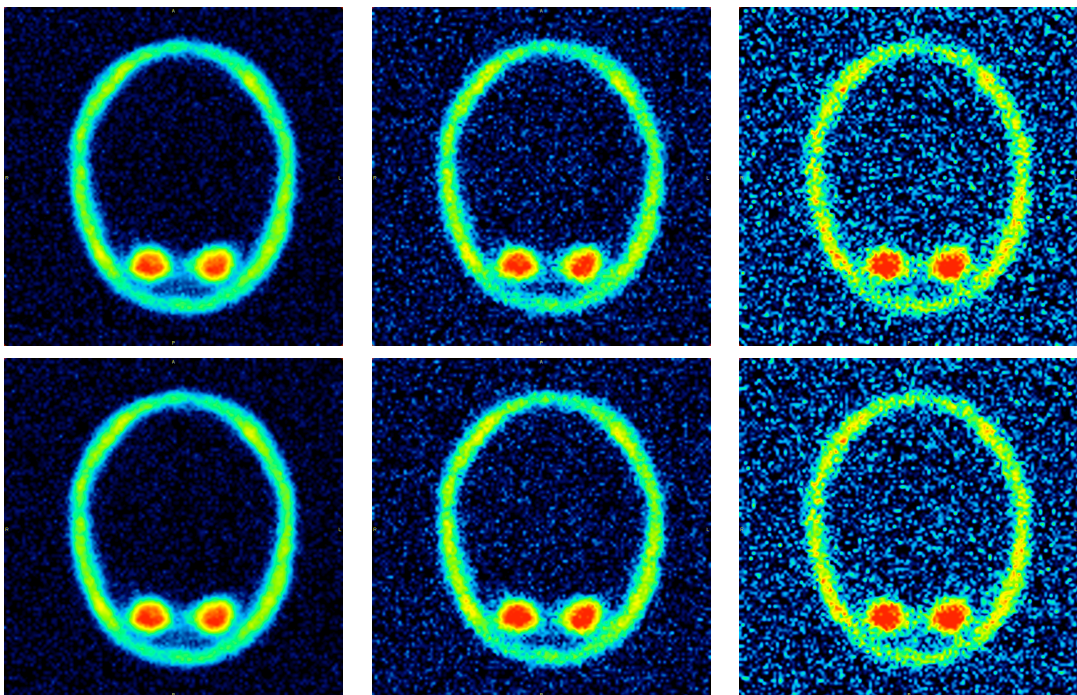


Figure 6-4. The first row shows images with noise levels of 10%, 20%, and 40% Gaussian with mean=0; the second row shows the same images after applying the DW technique.

6.4.4 BLW analysis

The significant change made by the BLW technique is obvious in SD and μ , as all values of Ki were reduced at various percentages. The p-value and Wilks' lambda were

higher in their values at high levels of noise (40% and above), possibly indicating that BLW works better with lower levels of noise. With a reduction between 6% and 8%, BLW could be a promising method to reduce noise in PET data. The increasing SE and SSE values indicate a degrading regression analysis, but this has no significant effect; this issue can be resolved by using another regression model after removing the noise with BLW. In terms of visual appearance, no effects such as blurring or artefact removal were observed as a result of BLW. This suggests that the impact can be seen during quantification analysis only.

6.5 Conclusion

The quantification of PET data allows for the provision of more useful information, but one of the most confounding factors is the noise within the images. Four methods have been applied based on anisotropic diffusion and wavelets to reduce noise and produce better image analysis accuracy. Gradient and curvature anisotropic diffusion as well as DWs showed no significant change in K_i values, although they had obvious impacts on the appearance of images. The percentage reductions in the previous methods for the mean K_i values were 1.5%, 1.13%, and 4%. The BLW method showed a significant change in K_i values with 6-8% reduction and non-significant increases in SE and SSE. The study suggests that the BLW method could potentially reduce noise in PET data, but the regression of the goodness of fit parameters can change negatively. The BLW method shows the most effective results in reducing the impact of noise on simulated data compared to other methods, making it the best option for noisy images.

7 Noise Reduction in Simulated PET Data in Patlak Analysis

7.1 Introduction

In order to generate a Patlak plot, it is necessary to calculate both the x and y terms. Whilst the x term can be accurately calculated with limited noise, the parameters used to calculate the y term are prone to noise. As a result, the Patlak plot is influenced by noise in the y axis. In quantification of peaks, for example, the noise can shift the location of the signal peak, which can cause a systemic overestimation for the signal. Another example is analysis based on differentiation, as the noise is amplified with this type of calculation (van den Bogert 1996). These changes in data amplitude can also significantly affect the calculation of the gradient from the Patlak plot. Reducing noise by using either a smoothing or filtering processes is a useful move to improve the SNR. Smoothing and filtering processes are similar, except that filtering is usually restricted to linear methods. Recent developments in software have enabled the enhancement of signals through the introduction of smoothing algorithms that decrease the noise.

A smoother signal is usually the result of two modifications, with data points affected by noise more than adjacent points subject to reduction. To the contrary, points with lower values than their closest points are increased, which could reduce sensitivity to signal changes. In other words, the high-frequency noise will be cut off and removed from the true data, meaning that the true signal will not be distorted much by the smoothing process. The smoothing operation works as a low-pass filter that allows the low-frequency component and cuts off the high-frequency one. The measurement of the signal and overall noise frequencies allows the smoothing procedure to improve SNR dependent on the frequency distribution of the noise (O'Haver 2016).

Smoothing algorithms usually depend on a technique called *shift and multiply* whereby a group of adjacent points in the original data are multiplied by a set of numbers (coefficients) which determine the smoothing shape. Then, the products are added up and divided by the number of coefficients to create one smoothed point of data. The set of coefficients that define the smoothing shape move down one point in the original data group and repeat the procedure to generate other smoothed points (O'Haver 2016). By applying this sort of function and assuming reasonable smoothing, more information can be extracted from the original data, plus the result of the analysis will be more robust (Simonoff 2012). Other methods for smoothing data are available, including the *Savitzky-Golay*, *Polynomial curve fitting*, and *Median filtering* methods. The selection of smoothing method is usually based on the nature of data and noise present. Data dimensions, type of noise included, and data point size spread on the x-axis play roles in selecting the smoothing technique. Different smoothing techniques offer a trade-off between reducing the noise and keeping the signal free of distortion.

In this chapter, several data-smoothing algorithms and filters are discussed and applied to our simulated PET data set with the aim of removing and/or reducing included noise and consequently improving the accuracy of the final result with lower fitting standard errors. Please be aware this experimental work is different from the curve-fitting concepts performed in Chapter 5, as it can be distinguished that smoothing has little consideration of the close matching of data values, while curve fitting pays more attention to achieving as close a match as possible and controlling the extent of smoothing.

7.2 Theory

7.2.1 Moving average filtering

Moving average filtering (MAF) aims to replace each point in data with the averaged value of the neighbouring points, similar to low-pass filtering. This can be expressed in the following difference equation:

$$(a_0 + a_1x + \dots + a_kx^k) \quad \text{Eq. 7-1}$$

With assuming that $y_s(i)$ is the smoothed value for the i^{th} data point, N is the number of neighbouring data points on either side of $y_s(i)$, and $2N+1$ is the span or filter width. This sort of filtering works by following some rules regarding data, as all data points must be at the centre and thus the end points usually are not smoothed. The noisy data $[y_1, y_2, \dots, y_N]$ is transformed to a new array of smoothed data. Let $y_s(i)$ be the smoothed point, which is the average of an odd number of consecutive $2N+1$ ($n=1, 2, 3, \dots$) points of the raw data $y(i+N) + y(i+N-1) + \dots + y(i-N)$. In other words, the level of smoothing is proportional to the amount of filter width (span). This can be clarified by the example below from (Einicke 2012).

Suppose that the moving averaged filter has a span of 5. Based on Equation 7-1, the four elements of y_s will be the following:

$$\begin{aligned} y_s(1) &= y(1) \\ y_s(2) &= (y(1) + y(2) + y(3)) / 3 \\ y_s(3) &= (y(1) + y(2) + y(3) + y(4) + y(5)) / 5 \\ y_s(4) &= (y(1) + y(2) + y(3) + y(4) + y(5) + y(6)) / 5 \end{aligned}$$

Smoothed points $y_s(1), y_s(2) \dots y_s(\text{end})$ represent the order of the smoothed data, not necessarily the original points. Smoothed values and their spans are illustrated in the plots in Figure 7-1.

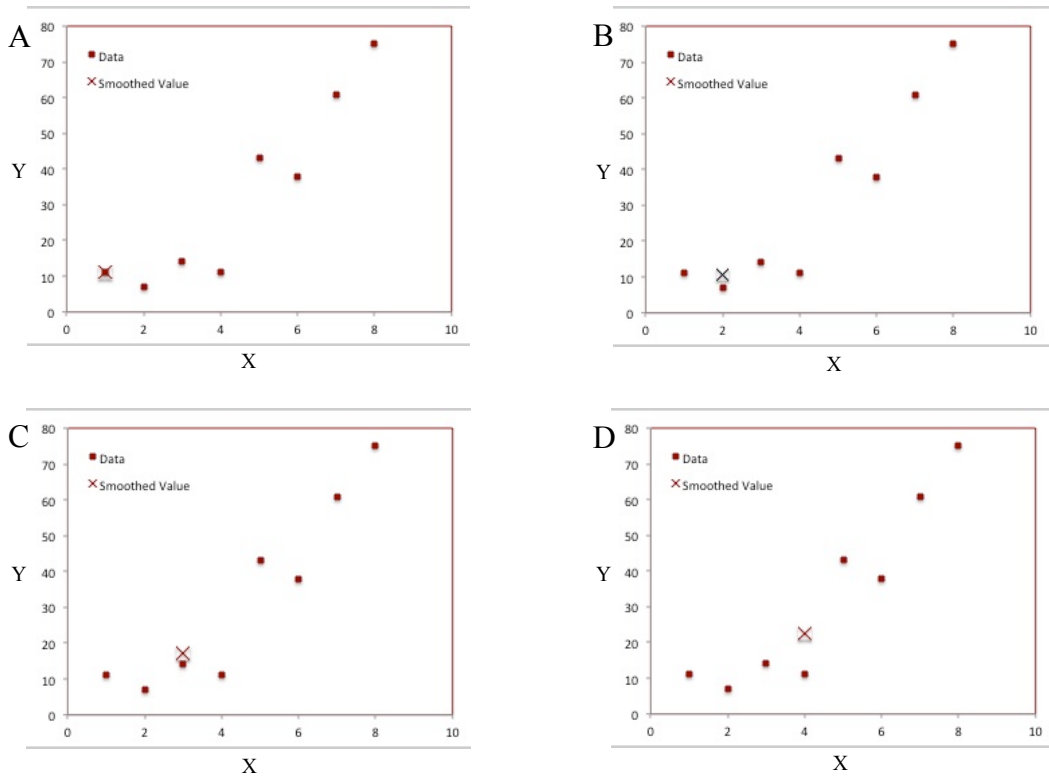


Figure 7-1. In plot (a), the first data point is not smoothed, as a span cannot be constructed. In plot (b), the second data point is smoothed using a span of three. Plots (c) and (d) show that a span of five is used to calculate the smoothed value.

In the previous example, the filter width is 5. The first five raw data points are averaged, and their average value is plotted as a smoothed data point (black cross). Then the process is moved one point to the right, the next five points are averaged, the average is plotted, and so on. This procedure is called 5-point unweight smoothing. Smoothing the data multiple times or increasing the filter width may further enhance the SNR in the data set.

7.2.2 Savitzky-Golay filtering

The Savitzky-Golay filtering (SGF) technique obtains the filtering coefficients with unweighted linear least squares, and a certain degree of polynomial defines the data fitting. A higher-degree polynomial allows a high level of smoothing whilst avoiding data distortion. With a regression around each point, a new smoothed value is generated for each data point. In data that include normally distributed noise, SGF is a good option to reduce the noise and its impact on the final result (O'Haver 2016). Savitzky

and Golay (Savitzky and Golay 1964) showed that the process can be performed by fitting adjacent sub-set data points with low polynomial degrees by linear least squares. A single set of convolution coefficients is generated after spacing the data points equally and is applied to all data sub-sets. Then, estimates are obtained of the smoothed signal (or derivatives) at the central point of each data sub-set. Savitzky and Golay's work has been extended to be applicable to both 2- and 3-dimensional data. Figure 7-2 shows an example of applying SGF to noisy TAC obtained from the dPETSTEP simulation.

Mathematical expressions for SGF are obtained and summarised from (Einicke 2012; Gander and Hrebicek 2011; Simonoff 2012). Let the measured data be denoted by f_i , $i=1, \dots, n$, and the smoothed data by g_i , $i=1, \dots, n$. After fitting the polynomial through the data points, its value at x_i gives the smoothed value g_i . n_L denotes the number of the points to the left of x_i , while n_R refers to the number of points to the right of x_i . $p_i(x_i)$ is the polynomial of degree M that has the least-squares fit through the $n_L + n_R + 1$ points.

$$g_i = p_i(x_i) \quad \text{Eq. 7-2}$$

$p_i(x_i)$ of degree M that fits the data f_i can be expressed as

$$p_i(x) = \sum_{k=0}^M b_k \left(\frac{x - x_i}{\Delta x} \right)^k \quad \text{Eq. 7-3}$$

assuming that x_i abscissas are uniformly spaced with $x_{i+1} - x_i = \Delta x$. Fitting $p_i(x_i)$ in the least squares through the measured data requires determining coefficient b_k by

$$\sum_{j=i-n_L}^{i+n_R} (p_i(x_j) - f_j)^2 = \min. \quad \text{Eq. 7-4}$$

The matrix can be defined as

$$A := \begin{bmatrix} (-n_L)^M & \cdots & -n_L & 1 \\ \vdots & & \vdots & \vdots \\ 0 & \cdots & 0 & 1 \\ \vdots & & \vdots & \vdots \\ n_R^M & \cdots & n_R & 1 \end{bmatrix} \in \mathbf{R}^{(n_L+1) \times (M+1)} \quad \text{Eq. 7-5}$$

Then, the two vectors:

$$\mathbf{b} := \begin{bmatrix} b_M \\ \vdots \\ b_1 \\ b_0 \end{bmatrix} \in \mathbf{R}^{(M+1)} \quad \text{Eq. 7-6}$$

$$\mathbf{f} := \begin{bmatrix} f_i - n_L \\ \vdots \\ f_i \\ \vdots \\ f_i + n_R \end{bmatrix} \in \mathbf{R}^{n_L+n_R+1}$$

By the previous definition, it can restate Equation 7-4 in matrix terms as

$$\|A\mathbf{b} - \mathbf{f}\|_2 = \min \quad \text{Eq. 7-7}$$

One can solve for \mathbf{b} by means of the *QR* decomposition of A . The solution of \mathbf{b} can be expressed as

$$A^T A \mathbf{b} = A^T \mathbf{f} \quad \text{Eq. 7-8}$$

Then

$$\mathbf{g}_i = \mathbf{e}_{M+1}^T (A^T A)^{-1} A^T \mathbf{f} \quad \text{Eq. 7-9}$$

\mathbf{e}_{M+1}^T denotes the $(M+1)$ st unit vector. By defining vector \mathbf{c} , \mathbf{g}_i can be represented as a

linear combination of f_i

$$\mathbf{c} := A(A^T A)^{-1} \mathbf{e}_{M+1} \quad \text{Eq. 7-10}$$

Where \mathbf{c} contains the filter coefficients c_{-n_L}, \dots, c_{n_R} , does not depend on x_i or Δx , and needs to be evaluated once. Finally, g_i smoothed data can be calculated by

$$g_i = \mathbf{c}^T \mathbf{f} = \sum_{j=i-n_L}^{i+n_R} c_{j-i} f_j \quad \text{Eq. 7-11}$$

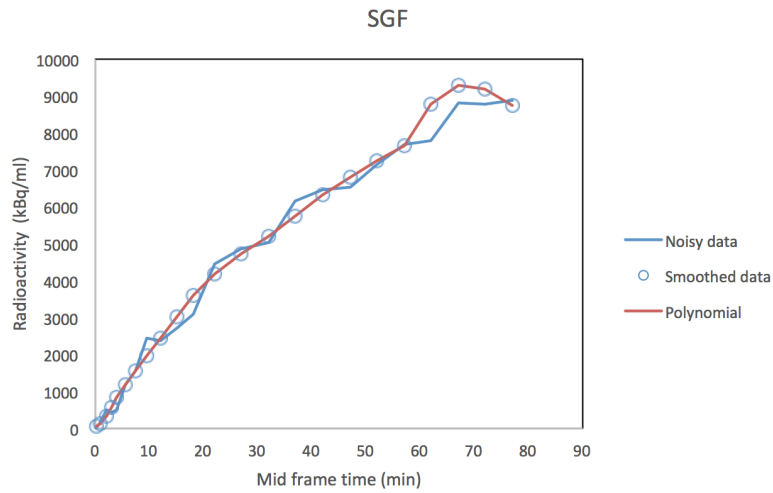


Figure 7-2. SGF smoothing being applied, passing through the data from left to right. The red line represents the local polynomial being used to fit a sub-set of the data. The smoothed values are shown as circles and noisy TAC data is the blue line.

7.2.3 Curve fitting

Curve fitting involves forming a function or a curve that provides the best fit of a data series. It is part of regression analysis and can be used to smooth the data for better plot appearance. Curve fitting can be divided into three main categories: least squares, nonlinear, and smoothing curve fits. In least-squares fitting, the square of the error between original and predicted values is minimised by the equation (Press et al. 2007). Nonlinear curve fitting is based on an iterative algorithm introduced by Levenberg-Marquardt (Gavin 2011; Moré 1978) which starts by estimating unknown parameters and then calculates the sum of the squared error (chi square) between original and fitted data. This procedure is repeated until the best fit is derived. Smoothing curve fits do not generate an equation and are mainly used to enhance the appearance of the curve by smoothing the data.

7.2.3.1 Polynomial curve fitting

Polynomial curve fitting (PCF) works to fit a curve through the data, and its complexity is dependent on the curvature of the data. More complex curvature requires higher polynomial orders (degrees) to be fitted with no data restrictions associated with this method. The equation of the fitted curve can be calculated and displayed once the best fit is determined. The coefficients that best fit the curve to the data are determined by selecting the minimum errors between original observations and the predicted values.

The form of the polynomial starts from a straight line (1st degree) to a k^{th} degree, and can be expressed as (Weisstein 2006):

$$y = a_0 + a_1x + \dots + a_kx^k + \varepsilon \quad \text{Eq. 7-12}$$

The previous equation represents the general polynomial regression model including the coefficients ($a_0 + a_1x + \dots + a_kx^k$) and the error ε . The error value ε indicates that the polynomial provides an estimated value rather than one implicit to the data set. The

number of data points in the curve determines the maximum order of the polynomial used. In a set of N data points, the maximum order of the polynomial is $k=N-1$ (Kreyszig 2010). The residual can be calculated by

$$R^2 = \sum_{i=1}^n [y_i + (a_0 + a_1x + \dots + a_kx^k)]^2 \quad \text{Eq. 7-13}$$

The partial derivatives are

$$\begin{aligned} \frac{\partial(R^2)}{\partial a_0} &= 2 \sum_{i=1}^n [y - (a_0 + a_1x + \dots + a_kx^k)] = 0 \\ \frac{\partial(R^2)}{\partial a_1} &= -2 \sum_{i=1}^n [y - (a_0 + a_1x + \dots + a_kx^k)]x = 0 \\ \frac{\partial(R^2)}{\partial a_k} &= -2 \sum_{i=1}^n [y - (a_0 + a_1x + \dots + a_kx^k)]x^k = 0 \end{aligned} \quad \text{Eq. 7-14}$$

This leads to the following equations

$$\begin{aligned} a_0 n + a_1 \sum_{i=1}^n x_i + \dots + a_k \sum_{i=1}^n x_i^k &= \sum_{i=1}^n y_i \\ a_0 \sum_{i=1}^n x_i + a_1 \sum_{i=1}^n x_i^2 + \dots + a_k \sum_{i=1}^n x_i^{k+1} &= \sum_{i=1}^n x_i y_i \\ a_0 \sum_{i=1}^n x_i^k + a_1 \sum_{i=1}^n x_i^{k+1} + \dots + a_k \sum_{i=1}^n x_i^{2k} &= \sum_{i=1}^n x_i^k y_i \end{aligned} \quad \text{Eq. 7-15}$$

In matrix form, these can be expressed as

$$\begin{bmatrix} n & \sum_{i=1}^n x_i & \cdots & \sum_{i=1}^n x_i^k \\ \sum_{i=1}^n x_i & \sum_{i=1}^n x_i^2 & \cdots & \sum_{i=1}^n x_i^{k+1} \\ \vdots & \vdots & \ddots & \vdots \\ \sum_{i=1}^n x_i^k & \sum_{i=1}^n x_i^{k+1} & \cdots & \sum_{i=1}^n x_i^{2k} \end{bmatrix} \begin{bmatrix} a_0 \\ a_1 \\ \vdots \\ a_k \end{bmatrix} = \begin{bmatrix} \sum_{i=1}^n y_i \\ \sum_{i=1}^n x_i y_i \\ \vdots \\ \sum_{i=1}^n x_i^k y_i \end{bmatrix} a_0, \dots, a_k \quad \text{Eq. 7-16}$$

The least squares can be obtained by

$$\begin{bmatrix} 1 & x_1 & \cdots & x_1^k \\ 1 & x_2 & \cdots & x_2^k \\ \vdots & \vdots & \ddots & \vdots \\ 1 & x_n & \cdots & x_n^k \end{bmatrix} \begin{bmatrix} a_0 \\ a_1 \\ \vdots \\ a_k \end{bmatrix} = \begin{bmatrix} y_1 \\ y_2 \\ \vdots \\ y_n \end{bmatrix} \quad \text{Eq. 7-17}$$

Multiplying both sides by the transpose of the first matrix gives

$$\begin{bmatrix} 1 & 1 & \cdots & 1 \\ x_1 & x_2 & \cdots & x_n \\ \vdots & \vdots & \ddots & \vdots \\ x_1^k & x_2^k & \cdots & x_n^k \end{bmatrix} \begin{bmatrix} 1 & x_1 & \cdots & x_1^k \\ 1 & x_2 & \cdots & x_2^k \\ \vdots & \vdots & \ddots & \vdots \\ 1 & x_n & \cdots & x_n^k \end{bmatrix} \begin{bmatrix} a_0 \\ a_1 \\ \vdots \\ a_k \end{bmatrix} = \begin{bmatrix} 1 & 1 & \cdots & 1 \\ x_1 & x_2 & \cdots & x_n \\ \vdots & \vdots & \ddots & \vdots \\ x_1^k & x_2^k & \cdots & x_n^k \end{bmatrix} \begin{bmatrix} y_1 \\ y_2 \\ \vdots \\ y_n \end{bmatrix}$$

then

$$\begin{bmatrix} n & \sum_{i=1}^n x_i & \cdots & \sum_{i=1}^n x_i^k \\ \sum_{i=1}^n x_i & \sum_{i=1}^n x_i^2 & \cdots & \sum_{i=1}^n x_i^{k+1} \\ \vdots & \vdots & \ddots & \vdots \\ \sum_{i=1}^n x_i^k & \sum_{i=1}^n x_i^{k+1} & \cdots & \sum_{i=1}^n x_i^{2k} \end{bmatrix} \begin{bmatrix} a_0 \\ a_1 \\ \vdots \\ a_k \end{bmatrix} = \begin{bmatrix} \sum_{i=1}^n y_i \\ \sum_{i=1}^n x_i y_i \\ \vdots \\ \sum_{i=1}^n x_i^k y_i \end{bmatrix} \quad \text{Eq. 7-18}$$

For a given n points (x_i, y_i) , the polynomial coefficient a_0, \dots, a_k can be fitted, which gives

$$\begin{bmatrix} y_1 \\ y_2 \\ \vdots \\ y_n \end{bmatrix} = \begin{bmatrix} 1 & x_1 & x_1^2 & \cdots & x_1^k \\ 1 & x_2 & x_2^2 & \cdots & x_2^k \\ \vdots & \vdots & \vdots & \ddots & \vdots \\ 1 & x_n & x_n^2 & \cdots & x_n^k \end{bmatrix} \begin{bmatrix} a_0 \\ a_1 \\ \vdots \\ a_k \end{bmatrix} \quad \text{Eq. 7-19}$$

The equation for a polynomial fit in matrix notation is given as

$$\mathbf{y} = \mathbf{Xa} \quad \text{Eq. 7-20}$$

And the solution can be obtained by multiplying the transpose \mathbf{X}^T

$$\mathbf{X}^T \mathbf{y} = \mathbf{X}^T \mathbf{Xa} \quad \text{Eq. 7-21}$$

The solution vector is then given as

$$\mathbf{a} = (\mathbf{X}^T \mathbf{X})^{-1} \mathbf{X}^T \mathbf{y}$$

Eq. 7-22

A polynomial curve-fitting example to the 3rd degree for a noisy TAC is illustrated in Figure 7-3.

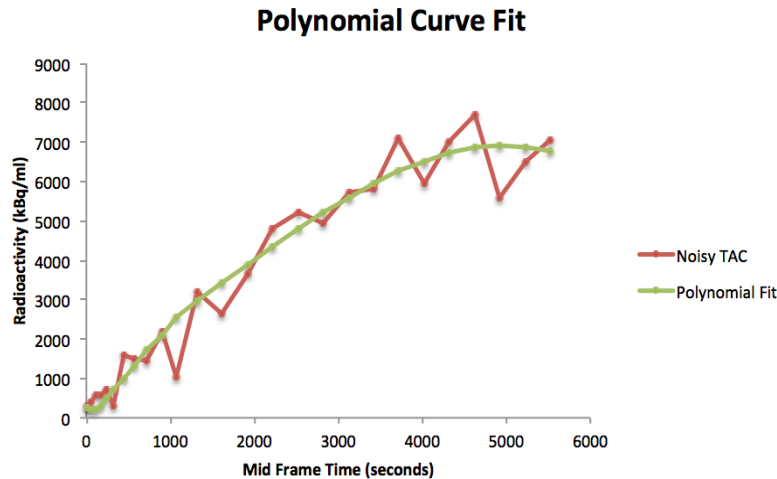


Figure 7-3. PCF applied to noisy TAC as represented by a red line. The green line represents polynomial curve fitting of the 3rd degree.

7.2.4 Median filtering

1-D median filtering (MF) is an effective method that can distinguish out-of-range isolated noise from the signals to some extent by replacing a data point using the median instead of the average. MF is widely used in signal processing for smoothing and suppressing impulse noise and is considered a non-linear filter (Moshnyaga and Hashimoto 2009). The main idea of MF is to run across the signal entry by entry and substitute each entry with the median of near entries. The pattern of neighbours, which is called the window, moves over the entire signal. The window for a 1-D signal is just the few preceding and following entries, whilst in 2-D or higher signals, complex window patterns are generated. The median is simple to define when the window has an odd number of entries, where it is just the middle value after sorting the entries numerically. In an even number of entries, more than one possible median is available (Pitas and Venetsanopoulos 2013).

The median of n observations $x_i, i = 1, \dots, n$ is denoted by $\text{med}(x_i)$ and is given by:

$$\text{med}(x_i) = \begin{cases} x_{(v+1)} & n = 2v + 1 \\ \frac{1}{2}(x_{(v)} + x_{(v+1)}) & n = 2v \end{cases} \quad \text{Eq. 7-23}$$

When x_i denotes the i^{th} order, the previous formula is the main definition when n is odd. A 1-D median filter of size $n = 2v + 1$ is the filter window length and is identified by the expression:

$$y_i = \text{med}(x_{i-v}, \dots, x_i, \dots, x_{i+v}) \quad i \in \mathbf{Z} \quad \text{Eq. 7-24}$$

x_i is the input series from which the points are selected, while y_i is the output and both are $i \in \mathbf{Z}$. Equation 7-23 is called a moving, or running, median. The filter window values are sorted for each input signal data point and the middle value is chosen to replace the original signal value. In cases where impulsive noise is more than $v + 1$, the filter has no effect on the noise, whereas if the noise width is less than $v + 1$, it will be removed completely. The window length controls how the filter affects the signal; the bigger the window length, the smoother the signal will be (Mitra and Kaiser 1993; Moshnyaga and Hashimoto 2009).

7.3 Results

7.3.1 MAF results

Different window sizes (span value) were applied to find the best result of this type of filtering. Window size of 7 points showed the best fitted data and figure 7-4 illustrates the differences in noisy data before and after applying MAF. A one-way repeated measured analysis of variance (ANOVA) was conducted to evaluate the null hypothesis that there is no change in the noisy simulations' Ki, SE or SSE values when calculated with MAF in all simulations ($N = 6$) during the 10 noise levels. The results are summarized in tables 7-1, 7-2 and 7-3. In the Ki values table 7-1, the ANOVA test results indicate that there is no significant effect for MAF filters in noisy data for low levels between 5% and 10% or for high levels between 35% and 50%, $p > 0.05$, averaged Wilks' lambda = 0.569. In the middle noise levels between 15% and 30%, there is a significant change, $p < 0.05$, averaged Wilks' lambda = 0.383. Thus, in a medium level of noise, there is significant evidence to reject the null hypothesis for MAF. The average reductions in standard deviation (SD) and the mean (μ) are 12% and 8% respectively, and averaged partial eta squared (η^2) = 0.506. In SE values table 7-2, the results indicate that there is a significant effect of MAF filtering in curve-fitting parameters for noisy data, $p < 0.05$ in all points, averaged Wilks' lambda = 0.569, and averaged partial $\eta^2 = 0.685$. The average reductions in SD and μ are 2% and 32%, respectively. The results in SSE values table 7-3 indicate as well that there is a significant effect of MAF filtering in curve-fitting parameters, $p < 0.05$, averaged Wilks' lambda = 0.320, and averaged partial $\eta^2 = 0.680$. The average reductions in SD and μ are 35% and 52%, respectively.

Table 7-1. ANOVA results for Ki values in simulations before and after applying MAF.

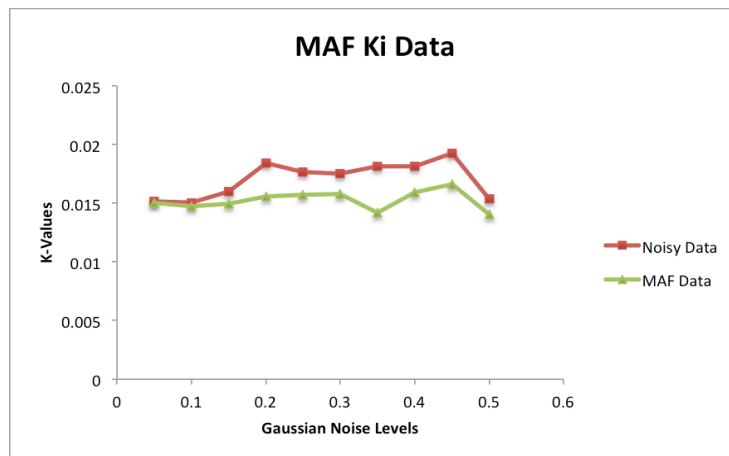
Test	Statistics	Noise levels										
		0.05	0.1	0.15	0.2	0.25	0.3	0.35	0.4	0.45	0.5	
RM-ANOVA (n=6)	p-value	.334	.117	.034	.041	.026	.046	.116	.063	.069	.068	
	Wilks' lambda	.814	.583	.373	.401	.340	.418	.581	.469	.484	.481	
	η^2	.186	.417	.627	.599	.660	.582	.419	.531	.516	.519	
	SD	Sim	.00462	.00495	.00482	.00585	.00540	.00527	.00550	.00550	.00636	.00556
		MAF	.00469	.00464	.00462	.00485	.00489	.00489	.00446	.00492	.00514	.00451
	μ	Sim	.00904	.00945	.00938	.01024	.00988	.00982	.00994	.00994	.01084	.01025
		MAF	.00894	.00893	.00896	.00908	.00909	.00908	.00884	.00917	.00947	.00897

Table 7-2. ANOVA results for SE values in simulations before and after applying MAF.

Test	Statistics	Noise levels										
		0.05	0.1	0.15	0.2	0.25	0.3	0.35	0.4	0.45	0.5	
RM-ANOVA (n=6)	p-value	.004	.038	.019	.022	.018	.027	.042	.023	.010	.035	
	Wilks' lambda	.171	.388	.302	.320	.292	.345	.405	.321	.232	.378	
	η^2	.829	.612	.698	.680	.708	.655	.595	.679	.768	.622	
	SD	Sim	.03969	.05604	.04894	.04522	.03886	.06578	.05353	.08142	.07375	.06027
		MAF	.05393	.05409	.05551	.06096	.05805	.06076	.05457	.06141	.06413	.05141
	μ	Sim	.30082	.28655	.29380	.27297	.28570	.31077	.29777	.28500	.28023	.28527
		MAF	.20017	.20083	.19943	.19828	.19788	.19787	.20058	.19633	.18872	.19938

Table 7-3. ANOVA result for SSE values in simulations before and after applying MAF.

Test	Statistics	Noise levels										
		0.05	0.1	0.15	0.2	0.25	0.3	0.35	0.4	0.45	0.5	
RM-ANOVA (n=6)	p-value	.003	.031	.016	.017	.012	.036	.043	.048	.016	.033	
	Wilks' lambda	.153	.360	.279	.287	.249	.382	.409	.424	.283	.371	
	η^2	.847	.640	.721	.713	.751	.618	.591	.576	.717	.629	
	SD	Sim	.00224	.00280	.00246	.00229	.00191	.00394	.00300	.00427	.00346	.00310
		MAF	.00183	.00187	.00188	.00203	.00194	.00203	.00186	.00199	.00200	.00179
	μ	Sim	.00831	.00770	.00803	.00693	.00753	.00911	.00828	.00789	.00755	.00767
		MAF	.00386	.00389	.00385	.00386	.00382	.00384	.00388	.00379	.00355	.00381



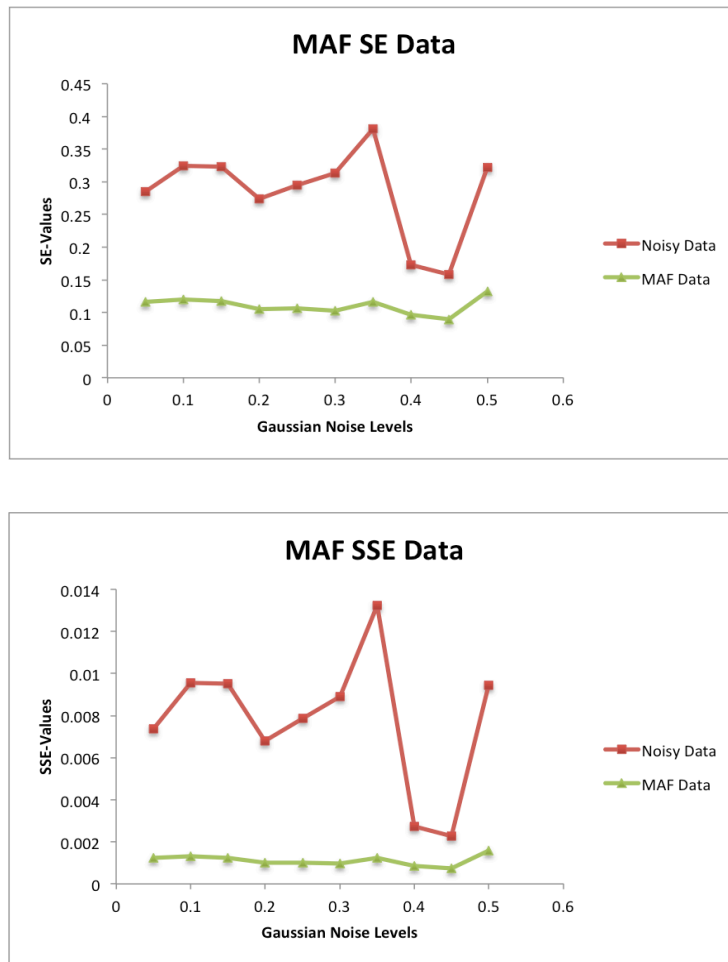


Figure 7-4. In the first plot (left), there is a slight reduction in noise at the beginning and at the end of the noise levels, but significant noise in the intervening levels. The centre plot illustrates the reduction in SE values, and the third plot shows the SSE values. Both have a significant reduction of noisy Ki values after applying MAF.

7.3.2 SGF results

In all simulations ($N = 6$) and for all 10 noise levels, RM-ANOVA was conducted. The results are summarized in tables 7-4, 7-5, and 7-6. In Ki values table 7-4, the test results indicate that there is a significant effect of SGF filtering in most of the noisy data points except for levels 10%, 45%, and 50%, where $p > 0.05$. The averaged p-value for other levels is $= 0.028$, Wilks' lambda $= 0.332$. The average reductions in SD and μ are 10% and 8% respectively, and η^2 in total $= 0.668$. In SE values table 7-5, results indicate that there is a significant effect of SGF filter on curve-fitting parameters for noisy data, $p \leq 0.05$ in all points, averaged $p = 0.0181$, averaged Wilks' lambda $= 0.250$, and $\eta^2 = 0.750$. The average fold change in SD and μ are +21% and -31%, respectively. The

result of SSE values table 7-6 also indicate a significant effect of SGF filter on curve-fitting parameters, $p \leq 0.05$, averaged $p = 0.0175$, averaged Wilks' lambda = 0.244, and $\eta^2 = 0.757$. The average reductions in SD and μ were 15% and 49%, respectively. Figure 7-5 illustrates the differences in noisy data before and after applying the SGF method.

Table 7-4. ANOVA results for Ki values in simulations before and after applying SGF.

Test	Statistics	Noise levels										
		0.05	0.1	0.15	0.2	0.25	0.3	0.35	0.4	0.45	0.5	
RM-ANOVA (n=6)	p-value	.006	.214	.023	.046	.022	.042	.013	.045	.055	.077	
	Wilks' lambda	.187	.712	.323	.419	.315	.405	.259	.414	.447	.503	
	η^2	.813	.288	.677	.581	.685	.595	.741	.586	.553	.497	
	SD	Sim	.00462	.00495	.00482	.00585	.00540	.00527	.00473	.00550	.00636	.00556
		SGF	.00463	.00461	.00464	.00489	.00494	.00498	.00454	.00493	.00516	.00455
	μ	Sim	.00904	.00945	.00938	.01024	.00988	.00982	.00943	.00994	.01084	.01025
SGF		.00890	.00891	.00895	.00910	.00912	.00917	.00886	.00915	.00937	.00897	

Table 7-5. ANOVA results for SE values in simulations before and after applying SGF.

Test	Statistics	Noise levels										
		0.05	0.1	0.15	0.2	0.25	0.3	0.35	0.4	0.45	0.5	
RM-ANOVA (n=6)	p-value	.001	.026	.016	.006	.010	.020	.050	.001	.001	.050	
	Wilks' lambda	.077	.339	.284	.189	.231	.306	.445	.095	.093	.445	
	η^2	.923	.661	.716	.811	.769	.694	.555	.905	.907	.555	
	SD	Sim	.03969	.05604	.04894	.04522	.03886	.06578	.05353	.08142	.07375	.06027
		SGF	.06352	.06190	.06906	.06654	.06580	.06665	.06797	.07337	.08189	.06418
	μ	Sim	.30082	.28655	.29380	.27297	.28570	.31077	.29777	.28500	.28023	.28527
SGF		.19670	.20052	.20878	.18952	.18952	.18917	.20790	.20525	.20755	.20772	

Table 7-6. ANOVA results for SSE values in simulations before and after applying SGF.

Test	Statistics	Noise levels										
		0.05	0.1	0.15	0.2	0.25	0.3	0.35	0.4	0.45	0.5	
RM-ANOVA (n=6)	p-value	.000	.019	.010	.002	.006	.030	.050	.010	.001	.047	
	Wilks' lambda	.030	.298	.235	.127	.190	.355	.454	.235	.090	.421	
	η^2	.970	.702	.765	.873	.810	.645	.546	.765	.910	.579	
	SD	Sim	.00224	.00280	.00246	.00229	.00191	.00394	.00300	.00427	.00346	.00310
		SGF	.00242	.00235	.00258	.00243	.00241	.00242	.00252	.00263	.00299	.00242
	μ	Sim	.00831	.00770	.00803	.00693	.00753	.00911	.00828	.00789	.00755	.00767
SGF		.00382	.00395	.00432	.00360	.00359	.00359	.00428	.00424	.00442	.00423	

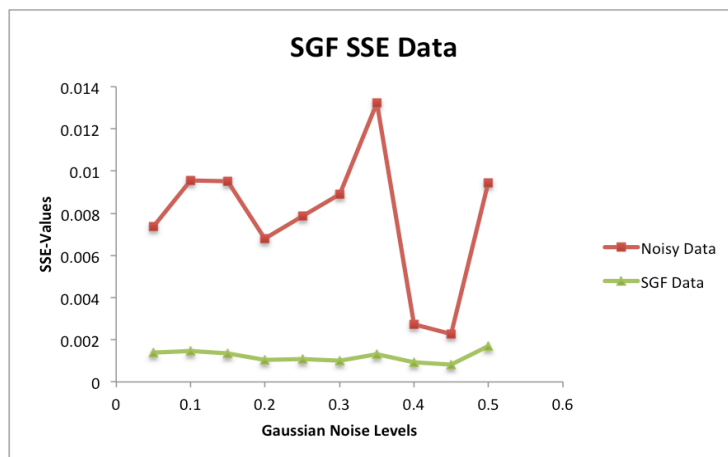
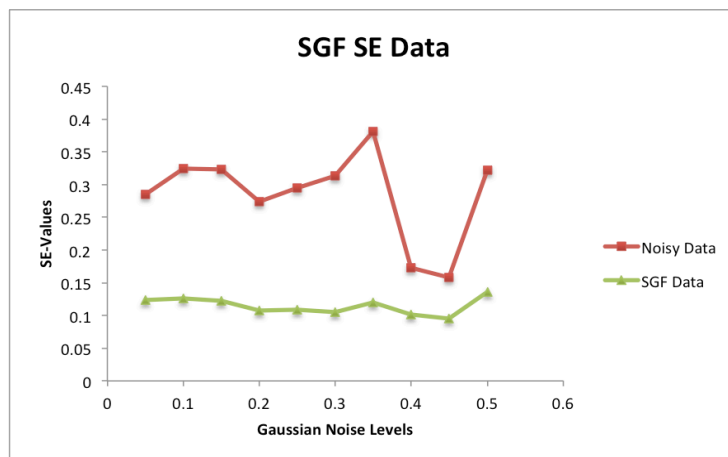
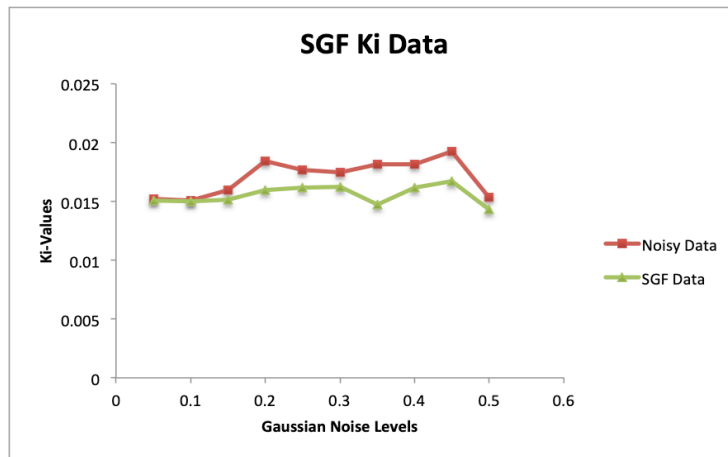


Figure 7-5. In the first plot (left), a slight reduction in Ki value at the beginning is shown, while it is more substantial in the other levels. The second plot in the middle illustrates the reduction in SE values, and the third plot shows the SSE values; both have a significant reduction of noisy Ki values and are more stabilised after applying SGF.

7.3.3 PCF results

Different polynomial degrees from 1st to 9th, have been applied on one simulated data to determine the most effective one to the noise. Table 7-7 shows that the 1st polynomial

order has the greatest difference between these values. Increasing the order of the polynomial reduces that difference; at the 9th degree, it is 11% to the original K_i and 9% lower than noisy data. This suggests to use the 9th PCF degree on all simulated data to reduce the noise effect. Figure 7-6 illustrates the differences in noisy data before and after applying the PCF method. The fold change percentage shows the difference of 0.0140 min^{-1} between the ground truth K_i value without noise and the new value after applying the polynomial. The minus sign means the value is below the original point. RM-ANOVA is conducted for the data before and after applying PCF and results are summarized in tables 7-8, 7-9 and 7-10. In K_i values table 7-8, the test results indicate that there is no significant effect of PCF on most of the noisy data points where $p > 0.05$. Four levels from the simulated data show significant effects where $p < 0.05$. The averaged p -value in general for all levels is $= 0.094$, Wilks' lambda $= 0.465$. The average reduction in SD and μ for both is 6%, and total average partial $\eta^2 = 0.535$. In SE values table 7-9, the results indicate that there is a significant effect of PCF in curve-fitting parameters for noisy data, $p \leq 0.01$ in all points, averaged $p = 0.0003$, averaged Wilks' lambda $= 0.0551$ and average partial $\eta^2 = 0.945$. The average reductions in SD and μ are 28% and 59%, respectively. As shown in SSE values table 7-10, results indicate as well that there is a significant effect of PCF in fitting parameters where $p \leq 0.01$, averaged $p = 0.002$, averaged Wilks' lambda $= 0.108$, and average partial $\eta^2 = 0.8922$. The average reductions in SD and μ are 68% and 82%, respectively.

Table 7-7. Ki value results in simulation 1 before and after applying different degrees of PCF starts from 1st to 9th order.

Poly. Degree	Averaged Ki	Fold Change %	SE%	Poly. Degree	Averaged Ki	Fold Change %	SE%
Noisy Sim 1	0.0168	20%	28%	5	0.0132	-5%	11%
1	0.0027	-81%	5%	6	0.0136	-3%	16%
2	0.0126	-10%	1%	7	0.0135	-4%	16%
3	0.0129	-8%	6%	8	0.0137	-2%	15%
4	0.0125	-11%	15%	9	0.0155	11%	13%

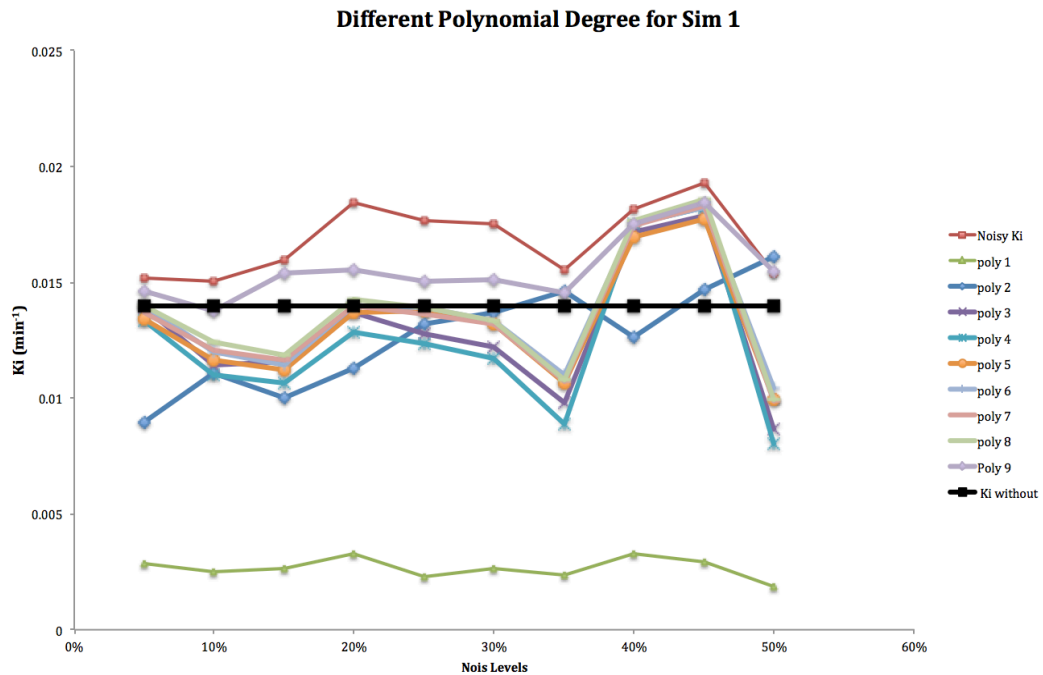


Figure 7-6. Curves for Ki values in simulation 1 before and after applying different degrees of PCF starts from 1st to 9th order. In the middle of the graph, the black line represents the Ki value (0.0140 min⁻¹) without noise for comparison to other curves.

Table 7-8. ANOVA results for Ki values in simulations before and after applying PCF.

Test	Statistics	Noise levels										
		0.05	0.1	0.15	0.2	0.25	0.3	0.35	0.4	0.45	0.5	
RM-ANOVA (n=6)	p-value	.315	.031	.003	.176	.128	.095	.037	.083	.003	.065	
	Wilks' lambda	.800	.360	.145	.668	.600	.542	.386	.518	.153	.474	
	η ²	.200	.640	.855	.332	.400	.458	.614	.482	.847	.526	
	SD	Sim	.00462	.00495	.00482	.00585	.00540	.00527	.00473	.00550	.00636	.00556
		PCF	.00457	.00453	.00472	.00518	.00484	.00448	.00438	.00527	.00609	.00562
	μ	Sim	.00904	.00945	.00938	.01024	.00988	.00982	.00943	.00994	.01084	.01025
PCF		.00882	.00885	.00903	.00954	.00917	.00896	.00900	.00934	.01015	.00978	

Table 7-9. ANOVA results for SE values in simulations before and after applying PCF.

Test	Statistics	Noise levels										
		0.05	0.1	0.15	0.2	0.25	0.3	0.35	0.4	0.45	0.5	
RM-ANOVA (n=6)	p-value	.000	.000	.000	.000	.000	.000	.000	.001	.002	.000	
	Wilks' lambda	.029	.026	.020	.032	.067	.057	.055	.078	.131	.056	
	η^2	.971	.974	.980	.968	.933	.943	.945	.922	.869	.944	
	SD	Sim	.03969	.05604	.04894	.04522	.03886	.06578	.05353	.08142	.07375	.06027
		PCF	.02657	.03278	.03667	.02838	.03753	.04440	.02870	.08116	.04511	.04342
	μ	Sim	.30082	.28655	.29380	.27297	.28570	.31077	.29777	.28500	.28023	.28527
		PCF	.12295	.11330	.11453	.11450	.12050	.10128	.11333	.12275	.12377	.13648

Table 7-10. ANOVA results for SSE values in simulations before and after applying PCF.

Test	Statistics	Noise levels										
		0.05	0.1	0.15	0.2	0.25	0.3	0.35	0.4	0.45	0.5	
RM-ANOVA (n=6)	p-value	.000	.001	.000	.001	.000	.003	.002	.002	.005	.002	
	Wilks' lambda	.067	.090	.064	.083	.072	.153	.118	.131	.182	.118	
	η^2	.933	.910	.936	.917	.928	.847	.882	.869	.818	.882	
	SD	Sim	.00224	.00280	.00246	.00229	.00191	.00394	.00300	.00427	.00346	.00310
		PCF	.00053	.00067	.00075	.00063	.00080	.00076	.00058	.00235	.00122	.00111
	μ	Sim	.00831	.00770	.00803	.00693	.00753	.00911	.00828	.00789	.00755	.00767
		PCF	.00143	.00125	.00129	.00125	.00143	.00108	.00123	.00187	.00155	.00184

7.3.4 MF results

Figure 7-7 illustrates the differences in noisy data within diverse MFs up to the 4th order. The fold change percentage shows the difference between the ground truth K_i value without noise of 0.0140 min^{-1} and the new value after applying the MF. The minus sign means the averaged value is below the original point (0.0140 min^{-1}). Note in table 7-11 that 1st-order MF has the same value as the noisy data, confirming no effect of MF. In the second order, averaged K_i is lower 6% than original point. Increasing the order reduces the effect of noise on data, and at the 4th order, it is 8% closer to the original K_i . Observing the plot in fig 7-7 shows that MF order 4 has four data points lower than the original K_i value compared to MF order 3, which has only one below the original value. This led us to select the 3rd-order MF for use on simulated data due to its stability and robustness in final result analysis, plus a reasonable goodness of fit with SE values.

Table 7-11. Result for Ki values in simulation 1 before and after applying different degrees of MF starts from 1st to 4th order.

MF Degree	Averaged Ki	Fold Change %	SE%
Noisy Sim 1 (before)	0.0168	20%	28%
1	0.0168	20%	28%
2	0.0132	-6%	32%
3	0.0156	12%	21%
4	0.0151	8%	19%

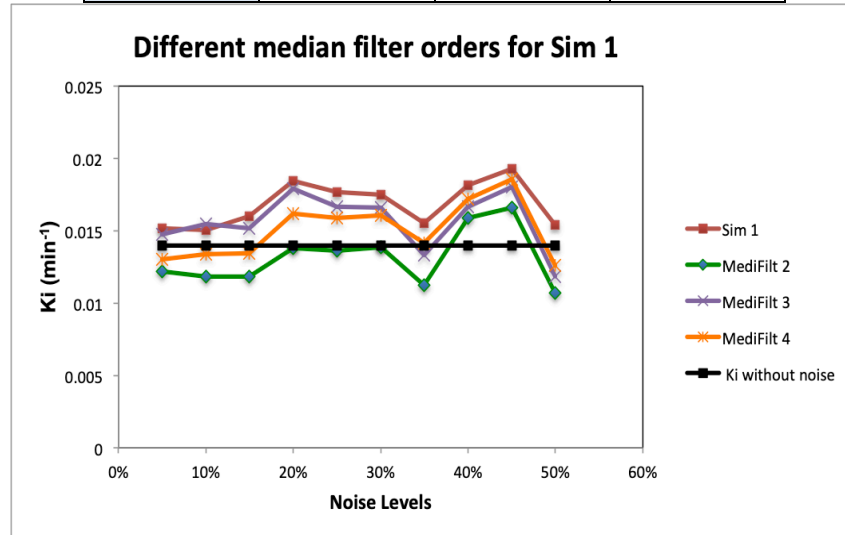


Figure 7-7. Curves for Ki values in simulation 1 before and after applying different orders of MF up to 4th order. In the middle of the graph, the black line represents the original Ki value (0.0140 min⁻¹) without noise for comparison to other curves.

RM-ANOVA was conducted for the data before and after applying MF, and the results are summarized in tables 7-12, 7-13, and 7-14. In Ki values table 7-12, the test results indicate that there is no significant effect of MF in most the noisy data points, $p > 0.05$. The averaged p -value in general for all levels is 0.486, Wilks' lambda = 0.866. The average reductions in SD and μ are 7% and 3%, respectively, total averaged partial $\eta^2 = 0.134$. In SE values table 7-13, the results indicate that there is no significant effect in all points as well of MF in curve fitting parameters, $p > 0.05$, averaged $p = 0.161$, averaged Wilks' lambda = 0.638, and averaged partial $\eta^2 = 0.362$. The average reduction in SD and μ are 13% and 17%, respectively. SSE values in table 7-14 shows as well no significant effect where $p > 0.05$, averaged $p = 0.161$ and averaged Wilks' lambda = 0.637 and averaged partial $\eta^2 = 0.363$. The average reductions in SD and μ are 24% and 30%, respectively.

Table 7-12. ANOVA results for Ki values in simulations before and after applying MF.

Test	Statistics	Noise levels										
		0.05	0.1	0.15	0.2	0.25	0.3	0.35	0.4	0.45	0.5	
RM-ANOVA (n=6)	p-value	.725	.596	.533	.348	.302	.364	.460	.439	.953	.138	
	Wilks' lambda	.973	.940	.918	.823	.790	.834	.887	.876	.999	.617	
	η^2	.027	.060	.082	.177	.210	.166	.113	.124	.001	.383	
	SD	Sim	.00462	.00495	.00482	.00585	.00540	.00527	.00473	.00550	.00636	.00556
		MF	.00449	.00491	.00454	.00567	.00506	.00496	.00430	.00500	.00620	.00437
	μ	Sim	.00904	.00945	.00938	.01024	.00988	.00982	.00943	.00994	.01084	.01025
		MF	.00894	.00928	.00917	.00996	.00954	.00955	.00901	.00966	.01082	.00913

Table 7-13. ANOVA result for SE values in simulations before and after applying MF.

Test	Statistics	Noise levels										
		0.05	0.1	0.15	0.2	0.25	0.3	0.35	0.4	0.45	0.5	
RM-ANOVA (n=6)	p-value	.151	.221	.104	.179	.172	.079	.183	.171	.084	.269	
	Wilks' lambda	.635	.719	.559	.672	.663	.509	.677	.662	.519	.764	
	η^2	.365	.281	.441	.328	.337	.491	.323	.338	.481	.236	
	SD	Sim	.03969	.05604	.04894	.04522	.03886	.06578	.05353	.08142	.07375	.06027
		MF	.04579	.04925	.03370	.04017	.04415	.05781	.04608	.08410	.05485	.03715
	μ	Sim	.30082	.28655	.29380	.27297	.28570	.31077	.29777	.28500	.28023	.28527
		MF	.24758	.24060	.23482	.22713	.23880	.25048	.25467	.24428	.22780	.24533

Table 7-14. ANOVA result for SSE values in simulations before and after applying MF.

Test	Statistics	Noise levels										
		0.05	0.1	0.15	0.2	0.25	0.3	0.35	0.4	0.45	0.5	
RM-ANOVA (n=6)	p-value	.165	.229	.094	.188	.167	.070	.164	.183	.094	.257	
	Wilks' lambda	.654	.727	.540	.683	.657	.487	.653	.677	.540	.753	
	η^2	.346	.273	.460	.317	.343	.513	.347	.323	.460	.247	
	SD	Sim	.00224	.00280	.00246	.00229	.00191	.00394	.00300	.00427	.00346	.00310
		MF	.00204	.00229	.00146	.00176	.00195	.00285	.00212	.00407	.00199	.00173
	μ	Sim	.00831	.00770	.00803	.00693	.00753	.00911	.00828	.00789	.00755	.00767
		MF	.00573	.00545	.00510	.00481	.00533	.00596	.00606	.00596	.00495	.00558

Table 7-15 summarises the changes and reductions in percentage for K_i , SE, and SSE values for all methods used with simulated data before and after the denoising process. The first section represents the mean K_i values, the second illustrates mean SE values, and the third shows the mean SSE values. The MAF method has the greatest reduction value (fold change %) of averaged K_i , with -8.35%, while the MF method has the lowest reduction value, with -3.27%. The greatest reduction in SE was -59.18% obtained by PCF, and the least was -4.87% using MF. In SSE, the greatest reduction of -82% was found in PCF, and the least was -30.47% using the MF method.

Table 7-15. A comparison of reductions in Ki, SE, and SSE values for all methods used with simulated data before and after the denoising process.

Mean Ki values ($\times 10^{-2}$)					
Denoising Method	Type (Iterations, coefficients)	Simulated noisy data	After denoising process	Change	Fold change %
MAF	Double Span	0.9878 \pm 0.5383	0.9053 \pm 0.4761	-0.0825	-8.35%
SGF	-	0.9827 \pm 0.5306	0.905 \pm 0.4787	-0.0777	-7.91%
PCF	9 th Order	0.9827 \pm 0.5306	0.9264 \pm 0.4968	-0.056	-5.73%
MF	3 rd Order	0.9827 \pm 0.5306	0.9506 \pm 0.495	-0.0321	-3.27%
Mean SE values (%)					
Denoising Method	Type (Iterations, coefficients)	Simulated noisy data	After denoising process	Change	Fold change
MAF	Double Span	28.99% \pm 5.64%	19.79% \pm 5.75%	-9.19%	-31.72%
SGF	-	28.99% \pm 5.64%	20.03% \pm 6.81%	-8.96%	-30.92%
PCF	9 th Order	28.99% \pm 5.64%	11.83% \pm 4.05%	-17.15%	-59.18%
MF	3 rd Order	28.99% \pm 5.64%	24.11% \pm 4.93%	-17%	-4.87%
Mean (μ \pm SD) SSE values ($\times 10^{-2}$)					
Denoising Method	Type (Iterations, coefficients)	Simulated noisy data	After denoising process	Change	Fold change
MAF	Double Span	0.79 \pm 0.2947	0.3815 \pm 0.1922	-0.4085	-51.71%
SGF	-	0.79 \pm 0.2947	0.4004 \pm 0.2517	-0.3896	-49.32%
PCF	9 th Order	0.79 \pm 0.2947	0.1422 \pm 0.094	-0.6478	-82%
MF	3 rd Order	0.79 \pm 0.2947	0.5493 \pm 0.2226	-0.2407	-30.47%

7.4 Discussion

7.4.1 MAF analysis

The aim of applying MAF is to remove the noise and its effects on regression fitting parameters. This is already achieved on all Ki values non-significantly in low and high noise and significantly during medium noise levels. SE and SSE values both have significant changes and reduction in their values, indicating better goodness of fit in applied regression analysis. The result shows the suitability of the MAF method to reduce the effect of Gaussian noise by having a probability density function equal to the normal distribution. The filtering width (span) that was given to TACs data are different

due to the variety of the impact of cerebellum activity concentration, which is higher compared to the striatum as can be seen in the Patlak equation. Thus, the span value given to reference tissue TAC was usually double the value of ROI's TAC. Table 7-16 and Figure 7-8 show the results of applying the same and doubled span values on TACs required for Patlak analysis compared to original and noisy data. It can be seen that the huge reduction in Ki values with same-span MAF makes the result much further away from the original value line. In contrast, a double span for reference TAC shows a reduction of noise impact and brings Ki values closer to the non noisy origins. There is an increase in the SD of SE by 21%, and this indicates that the data points are spread out over a wider range of values. This is considered a consequence of preserving the high peaks contained within noisy data.

Table 7-16. Difference in Ki values of the first simulation in noisy, same span value, and double span value for reference tissue TAC.

Ki-values (0.0140)	Noise levels										SE	SSE	change
	0.05	0.1	0.15	0.2	0.25	0.3	0.35	0.4	0.45	0.5			
Noisy Sim1	0.015	0.015	0.016	0.018	0.018	0.018	0.018	0.018	0.019	0.015	0.017	0.017	22%
Same Span value	0.003	0.002	0.002	0.003	0.003	0.003	0.002	0.004	0.005	0.013	0.004	0.004	-71%
Different Span value (double)	0.015	0.015	0.015	0.016	0.016	0.016	0.014	0.016	0.017	0.014	0.015	0.015	9%

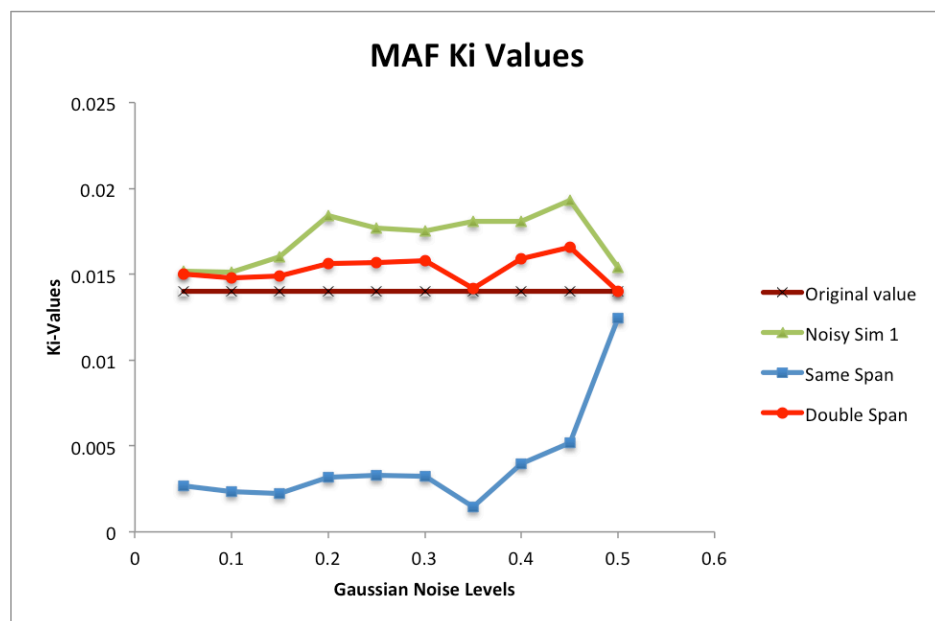


Figure 7-8. Comparison between original Ki values and noisy, same, and double spans. This shows that double-span MAF brings much better results compared to other values.

7.4.2 SGF Analysis

By comparison to MAF, SGF tends to keep the high peaks of the signal, which makes this method less successful in removing the impact of the noise within the data. In contrast, the MAF method filters the high peaks in the signal and removes them. This leads to us avoiding the use of the SGF method with data containing high peaks; however, the method can be used in studying and measuring the impact of Gaussian noise on the data curve by using other functions. Additionally, the SGF method can be used in case retaining the original data is a priority for sensitive quantitative analysis. Visual presentation could help to decide upon a suitable option for smoothing data. In Ki analysis, it can be seen that in most data points (70%), the noise impact is significantly reduced without biasing the original data values. The average fold change from original values after applying noise is 15%, and this is reduced to 6% after applying the SGF method. The average reductions in μ for SE and SSE are 31% and 49%, respectively, indicating an improvement in least squares analysis performed on the Patlak equation and reduction in the SD of error in regression, which in the end provide more robust results in PET analysis. Figure 7-5 shows the data represented by curves after using SGF. More stability is seen with SE and SSE fitting parameters.

7.4.3 PCF analysis

PCF aims to remove the noise impact on TACs by providing the best fit for curves before applying Patlak analysis. The degree used for all data sets is 9, and it is applied on both references and ROI data. This is already achieved on all Ki values non-significantly in most of the data (six levels). Four levels show significant change in Ki values. This suggests more investigation is needed about the polynomial degrees selected. SE and SSE values both show significant changes and reduction, indicating a better fit in Patlak regression analysis. The result shows the suitability of the PCF

method for reducing the effect of Gaussian noise on radioactivity data. With the above reduction achieved, using polynomial fitting will yield more advantages in enhancing the regression analysis for Patlak than improving the final K_i result. Table 7-7 and Figure 7-6 show that a higher polynomial order offers best fit to the curve and more accurate results. A first-degree polynomial generates a result with the greatest difference, which makes this degree the worst option to fit TACs for Patlak analysis.

7.4.4 MF analysis

The effect of MF in removing the noise impact is non-significant on TACs and regression-fitting parameters. This can be noticed from results at all K_i values and noise levels. There are reductions in K_i , SE, and SSE values, however, indicating a slight improvement in removing the noise impact. This also indicates goodness of fit when regression analysis is applied. The result shows the suitability of a 3rd-order MF method to reduce somewhat the effects of Gaussian noise and provide better-fitting parameters. The filtering was applied to data (TACs) for both ROI and reference tissue equally. The TACs were extended by endpoints at the beginning and end, then at the starting point filter window will be complete. The filter window values are sorted, and the middle value is chosen to replace the original signal value. Table 7-11 shows that the window length affects the filter's impact on noisy TACs. The bigger the window length, the smoother the signal will be and vice versa. In smaller window lengths, the filtered signal becomes close to the input noisy curves. MF aims to recover the original signal merged with Gaussian noise, and is particularly good at preserving trends in curves, as can be seen in Figure 7-7. The limited parametric requirement of only the window size makes MF flexible and easy to adapt for a specific signal issue. In addition, the unique structure of this type of filter enables extending and expanding the TAC processing to include threshold decomposition, weighted median filtering, and recursive median filtering.

7.5 Conclusion

PET data in experiments cannot always be presented smoothly, as random changes between points can appear in TACs and significantly affect Patlak analysis. Reducing the noise is a useful move to improve SNR and can be performed by either smoothing or filtering processes. By applying one of these methods, more valuable information can be extracted from the original data and the results of analysis will be more accurate.

The methods applied in this study include moving average filtering (MAF), Savitzky-Golay filtering (SGF), polynomial curve fitting (PCF), and median filtering (MF), with the aim of removing or reducing noise. The methods used show various reductions in noise impact on simulated data and all provided better fit for regression analysis. SGF yielded significant improvements in most data analysis in this study, suggesting that this method was the best option among all methods tested. Using SGF with TACs extracted from ROIs and reference tissues could provide more accurate Patlak analysis. Further analysis of the SGF technique used on clinical PET data obtained from patient images will be performed in the next chapter.

8 Improving the Quantitative ^{18}F -FDOPA Images in Human Dynamic PET Data for Parkinson's Disease Patients

8.1 *Introduction*

Positron emission tomography (PET) scanner are used to help evaluate organ and tissue functions by injecting small amounts of radioactive materials. The computer displays and creates PET images where each measurement is reconstructed as a series of tiny voxels where each voxel intensity represents the uptake of tracer. Most of the modern scanners are now fused with a computed tomography CT or magnetic resonance imaging MRI scanner to correct for attenuation and provide additional anatomical information missing on the PET scan. PET is advantageous for movement disorders as investigational models of Parkinson's disease (PD), Alzheimer's disease, Stroke and Epilepsy. It facilitates the investigation and imaging of brain metabolic activity. By mapping the functional aspects in different regions of brain involved in the above disorders, it is possible to identify and quantify disease in real time. Radiotracers could be used to diagnose, assess prognosis, and assist in therapy development for motor neuron diseases (neurodegenerative disorders) (Lu and Yuan 2015). Potential neural protective agents are under investigation currently in many trials and results from these trials could improve the way of diagnosis process and interventions.

PD is considered as the second most common disorder as a result of neuron degeneration in the mid-brain after Alzheimer's disease (de Lau and Breteler 2006). In Parkinson's disease, 6- ^{18}F Fluoro-L-DOPA (^{18}F -DOPA), where [^{18}F]F₂ is produced from [^{18}O]₂, can be used in studying the dopamine synthesis in the brain based on measuring the physiological processes involved. ^{18}F -DOPA, usually abbreviated to FDOPA, has been used to monitor PD progression by evaluating the striatal uptake in mid brain,

where the fall of the striatal uptake over time indicates the degeneration of dopaminergic neurons. FDOPA PET can also be important for determining the outcomes of treatment of the underlying pathophysiology and to consider whether the therapy has provided a significant effect. FDOPA traps in the synaptic vesicles of neurons and for this reason specific radiolabeling of dopaminergic neurons could be visualized usually between 90- 95 min after injecting the tracer (Lu and Yuan 2015; Vanitha 2011; Whone et al. 2004). Quantitative PET imaging can provide numerical assessment of the physiological, metabolic and functional status in a region of interest (ROI). Fully quantitative approach requires long scan (dynamic images), analysis and input function (blood sample or reference image tissue). This step is the last stage and comes after completion of scanning patient and image processing. Dynamic scans are usually the preferred option for quantitative analysis and high image quality is usually not required. Absolute quantification has the potential to improve diagnostic accuracy in different clinical PET studies (Ohira et al. 2014; Salomaki et al. 2017). It is assumed that physiological processes and molecular interactions are in a constant state (steady state) during the PET measurement (Bentourkia 2011; Carson 2005; Erlandsson 2011). Graphical analysis (GA) is a common method of quantitative PET imaging where the tracer time activity curves (TACs) of ROI and arterial plasma or reference tissue region are combined into one curve that introduces linearity. The data could be plotted in a graph and by applying statistical regression analysis; a regression line (RL) can be fitted within the data points while minimizing errors as much as it can. GA methods are independent of any particular model structure and have been developed for reversibly and irreversibly binding tracers. FDOPA in brain imaging is considered to be an irreversible binding tracer where it trapped within the cell for the duration of the scan. Thus, Patlak graphical plot is the preferred option to quantify dynamic FDOPA images for Parkinson's disease. The slope in the linear phase of the Patlak plot represents the

net uptake rate (K_i) of the tracer or volume of distribution V_t . The Patlak equation principle is based on the existence of at least one irreversible reaction or transport step, where the tracer traps and cannot escape with assuming all the reversible compartments must be in equilibrium with plasma (Logan 2000, 2003; Patlak and Blasberg 1985; Patlak et al. 1983). This chapter includes in details the entire image analysis that is performed to quantify the FDOPA PET dynamic images from the GDNF clinical trial. In addition, other steps have been discussed to improve the sensitivity and accuracy of the image analysis results and provide further techniques, which could enhance the Patlak PET quantification process in general, which is the main aim of this thesis. Equations, models, materials and methods used in the study are all explained and justified in this chapter. First, FDOPA images for PD patients were analysed with the current standard method of quantitative image analysis steps and then the methods identified with the dPETSTEP simulation in order to ascertain if there was a difference in the result produced with each method. Feasible generalised least squares (FGLS), Savitzky-Golay filter (SGF) noise reduction method in 2D, and Battle-Lemarie wavelet (BLW) in 3D data that are discussed earlier in previous chapters are applied to the clinical data obtained from quantifying FDOPA dynamic images.

8.2 Results

Statistical analysis of the data was performed using IBM® SPSS® Statistics, version 23 for the primary stage subjects only. The hypothesis was performed at an alpha level of 0.05 with a 2-sided alternative and no adjustments made for multiplicity. Analysis of covariance (ANCOVA) model was used to determine whether there was a difference in the means of the dependant variable and independent variable categories, which is the treatment group (40 Weeks), while controlling the effects of other continuous variables which are known as covariates and represented by baseline group. ANCOVA model is a

mixed method between ANOVA and regression where the variance in the dependant variable is decomposed into variance explained by the covariates, categorical independent variables and residual variance (Green and Salkind 2016; Kirk 2007).

The mean (\pm SD) of patients' age in the primary stage (35 subjects) is 56.4 ± 7.9 with a mean (\pm SD) of disease duration equal to 10.9 ± 5.3 since the first symptom observed. There is a similarity between treatment groups in terms of baseline PD and all other demographic characteristics, except for gender. According to the study report (Whone et al. 2019), after surgery implementation of the CED system, MRI shows that the CED's catheters were accurately placed. The drug infusion was scheduled into 350 administered sessions and the compliance was high in 347 visits (99.1%). There were a few sessions, that were interrupted or terminated early; 9 (5.4%) of 167 GDNF infusions and 10 (5.6%) of 180 placebo infusions. Early termination due to misalignment of the connector to the skull-mounted port for four infusions in each group was accounted. Other interruptions were reported due to two occluded infusion channels as a result of an automatic safety pump shut down due to transient high catheter pressure with no adverse effect on subjects. Doubling the volume dose for all study infusions for those two subjects solved this issue in line with the study protocol.

8.2.1 Regional and Sub-Regional Outcomes and Analysis

In this study no patient dropped out or was excluded after randomization process. The main outcome assessed was the uptake rate K_i (expressed as 10^{-2} min^{-1}); Table 8-1 illustrates FDOPA mean K_i outcomes for GDNF and placebo groups. In this study striatum has been divided in each subject's image into different 14 parts including: whole striatum left (L) and right (R), caudate head (L and R), caudate body (L and R), putamen (L and R). Then, the putamen was then divided further into three parts; anterior, central and posterior for L and R sides. For placebo group, it was reported that

there was a gradient of neurodegenerative changes (reduction) in 10 of 14 parts of the striatum between baseline and week 40 groups. Four parts show slight increased mean Ki values, which are: right caudate head 0.8% (from 0.908 ± 0.160 to 0.915 ± 0.130), left anterior putamen 1.7% (0.724 ± 0.214 to 0.736 ± 0.157), right central putamen 5.1% (0.432 ± 0.131 to 0.453 ± 0.101) and left posterior putamen 0.7% (0.304 ± 0.113 to 0.307 ± 0.073). The remaining 10 parts show a decrease in Ki mean value and the highest reduction found in right posterior putamen decreased by -6.2% (from 0.321 ± 0.094 to 0.302 ± 0.061) while the lowest change found in left caudate head by -0.2% (from 0.931 ± 0.170 to 0.929 ± 0.144). In placebo-baseline group the highest was found in left caudate head with 0.931 ± 0.170 and the lowest was in left posterior putamen with 0.304 ± 0.113 . For placebo-week40 group, the highest was found in left caudate head with 0.929 ± 0.144 and the lowest was in right posterior putamen with 0.302 ± 0.61 . Figure 8-1, illustrates a comparison between the whole striatum (R and L) in baseline vs. week 40 in placebo group which is very low change.

In GDNF group (Table 8-1 and 8-2), all striatum parts show an increase in mean Ki in week 40 vs. baseline group with 23.4% (average), p -value=0.0002 vs. placebo. An ANCOVA model was applied with the result obtained with the baseline variable as a covariate and treatment group as a fixed factor. The highest change found in the right posterior putamen increased by 50.7% (from 0.367 ± 0.146 to 0.553 ± 0.147 , $p < 0.0001$ vs. placebo) while the lowest change found in the left caudate head by 2.6% (from 0.939 ± 0.229 to 0.9262 ± 0.220 , $p = 0.496$ vs. placebo). The highest mean Ki at baseline was found in the right caudate head with 1.0 ± 0.174 , and the lowest value was found in right posterior putamen with 0.367 ± 0.146 . At week 40 group, the highest was found in right caudate head with mean Ki 1.051 ± 0.215 ($p = 0.143$ vs. placebo) and the lowest was in left posterior putamen with 0.522 ± 0.162 ($p < 0.0001$ vs. placebo). Figure 8-2, illustrates a comparison between the whole striatum (R and L) in baseline vs. week 40

in the GDNF group. It can be seen the different between the two groups, each data point represent a subject (17 patients) and reorganised ascending. Boxes of plot in Figure 8-3 represent GDNF and placebo groups with assign the Ki change as a y-axis shows the differences in mean and outliers.

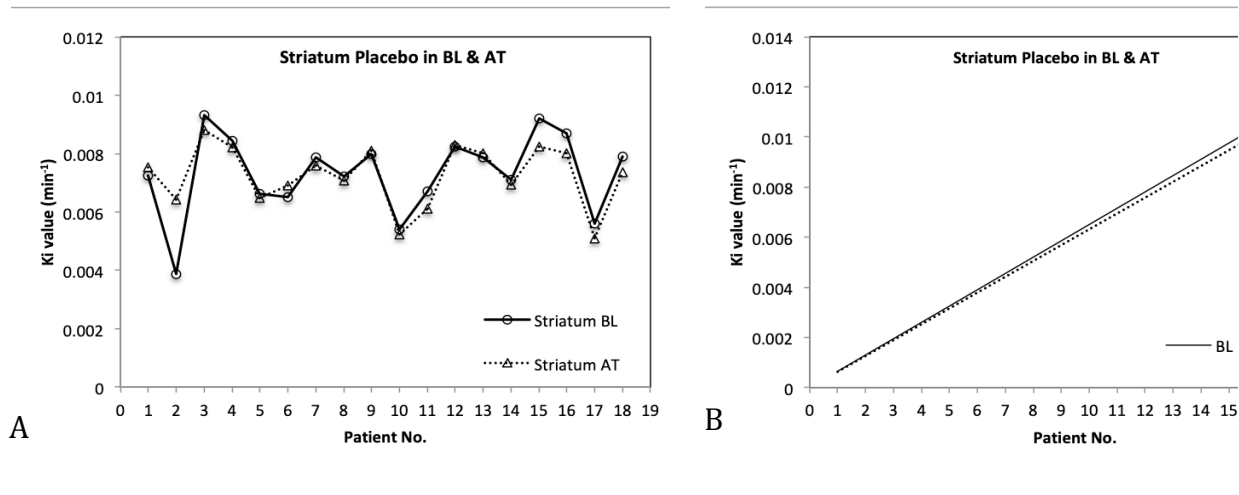


Figure 8-1. Chart (A) shows a comparison between the whole striatum (R and L) in baseline (BL) vs. after treatment placebo group. Chart (B), shows the same group after organise the Ki values ascending and show the trend lines.

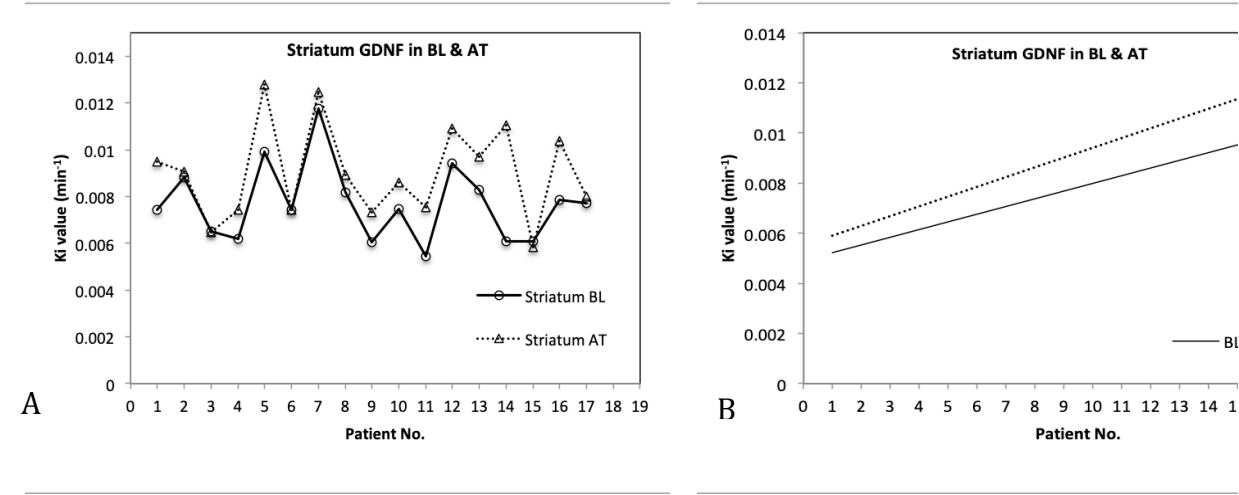


Figure 8-2. Chart (A) shows a comparison between the whole striatum (R and L) in baseline (BL) vs. after treatment GDNF group. Chart (B), shows the same group after showing the trend lines of the Ki values ascending.

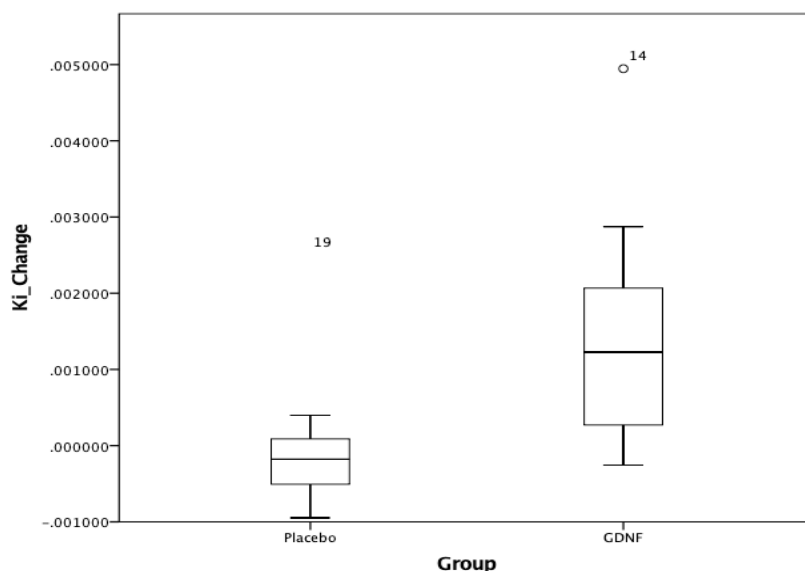


Figure 8-3. Boxes of plot represent GDNF and placebo groups with assign the Ki change as a y-axis shows the diff mean and outliers.

Table 8-1. Mean Ki values \pm SD are obtained from patients' FDOPA images baseline and after treatment (40 weeks) scans of left and right side of brain by Patlak analysis included both GDNF and placebo groups.

FDOPA Uptake Regions		GDNF (N=17)			Placebo (N=18)		
		Baseline (Ki) $\times 10^{-2}$ min $^{-1}$	Week 40 (Ki) $\times 10^{-2}$ min $^{-1}$	Change, (Fold Change%)	Baseline (Ki) $\times 10^{-2}$ min $^{-1}$	Week 40 (Ki) $\times 10^{-2}$ min $^{-1}$	Change, (Fold Change%)
Striatum	Both	0.768 \pm 0.164	0.902 \pm 0.200	0.134 \pm 0.130, (+17.4%)	0.732 \pm 0.139	0.725 \pm 0.106	-0.008 \pm 0.074, (-1.1%)
	L	0.759 \pm 0.176	0.894 \pm 0.210	0.136 \pm 0.127, (+17.9%)	0.749 \pm 0.173	0.745 \pm 0.141	-0.004 \pm 0.072, (-0.5%)
	R	0.778 \pm 0.170	0.910 \pm 0.208	0.132 \pm 0.139, (+17%)	0.715 \pm 0.122	0.704 \pm 0.091	-0.012 \pm 0.085, (-1.7%)
Caudate Head	Both	0.970 \pm 0.182	1.01 \pm 0.206	0.037 \pm 0.152, (+3.8%)	0.920 \pm 0.155	0.922 \pm 0.125	0.003 \pm 0.097, (+0.3%)
	L	0.939 \pm 0.229	0.962 \pm 0.220	0.024 \pm 0.153, (+2.6%)	0.931 \pm 0.170	0.929 \pm 0.144	-0.002 \pm 0.104, (-0.2%)
	R	1.0 \pm 0.174	1.051 \pm 0.215	0.050 \pm 0.170, (+5%)	0.908 \pm 0.160	0.915 \pm 0.130	0.007 \pm 0.113, (+0.8%)
Caudate Body	Both	0.724 \pm 0.204	0.828 \pm 0.212	0.104 \pm 0.174, (+14.4%)	0.753 \pm 0.125	0.734 \pm 0.108	-0.019 \pm 0.115, (-2.5%)
	L	0.690 \pm 0.218	0.779 \pm 0.229	0.088 \pm 0.166, (+12.8%)	0.763 \pm 0.162	0.734 \pm 0.144	-0.028 \pm 0.116, (-3.7%)
	R	0.757 \pm 0.220	0.877 \pm 0.228	0.120 \pm 0.201, (+15.9%)	0.744 \pm 0.119	0.734 \pm 0.114	-0.010 \pm 0.140, (-1.3%)
Putamen	Both	0.614 \pm 0.183	0.817 \pm 0.230	0.203 \pm 0.136, (+33.1%)	0.592 \pm 0.146	0.584 \pm 0.114	-0.008 \pm 0.079, (-1.4%)
	L	0.615 \pm 0.189	0.821 \pm 0.251	0.206 \pm 0.141, (+33.5%)	0.616 \pm 0.193	0.609 \pm 0.150	-0.007 \pm 0.087, (-1.1%)
	R	0.613 \pm 0.199	0.813 \pm 0.231	0.201 \pm 0.157, (+32.8%)	0.568 \pm 0.120	0.559 \pm 0.109	-0.009 \pm 0.093, (-1.6%)
Putamen P1 (Anterior)	Both	0.752 \pm 0.192	0.904 \pm 0.206	0.152 \pm 0.144, (+20.2%)	0.722 \pm 0.165	0.717 \pm 0.127	-0.004 \pm 0.096, (-0.6%)
	L	0.748 \pm 0.240	0.903 \pm 0.244	0.155 \pm 0.156, (+20.7%)	0.724 \pm 0.214	0.736 \pm 0.157	0.012 \pm 0.126, (+1.7%)
	R	0.755 \pm 0.185	0.905 \pm 0.217	0.150 \pm 0.156, (+19.9%)	0.719 \pm 0.138	0.698 \pm 0.142	-0.021 \pm 0.095, (-3%)
Putamen P2 (Central)	Both	0.544 \pm 0.266	0.712 \pm 0.157	0.168 \pm 0.202, (+30.9%)	0.460 \pm 0.123	0.466 \pm 0.100	0.006 \pm 0.097, (+1.3%)
	L	0.527 \pm 0.259	0.704 \pm 0.201	0.178 \pm 0.167, (+33.8%)	0.490 \pm 0.151	0.480 \pm 0.123	-0.010 \pm 0.118, (-2%)
	R	0.561 \pm 0.290	0.719 \pm 0.154	0.158 \pm 0.267, (+28.2%)	0.432 \pm 0.131	0.453 \pm 0.101	0.022 \pm 0.103, (+5.1%)
Putamen P3 (Posterior)	Both	0.373 \pm 0.216	0.538 \pm 0.148	0.164 \pm 0.187, (+44%)	0.313 \pm 0.089	0.304 \pm 0.048	-0.009 \pm 0.078, (-2.9%)
	L	0.379 \pm 0.299	0.522 \pm 0.162	0.143 \pm 0.250, (+37.7%)	0.304 \pm 0.113	0.307 \pm 0.073	0.002 \pm 0.084, (+0.7%)
	R	0.367 \pm 0.146	0.553 \pm 0.147	0.186 \pm 0.150, (+50.7%)	0.321 \pm 0.094	0.302 \pm 0.061	-0.020 \pm 0.104, (-6.2%)

The right side of table 8-2 shows the mean SE% and SSE% as well for the regression analysis of Patlak equation. For SE%, in baseline group, the highest value was found in left posterior putamen with $18.50\% \pm 10.85$ and the lowest was in whole right striatum with $4.303\% \pm 1.593$. In week 40 group, the highest value was found in left posterior putamen as well with $14.10\% \pm 6.117$ and the lowest was in whole left striatum with $4.061\% \pm 1.324$. Table 8-3 shows the result of RM-ANOVA model, where it is applied for SE and SSE means in baseline vs. week 40 group with significant effect change between them, SE p-value < 0.0001 and SSE p-value $= 0.0003$. The average SE in baseline is $9.2\% \pm 4.35$ and in week 40 is $7.21\% \pm 2.85$ for all striatum parts and the total SE for all groups is $8.20\% \pm 3.77$. For SSE, in baseline group, the highest value was found in left posterior putamen with 0.415 ± 0.713 and the lowest was in whole right striatum with 0.019 ± 0.018 . In week 40 group, the highest value was found in left posterior putamen as well with 0.214 ± 0.190 and the lowest was in whole left striatum with 0.017 ± 0.008 . The average SSE in baseline is 0.125 ± 0.118 and in week 40 is 0.062 ± 0.055 for all striatum parts and the total SSE for all is 0.094 ± 0.097 .

Table 8-2. ANCOVA model result , SE and SSE means are obtained from patients' FDOPA images baseline and after treatment scans by Patlak analysis including both GDNF and placebo groups.

FDOPA Uptake Regions		Least squares mean difference vs. placebo (95% CI); p		SE% mean (N=35)		SSE% mean (N=35)	
		LSM vs. placebo	p-value	Baseline %	Week 40 %	Baseline %	Week 40 %
Striatum	Both	-.001 (-.002, -.001)	0.0002	4.528 ±1.630	4.116 ±1.056	0.022 ±0.018	0.017 ±0.008
	L	-.001 (-.002, -.001)	0.0002	4.752 ±2.048	4.061 ±1.324	0.024 ±0.024	0.017 ±0.011
	R	-.002 (-.002, -.001)	0.0003	4.303 ±1.593	4.170 ±1.183	0.019 ±0.018	0.017 ±0.009
Caudate Head	Both	.000 (-.001, .001)	0.246	5.639 ±1.940	5.421 ±1.477	0.034 ±0.028	0.030 ±0.016
	L	.000 (-.001, .001)	0.496	5.926 ±2.482	5.314 ±2.159	0.037 ±0.036	0.030 ±0.026
	R	-.001 (-.002, .000)	0.143	5.352 ±2.034	5.528 ±1.449	0.030 ±0.029	0.030 ±0.014
Caudate Body	Both	-.001 (-.002, .000)	0.0189	7.616 ±2.719	6.795 ±2.211	0.062 ±0.046	0.048 ±0.031
	L	-.001 (-.002, -.00002)	0.0452	7.459 ±2.931	6.872 ±2.686	0.058 ±0.043	0.049 ±0.041
	R	-.001 (-.002, .000)	0.0138	7.774 ±3.478	6.718 ±2.737	0.066 ±0.068	0.048 ±0.038
Putamen	Both	-.002 (-.003, -.001)	<0.0001	7.011 ±3.578	5.623 ±1.523	0.058 ±0.084	0.031 ±0.017
	L	-.002 (-.003, -.001)	<0.0001	7.350 ±4.672	5.669 ±1.972	0.068 ±0.122	0.033 ±0.022
	R	-.002 (-.003, -.001)	<0.0001	6.671 ±2.957	5.577 ±1.442	0.048 ±0.051	0.030 ±0.015
Putamen P1 (Anterior)	Both	-.002 (-.003, -.001)	0.0001	8.992 ±7.142	6.452 ±1.771	0.120 ±0.318	0.042 ±0.023
	L	-.002 (-.003, -.001)	0.0008	9.115 ±7.486	6.610 ±2.256	0.125 ±0.338	0.044 ±0.030
	R	-.002 (-.003, -.001)	0.0001	8.869 ±7.054	6.294 ±2.025	0.115 ±0.299	0.040 ±0.025
Putamen P2 (Central)	Both	-.002 (-.003, -.002)	<0.0001	13.18 ±8.249	9.002 ±2.870	0.237 ±0.397	0.082 ±0.049
	L	-.002 (-.003, -.001)	<0.0001	13.68 ±9.035	8.820 ±3.079	0.242 ±0.390	0.079 ±0.051
	R	-.003 (-.003, -.002)	<0.0001	12.68 ±8.644	9.184 ±3.080	0.212 ±0.452	0.085 ±0.055
Putamen P3 (Posterior)	Both	-.002 (-.003, -.002)	<0.0001	17.41 ±8.598	13.04 ±4.662	0.355 ±0.499	0.182 ±0.138
	L	-.002 (-.003, -.001)	<0.0001	18.50 ±10.85	14.10 ±6.117	0.415 ±0.713	0.214 ±0.190
	R	-.002 (-.003, -.002)	<0.0001	16.33 ±7.686	11.98 ±4.761	0.295 ±0.329	0.151 ±0.130

Table 8-3. RM-ANOVA model is applied for SE and SSE means in baseline vs. week 40 group and presented in the table below with significant change.

Test	Statistics	SE		SSE	
		Baseline	Week 40	Baseline	Week 40
RM-ANOVA (n=35)	p-value	<0.0001		0.0003	
	Wilks' Lambda	0.402		0.519	
	η²	0.598		0.481	
	μ	9.2%	7.21%	0.125	0.062
	SD	±4.35	±2.85	±0.118	±0.055
	μ (Total)	8.20%		0.094	
	SD (Total)	±3.77		±0.097	

8.2.2 Regional and Sub-Regional Analysis with optimised methods

The optimised methods suggested in previous chapters were applied to the FDOPA images with the aim of improving the accuracy of the measurements and removing/reducing noise present in the images. With repeating the same statistical analysis in previous section, Table 8-4 and 8-5 shows result with new methods application. For the placebo group, it can be noticed that there were a gradient of neurodegenerative changes (reduction) in 12 of 14 parts of the striatum between baseline and week 40 groups. Two parts only shows slight increased mean Ki values, which are: left caudate head 0.22% (from 0.926 ± 0.165 to 0.928 ± 0.145) and left anterior putamen 2.4% (0.721 ± 0.215 to 0.738 ± 0.160). The remaining 12 parts show a decrease in Ki mean value and the highest reduction found in right posterior putamen decreased by -6.5% (from 0.323 ± 0.090 to 0.302 ± 0.059) while the lowest change found in right caudate head by -0.1% (from 0.919 ± 0.145 to 0.918 ± 0.130). In placebo-baseline group the highest Ki value was found in left caudate head with 0.926 ± 0.165 and the lowest was in left posterior putamen with 0.312 ± 0.118 . For placebo-week40 group, the highest was found in left caudate head with 0.928 ± 0.145 and the lowest was in right posterior putamen with 0.302 ± 0.59 . Figure 8-4, illustrates a comparison between the whole striatum (R and L) in baseline vs. week 40 in placebo group. In GDNF group (Table 8-4 and 8-5), all striatum parts show an increase in mean Ki in week 40 vs. baseline group with 16.9% (average), $p\text{-value}=0.00014$ vs. placebo. ANCOVA model again was applied with the same settings used before. The highest change found in left posterior putamen increase by 62.7% (from 0.338 ± 0.158 to 0.550 ± 0.163 , $p < 0.0001$ vs. placebo) while the lowest change found in left caudate head by 2.2% (from 0.942 ± 0.232 to 0.964 ± 0.225 , $p=0.557$ vs. placebo). The highest mean Ki at baseline was found in the right caudate head with 1.003 ± 0.176 , and the lowest value was found in left posterior putamen with 0.338 ± 0.158 . At week 40 group, the highest was found in right caudate

head with mean K_i 1.046 ± 0.221 ($p=0.179$ vs. placebo) and the lowest was in left posterior putamen with 0.550 ± 0.163 ($p < 0.0001$ vs. placebo). Figure 8-5, illustrates a comparison between the whole striatum (R and L) in baseline vs. week 40 in GDNF plus the trendlines. Boxes of plot in Figure 8-6 represent GDNF and placebo groups with assign the K_i change as a y-axis.

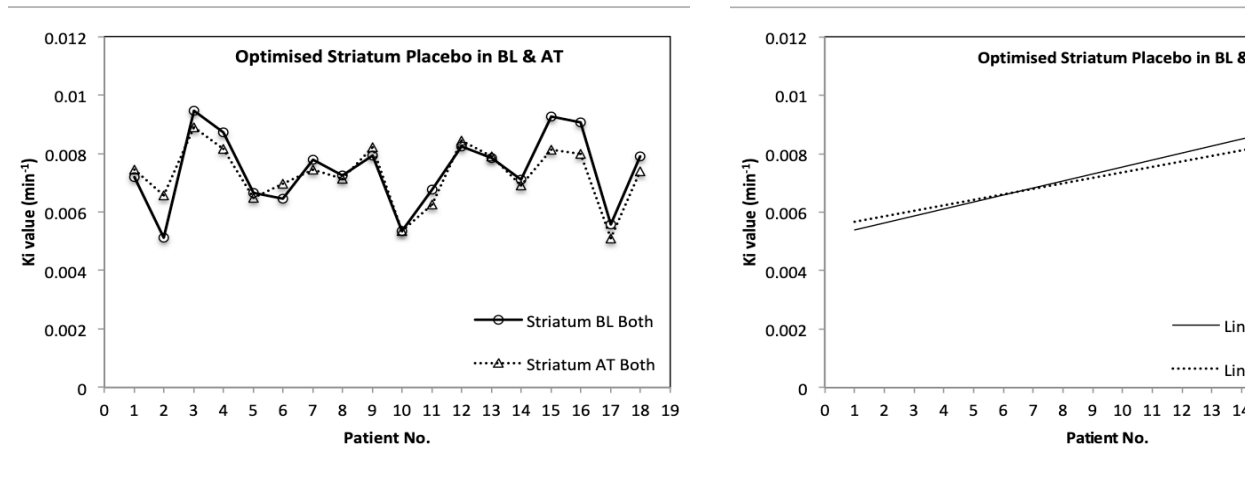


Figure 8-4. Chart 1 (left) shows a comparison between the whole striatum (R and L) in baseline vs. week 40 in placebo applying optimised methods. Chart 2 (right), shows the same group after organising the K_i values ascending and showing

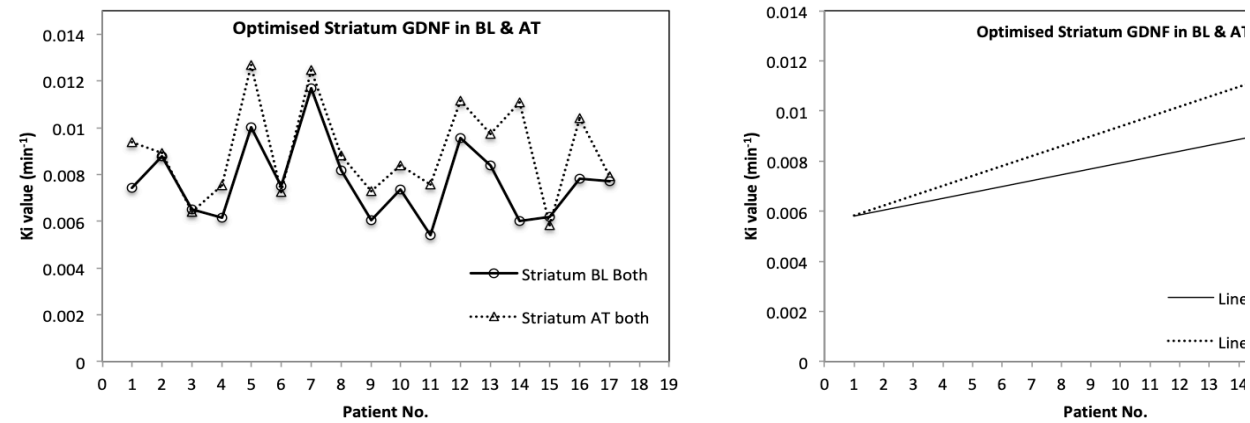


Figure 8-5. Chart 1 (left) shows a comparison between the whole striatum (R and L) in baseline vs. week 40 in GDNF. Chart 2 (right), shows the same group after showing the trend lines of the K_i values ascending.

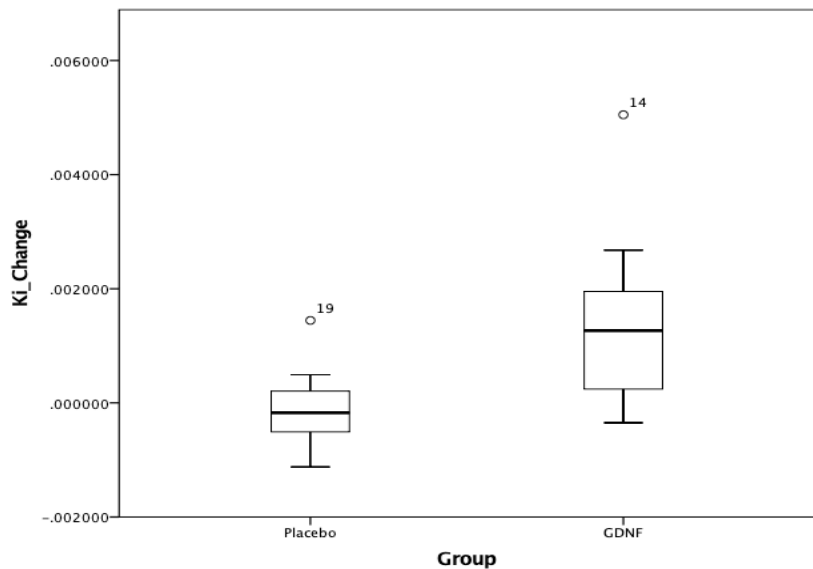


Figure 8-6. Boxes of plot represent GDNF and placebo groups after optimisation with assigning the striatum Ki cha the differences in mean and outliers are shown.

Table 8-5 shows the mean SE% and SSE% and for SE%, in baseline group, the highest value was found in left anterior putamen with $7.61\% \pm 8.91$ and the lowest was in right putamen with $4.51\% \pm 2.76$. In week 40 group, the highest value was found in left anterior putamen as well with $6.52\% \pm 4.01$ and the lowest was in left putamen with $4.15\% \pm 2.06$. Table 8-6 shows the result of RM-ANOVA for SE and SSE means in baseline vs. week 40 group, SE p-value < 0.003 and SSE p-value = 0.001 . The average SE in baseline is $5.7\% \pm 1$ and in week 40 is $4.7\% \pm 1.4$ for all striatum parts and the total SE for all groups is $5.2\% \pm 1.3$. For SSE, in baseline group, the highest value was found in left anterior putamen with 0.0012 ± 0.0046 and the lowest was in whole left striatum with 0.0002 ± 0.0002 . In week 40 group, the highest value was found as well in left anterior putamen with 0.0005 ± 0.0007 and the lowest was in multiple areas with 0.0002 . The average SSE in baseline is 0.0005 ± 0.0003 and in week 40 is 0.0003 ± 0.0009 for all striatum parts and the total SSE for all is 0.0004 ± 0.0002 .

Table 8-4. Mean Ki values \pm SD are obtained, after applying optimised methods suggested, from patients' FDOPA images baseline and after treatment (40 weeks) scans of left and right side of brain by Patlak analysis included both GDNF and placebo groups.

FDOPA Uptake Regions		GDNF (N=17)			Placebo (N=18)		
		Baseline (Ki) $\times 10^{-2}$ min ⁻¹	Week 40 (Ki) $\times 10^{-2}$ min ⁻¹	Change, (Fold Change%)	Baseline (Ki) $\times 10^{-2}$ min ⁻¹	Week 40 (Ki) $\times 10^{-2}$ min ⁻¹	Change, (Fold Change%)
Striatum	Both	0.769 \pm 0.266	0.899 \pm 0.203	0.130 \pm 0.1, (+16.9%)	0.743 \pm 0.130	0.727 \pm 0.103	-0.016 \pm 0.060, (-2.15%)
	L	0.758 \pm 0.180	0.898 \pm 0.214	0.140 \pm 0.140, (+18.5%)	0.758 \pm 0.167	0.749 \pm 0.138	-0.010 \pm 0.071, (-1.3%)
	R	0.780 \pm 0.170	0.900 \pm 0.213	0.120 \pm 0.145, (+15.4%)	0.727 \pm 0.109	0.705 \pm 0.092	-0.022 \pm 0.060, (-3%)
Caudate Head	Both	0.973 \pm 0.185	1.005 \pm 0.211	0.032 \pm 0.152, (+3.3%)	0.923 \pm 0.145	0.923 \pm 0.124	0.000 \pm 0.083, (0%)
	L	0.942 \pm 0.232	0.964 \pm 0.225	0.021 \pm 0.150, (+2.2%)	0.926 \pm 0.165	0.928 \pm 0.145	0.002 \pm 0.101, (+0.22%)
	R	1.003 \pm 0.176	1.046 \pm 0.221	0.043 \pm 0.171, (+4.3%)	0.919 \pm 0.145	0.918 \pm 0.130	-0.001 \pm 0.089, (-0.1%)
Caudate Body	Both	0.722 \pm 0.209	0.826 \pm 0.214	0.104 \pm 0.179, (+14.4%)	0.767 \pm 0.109	0.738 \pm 0.110	-0.029 \pm 0.103, (-3.8%)
	L	0.693 \pm 0.222	0.780 \pm 0.227	0.087 \pm 0.163, (+12.6%)	0.771 \pm 0.159	0.739 \pm 0.143	-0.032 \pm 0.115, (-4.1%)
	R	0.752 \pm 0.224	0.872 \pm 0.236	0.121 \pm 0.217, (+16.1%)	0.763 \pm 0.090	0.737 \pm 0.116	-0.025 \pm 0.118, (-3.3%)
Putamen	Both	0.615 \pm 0.186	0.817 \pm 0.230	0.202 \pm 0.136, (+32.8%)	0.602 \pm 0.134	0.586 \pm 0.115	-0.016 \pm 0.055, (-2.7%)
	L	0.617 \pm 0.197	0.823 \pm 0.251	0.206 \pm 0.136, (+33.4%)	0.625 \pm 0.181	0.612 \pm 0.150	-0.013 \pm 0.070, (-2.1%)
	R	0.613 \pm 0.199	0.812 \pm 0.231	0.198 \pm 0.162, (+32.3%)	0.578 \pm 0.116	0.560 \pm 0.112	-0.018 \pm 0.078, (-3.1%)
Putamen P1 (Anterior)	Both	0.760 \pm 0.201	0.933 \pm 0.229	0.173 \pm 0.152, (+22.8%)	0.720 \pm 0.167	0.717 \pm 0.125	-0.003 \pm 0.101, (-0.4%)
	L	0.750 \pm 0.254	0.930 \pm 0.270	0.180 \pm 0.155, (+24%)	0.721 \pm 0.215	0.738 \pm 0.160	0.018 \pm 0.136, (+2.4%)
	R	0.769 \pm 0.182	0.935 \pm 0.227	0.166 \pm 0.172, (+21.6%)	0.719 \pm 0.138	0.695 \pm 0.149	-0.024 \pm 0.110, (-3.3%)
Putamen P2 (Central)	Both	0.521 \pm 0.190	0.736 \pm 0.165	0.215 \pm 0.146, (+41.3%)	0.474 \pm 0.099	0.460 \pm 0.109	-0.014 \pm 0.053, (-3%)
	L	0.521 \pm 0.238	0.729 \pm 0.214	0.208 \pm 0.151, (+39.9%)	0.493 \pm 0.147	0.485 \pm 0.120	-0.008 \pm 0.111, (-1.6%)
	R	0.520 \pm 0.163	0.743 \pm 0.155	0.223 \pm 0.166, (+42.9%)	0.455 \pm 0.103	0.434 \pm 0.134	-0.021 \pm 0.106, (-4.6%)
Putamen P3 (Posterior)	Both	0.350 \pm 0.135	0.558 \pm 0.143	0.208 \pm 0.126, (+59.4%)	0.318 \pm 0.092	0.305 \pm 0.048	-0.012 \pm 0.081, (-3.8%)
	L	0.338 \pm 0.158	0.550 \pm 0.163	0.212 \pm 0.158, (+62.7%)	0.312 \pm 0.118	0.309 \pm 0.071	-0.004 \pm 0.091, (-1.3%)
	R	0.361 \pm 0.126	0.566 \pm 0.142	0.205 \pm 0.132, (+56.8%)	0.323 \pm 0.090	0.302 \pm 0.059	-0.021 \pm 0.102, (-6.5%)

Table 8-5. ANCOVA model result , SE and SSE means are obtained from patients' FDOPA images baseline and after treatment scans by Patlak analysis including both GDNF and placebo groups.

FDOPA Uptake Regions		Least squares mean difference vs. placebo (95% CI); p		SE% mean (N=35)		SSE% mean (N=35)	
		LSM vs. placebo	p-value	Baseline %	Week 40 %	Baseline %	Week 40 %
Striatum	Both	-.002 (-.002, -.001)	.00014	4.7 ±2.0	2.5 ±0.9	0.0003 ±0.0002	0.0003 ±0.0002
	L	-.001 (-.002, -.001)	.00014	4.8 ±2.0	4.6 ±2.3	0.0002 ±0.0002	0.0002 ±0.0002
	R	-.001 (-.002, -.001)	.00038	4.7 ±2.9	5.2 ±2.5	0.0003 ±0.0003	0.0003 ±0.0003
Caudate Head	Both	.000 (-.001, .000)	.285	5.95 ±1.83	1.77 ±0.62	0.0004 ±0.0003	0.0004 ±0.0003
	L	.000 (-.001, .001)	.557	6.24 ±3.01	5.96 ±2.76	0.0004 ±0.0004	0.0004 ±0.0003
	R	-.001 (-.002, .000)	.179	5.65 ±2.62	6.22 ±3.06	0.0004 ±0.0003	0.0004 ±0.0004
Caudate Body	Both	-.001 (-.002, .000)	.016	6.53 ±3.01	1.52 ±0.60	0.005 ±0.0005	0.0003 ±0.0003
	L	-.001 (-.002, -.00005)	.040	5.69 ±2.84	4.97 ±2.31	0.0004 ±0.0004	0.0003 ±0.0003
	R	-.001 (-.003, .000)	.013	7.37 ±4.63	5.43 ±3.15	0.0007 ±0.0009	0.0004 ±0.0005
Putamen	Both	-.002 (-.003, -.001)	< .0001	4.58 ±2.16	4.26 ±1.59	0.0003 ±0.0003	0.0002 ±0.0002
	L	-.002 (-.003, -.001)	< .0001	4.65 ±2.58	4.15 ±2.06	0.0003 ±0.0003	0.0002 ±0.0002
	R	-.002 (-.003, -.001)	< .0001	4.51 ±2.76	4.37 ±2.21	0.0003 ±0.0003	0.0002 ±0.0002
Putamen P1 (Anterior)	Both	-.002 (-.003, -.001)	< .0001	7.21 ±7.35	6.16 ±2.65	0.0010 ±0.0035	0.0005 ±0.0004
	L	-.002 (-.003, -.001)	.0008	7.61 ±8.91	6.52 ±4.01	0.0012 ±0.0046	0.0005 ±0.0007
	R	-.002 (-.003, -.001)	.0003	6.81 ±6.45	5.81 ±3.29	0.0008 ±0.0024	0.0004 ±0.0005
Putamen P2 (Central)	Both	-.002 (-.003, -.001)	< .0001	5.85 ±5.51	4.92 ±1.86	0.0006 ±0.0019	0.0003 ±0.0002
	L	-.002 (-.003, -.001)	< .0001	6.04 ±6.02	4.94 ±2.14	0.0007 ±0.0022	0.0003 ±0.0002
	R	-.002 (-.003, -.002)	< .0001	5.66 ±5.41	4.89 ±2.37	0.0006 ±0.0016	0.0003 ±0.0003
Putamen P3 (Posterior)	Both	-.002 (-.003, -.002)	< .0001	5.28 ±3.04	4.92 ±2.39	0.0004 ±0.0006	0.0003 ±0.0003
	L	-.002 (-.003, -.002)	< .0001	5.74 ±3.98	5.16 ±3.16	0.0004 ±0.0009	0.0003 ±0.0004
	R	-.002 (-.003, -.002)	< .0001	4.83 ±3.23	4.69 ±2.62	0.0003 ±0.0005	0.0003 ±0.0003

Table 8-6. RM-ANOVA model is applied for SE and SSE means in baseline vs. week 40 group after applying optimised methods for PET data and presented in the table below with no significant change.

Test	Statistics	SE		SSE	
		Baseline	Week 40	Baseline	Week 40
RM-ANOVA (n=35)	p-value	.003		.001	
	Wilks' Lambda	.629		.593	
	η²	.371		.407	
	μ	5.7%	4.7%	0.0005	0.0003
	SD	±1.0%	±1.4%	0.0003	0.0009
	μ (Total)	5.2%		0.0004	
	SD (Total)	±1.3%		±0.0002	

Table 8-7 shows the RM-ANOVA result made to compare between ordinary vs. new optimisation methods, a comparison performed between each group; baseline and week 40 to evaluate the change in SE and SSE. In baseline group, after applying new methods the mean and standard error in SE and SSE are reduced, 38% reduction in SE mean and it is decreased from 9.2% to 5.7%, the SD is less with 77% changing from ±4.35% to ±1.0%, p=.002. In week 40 group, SE is reduced with 35% from 7.2% to 4.7% and SD is reduced as well from ±2.85% to ±1.4%, p=.001. For SSE values, in both baseline and

week 40 the mean and SD are reduced almost 100%, p-value in baseline =.0001 while in week 40 is < .0001.

Table 8-7. RM-ANOVA model is applied for SE and SSE means in baseline vs. week 40 group after applying optimised methods for PET data and presented in the table below with no significant change.

Test	Statistics	SE		SE		SSE		SSE	
		Baseline	Baseline	Week 40	Week 40	Baseline	Baseline	Week 40	Week 40
RM-ANOVA (n=35)	p-value	.002		.001		.0001		< .0001	
	Wilks' Lambda	.604		.562		.461		.432	
	η^2	.396		.438		.539		.568	
	μ	9.2%	5.7%	7.21%	4.7%	0.125	0.0005	0.062	0.0003
	SD	±4.35%	±1.0%	±2.85	±1.4%	±0.118	±0.0003	±0.055	0.0009

8.3 Discussion

GDNF treatment is amongst the most promising therapies in reversing neurodegenerative disease, Allen et al. (2013) demonstrated neuroprotective and neurorestorative potentials in PD of animal models. Another challenge, which is translating the findings into the clinic, is to find a way of delivering the GDNF intraputamenal infusions across the BBB to targeted volumes within brain and possibly over the lifetime of the patients. This challenge has been met in the clinical trial conducted in collaboration with PETIC by (Whone et al. 2019) with the development of CED system used during the study period. The randomised patients are all diagnosed with moderate stage PD, they received 40 weeks of same dose level of GDNF intraputamenal infusions (120 μ g GDNF in 600 μ L aCSF) to each putamen and administered every 4 weeks. Patlak model analysis performed on the PET images revealed a significant increase in 18 F-DOPA uptake in the GDNF group in all striatum parts excluding the caudate head and a non significant result in the placebo group for all parts. A significant increase in putamenal and caudate body FDOPA uptake are shown in the analysis with no or little differences in absolute improvement between the anterior, central and posterior putamen suggests that these ROIs have most treatment benefits with considering that the spatial resolution around 4mm. The low significant

change percentage in caudate body and non-significant change in caudate head clearly shows the effect of the infusion catheter position as non-infused ROI. The increase in Ki rate obtained from ^{18}F -FDOPA PET images could indicate all or one of the following; terminal sprouting, reawakening of hibernating terminals and up-regulation of aromatic amino acid decarboxylase (Moore et al. 2003).

The PET analysis clinical findings are correlated with earlier outcomes found by previous PD GDNF clinical trials conducted by (Grondin et al. 2018; Lang et al. 2006). These two studies lead to apply further clinical test and motor evaluation for the subjects to be able to accept or reject the hypothesis that underlying growth factor. Other factors should be considered in case that this hypothesis is still valid, these include; the effectiveness of GDNF in early stage PD, the GDNF dose sufficiency and the treatment duration. These factors could help to reveal limitations in the present study and should be overcome for next trials design.

In the placebo group, a slight decrease in Ki values has been noticed in 10 of 14 striatum parts and this was expected due to degeneration in neurons. In contrast, unusual a slight increase in the remaining parts of striatum raises a question about the reason for that. There are clinical, physical and technical effects that could cause this during the analysis. Clinical aspects include the trauma assumed to be large with the current CED system used for GDNF infusion as it includes two catheters per putamen (Whone et al. 2019). Another reason that can be considered is the residual effect of symptomatic medication in these regions. Physical factors like the limitation of the spatial resolution of PET scanner could be a reason for inaccurate quantitative analysis. The spatial resolution FWHM of the system used in this trial is between 4-5 mm and this limitation can downgrade measurements in small anatomical parts. Technical reasons are similar to those discussed in details previously in chapter 5, 6 and 7 such as statistical noise caused by outlier data and noise in images voxels. Due to the low increase in Ki

percentages that are noticed within the placebo group, technical reasons are more considerable than others and this is solved partially after applying the three-optimisation methods suggested earlier.

The mean SE and SSE is decreased in week 40 compared to the baseline data and this as a cause of the improved FDOPA signal where Ki rate enhanced as a response to the GDNF treatment. This can be noticed as well after applying optimisation methods on data. A comparison made between old and new methods shows a significant change in SE and SSE values where baseline vs. baseline and Week 40 vs. week 40 is performed. With assuming that the after treatment scans generally has higher signals due to the therapy enhancement of ROIs, the reduction is higher within the two groups of baseline suggesting that optimisation methods works further with low signal to noise ratio data (SNR) rather than higher one in data. The disappearing of increasing Ki in placebo confirms that the reason is more likely to be technical rather than clinical.

The reduction in SE and SSE is a result to apply FGLS model where the PET data with low variance is given more weight than the other parts to generate a more accurate fitted line. The estimator's accuracy in this model can be improved by an iterative process where residuals are used to update the errors covariance estimator, and consequently final estimation is updated (Freedman 2008; Gujarati 2009). In addition, BLW wavelet function used with the analysis were originally designed to produce useful characterisations of images made up of signals. BLW aims to provide details about unknown parts of the signal using several convolutional techniques and then, the original signal is recovered with minimal information loss depending on compression and decompression algorithms (Chui 2016; Graps 1995). The SGF technique used in the analysis targets the PET data before applying the FGLS method where the filtering coefficient is obtained first by using un-weighted linear least squares fitting with a certain degree of polynomial and then, the polynomial degree determines the level of

smoothing whilst keeping minimum attenuation of data structures. SGF in this analysis was applied directly to TACs required for Patlak analysis, which is considered a good option to reduce the TACs noise and has a positive impact on the final Ki result. The result suggests extending SGF to be applied to 3-dimensional PET data. Limitations found in this analysis are that the effect of each method alone was not clear as all techniques were applied at the same time for PET data. Another limitation involves the increasing Ki value found in one ROI in the placebo group, this suggests considering clinical and biological effect again. Further analysis with applying each method separated from others could reveal the real effect of noise reduction plus clarifying the most affected technique. This will lead to probably other opportunity to improve and enhance the Patlak analysis for PD.

8.4 Conclusion

Patlak analysis in ^{18}F -FDOPA PET images were conducted for the first randomised trial in Parkinson's disease employing a CED system to administer a trophic factor to the putamen. This study aims to improve Patlak calculation that used to obtain the net influx rate parameter Ki that is the main outcome in diagnosis and monitoring the PD. PET data are obtained from a clinical trial that was recruiting patients from across the UK and delivering study treatment in PETIC department, University Hospital of Wales. First, ordinary analysis method was used and shows there is an evidence that GDNF can achieve a biological effect across the entire putamen and caudate body. Second, new optimisation methods to improve Patlak analysis were applied and result reveals a significant reduction in SE and SSE and this decrease indicates a drop in noise in images, TACs and statistical data. In addition, ROIs in placebo show increasing Ki values in first analysis with old methods are corrected after using new techniques and reduced to be only on ROI. Future optimisation process will need to address which

method has the most effect on data and then iterative process for this method could provide better accuracy and/or noise reduction. Extra application of these methods on other PET images that require Patlak quantification model could confirm the conclusion made by this study.

9 Conclusion and Future Work

9.1 *Summary and Conclusions*

PET plays a major role in functional brain imaging and mapping of in vivo functions with a purpose of study and evaluation. PET data can be quantified to provide physiological and pathological information, which is valuable for the diagnosis and evaluation of diseases. Quantitative analysis of FDOPA PET images allows the direct measurement of the dopamine system (DA) mechanisms in the living human brain, where the radiotracer crosses the blood-brain barrier and can be metabolized, bound to neuroreceptors, or stored in the vesicles in neurons. The distribution of radiotracer activity in the ROI tissue can be reconstructed as dynamic images and analysed quantitatively to extract physiological parameters. The primary objective of this research project was to optimise the quantitative analysis of the Patlak model used for this purpose. The model is based on linear regression and is usually applied to irreversible tracers such as ^{18}F -FDOPA. For this purpose, firstly the dynamic images were generated from dPETSTEP simulator in order to provide a ground truth which could be used to then assess the accuracy of the methods investigated. The features and settings of the PET scanner, scan protocol, and reconstruction algorithms were all utilised in the simulator to obtain dynamic images. Secondly, successful techniques were validated in sequential clinical ^{18}F -FDOPA images, which were obtained from the PET/CT scanner in PETIC department. The optimization process was applied to images obtained from the GDNF clinical trial in subjects with Parkinson's disease and the input function for the analysis was extracted from the images its self.

Patlak equation with irreversible tracers was used to measure mainly the K_i rate constant, which is used to diagnose and evaluate Parkinson's disease. The first experiment shows that selecting and applying different statistical models for linear

regression can reduce errors and sensitivity to noise. There was a significant difference between the statistical models used, suggesting that using a different linear regression model reveals a different K_i value. Analysing the PET data using different statistical regression approaches could improve the final result and offer more accurate and reproducible diagnosis.

The second experiment dealt with one of the most confounding factors which is the noise existing within the dynamic images. Four different image processing noise reduction methods have been applied to deal with noise in order to improve the accuracy of image analysis. Gradient and curvature anisotropic diffusion in addition to Daubechies' wavelets all show no significant change on K_i values although they have obvious impact on visual appearance of images. The percentage reductions in the previous methods for the mean value in K_i values are 1.5%, 1.13% and 4% respectively. Battle-Lemarie wavelets (BLW) is the only method, that demonstrated a significant change and reduction in noisy K_i data. BLW reduced significantly the impact of noise on data in comparison to other methods used. The only concern with this technique was the goodness of fitting parameters where there was an increase in both SE and SSE values.

The third experiment addressed the problem of noise in TACs data which, significantly affects the Patlak equation result. This step aimed to improve the signal to noise ratio using a smoothing and filtering process. All methods used showed a reduction in noise impact on simulated data and provided better fitting for regression analysis. SGF illustrated a significant change in most data analysis in the third study conducted, using SGF, on TACs extracted from ROIs and reference tissues provided more accurate K_i values for ROIs.

The final technical chapter in this thesis is an application of our suggested techniques on FDOPA clinical images data. ^{18}F -FDOPA PET images were obtained from a clinical

trial involving patients from across the UK scanned in the PETIC department at Cardiff University. First, ordinary analysis method was used, which showed there is evidence that GDNF can achieve biological effect across the entire putamen and caudate body. In second part, the optimisation methods suggested by this thesis were used to improve the results of Patlak analysis. The result revealed a significant reduction in SE and SSE, which suggested a better fitting to PET data due to a drop of noise in the images, TACs and statistical data. In addition, ROIs in placebo, which showed increasing K_i values when using standard analysis were corrected after using new methods and reduced to only one ROI.

9.2 Summary of significant findings

The significant findings of the thesis work can be summarised and broken down as follows:

- The statistical models including OLS, TLS, RFR and FGLS were applied to simulated PET data. The simulated data represented both normal and abnormal K_i values. The minimum averaged SE and SSE plus the highest averaged reduction of noisy K_i values were found with FGLS model with 0.4%, 0.1×10^{-4} and 58.42% respectively.
- Noise was applied to the simulated dynamic images and several noise reduction methods were used including anisotropic diffusion (Gradient and curvature) and wavelets (Daubechies and Battle-Lemarie). BLW showed significant change in all noise levels with averaged reduction -6.38% for the 3D images.
- Simulated noise was added to TACs data extracted from simulated images and smoothing and filtering methods including MAF, SGF, PCF and MF aiming to improve the signal to noise ratio were applied. SGF demonstrated significant change for most of the ten noise levels (7 of 10) with averaged reduction -7.91%

for Ki values, -30.92% and -49.32% in SE and SSE respectively. Other techniques showed high reduction but with no significance for all or most noise levels.

- Ordinary analysis method was used and showed there was evidence that GDNF can achieve a biological effect across the entire putamen and caudate body. Optimisation methods were applied with results revealing significant reduction where in baseline group, the mean and standard deviation of SE were both reduced, -38% decline in the mean from 9.2% to 5.7%, the SD less with -77% changing from $\pm 4.35\%$ to $\pm 1.0\%$, $p=.002$. In week 40 group, SE is reduced with -35% from 7.2% to 4.7% and SD is reduced as well from $\pm 2.85\%$ to $\pm 1.4\%$, $p=.001$. For SSE values, in both baseline and week 40 the mean and SD are reduced almost 100%, p-value in baseline =.0001 while in week 40 is $< .0001$.

9.3 *Future Work and directions*

Further validation on clinical data is required to evaluate the methodology and analyse the impact on PET data. Repeating the methods separately, applying the RM-ANOVA test will reveal which technique has the most significant effect.

Extended work for the optimising methodology discussed in the thesis through other clinical PET data set is necessary for a full validation. Other tracers can be used for further validation that are based quantitatively on Patlak equation such as ^{18}F -FDG (Fluoro-deoxy-glucose) which is the analog of glucose or ^{18}F -FTHA (fluoro-thia-heptadecanoic), the analog of fatty acids, when they trapped metabolically in the ROI. Improvements in the quantitative accuracy for brain data has been described imaging and this optimising methodology could be extended with other organ images if the tracer used shows irreversibility. Applying and extending the methodology contained in

this thesis with other reconstruction algorithms such as filtered back projection (FBP) could reveal more information.

The implementation of methods is relies on regional and sub-regional volumes, for each ROI the average TAC is calculated of each voxel in the drawn contour. Extending these methods to parametric mapping analysis in neuroimaging would be beneficial as each pixel value (Pixel-wise analysis) is involved in Patlak analysis and reducing the noise exist will be more challenging. This could be performed initially by using dPETSTEP simulator to generate parametric images and simulate the FDOPA tracer features with different reconstruction algorithms. At the initial stage, few number of frames will be suitable as the pixel amount for each slice will be huge, lower frames can be helpful to handle the data in analysis. Normal and abnormal Ki mapping template could be advantageous in pixel-wise analysis as descriptive statistics will be more important than other fitting parameters.

Sensitivity to data outliers and non-linear data relationship have disadvantages in PET quantitative analysis. Machine learning and or deep learning can optimise linear regression analysis that is the basis of Patlak equation. Designing and coding a tool to work as a library contains many blocks already optimised for better linear regression prediction after training a model to provide regression coefficients. The iteration of methods used in this thesis can be a part of the training process that allow for better understanding of noise, errors and other fitting parameters. Including weighting data analysis in this model could reveal more advantageous information regarding data classification.

Appendices

Appendix A

Table A-1. OLS regression method used for kinetic Patlak analysis on all simulation data and Ki values illustrated within 10 noise levels.

OLS	30	without	0.05	0.1	0.15	0.2	0.25	0.3	0.35	0.4	0.45	0.50	μ
SIM 1 (Ki)	0.0122	0.0124	0.0122	0.0090	0.0130	0.0127	0.0140	0.0126	0.0139	0.0131	0.0119	0.0124	
SE	0.0597	0.1253	0.1252	0.1525	0.1301	0.0888	0.0830	0.1007	0.1119	0.1344	0.1554	0.1151	
SSE	0.0003	0.0014	0.0014	0.0021	0.0015	0.0007	0.0006	0.0009	0.0011	0.0016	0.0022	0.0012	
SIM 2 (Ki)	0.0123	0.0133	0.0166	0.0167	0.0208	0.0210	0.0212	0.0255	0.0267	0.0247	0.0254	0.0204	
SE	0.0608	0.1844	0.1678	0.1534	0.1056	0.1828	0.1703	0.1401	0.1397	0.1447	0.1384	0.1443	
SSE	0.0003	0.0030	0.0025	0.0021	0.0010	0.0030	0.0026	0.0017	0.0017	0.0019	0.0017	0.0020	
SIM 3 (Ki)	0.0126	0.0103	0.0111	0.0100	0.0099	0.0141	0.0169	0.0155	0.0173	0.0163	0.0180	0.0138	
SE	0.0630	0.1876	0.3458	0.4422	0.3961	0.4405	0.2921	0.3406	0.3318	0.2804	0.1975	0.3016	
SSE	0.0003	0.0032	0.0108	0.0177	0.0142	0.0176	0.0077	0.0105	0.0100	0.0071	0.0035	0.0093	
SIM 4 (Ki)	0.0128	0.0130	0.0136	0.0168	0.0161	0.0132	0.0130	0.0163	0.0197	0.0180	0.0396	0.0174	
SE	0.0663	0.1586	0.2340	0.2543	0.3550	0.4697	0.5132	0.4488	0.3911	0.4752	0.2377	0.3276	
SSE	0.0004	0.0022	0.0049	0.0058	0.0114	0.0200	0.0239	0.0183	0.0139	0.0205	0.0051	0.0115	
SIM 5 (Ki)	0.0130	0.0133	0.0155	0.0188	0.0167	0.0171	0.0200	0.0172	0.0153	0.0148	0.0288	0.0173	
SE	0.0665	0.1705	0.2970	0.2628	0.2628	0.2520	0.2515	0.3847	0.5453	0.7094	0.3558	0.3234	
SSE	0.0004	0.0026	0.0080	0.0062	0.0062	0.0057	0.0057	0.0134	0.0270	0.0457	0.0115	0.0120	
SIM 6 (Ki)	0.0132	0.0164	0.0183	0.0212	0.0220	0.0219	0.0242	0.0223	0.0240	0.0230	0.0254	0.0211	
SE	0.0677	0.0771	0.1127	0.1249	0.0770	0.0904	0.1197	0.1138	0.0951	0.0858	0.0568	0.0928	
SSE	0.0004	0.0005	0.0011	0.0014	0.0005	0.0007	0.0013	0.0011	0.0008	0.0006	0.0002	0.0008	
SIM 7 (Ki)	0.0134	0.0141	0.0154	0.0148	0.0212	0.0266	0.0256	0.0263	0.0253	0.0250	0.0243	0.0211	
SE	0.0700	0.1416	0.1714	0.2697	0.2411	0.1813	0.1490	0.1553	0.1495	0.1221	0.1131	0.1603	
SSE	0.0004	0.0018	0.0026	0.0066	0.0052	0.0029	0.0020	0.0021	0.0020	0.0013	0.0011	0.0026	
SIM 8 (Ki)	0.0136	0.0094	0.0118	0.0133	0.0143	0.0110	0.0150	0.0164	0.0092	0.0112	0.0154	0.0128	
SE	0.0711	0.2621	0.1887	0.1817	0.2044	0.3312	0.5241	0.4335	1.0107	0.8254	0.5715	0.4185	
SSE	0.0004	0.0062	0.0032	0.0030	0.0038	0.0099	0.0249	0.0170	0.0928	0.0619	0.0296	0.0230	
SIM 9 (Ki)	0.0138	0.0197	0.0161	0.0149	0.0197	0.0229	0.0265	0.0295	0.0320	0.0352	0.0334	0.0240	
SE	0.0734	0.1261	0.1823	0.2914	0.2433	0.2885	0.2268	0.2273	0.2811	0.2499	0.2312	0.2201	
SSE	0.0004	0.0014	0.0030	0.0077	0.0053	0.0075	0.0046	0.0047	0.0071	0.0056	0.0048	0.0047	
SIM 10	0.0140	0.0145	0.0169	0.0145	0.0112	0.0106	0.0154	0.0178	0.0198	0.0193	0.0190	0.0157	
SE	0.0738	0.2620	0.1460	0.3023	0.3417	0.4534	0.2873	0.2080	0.2180	0.2355	0.2329	0.2509	
SSE	0.0005	0.0062	0.0019	0.0083	0.0106	0.0186	0.0075	0.0039	0.0043	0.0050	0.0049	0.0065	

Table A-2. FGLS regression method used for kinetic Patlak analysis on all simulation data and Ki values illustrated within 10 noise levels.

FGLS 30	without	0.05	0.1	0.15	0.2	0.25	0.3	0.35	0.4	0.45	0.50	μ
SIM 1	0.0133	0.0157	0.0149	0.0142	0.0179	0.0216	0.0214	0.0235	0.0215	0.0207	0.0224	0.01888
SE	0.0012	0.0024	0.0014	0.0017	0.0031	0.0021	0.0015	0.0023	0.0022	0.0025	0.0032	0.00220
SSE	0.0000	0.0000	0.0000	0.0000	0.0000	0.0000	0.0000	0.0000	0.0000	0.0000	0.0000	0.00000
SIM 2	0.0135	0.0134	0.0164	0.0200	0.0214	0.0222	0.0211	0.0257	0.0268	0.0235	0.0268	0.02104
SE	0.0013	0.0025	0.0026	0.0036	0.0022	0.0043	0.0035	0.0036	0.0037	0.0023	0.0042	0.00313
SSE	0.0000	0.0000	0.0000	0.0000	0.0000	0.0000	0.0000	0.0000	0.0000	0.0000	0.0000	0.00000
SIM 3	0.0137	0.0103	0.0182	0.0166	0.0125	0.0177	0.0200	0.0174	0.0236	0.0227	0.0228	0.01783
SE	0.0013	0.0020	0.0048	0.0061	0.0057	0.0067	0.0053	0.0056	0.0058	0.0043	0.0034	0.00468
SSE	0.0000	0.0000	0.0000	0.0000	0.0000	0.0000	0.0000	0.0000	0.0000	0.0000	0.0000	0.00000
SIM 4	0.0140	0.0126	0.0133	0.0190	0.0160	0.0189	0.0223	0.0265	0.0299	0.0306	0.0473	0.02281
SE	0.0014	0.0018	0.0031	0.0045	0.0056	0.0065	0.0061	0.0055	0.0047	0.0053	0.0044	0.00449
SSE	0.0000	0.0000	0.0000	0.0000	0.0000	0.0000	0.0000	0.0000	0.0000	0.0000	0.0000	0.00000
SIM 5	0.0141	0.0174	0.0207	0.0243	0.0211	0.0201	0.0227	0.0214	0.0181	0.0181	0.0387	0.02157
SE	0.0014	0.0038	0.0054	0.0056	0.0050	0.0048	0.0056	0.0068	0.0084	0.0105	0.0075	0.00594
SSE	0.0000	0.0000	0.0000	0.0000	0.0000	0.0000	0.0000	0.0000	0.0000	0.0000	0.0000	0.00000
SIM 6	0.0143	0.0164	0.0194	0.0255	0.0231	0.0283	0.0304	0.0261	0.0263	0.0239	0.0257	0.02363
SE	0.0015	0.0012	0.0027	0.0042	0.0033	0.0021	0.0025	0.0023	0.0021	0.0019	0.0012	0.00232
SSE	0.0000	0.0000	0.0000	0.0000	0.0000	0.0000	0.0000	0.0000	0.0000	0.0000	0.0000	0.00000
SIM 7	0.0145	0.0134	0.0172	0.0146	0.0176	0.0298	0.0310	0.0276	0.0273	0.0270	0.0250	0.02230
SE	0.0015	0.0030	0.0044	0.0038	0.0072	0.0052	0.0044	0.0042	0.0040	0.0034	0.0028	0.00404
SSE	0.0000	0.0000	0.0000	0.0000	0.0000	0.0000	0.0000	0.0000	0.0000	0.0000	0.0000	0.00000
SIM 8	0.0147	0.0101	0.0109	0.0130	0.0134	0.0099	0.0159	0.0215	0.0185	0.0282	0.0347	0.01739
SE	0.0016	0.0029	0.0014	0.0020	0.0037	0.0030	0.0079	0.0074	0.0099	0.0100	0.0072	0.00523
SSE	0.0000	0.0000	0.0000	0.0000	0.0000	0.0000	0.0000	0.0000	0.0000	0.0000	0.0000	0.00000
SIM 9	0.0149	0.0249	0.0216	0.0210	0.0221	0.0292	0.0330	0.0323	0.0354	0.0389	0.0350	0.02807
SE	0.0017	0.0035	0.0036	0.0040	0.0072	0.0054	0.0048	0.0049	0.0074	0.0081	0.0070	0.00529
SSE	0.0000	0.0000	0.0000	0.0000	0.0000	0.0000	0.0000	0.0000	0.0000	0.0000	0.0000	0.00000
SIM 10	0.0151	0.0236	0.0191	0.0169	0.0109	0.0118	0.0193	0.0227	0.0255	0.0232	0.0225	0.01919
SE	0.0017	0.0058	0.0033	0.0050	0.0036	0.0057	0.0058	0.0050	0.0050	0.0050	0.0047	0.00465
SSE	0.0000	0.0000	0.0000	0.0000	0.0000	0.0000	0.0000	0.0000	0.0000	0.0000	0.0000	0.00000

Table A-3. TLS regression method used for kinetic Patlak analysis on all simulation data and K_i values illustrated within 10 noise levels.

TLS 30	withou	0.05	0.1	0.15	0.2	0.25	0.3	0.35	0.4	0.45	0.50	μ
SIM 1	0.0122	0.0145	0.0154	0.0145	0.0177	0.0214	0.0213	0.0235	0.0213	0.0204	0.0222	0.0186
SE	0.0533	0.3732	0.4832	0.9099	1.6583	1.4762	1.5051	2.8658	3.1926	4.2392	9.9722	2.4299
SSE	0.0002	0.0126	0.0212	0.0752	0.2500	0.1981	0.2059	0.7466	0.9266	1.6337	9.0404	1.1919
SIM 2	0.0123	0.0133	0.0166	0.0167	0.0221	0.0211	0.0212	0.0256	0.0268	0.0247	0.0254	0.0205
SE	0.0566	0.5529	0.8217	0.8025	0.8999	1.6055	1.6299	1.9724	2.0938	2.1751	2.5731	1.3803
SSE	0.0002	0.0278	0.0613	0.0585	0.0736	0.2343	0.2415	0.3536	0.3985	0.4301	0.6019	0.2256
SIM 3	0.0126	0.0103	0.0111	0.0100	0.0095	0.0141	0.0170	0.0155	0.0174	0.0163	0.0180	0.0138
SE	0.0636	0.3869	1.1911	1.5720	1.5284	3.4063	2.9366	3.6313	3.7929	3.2140	3.6088	2.3029
SSE	0.0003	0.0136	0.1289	0.2246	0.2123	1.0548	0.7840	1.1987	1.3078	0.9390	1.1840	0.6407
SIM 4	0.0128	0.0130	0.0136	0.0168	0.0150	0.0132	0.0130	0.0163	0.0197	0.0180	0.0396	0.0174
SE	0.0721	0.4521	0.9595	2.0126	3.2752	3.2483	3.6237	5.6109	7.0787	8.4101	18.793	4.8670
SSE	0.0004	0.0185	0.0837	0.3682	0.9752	0.9592	1.1938	2.8620	4.5553	6.4300	32.108	4.5050
SIM 5	0.0130	0.0133	0.0155	0.0188	0.0176	0.0171	0.0200	0.0172	0.0153	0.0148	0.0288	0.0174
SE	0.0754	0.5033	1.9408	2.4042	1.8871	2.2367	3.0225	3.8755	4.1352	5.0077	5.6027	2.7901
SSE	0.0005	0.0230	0.3424	0.5255	0.3237	0.4548	0.8305	1.3654	1.5545	2.2797	2.8537	0.9594
SIM 6	0.0132	0.0164	0.0183	0.0212	0.0235	0.0218	0.0242	0.0223	0.0240	0.0229	0.0254	0.0212
SE	0.0797	0.1930	0.5640	0.9390	2.2727	0.8051	1.7893	1.6320	2.5528	2.9025	4.3337	1.6422
SSE	0.0005	0.0033	0.0289	0.0801	0.4696	0.0589	0.2910	0.2421	0.5924	0.7659	1.7073	0.3855
SIM 7	0.0134	0.0141	0.0171	0.0148	0.0178	0.0267	0.0281	0.0264	0.0254	0.0251	0.0244	0.0212
SE	0.0889	0.4054	0.8919	1.3437	5.6375	3.3017	3.5639	2.7116	2.5437	1.7339	1.3106	2.1393
SSE	0.0007	0.0149	0.0723	0.1641	2.8892	0.9910	1.1547	0.6684	0.5882	0.2733	0.1561	0.6339
SIM 8	0.0136	0.0094	0.0118	0.0133	0.0136	0.0110	0.0150	0.0164	0.0092	0.0112	0.0154	0.0127
SE	0.0937	0.5204	0.5605	0.7227	2.1944	1.7689	6.7448	6.2127	6.4787	6.5004	7.3773	3.5613
SSE	0.0008	0.0246	0.0285	0.0474	0.4377	0.2844	4.1357	3.5088	3.8158	3.8414	4.9476	1.9157
SIM 9	0.0138	0.0197	0.0161	0.0149	0.0193	0.0229	0.0281	0.0295	0.0321	0.0352	0.0335	0.0241
SE	0.1039	0.7435	0.9564	1.8026	4.3159	5.7089	5.7900	8.8416	10.827	11.856	13.489	5.8577
SSE	0.0009	0.0502	0.0831	0.2954	1.6934	2.9629	3.0476	7.1068	10.656	12.779	16.541	5.0198
SIM 10	0.0140	0.0145	0.0169	0.0145	0.0109	0.0106	0.0154	0.0178	0.0198	0.0193	0.0190	0.0157
SE	0.1074	1.2592	0.6031	1.4204	1.0679	1.7000	2.1014	2.1027	2.7083	2.9531	2.6997	1.7021
SSE	0.0010	0.1441	0.0330	0.1834	0.1036	0.2627	0.4014	0.4019	0.6668	0.7928	0.6625	0.3321

Table A-4. RFR regression method used for kinetic Patlak analysis on all simulation data and K_i values illustrated within 10 noise levels.

RFR 30	without	0.05	0.1	0.15	0.2	0.25	0.3	0.35	0.4	0.45	0.50	μ
SIM 1	0.0120	0.0145	0.0157	0.0146	0.0181	0.0213	0.0209	0.0224	0.0214	0.0209	0.0226	0.0186
SE	0.0702	0.1873	0.1998	0.2405	0.3324	0.2352	0.2290	0.3448	0.3323	0.3836	0.5217	0.2797
SSE	0.0004	0.0031	0.0036	0.0052	0.0100	0.0050	0.0047	0.0108	0.0100	0.0133	0.0247	0.0083
SIM 2	0.0121	0.0139	0.0169	0.0169	0.0234	0.0203	0.0208	0.0245	0.0261	0.0244	0.0250	0.0204
SE	0.0728	0.2434	0.2893	0.2648	0.2607	0.3830	0.3833	0.3606	0.3915	0.3760	0.4015	0.3115
SSE	0.0004	0.0053	0.0076	0.0063	0.0061	0.0133	0.0133	0.0118	0.0139	0.0128	0.0146	0.0096
SIM 3	0.0124	0.0109	0.0112	0.0087	0.0097	0.0144	0.0164	0.0148	0.0174	0.0161	0.0179	0.0136
SE	0.0782	0.1763	0.3619	0.4226	0.4236	0.5989	0.5115	0.5484	0.6262	0.5256	0.4055	0.4253
SSE	0.0005	0.0028	0.0119	0.0162	0.0163	0.0326	0.0237	0.0273	0.0356	0.0251	0.0149	0.0188
SIM 4	0.0125	0.0133	0.0137	0.0171	0.0158	0.0136	0.0130	0.0159	0.0190	0.0166	0.0181	0.0153
SE	0.0829	0.1964	0.3136	0.4221	0.5306	0.5663	0.6096	0.7137	0.7858	0.8687	0.6690	0.5235
SSE	0.0006	0.0035	0.0089	0.0162	0.0256	0.0291	0.0337	0.0463	0.0561	0.0686	0.0406	0.0299
SIM 5	0.0129	0.0136	0.0142	0.0179	0.0177	0.0173	0.0202	0.0175	0.0158	0.0132	0.0252	0.0169
SE	0.0861	0.2290	0.4000	0.4415	0.4243	0.4483	0.5242	0.6446	0.7921	0.8864	0.8405	0.5197
SSE	0.0006	0.0047	0.0145	0.0177	0.0163	0.0182	0.0249	0.0377	0.0570	0.0714	0.0642	0.0298
SIM 6	0.0130	0.0164	0.0182	0.0214	0.0195	0.0180	0.0164	0.0148	0.0239	0.0227	0.0161	0.0182
SE	0.0886	0.1208	0.2149	0.2988	0.3103	0.1413	0.1942	0.2106	0.2753	0.2907	0.2278	0.2157
SSE	0.0007	0.0013	0.0042	0.0081	0.0087	0.0018	0.0034	0.0040	0.0068	0.0076	0.0047	0.0047
SIM 7	0.0133	0.0140	0.0172	0.0154	0.0117	0.0178	0.0201	0.0255	0.0246	0.0252	0.0245	0.0190
SE	0.0934	0.2111	0.2968	0.3376	0.4959	0.3210	0.3351	0.4008	0.3826	0.3133	0.2859	0.3158
SSE	0.0007	0.0040	0.0080	0.0103	0.0223	0.0093	0.0102	0.0146	0.0133	0.0089	0.0074	0.0099
SIM 8	0.0134	0.0100	0.0123	0.0133	0.0136	0.0112	0.0145	0.0159	0.0094	0.0110	0.0156	0.0128
SE	0.0960	0.2184	0.2062	0.2527	0.4333	0.3874	0.7754	0.7419	0.9162	0.9072	0.9216	0.5324
SSE	0.0008	0.0043	0.0038	0.0058	0.0170	0.0136	0.0546	0.0500	0.0763	0.0748	0.0772	0.0344
SIM 9	0.0137	0.0198	0.0153	0.0150	0.0195	0.0229	0.0283	0.0321	0.0500	0.0528	0.0490	0.0289
SE	0.1015	0.2490	0.3091	0.4175	0.6712	0.6195	0.6355	0.7318	0.7786	0.7340	0.6185	0.5333
SSE	0.0009	0.0056	0.0086	0.0158	0.0409	0.0348	0.0367	0.0486	0.0551	0.0489	0.0347	0.0301
SIM 10	0.0139	0.0146	0.0169	0.0142	0.0103	0.0102	0.0155	0.0179	0.0198	0.0193	0.0191	0.0156
SE	0.1031	0.2913	0.2367	0.3978	0.3425	0.4232	0.4054	0.3524	0.4067	0.4349	0.4185	0.3466
SSE	0.0009	0.0077	0.0051	0.0143	0.0106	0.0162	0.0149	0.0112	0.0150	0.0172	0.0159	0.0117

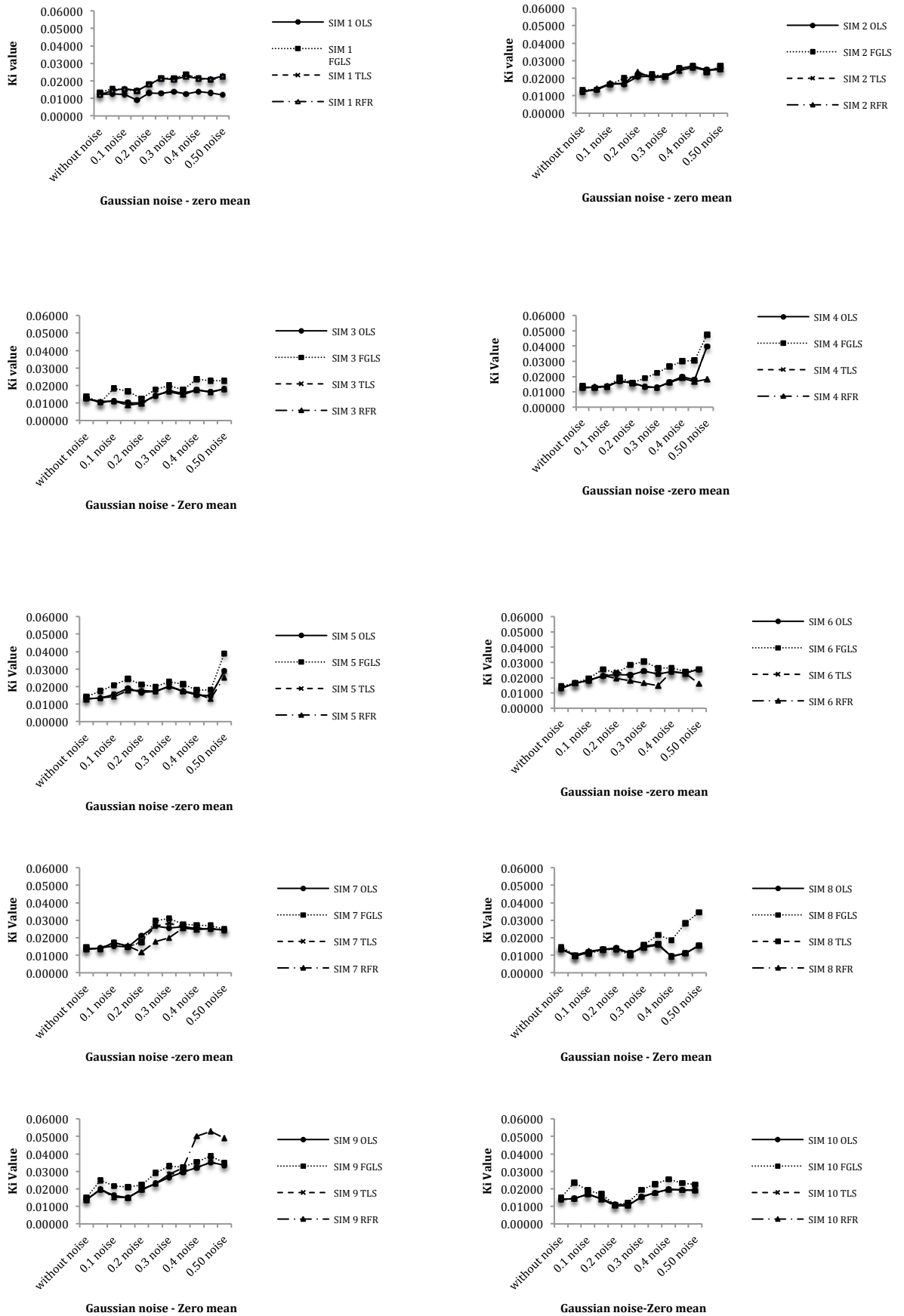


Figure A-1. A comparison between all statistical methods performed with the same data for all simulations to evaluate how each method behaves with various noise levels.

Appendix B

Table B- 1. GADF filtering method used for simulated 3D ¹⁸F-FDOPA images of the brain with different Ki values illustrated with ten noise levels.

	without	0.05	0.1	0.15	0.2	0.25	0.3	0.35	0.4	0.45	0.50
dPETST	Ki Values										
SIM 1	0.013969	0.015181	0.015047	0.015985	0.018431	0.017677	0.017494	0.015546	0.013737	0.013966	0.015378
SE	0.333	0.2848	0.3242	0.3235	0.2737	0.2944	0.3132	0.3816	0.4136	0.4136	0.322
SSE	0.010080	0.0073737	0.0095550	0.0095138	0.0068101	0.0078792	0.0089176	0.0132380	0.0155513	0.0155513	0.0094258
GADF-5	0.013969	0.01467	0.014159	0.017414	0.014065	0.015953	0.017564	0.015143	0.013925	0.014171	0.014934
SE	0.333	0.3426	0.3143	0.4076	0.8964	0.5362	0.5621	0.3558	0.3631	0.3647	0.2981
SSE	0.010080	0.0106704	0.0089804	0.0151034	0.0730484	0.0261373	0.0287233	0.0115085	0.0119856	0.0120914	0.0080785
GADF1	0.013969	0.013871	0.014456	0.015384	0.017197	0.016558	0.016635	0.01535	0.014625	0.014618	0.015479
SE	0.333	0.303	0.2977	0.2919	0.2565	0.2606	0.2849	0.3264	0.3249	0.3297	0.2689
SSE	0.010080	0.0083462	0.0080568	0.0077459	0.0059811	0.0061738	0.0073789	0.0096851	0.0095963	0.0098820	0.0065733
SIM 2	0.012157	0.0120392	0.0147138	0.0123390	0.0144602	0.0105078	0.0125777	0.0129710	0.0163446	0.0063205	0.0167243
SE	0.2863	0.2918	0.1978	0.3211	0.2379	0.3632	0.4209	0.2811	0.349	0.8899	0.2059
SSE	0.007451	0.0077406	0.0035568	0.0093732	0.0051451	0.0119922	0.0161051	0.0071833	0.0110728	0.0719929	0.0038540
GADF-	0.012157	0.011948	0.01476	0.012644	0.014845	0.012038	0.013616	0.013554	0.017058	0.006846	0.017374
SE	0.2863	0.2825	0.1953	0.3066	0.23	0.3143	0.3649	0.2707	0.3241	0.8479	0.1863
SSE	0.007451	0.0072551	0.0034674	0.0085457	0.0048090	0.0089804	0.0121047	0.0066616	0.0095491	0.0653576	0.0031552
GADF1	0.012157	0.01186	0.014475	0.012745	0.01513	0.012669	0.014092	0.014721	0.017845	0.008086	0.018256
SE	0.2863	0.2799	0.1988	0.3019	0.2208	0.2925	0.3406	0.243	0.3067	0.7088	0.1784
SSE	0.007451	0.0071221	0.0035928	0.0082857	0.0044320	0.0077778	0.0105462	0.0053680	0.0085513	0.0456724	0.0028933
SIM 3	0.010018	0.009995	0.01059	0.011413	0.00969	0.010542	0.010577	0.010704	0.011364	0.012654	0.011939
SE	0.2678	0.2736	0.2702	0.2155	0.3333	0.3002	0.3136	0.3317	0.2728	0.2728	0.3021
SSE	0.006519	0.0068051	0.0066370	0.0042218	0.0100989	0.0081927	0.0089404	0.0100022	0.0067654	0.0067654	0.0082967
GADF-	0.010018	0.010023	0.010581	0.011374	0.008931	0.010378	0.010317	0.00527	0.011319	0.012674	0.011014
SE	0.2678	0.2784	0.2684	0.2214	0.2675	0.296	0.322	0.7162	0.2809	0.2859	0.3242
SSE	0.006519	0.0070460	0.0065489	0.0044561	0.0065051	0.0079650	0.0094258	0.0466311	0.0071731	0.0074308	0.0095550
GADF1	0.010018	0.009972	0.010442	0.011401	0.00932	0.010464	0.010553	0.005887	0.011391	0.012624	0.011271
SE	0.2678	0.2834	0.2717	0.2232	0.2599	0.2886	0.3056	0.6369	0.2696	0.2945	0.3106
SSE	0.006519	0.0073014	0.0067109	0.0045289	0.0061407	0.0075718	0.0084901	0.0368765	0.0066076	0.0078845	0.0087702
SIM 4	0.007541	0.008129	0.008131	0.008136	0.008081	0.008191	0.008285	0.008161	0.008218	0.00836	0.008503
SE	0.2823	0.2598	0.2544	0.2499	0.2582	0.2572	0.2537	0.2534	0.2497	0.2368	0.236
SSE	0.007244	0.0061360	0.0058835	0.0056772	0.0060606	0.0060138	0.0058512	0.0058374	0.0056681	0.0050976	0.0050632
GADF-	0.007541	0.008217	0.008198	0.008142	0.008101	0.008268	0.008295	0.008167	0.008195	0.008305	0.008494
SE	0.2823	0.2582	0.2557	0.2547	0.2633	0.2598	0.2596	0.2601	0.2582	0.2458	0.2425
SSE	0.007244	0.0060606	0.0059438	0.0058974	0.0063024	0.0061360	0.0061265	0.0061501	0.0060606	0.0054925	0.0053460
GADF1	0.007541	0.008252	0.008211	0.008149	0.008125	0.008295	0.008315	0.008181	0.008211	0.008319	0.00849
SE	0.2823	0.2585	0.2579	0.2568	0.2659	0.2616	0.2623	0.2633	0.262	0.2494	0.2472
SSE	0.007244	0.0060747	0.0060465	0.0059951	0.0064275	0.0062213	0.0062546	0.0063024	0.0062403	0.0056545	0.0055552
SIM 5	0.004957	0.005323	0.005551	0.005619	0.005494	0.005583	0.005698	0.005764	0.005544	0.005594	0.005512
SE	0.3876	0.3443	0.324	0.3178	0.3134	0.3112	0.3095	0.3082	0.3339	0.3366	0.3582
SSE	0.013657	0.0107765	0.0095432	0.0091815	0.0089290	0.0088041	0.0087082	0.0086352	0.0101353	0.0102999	0.0116642
GADF-	0.004957	0.005227	0.005426	0.00542	0.005341	0.005415	0.005473	0.005516	0.005403	0.005492	0.005294
SE	0.3876	0.3564	0.3364	0.3348	0.3277	0.3246	0.3247	0.3221	0.3432	0.3413	0.3714
SSE	0.013657	0.0115473	0.0102877	0.0101900	0.0097624	0.0095786	0.0095845	0.0094316	0.0107078	0.0105896	0.0125398
GADF1	0.004957	0.005227	0.005415	0.005382	0.005299	0.005371	0.005402	0.005407	0.005331	0.005437	0.005213
SE	0.3876	0.3575	0.3402	0.3391	0.3325	0.3287	0.329	0.3274	0.347	0.3423	0.3719
SSE	0.013657	0.0116187	0.0105214	0.0104535	0.0100505	0.0098221	0.0098400	0.0097446	0.0109462	0.0106517	0.0125736
SIM 6	0.002465	0.002667	0.0027	0.002767	0.002803	0.002921	0.002866	0.00283	0.002916	0.002831	0.002807
SE	0.3852	0.354	0.3477	0.3356	0.3369	0.3191	0.3325	0.328	0.3186	0.3285	0.3307
SSE	0.013489	0.0113923	0.0109904	0.0102388	0.0103183	0.0092568	0.0100505	0.0097803	0.0092278	0.0098102	0.0099420
GADF-	0.002465	0.00266	0.002695	0.002766	0.002792	0.002903	0.002856	0.002822	0.002892	0.002791	0.002775
SE	0.3852	0.3578	0.3528	0.3404	0.3452	0.3284	0.3416	0.3349	0.328	0.3405	0.3421
SSE	0.013489	0.0116382	0.0113152	0.0105338	0.0108330	0.0098042	0.0106082	0.0101961	0.0097803	0.0105400	0.0106393
GADF1	0.002465	0.00266	0.002697	0.002774	0.00279	0.002889	0.00284	0.002821	0.002883	0.002774	0.002756
SE	0.3852	0.3601	0.3553	0.3417	0.3481	0.3328	0.3465	0.3375	0.3316	0.3447	0.3473
SSE	0.013489	0.0117883	0.0114761	0.0106144	0.0110157	0.0100687	0.0109147	0.0103551	0.0099962	0.0108016	0.0109652

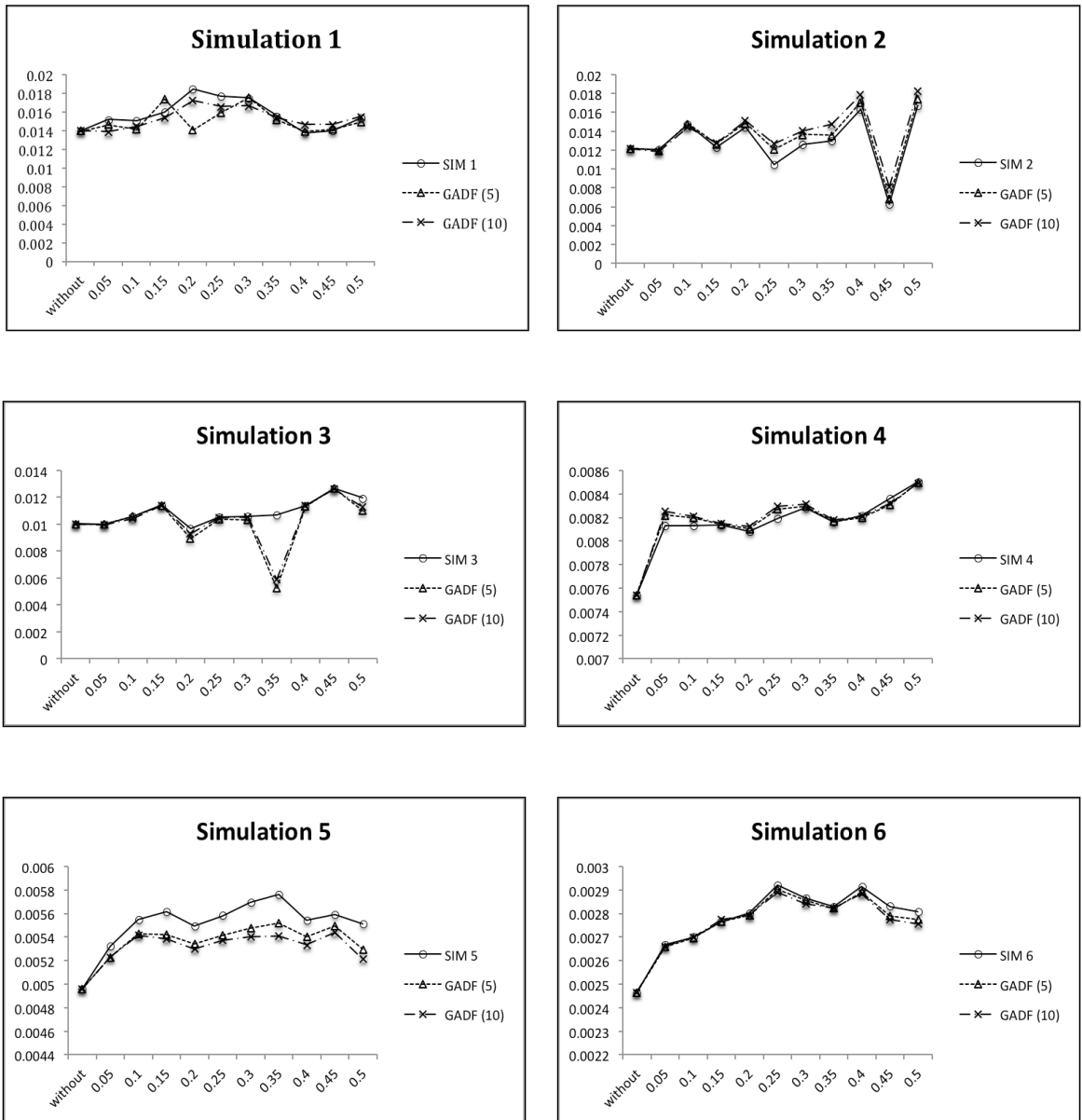


Figure B- 1. GADF 5 and 10 iterations used for 3D images and Ki values illustrated within ten noise levels.

Appendix C

Table C- 1. MAF method used with different Ki values illustrated by applying ten noise levels.

	without	0.05	0.1	0.15	0.2	0.25	0.3	0.35	0.4	0.45	0.50
dPETSTEP	Ki Values										
SIM1	0.01396	0.01518	0.01504	0.01598	0.01843	0.01767	0.01749	0.01812	0.01812	0.01926	0.01537
SE	0.333	0.2848	0.3242	0.3235	0.2737	0.2944	0.3132	0.3816	0.1728	0.1577	0.322
SSE	0.01008	0.00737	0.00955	0.00951	0.00681	0.00787	0.00891	0.01323	0.00271	0.00226	0.00942
MAF		0.01503	0.01475	0.01491	0.01557	0.01572	0.01579	0.01420	0.01591	0.01657	0.01404
SE		0.1159	0.1197	0.1169	0.1045	0.1058	0.1029	0.1166	0.097	0.0896	0.132
SSE		0.00122	0.00130	0.00124	0.00099	0.00101	0.00096	0.00123	0.00085	0.00072	0.00158
SIM2	0.01215	0.01242	0.01471	0.01233	0.01446	0.0134	0.01257	0.01287	0.01287	0.01634	0.01672
SE	0.2863	0.2957	0.1978	0.3206	0.2379	0.3116	0.4209	0.2811	0.4002	0.349	0.2059
SSE	0.00745	0.00774	0.00355	0.00934	0.00514	0.00882	0.01610	0.00718	0.01456	0.01107	0.00385
MAF		0.01260	0.01287	0.01228	0.01269	0.01283	0.01268	0.01254	0.01268	0.01268	0.01290
SE		0.1943	0.1889	0.1974	0.199	0.1885	0.1906	0.1962	0.1946	0.1918	0.191
SSE		0.00343	0.00324	0.00354	0.00360	0.00323	0.00330	0.00349	0.00344	0.00334	0.00331
SIM 3	0.01001	0.01049	0.01053	0.01141	0.01215	0.01151	0.01198	0.01198	0.01198	0.01265	0.01256
SE	0.2678	0.2663	0.2712	0.2155	0.2177	0.2207	0.2348	0.2343	0.2348	0.2728	0.2588
SSE	0.00651	0.00644	0.00668	0.00422	0.00430	0.00442	0.00501	0.00499	0.00501	0.00676	0.00608
MAF		0.01057	0.01048	0.01100	0.01079	0.01048	0.01059	0.01068	0.01079	0.01155	0.01112
SE		0.1593	0.1589	0.1493	0.1466	0.1581	0.1531	0.1567	0.1526	0.1334	0.1451
SSE		0.00230	0.00229	0.00202	0.00195	0.00227	0.00213	0.00223	0.00211	0.00161	0.00191
SIM 4	0.00754	0.00812	0.00813	0.00813	0.00808	0.00819	0.00828	0.00821	0.00821	0.00836	0.00850
SE	0.2823	0.2598	0.2544	0.2499	0.2582	0.2572	0.2537	0.2534	0.2497	0.2368	0.236
SSE	0.00724	0.00613	0.00588	0.00567	0.00606	0.00601	0.00585	0.00583	0.00566	0.00509	0.00506
MAF		0.00764	0.00761	0.00771	0.00752	0.00762	0.00754	0.00770	0.00773	0.00811	0.00786
SE		0.247	0.2519	0.248	0.2555	0.2503	0.2574	0.2505	0.2519	0.2346	0.2457
SSE		0.00554	0.00576	0.00559	0.00593	0.00569	0.00602	0.00570	0.00576	0.00500	0.00548
SIM 5	0.00495	0.00532	0.00555	0.00561	0.00549	0.00558	0.00569	0.00554	0.00554	0.00559	0.00551
SE	0.3876	0.3443	0.324	0.3177	0.3134	0.3112	0.3095	0.3082	0.3339	0.3366	0.3582
SSE	0.01365	0.01077	0.00954	0.00917	0.00892	0.00880	0.00870	0.00863	0.01013	0.01029	0.01166
MAF		0.00525	0.00533	0.00534	0.00532	0.00531	0.00533	0.00533	0.00534	0.00532	0.00532
SE		0.241	0.2402	0.2401	0.24	0.2406	0.2389	0.2395	0.2391	0.24	0.2392
SSE		0.00528	0.00524	0.00524	0.00523	0.00526	0.00518	0.00521	0.00519	0.00523	0.00520
SIM 6	0.00246	0.00266	0.0027	0.00276	0.00280	0.00292	0.00286	0.00291	0.00291	0.00283	0.00280
SE	0.3852	0.354	0.3477	0.3356	0.3369	0.3191	0.3325	0.328	0.3186	0.3285	0.3307
SSE	0.01348	0.01139	0.01099	0.01023	0.01031	0.00925	0.01005	0.00978	0.00922	0.00981	0.00994
MAF		0.00250	0.00251	0.00252	0.00253	0.00253	0.00252	0.00253	0.00255	0.00253	0.00253
SE		0.2435	0.2454	0.2449	0.2441	0.244	0.2443	0.244	0.2428	0.2429	0.2433
SSE		0.00539	0.00547	0.00545	0.00541	0.00541	0.00542	0.00541	0.00535	0.00536	0.00538

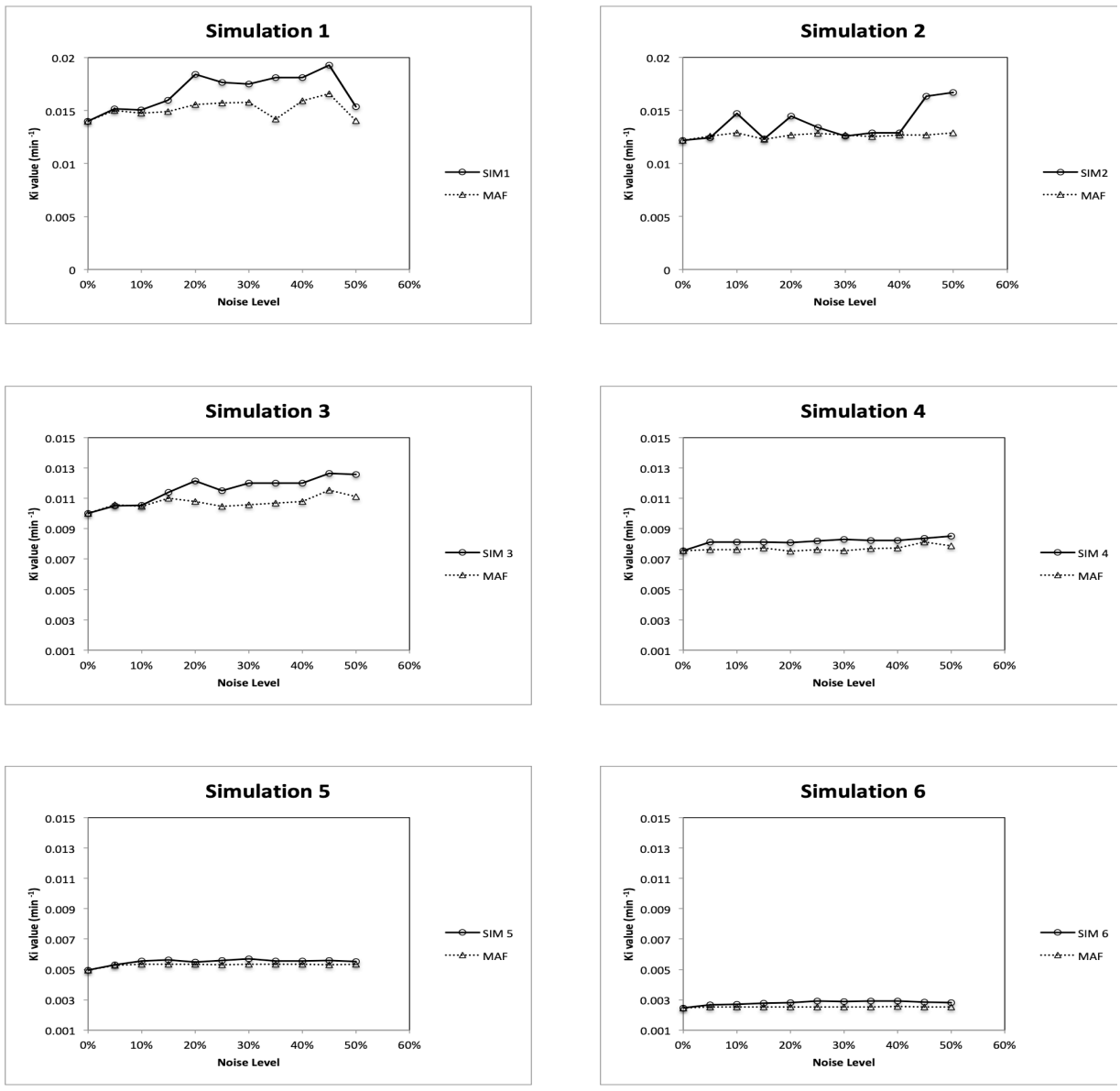


Figure C- 1. MAF method used for TACs and Ki values shown at ten different noise levels.

Table C- 2. SGF method used with different Ki values illustrated with applying ten noise levels.

	without	0.05	0.1	0.15	0.2	0.25	0.3	0.35	0.4	0.45	0.50
dPETSTEP	Ki Values										
SIM1	0.01396	0.01518	0.01504	0.01598	0.01843	0.01767	0.01749	0.01554	0.01812	0.01926	0.01537
SE	0.333	0.2848	0.3242	0.3235	0.2737	0.2944	0.3132	0.3816	0.1728	0.1577	0.322
SSE	0.01008	0.00737	0.00955	0.00951	0.00681	0.00787	0.00891	0.01323	0.00271	0.00226	0.00942
SGF		0.01510	0.01498	0.01517	0.01594	0.01615	0.01625	0.01475	0.01614	0.01670	0.01430
SE		0.123	0.1264	0.1223	0.1076	0.1089	0.1051	0.1196	0.1019	0.0951	0.1363
SSE		0.00137	0.00145	0.00135	0.00105	0.00107	0.00100	0.00130	0.00094	0.00082	0.00168
SIM2	0.01215	0.01242	0.01471	0.01233	0.01446	0.0134	0.01257	0.01297	0.01287	0.01634	0.01672
SE	0.2863	0.2957	0.1978	0.3206	0.2379	0.3116	0.4209	0.2811	0.4002	0.349	0.2059
SSE	0.00745	0.00774	0.00355	0.00934	0.00514	0.00882	0.01610	0.00718	0.01456	0.01107	0.00385
SGF		0.01218	0.01230	0.01210	0.01250	0.01250	0.01243	0.01236	0.01228	0.01254	0.01278
SE		0.1788	0.2027	0.2695	0.1678	0.1678	0.1647	0.2636	0.2685	0.2928	0.2539
SSE		0.00290	0.00373	0.00660	0.00255	0.00255	0.00246	0.00631	0.00655	0.00779	0.00586
SIM 3	0.01001	0.01049	0.01053	0.01141	0.01215	0.01151	0.01198	0.01129	0.01198	0.01265	0.01256
SE	0.2678	0.2663	0.2712	0.2155	0.2177	0.2207	0.2348	0.2343	0.2348	0.2728	0.2588
SSE	0.00651	0.00644	0.00668	0.00422	0.00430	0.00442	0.00501	0.00499	0.00501	0.00676	0.00608
SGF		0.01039	0.01042	0.01059	0.01039	0.01027	0.01047	0.01021	0.01061	0.01114	0.01088
SE		0.1644	0.1633	0.1557	0.1568	0.1579	0.1616	0.159	0.1588	0.1493	0.1495
SSE		0.00245	0.00242	0.00220	0.00223	0.00226	0.00237	0.00229	0.00229	0.00202	0.00203
SIM 4	0.00754	0.00812	0.00813	0.00813	0.00808	0.00819	0.00828	0.00816	0.00821	0.00836	0.00850
SE	0.2823	0.2598	0.2544	0.2499	0.2582	0.2572	0.2537	0.2534	0.2497	0.2368	0.236
SSE	0.00724	0.00613	0.00588	0.00567	0.00606	0.00601	0.00585	0.00583	0.00566	0.00509	0.00506
SGF		0.00806	0.00809	0.00809	0.00809	0.00813	0.00815	0.00813	0.00814	0.00813	0.00814
SE		0.1638	0.1625	0.163	0.1634	0.1626	0.1633	0.1639	0.163	0.164	0.1641
SSE		0.00243	0.00240	0.00241	0.00242	0.00240	0.00242	0.00244	0.00241	0.00244	0.00244
SIM 5	0.00495	0.00532	0.00555	0.00561	0.00549	0.00558	0.00569	0.00576	0.00554	0.00559	0.00551
SE	0.3876	0.3443	0.324	0.3177	0.3134	0.3112	0.3095	0.3082	0.3339	0.3366	0.3582
SSE	0.01365	0.01077	0.00954	0.00917	0.00892	0.00880	0.00870	0.00863	0.01013	0.01029	0.01166
SGF		0.00511	0.00513	0.00515	0.00511	0.00511	0.00515	0.00516	0.00516	0.00512	0.00514
SE		0.2761	0.2741	0.2714	0.2727	0.2724	0.2698	0.27	0.2699	0.2736	0.2718
SSE		0.00693	0.00683	0.00669	0.00676	0.00674	0.00661	0.00662	0.00662	0.00680	0.00671
SIM 6	0.00246	0.00266	0.0027	0.00276	0.00280	0.00292	0.00286	0.00283	0.00291	0.00283	0.00280
SE	0.3852	0.354	0.3477	0.3356	0.3369	0.3191	0.3325	0.328	0.3186	0.3285	0.3307
SSE	0.01348	0.01139	0.01099	0.01023	0.01031	0.00925	0.01005	0.00978	0.00922	0.00981	0.00994
SGF		0.00251	0.00252	0.00254	0.00256	0.00256	0.00253	0.00253	0.00255	0.00254	0.00253
SE		0.2741	0.2741	0.2708	0.2688	0.2675	0.2705	0.2713	0.2694	0.2705	0.2707
SSE		0.00683	0.00683	0.00666	0.00656	0.00650	0.00665	0.00669	0.00659	0.00665	0.00666

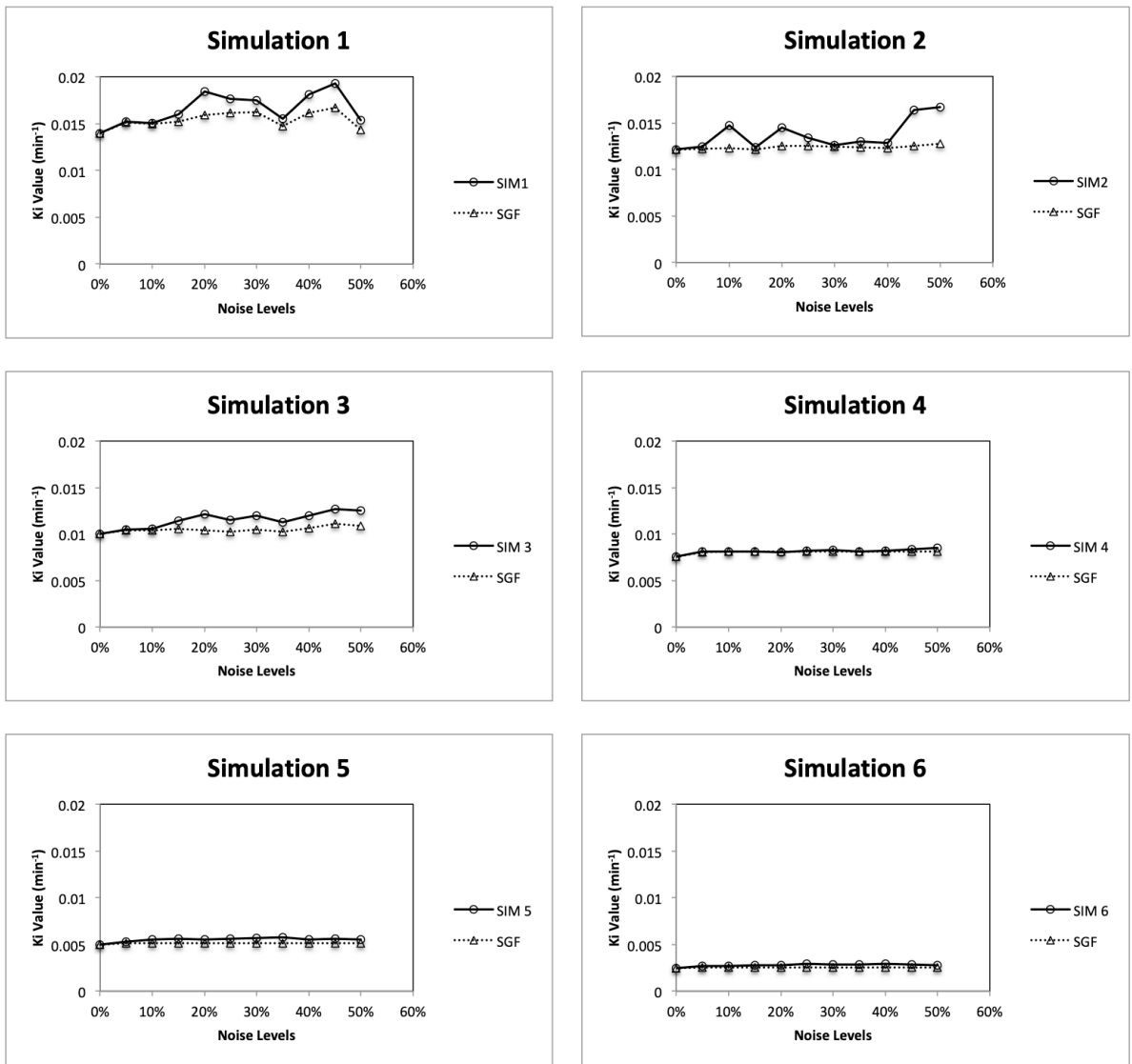


Figure C- 2. SGF method used for TACs and Ki values illustrated within ten noise levels.

Table C- 3. PCF method used with different Ki values illustrated with applying ten noise levels.

	without	0.05	0.1	0.15	0.2	0.25	0.3	0.35	0.4	0.45	0.50
dPETSTEP	Ki Values										
SIM1	0.01396	0.01518	0.01504	0.01598	0.01843	0.01767	0.01749	0.01554	0.01812	0.01926	0.01537
SE	0.333	0.2848	0.3242	0.3235	0.2737	0.2944	0.3132	0.3816	0.1728	0.1577	0.322
SSE	0.01008	0.00737	0.00955	0.00951	0.00681	0.00787	0.00891	0.01323	0.00271	0.00226	0.00942
PCF		0.01462	0.01374	0.01540	0.01555	0.01505	0.01509	0.01456	0.01752	0.01844	0.01546
SE		0.1404	0.1397	0.1018	0.0979	0.1313	0.1329	0.1328	0.1015	0.1035	0.1721
SSE		0.00179	0.00177	0.00094	0.00087	0.00156	0.00160	0.00160	0.00093	0.00097	0.00269
SIM2	0.01215	0.01242	0.01471	0.01233	0.01446	0.0134	0.01257	0.01297	0.01287	0.01634	0.01672
SE	0.2863	0.2957	0.1978	0.3206	0.2379	0.3116	0.4209	0.2811	0.4002	0.349	0.2059
SSE	0.00745	0.00774	0.00355	0.00934	0.00514	0.00882	0.01610	0.00718	0.01456	0.01107	0.00385
PCF		0.01296	0.01359	0.01213	0.01402	0.01334	0.01229	0.01247	0.01242	0.01521	0.01648
SE		0.143	0.0798	0.1481	0.1082	0.0691	0.1113	0.141	0.2671	0.101	0.1126
SSE		0.00185	0.00057	0.00199	0.00106	0.00043	0.00112	0.00180	0.00648	0.00092	0.00115
SIM 3	0.01001	0.01049	0.01053	0.01141	0.01215	0.01151	0.01198	0.01129	0.01198	0.01265	0.01256
SE	0.2678	0.2663	0.2712	0.2155	0.2177	0.2207	0.2348	0.2343	0.2348	0.2728	0.2588
SSE	0.00651	0.00644	0.00668	0.00422	0.00430	0.00442	0.00501	0.00499	0.00501	0.00676	0.00608
PCF		0.00963	0.01015	0.01090	0.01212	0.01102	0.01005	0.01060	0.01005	0.01168	0.01121
SE		0.1127	0.0962	0.0729	0.1019	0.1273	0.0286	0.0983	0.0286	0.1274	0.1377
SSE		0.00115	0.00084	0.00048	0.00094	0.00147	0.00007	0.00087	0.00007	0.00147	0.00172
SIM 4	0.00754	0.00812	0.00813	0.00813	0.00808	0.00819	0.00828	0.00816	0.00821	0.00836	0.00850
SE	0.2823	0.2598	0.2544	0.2499	0.2582	0.2572	0.2537	0.2534	0.2497	0.2368	0.236
SSE	0.00724	0.00613	0.00588	0.00567	0.00606	0.00601	0.00585	0.00583	0.00566	0.00509	0.00506
PCF		0.00787	0.0078	0.00785	0.00782	0.00789	0.00792	0.00780	0.00783	0.00783	0.00793
SE		0.0744	0.0772	0.0743	0.0824	0.0829	0.08	0.0776	0.0751	0.0783	0.0776
SSE		0.00050	0.00054	0.00050	0.00061	0.00062	0.00058	0.00054	0.00051	0.00055	0.00054
SIM 5	0.00495	0.00532	0.00555	0.00561	0.00549	0.00558	0.00569	0.00576	0.00554	0.00559	0.00551
SE	0.3876	0.3443	0.324	0.3177	0.3134	0.3112	0.3095	0.3082	0.3339	0.3366	0.3582
SSE	0.01365	0.01077	0.00954	0.00917	0.00892	0.00880	0.00870	0.00863	0.01013	0.01029	0.01166
PCF		0.00531	0.00539	0.00540	0.00529	0.00522	0.00553	0.00571	0.00561	0.00518	0.00509
SE		0.1418	0.1518	0.1555	0.1592	0.1679	0.1562	0.1422	0.145	0.2084	0.1986
SSE		0.00182	0.00209	0.00219	0.00230	0.00256	0.00221	0.00183	0.00191	0.00394	0.00358
SIM 6	0.00246	0.00266	0.0027	0.00276	0.00280	0.00292	0.00286	0.00283	0.00291	0.00283	0.00280
SE	0.3852	0.354	0.3477	0.3356	0.3369	0.3191	0.3325	0.328	0.3186	0.3285	0.3307
SSE	0.01348	0.01139	0.01099	0.01023	0.01031	0.00925	0.01005	0.00978	0.00922	0.00981	0.00994
PCF		0.0025	0.00243	0.00246	0.00244	0.00249	0.00283	0.00282	0.00258	0.00250	0.0025
SE		0.1254	0.1351	0.1346	0.1374	0.1445	0.0987	0.0881	0.1192	0.124	0.1203
SSE		0.00142	0.00165	0.00164	0.00171	0.00189	0.00088	0.00070	0.00129	0.00139	0.00131

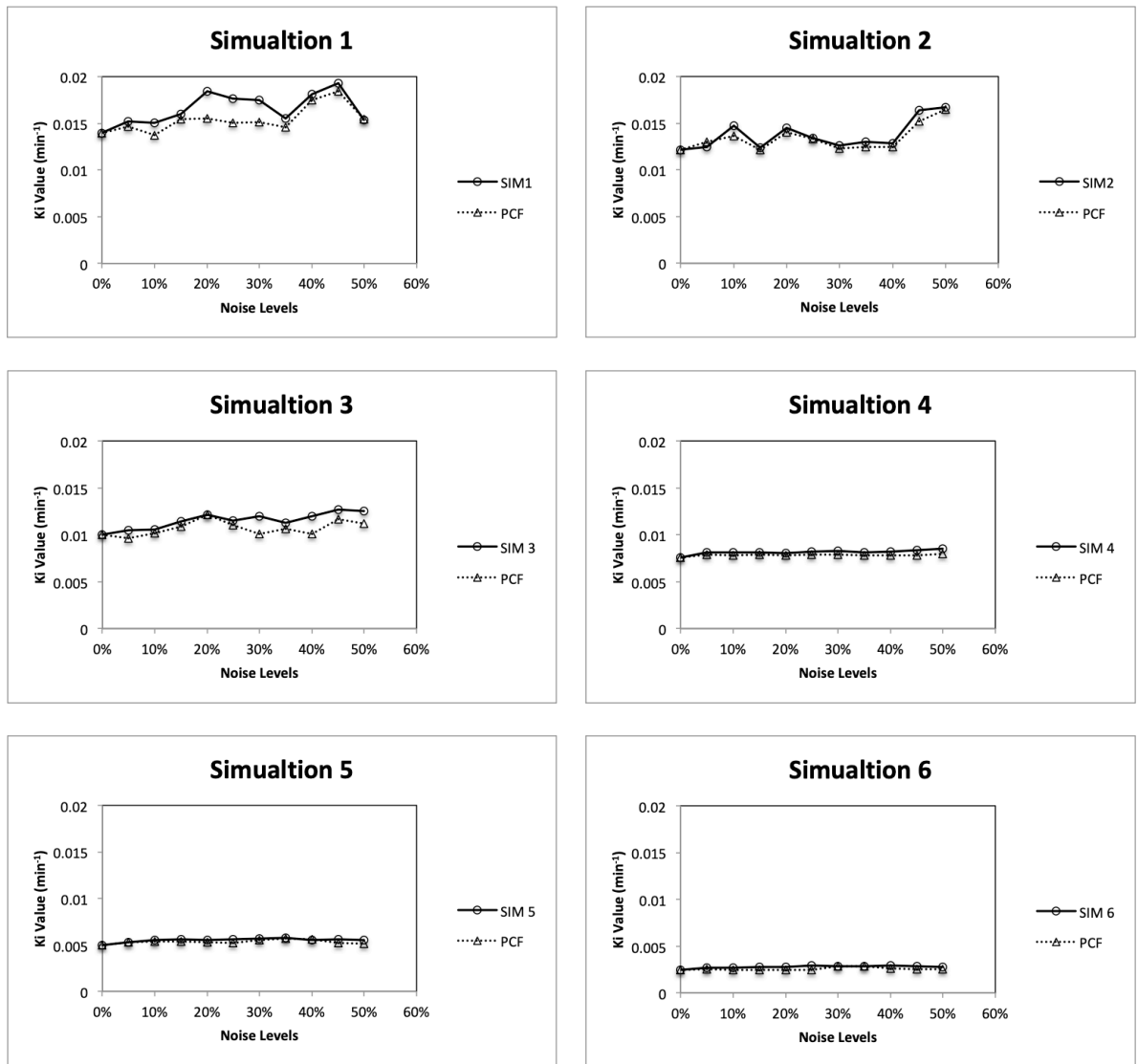


Figure C- 3. PCF method used for TACs and Ki values illustrated within ten noise levels.

Table C- 4. MF method used with different Ki values illustrated with applying ten noise levels.

	without	0.05	0.1	0.15	0.2	0.25	0.3	0.35	0.4	0.45	0.50
dPETSTEP	Ki Values										
SIM1	0.01396	0.01518	0.01504	0.01598	0.01843	0.01767	0.01749	0.01554	0.01812	0.01926	0.01537
SE	0.333	0.2848	0.3242	0.3235	0.2737	0.2944	0.3132	0.3816	0.1728	0.1577	0.322
SSE	0.01008	0.00737	0.00955	0.00951	0.00681	0.00787	0.00891	0.01323	0.00271	0.00226	0.00942
MF		0.01462	0.01374	0.01540	0.01555	0.01505	0.01509	0.01456	0.01752	0.01844	0.01546
SE		0.1404	0.1397	0.1018	0.0979	0.1313	0.1329	0.1328	0.1015	0.1035	0.1721
SSE		0.00179	0.00177	0.00094	0.00087	0.00156	0.00160	0.00160	0.00093	0.00097	0.00269
SIM2	0.01215	0.01242	0.01471	0.01233	0.01446	0.0134	0.01257	0.01297	0.01287	0.01634	0.01672
SE	0.2863	0.2957	0.1978	0.3206	0.2379	0.3116	0.4209	0.2811	0.4002	0.349	0.2059
SSE	0.00745	0.00774	0.00355	0.00934	0.00514	0.00882	0.01610	0.00718	0.01456	0.01107	0.00385
MF		0.01296	0.01359	0.01213	0.01402	0.01334	0.01229	0.01247	0.01242	0.01521	0.01648
SE		0.143	0.0798	0.1481	0.1082	0.0691	0.1113	0.141	0.2671	0.101	0.1126
SSE		0.00185	0.00057	0.00199	0.00106	0.00043	0.00112	0.00180	0.00648	0.00092	0.00115
SIM 3	0.01001	0.01049	0.01053	0.01141	0.01215	0.01151	0.01198	0.01129	0.01198	0.01265	0.01256
SE	0.2678	0.2663	0.2712	0.2155	0.2177	0.2207	0.2348	0.2343	0.2348	0.2728	0.2588
SSE	0.00651	0.00644	0.00668	0.00422	0.00430	0.00442	0.00501	0.00499	0.00501	0.00676	0.00608
MF		0.00963	0.01015	0.01090	0.01212	0.01102	0.01005	0.01060	0.01005	0.01168	0.01121
SE		0.1127	0.0962	0.0729	0.1019	0.1273	0.0286	0.0983	0.0286	0.1274	0.1377
SSE		0.00115	0.00084	0.00048	0.00094	0.00147	0.00007	0.00087	0.00007	0.00147	0.00172
SIM 4	0.00754	0.00812	0.00813	0.00813	0.00808	0.00819	0.00828	0.00816	0.00821	0.00836	0.00850
SE	0.2823	0.2598	0.2544	0.2499	0.2582	0.2572	0.2537	0.2534	0.2497	0.2368	0.236
SSE	0.00724	0.00613	0.00588	0.00567	0.00606	0.00601	0.00585	0.00583	0.00566	0.00509	0.00506
MF		0.00787	0.0078	0.00785	0.00782	0.00789	0.00792	0.00780	0.00783	0.00783	0.00793
SE		0.0744	0.0772	0.0743	0.0824	0.0829	0.08	0.0776	0.0751	0.0783	0.0776
SSE		0.00050	0.00054	0.00050	0.00061	0.00062	0.00058	0.00054	0.00051	0.00055	0.00054
SIM 5	0.00495	0.00532	0.00555	0.00561	0.00549	0.00558	0.00569	0.00576	0.00554	0.00559	0.00551
SE	0.3876	0.3443	0.324	0.3177	0.3134	0.3112	0.3095	0.3082	0.3339	0.3366	0.3582
SSE	0.01365	0.01077	0.00954	0.00917	0.00892	0.00880	0.00870	0.00863	0.01013	0.01029	0.01166
MF		0.00531	0.00539	0.00540	0.00529	0.00522	0.00553	0.00571	0.00561	0.00518	0.00509
SE		0.1418	0.1518	0.1555	0.1592	0.1679	0.1562	0.1422	0.145	0.2084	0.1986
SSE		0.00182	0.00209	0.00219	0.00230	0.00256	0.00221	0.00183	0.00191	0.00394	0.00358
SIM 6	0.00246	0.00266	0.0027	0.00276	0.00280	0.00292	0.00286	0.00283	0.00291	0.00283	0.00280
SE	0.3852	0.354	0.3477	0.3356	0.3369	0.3191	0.3325	0.328	0.3186	0.3285	0.3307
SSE	0.01348	0.01139	0.01099	0.01023	0.01031	0.00925	0.01005	0.00978	0.00922	0.00981	0.00994
MF		0.0025	0.00243	0.00246	0.00244	0.00249	0.00283	0.00282	0.00258	0.00250	0.0025
SE		0.1254	0.1351	0.1346	0.1374	0.1445	0.0987	0.0881	0.1192	0.124	0.1203
SSE		0.00142	0.00165	0.00164	0.00171	0.00189	0.00088	0.00070	0.00129	0.00139	0.00131

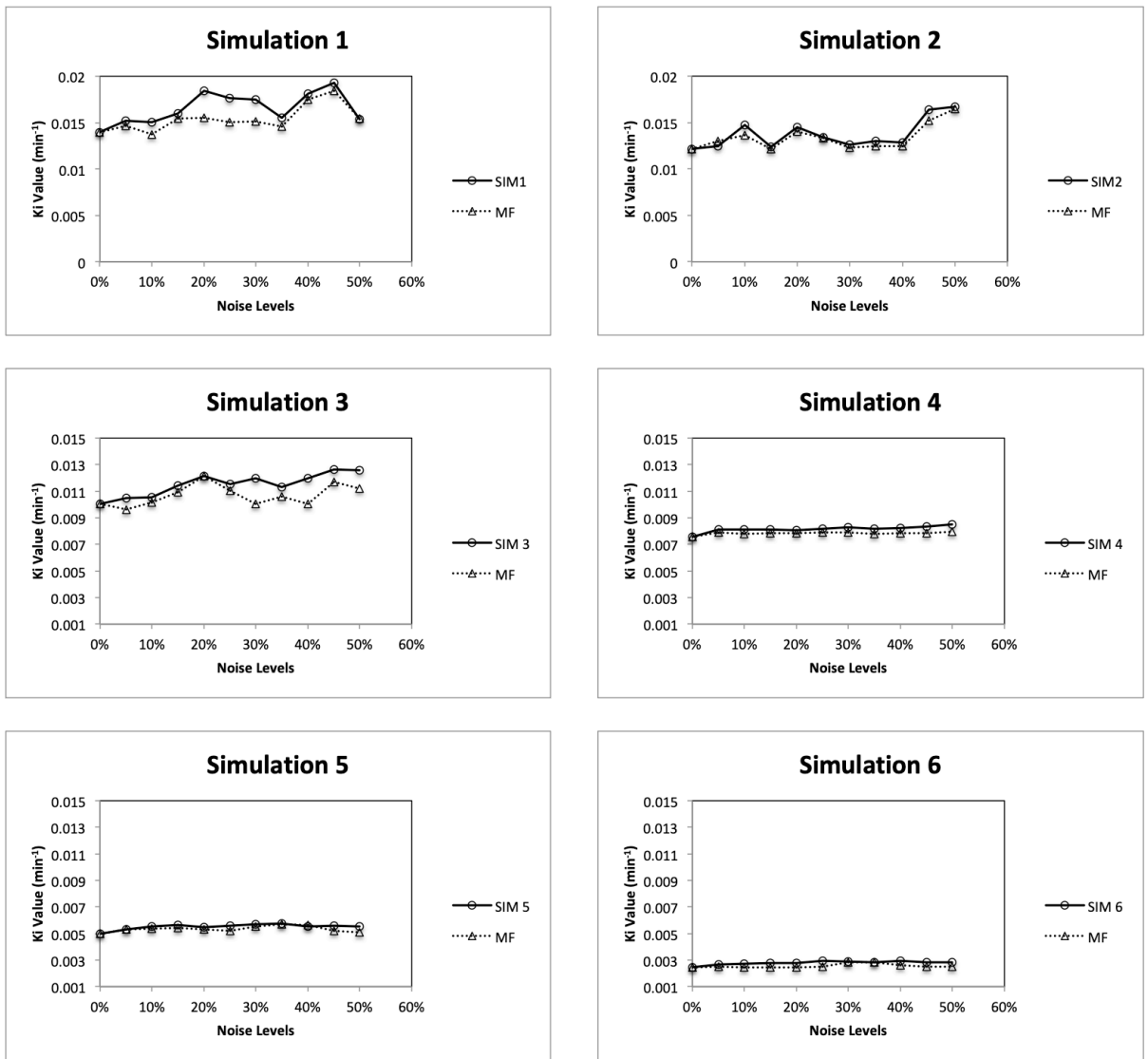


Figure C- 4. MF method used for TACs and Ki values illustrated within ten noise levels.

Appendix D

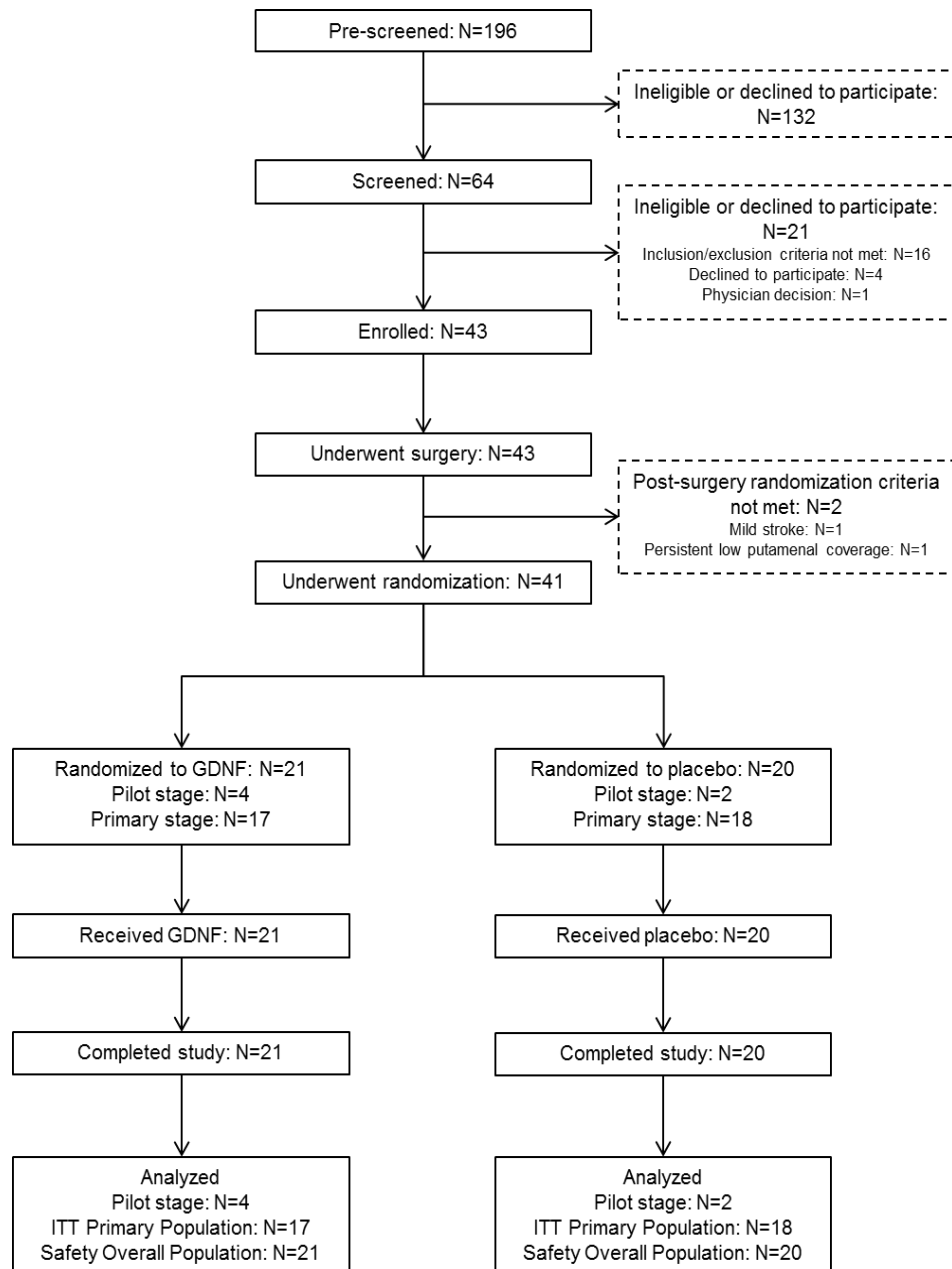


Figure D- 1. CONSORT flow diagram used initially in selecting the subjects and designing the clinical trial outline (Whone et al. 2019).

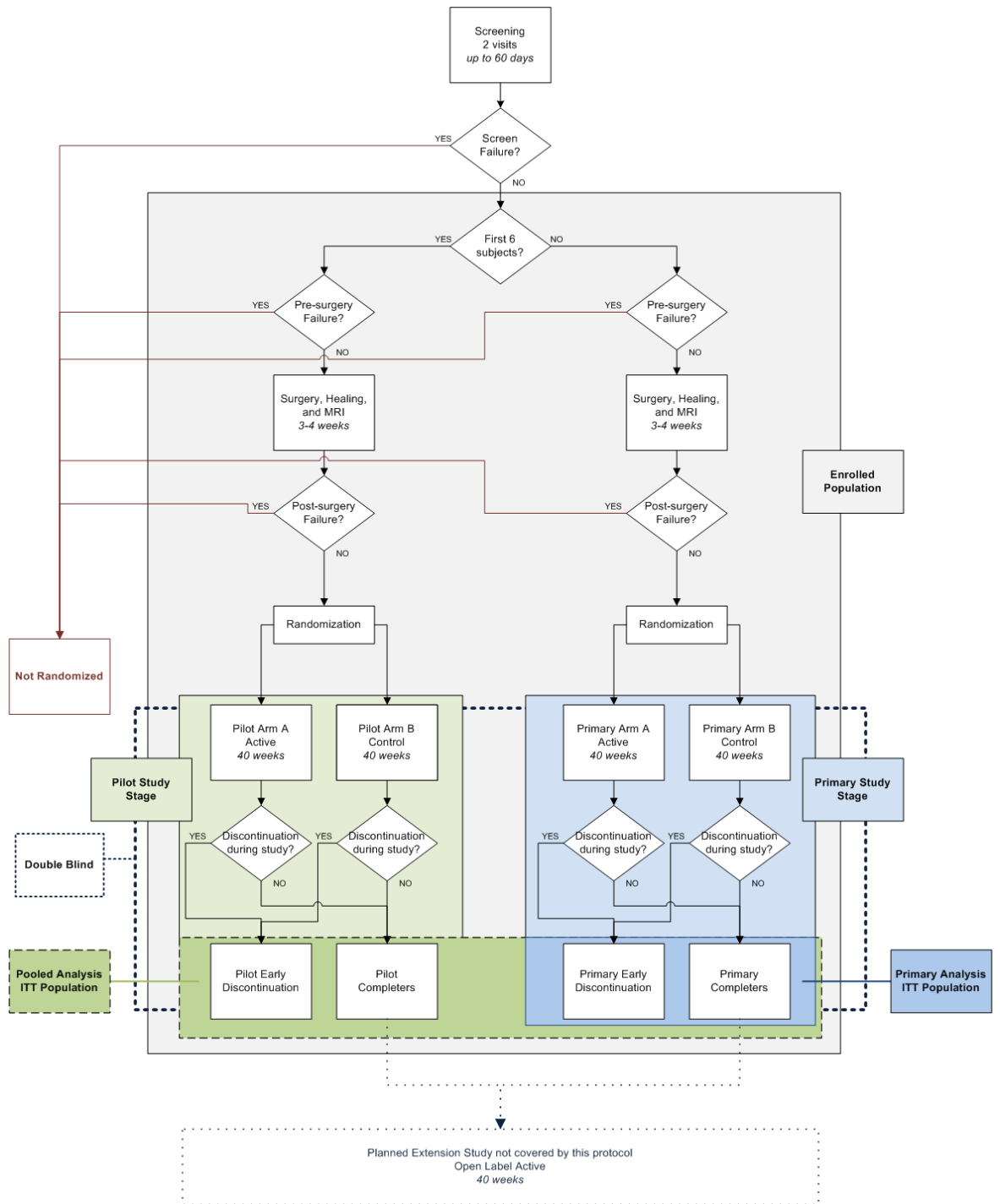


Figure D- 2. GDNF clinical trial outline followed in PETIC department in the University Hospital of Wales.

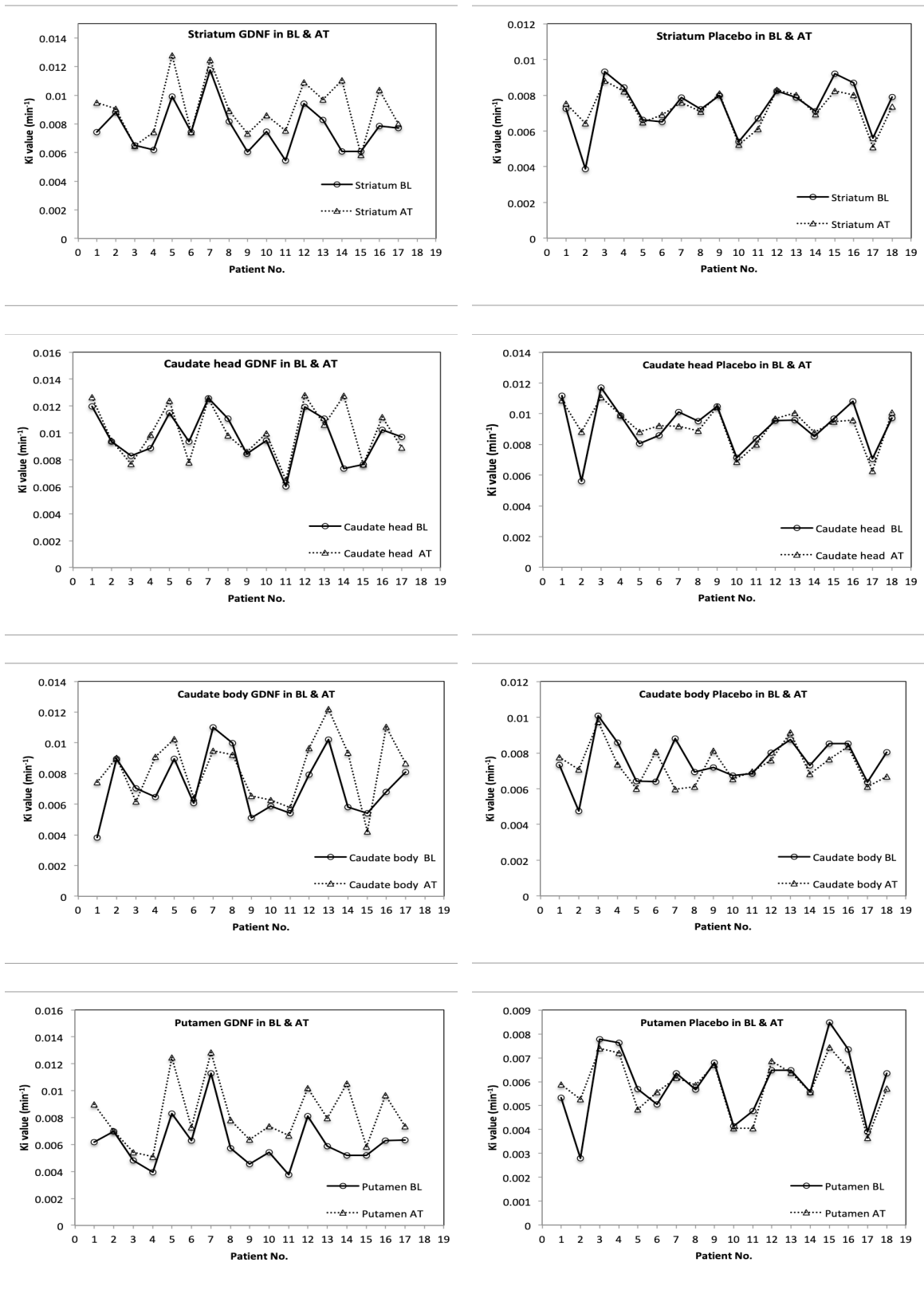


Figure D- 3. Graphs show a comparison between all striatum parts of both (R and L anatomical sides) in baseline vs. week 40 in both GDNF (left side) and placebo group (right side).

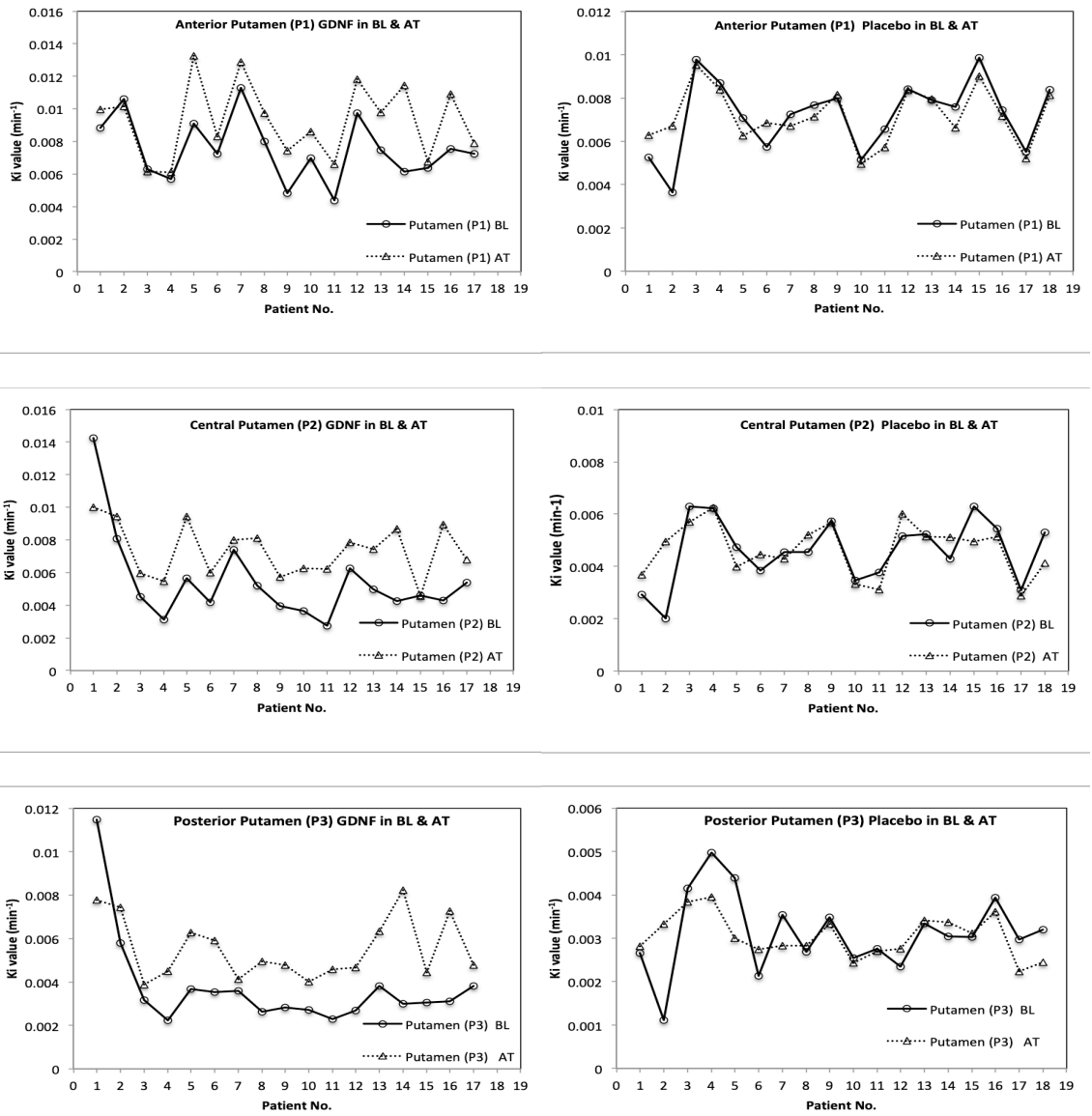


Figure D- 4. Graphs show a comparison between putamen parts of both (R and L anatomical sides) in baseline vs. week 40 in both GDNF (left side) and placebo group (right side) after dividing the putamen's contour into three parts: Anterior, central and posterior.

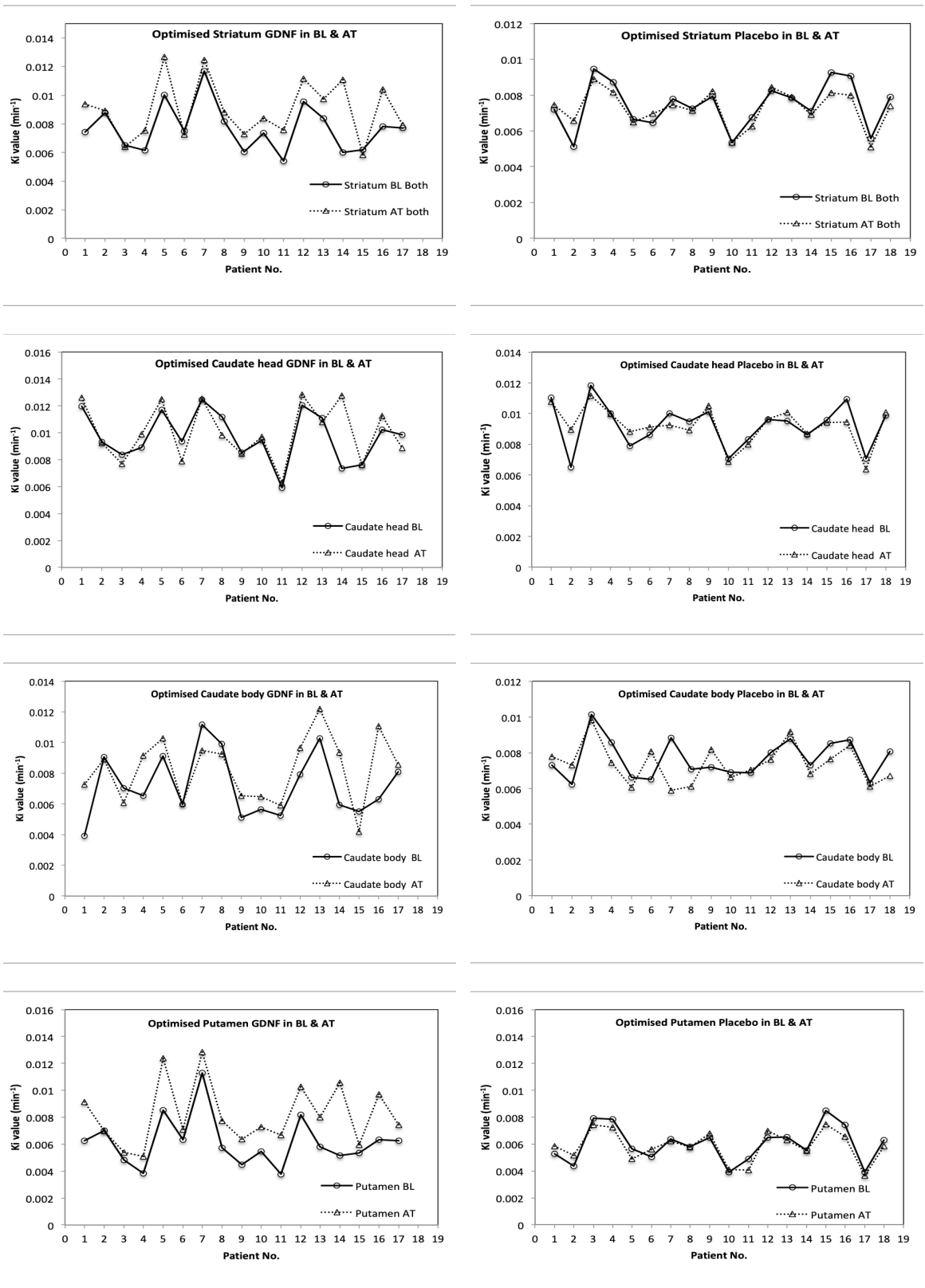


Figure D- 5. A comparison made after applying new methods between all striatum parts of both (R and L anatomical sides) in baseline vs. week 40 in both GDNF (left side) and placebo group (right side).

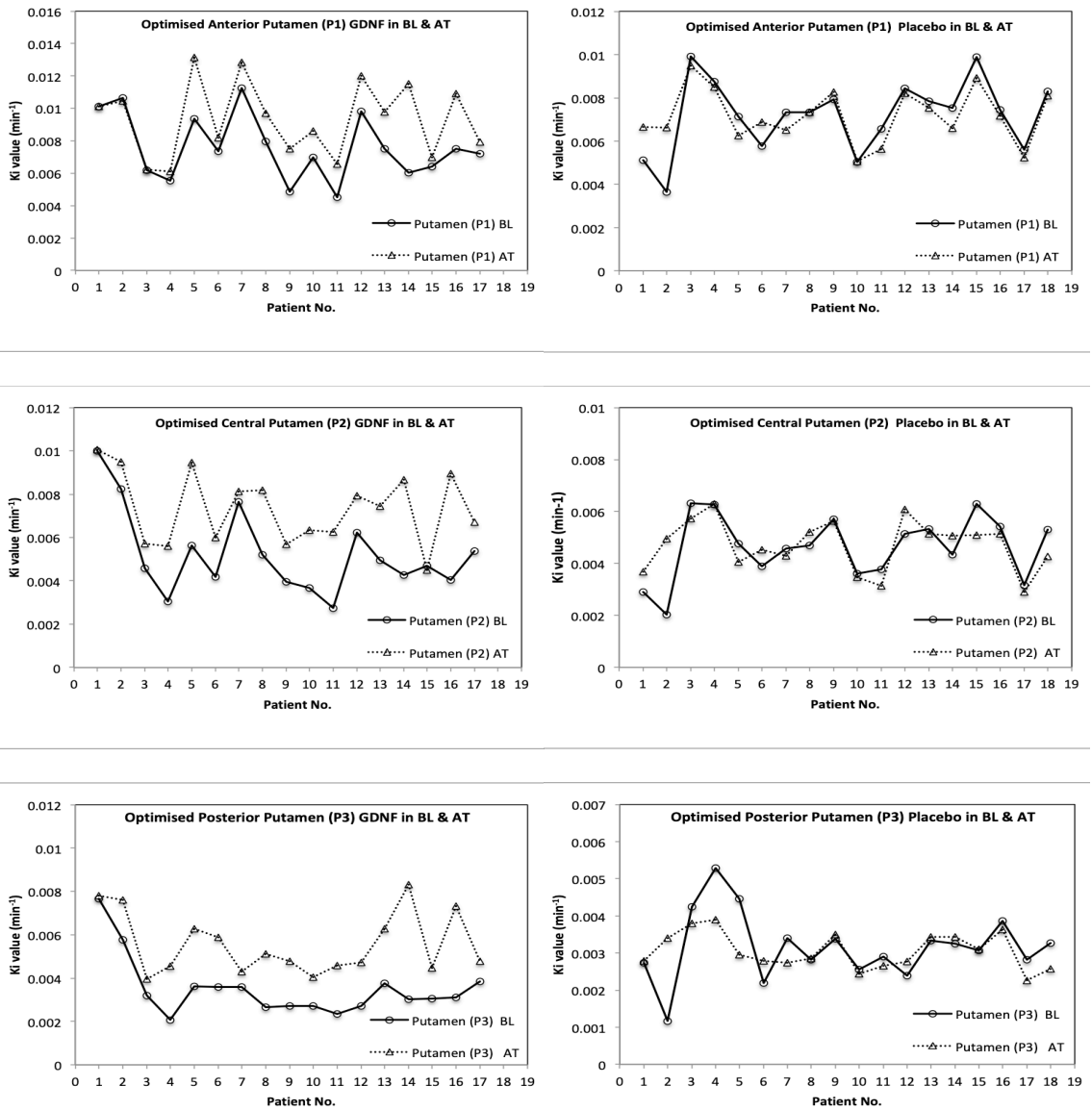


Figure D- 6. A comparison between putamen parts of both (R and L anatomical sides) after applying new methods in baseline vs. week 40 in both GDNF (left side) and placebo group (right side) after dividing the putamen’s contour into three parts: Anterior, central and posterior.

Appendix E: Published Work

Posters

- 7th of September 2016 - British Nuclear Medicine Society BNMS Autumn Meeting, Bath, UK, “Improving the Receptor Binding Estimate from Patlak Plot in PET Imaging”, Y. Alzamil, C. Marshall, Y. Hicks, X. Yang
- 7th of October 2016 - Institute of Physics and Engineering in Medicine, Quantitative Nuclear Medicine Conference, York, UK, “Improving the Receptor Binding Estimate from Patlak Plot in PET Imaging”, Y. Alzamil, C. Marshall, Y. Hicks, X. Yang
- 27th of June 2017 - Sensors, Signals and Imaging Symposium, Cardiff, UK, “Impact of Noise on Quantitative ¹⁸F-FDOPA PET Images”, Y. Alzamil, C. Marshall, Y. Hicks, X. Yang

Oral presentations

- 11th of November 2015- Health, Technology and the Digital World HTDW seminar, Cardiff University, Cardiff, UK, “Positron Emission Tomography Image Quantification”
- 17th of June 2016- Health, Technology and the Digital World HTDW seminar, Cardiff University, Cardiff, UK, “Impact of Noise on Quantitative ¹⁸F-FDOPA Images”
- 19th-21st of January 2018 – 5th International Conference on BIOIMAGING 2018, Madeira, Portugal, “Optimising Graphical Techniques Applied to Irreversible Tracers”
- 19th-21st of January 2018 – 5th International Conference on BIOIMAGING 2018, Madeira, Portugal, “Optimising Graphical Techniques Applied to Irreversible Tracers”
- 5th of October 2018- Wales Research and diagnostic Imaging Center PETIC, University Hospital of Wales UHW, Cardiff, UK, “Quantitative Analysis in Functional PET Brain Imaging”

Conference Paper

- Y. Alzamil, Y. Hicks, X. Yang, C. Marshall “Optimising Graphical Techniques Applied to Irreversible Tracers” submitted to 5th International Conference on BIOIMAGING 2018, Madeira, Portugal, DOI:10.5220/0006513700170026

References

- Abi-Dargham, A. et al. 2000. Measurement of striatal and extrastriatal dopamine D1 receptor binding potential with [¹¹C]NNC 112 in humans: validation and reproducibility. *J Cereb Blood Flow Metab* 20(2), pp. 225-243.
- Akamatsu, G. et al. 2017. A revisit to quantitative PET with ¹⁸F-FDOPA of high specific activity using a high-resolution condition in view of application to regenerative therapy. *Annals of nuclear medicine* 31(2), pp. 163-171.
- Alessio, A. and Kinahan, P. 2006. PET image reconstruction. *Nuclear medicine* 1, pp. 1-22.
- Allen, S. J. et al. 2013. GDNF, NGF and BDNF as therapeutic options for neurodegeneration. *Pharmacol. Ther* 138(2), pp. 155-175.
- Aston, J. A. D. et al. 2002. Positron Emission Tomography Partial Volume Correction: Estimation and Algorithms. *Journal of Cerebral Blood Flow & Metabolism* 22(8), pp. 1019-1034.
- Averbuch, A. Z. et al. 2015. *Spline and Spline Wavelet Methods with Applications to Signal and Image Processing: Volume II: Non-Periodic Splines*. Springer.
- Axelsson, J. and Sørensen, J. 2013. The 2D Hotelling filter-a quantitative noise-reducing principal-component filter for dynamic PET data, with applications in patient dose reduction. *BMC medical physics* 13(1), p. 1.
- Bailey, D. L. et al. 2005a. Physics and instrumentation in PET. *Positron emission tomography*. Springer, pp. 13-39.
- Bailey, D. L. et al. 2005b. *Positron emission tomography*. Springer.
- Balogova, S. et al. 2013. ¹⁸F-fluorodihydroxyphenylalanine vs other radiopharmaceuticals for imaging neuroendocrine tumours according to their type. *European journal of nuclear medicine and molecular imaging* 40(6), pp. 943-966.
- Ben-Jonathan, N. and Hnasko, R. 2001. Dopamine as a prolactin (PRL) inhibitor. *Endocrine reviews* 22(6), pp. 724-763.
- Bentourkia, M. h. 2011. Tracer Kinetic Modeling: Methodology and Applications. *Basic Sciences of Nuclear Medicine*. Springer, pp. 353-376.
- Berg, E. and Cherry, S. R. eds. 2018. *Innovations in instrumentation for positron emission tomography*. Seminars in Nuclear Medicine. Elsevier.
- Berthon, B. et al. 2015. PETSTEP: Generation of synthetic PET lesions for fast evaluation of segmentation methods. *Physica Medica* 31(8), pp. 969-980.
- Björklund, A. and Dunnett, S. B. 2007. Dopamine neuron systems in the brain: an update. *Trends in neurosciences* 30(5), pp. 194-202.

- Boellaard, R. 2009. Standards for PET Image Acquisition and Quantitative Data Analysis. *Journal of Nuclear Medicine* 50(Suppl 1), pp. 11S-20S.
- Boellaard, R. et al. 2015. FDG PET/CT: EANM procedure guidelines for tumour imaging: version 2.0. *European journal of nuclear medicine and molecular imaging* 42(2), pp. 328-354.
- Boellaard, R. et al. 2004. Effects of noise, image resolution, and ROI definition on the accuracy of standard uptake values: a simulation study. *Journal of Nuclear Medicine* 45(9), pp. 1519-1527.
- Boyat, A. K. and Joshi, B. K. 2015. A review paper: noise models in digital image processing. *arXiv preprint arXiv:1505.03489*.
- Brooks, D. et al. 1990. The relationship between locomotor disability, autonomic dysfunction, and the integrity of the striatal dopaminergic system in patients with multiple system atrophy, pure autonomic failure, and Parkinson's disease, studied with PET. *Brain* 113(5), pp. 1539-1552.
- Brooks, D. J. and Pavese, N. 2011. Imaging biomarkers in Parkinson's disease. *Progress in neurobiology* 95(4), pp. 614-628.
- Bruck, A. et al. 2009. A follow-up study on 6-[18F]fluoro-L-dopa uptake in early Parkinson's disease shows nonlinear progression in the putamen. *Mov Disord* 24(7), pp. 1009-1015.
- Carson, R. E. 2005. Tracer kinetic modeling in PET. *Positron Emission Tomography*. Springer, pp. 127-159.
- Cervenka, S. 2018. PET radioligands for the dopamine D1-receptor: Application in psychiatric disorders. *Neuroscience letters*.
- Chan, G. L.-Y. et al. 1992. Plasma L-[18F] 6-fluorodopa input function: a simplified method. *Journal of Cerebral Blood Flow & Metabolism* 12(5), pp. 881-884.
- Chen, W. et al. 2006. 18F-FDOPA PET imaging of brain tumors: comparison study with 18F-FDG PET and evaluation of diagnostic accuracy. *Journal of Nuclear Medicine* 47(6), pp. 904-911.
- Cherry, S. R. et al. 2012. *Physics in nuclear medicine*. Elsevier Health Sciences.
- Chondrogiannis, S. et al. 2013. Normal biodistribution pattern and physiologic variants of 18F-DOPA PET imaging. *Nucl Med Commun* 34(12), pp. 1141-1149.
- Christensen, A. N. et al. 2014. Calibrated image-derived input functions for the determination of the metabolic uptake rate of glucose with [18F]-FDG PET. *Nuclear medicine communications* 35(4), p. 353.
- Christian, P. E. and Waterstram-Rich, K. M. 2013. *Nuclear medicine and PET/CT: technology and techniques*. Elsevier Health Sciences.
- Christine, C. W. and Aminoff, M. J. 2004. Clinical differentiation of parkinsonian syndromes: prognostic and therapeutic relevance. *The American journal of medicine* 117(6), pp. 412-419.

- Chui, C. K. 2016. *An introduction to wavelets*. Elsevier.
- Ciarmiello, A. and Mansi, L. 2016. *PET-CT and PET-MRI in Neurology: SWOT Analysis Applied to Hybrid Imaging*. Springer.
- Coxson, P. G. et al. 1995. *Consequences of using a simplified kinetic model for dynamic PET data*. SCAN-9609051.
- Cropley, V. L. et al. 2008. Pre- and post-synaptic dopamine imaging and its relation with frontostriatal cognitive function in Parkinson disease: PET studies with [11C]NNC 112 and [18F]FDOPA. *Psychiatry Research: Neuroimaging* 163(2), pp. 171-182.
- Cumming, P. 2009. *Imaging dopamine*. Cambridge University Press.
- Daube-Witherspoon, M. E. et al. 2002. PET performance measurements using the NEMA NU 2-2001 standard. *Journal of Nuclear Medicine* 43(10), pp. 1398-1409.
- de Lau, L. M. L. and Breteler, M. M. B. 2006. Epidemiology of Parkinson's disease. *The Lancet Neurology* 5(6), pp. 525-535.
- de Souza, S. V. C. and Junqueira, R. G. 2005. A procedure to assess linearity by ordinary least squares method. *Analytica Chimica Acta* 552(1), pp. 25-35.
- Delbeke, D. et al. 2006. Procedure guideline for tumor imaging with 18F-FDG PET/CT 1.0. *Journal of nuclear Medicine* 47(5), pp. 885-895.
- DeLong, M. and Wichmann, T. 2010. Changing views of basal ganglia circuits and circuit disorders. *Clinical EEG and neuroscience* 41(2), pp. 61-67.
- Dhawan, V. et al. 1996. Combined FDOPA and 3OMFD PET studies in Parkinson's disease. *Journal of Nuclear Medicine* 37(2), pp. 209-215.
- Dhawan, V. et al. 2002. Comparative analysis of striatal FDOPA uptake in Parkinson's disease: ratio method versus graphical approach. *Journal of Nuclear Medicine* 43(10), pp. 1324-1330.
- Dickson, J. et al. eds. 2015. *Partial Volume Correction of Amyvid and FDG PET data using the discrete iterative Yang technique*. Annual Congress of the European Association of Nuclear Medicine–EANM 2015. Springer.
- Dickson, J. et al. 2019. Quantitative SPECT: the time is now. *EJNMMI Phys* 6(1), p. 4.
- Eidelberg, D. et al. 1993. Striatal ¹⁸F-DOPA Uptake: Absence of an Aging Effect. *Journal of cerebral blood flow and metabolism* 13, pp. 881-881.
- Einicke, G. A. 2012. *Smoothing, filtering and prediction: estimating the past, present and future*. InTech.
- Ellenbroek, B. et al. 2014. Alexander Rudolf Cools (1942–2013). *Psychopharmacology* 231(11), pp. 2219-2222.

- Elsinga, P. H. et al. 2006. PET tracers for imaging of the dopaminergic system. *Current medicinal chemistry* 13(18), pp. 2139-2153.
- Erlandsson, K. 2011. Tracer Kinetic Modeling: Basics and Concepts. *Basic Sciences of Nuclear Medicine*. Springer, pp. 333-351.
- Feng, D. et al. 1996. An unbiased parametric imaging algorithm for nonuniformly sampled biomedical system parameter estimation. *Medical Imaging, IEEE Transactions on* 15(4), pp. 512-518.
- Feng, D. et al. 1993. A study on statistically reliable and computationally efficient algorithms for generating local cerebral blood flow parametric images with positron emission tomography. *Medical Imaging, IEEE Transactions on* 12(2), pp. 182-188.
- Ferry, B. et al. 2014. Elements of Functional Neuroanatomy: The Major Neurotransmitter Systems. *Stereotaxic Neurosurgery in Laboratory Rodent*. Springer, pp. 37-68.
- Fox, J. 2002. Robust regression. *An R and S-Plus companion to applied regression*.
- Freedman, D. 2009. *Statistical models : theory and practice*. Cambridge ; New York: Cambridge University Press, pp. xvi, 442 p.
- Freedman, D. A. 2008. On regression adjustments to experimental data. *Advances in Applied Mathematics* 40(2), pp. 180-193.
- Freedman, N. M. et al. 2003. Comparison of SUV and Patlak slope for monitoring of cancer therapy using serial PET scans. *European journal of nuclear medicine and molecular imaging* 30(1), pp. 46-53.
- Frost, J. 2018. *7 Classical Assumptions of Ordinary Least Squares (OLS) Linear Regression* [Online]. Available at: <http://statisticsbyjim.com/regression/ols-linear-regression-assumptions/> [Accessed: 1 july 2018]
- Gallagher, C. L. et al. 2011. Rate of 6-[18F]fluorodopa uptake decline in striatal subregions in Parkinson's disease. *Mov Disord* 26(4), pp. 614-620.
- Gander, W. and Hrebicek, J. 2011. *Solving problems in scientific computing using Maple and Matlab®*. Springer Science & Business Media.
- Garnett, E. et al. 1983. Dopamine visualized in the basal ganglia of living man.
- Gavin, H. 2011. The Levenberg-Marquardt method for nonlinear least squares curve-fitting problems. *Department of Civil and Environmental Engineering, Duke University*, pp. 1-15.
- Gerasimou, G. P. 2006. Molecular imaging (SPECT and PET) in the evaluation of patients with movement disorders. *Nuclear Medicine Review* 9(2), pp. 147-153.
- Giovacchini, G. et al. 2004. Brain incorporation of ¹¹C-arachidonic acid, blood volume, and blood flow in healthy aging: a study with partial-volume correction. *J Nucl Med* 45(9), pp. 1471-1479.

- Gjedde, A. et al. 1991. Dopa decarboxylase activity of the living human brain. *Proceedings of the National Academy of Sciences* 88(7), pp. 2721-2725.
- Glaab, E. et al. 2019. Integrative analysis of blood metabolomics and PET brain neuroimaging data for Parkinson's disease. *Neurobiol Dis* 124, pp. 555-562.
- Granger, C. W. J. 1994. Learning and Practicing Econometrics - Griffiths, We, Hill, Rc, Judge, Gc. *Journal of Economic Literature* 32(1), pp. 115-122.
- Graps, A. 1995. An introduction to wavelets. *IEEE computational science and engineering* 2(2), pp. 50-61.
- Green, S. B. and Salkind, N. J. 2016. *Using SPSS for Windows and Macintosh, Books a la Carte*. Pearson.
- Grondin, R. et al. 2018. GDNF revisited: A novel mammalian cell-derived variant form of GDNF increases dopamine turnover and improves brain biodistribution. *Neuropharmacology*.
- Guidotti, P. 2009. Some anisotropic diffusions. *Ulmer Seminare* 14, pp. 215-221.
- Gujarati, D. N. 2009. *Basic econometrics*. Tata McGraw-Hill Education.
- Gunn, R. N. et al. 1997. Parametric imaging of ligand-receptor binding in PET using a simplified reference region model. *Neuroimage* 6(4), pp. 279-287.
- Haggstrom, I. et al. 2016. Dynamic PET simulator via tomographic emission projection for kinetic modeling and parametric image studies. *Med Phys* 43(6), p. 3104.
- Harris, R. J. et al. 2012. 18F-FDOPA and 18F-FLT positron emission tomography parametric response maps predict response in recurrent malignant gliomas treated with bevacizumab. *Neuro-Oncology* 14(8), pp. 1079-1089.
- Hayashi, F. 2000. *Econometrics*. Princeton, N.J. ; Oxford: Princeton University Press, pp. xxiii, 683 p.
- Healthcare, G. E. 2019. Discovery PET/CT 690. In: education-general-gehc_education_discovery_pet690_system1_jpg ed. *JPEG image*.
<https://www.gehealthcare.com/en/courses/discovery-petct-690>
 : General Electric Healthcare.
- Heiko Schöder, M. K. P., PhD; Serge Lyashchenko, PharmD; and Jorge Carrasquillo, MD. 2013. Fluorodopa F-18. *SNMMI PET Center of Excellence and the Center for Molecular Imaging Innovation & Translation* [Online]. Available at:
http://interactive.snm.org/docs/PET_PROS/FDOPA.pdf [Accessed: May 2013].
- Hintze, J. 2001. NCSS and Pass. *Number Cruncher Statistical Systems, Kaysville*. Available at:
[Whole Thesis Corrected.docx](#) *ncss.com*.
- Hogg, P. and Testanera, G. 2010. Principles and practice of PET/CT: part 1: a technologists guide. European Association of Nuclear Medicine.

- Hou, H. et al. 2012. Positron emission tomography molecular imaging of dopaminergic system in drug addiction. *The Anatomical Record* 295(5), pp. 722-733.
- Huber, P. J. 1964. Robust estimation of a location parameter. *The Annals of Mathematical Statistics* 35(1), pp. 73-101.
- Hurley, M. and Jenner, P. 2006. What has been learnt from study of dopamine receptors in Parkinson's disease? *Pharmacology & therapeutics* 111(3), pp. 715-728.
- Ibaraki, M. et al. 2016. Validation of a simplified scatter correction method for 3D brain PET with (15)O. *Annals of nuclear medicine* 30(10), pp. 690-698.
- Ichise, M. et al. 2002. Strategies to improve neuroreceptor parameter estimation by linear regression analysis. *J Cereb Blood Flow Metab* 22(10), pp. 1271-1281.
- Ikoma, Y. et al. 2008. PET kinetic analysis: error consideration of quantitative analysis in dynamic studies. *Annals of nuclear medicine* 22(1), pp. 1-11.
- Jadvar, H. and Parker, J. A. 2006. *Clinical PET and PET/CT*. Springer Science & Business Media.
- Jansen, M. 2012. *Noise reduction by wavelet thresholding*. Springer Science & Business Media.
- Johnson, H. et al. 2017. The ITK software guide book 1: introduction and development guidelines-volume 1. Kitware. Inc. <https://itk.org/ItkSoftwareGuide>.
- Jokinen, P. et al. 2009. Simple ratio analysis of 18F-fluorodopa uptake in striatal subregions separates patients with early Parkinson disease from healthy controls. *Journal of Nuclear Medicine* 50(6), p. 893.
- Joshi, A. et al. 2008. Improving PET receptor binding estimates from Logan plots using principal component analysis. *Journal of cerebral blood flow and metabolism : official journal of the International Society of Cerebral Blood Flow and Metabolism* 28(4), pp. 852-865.
- Kennedy, P. 2008. *A guide to econometrics*. 6th ed. Malden, MA: Blackwell Pub., pp. xii, 585 p.
- Kimura, Y. et al. 2007. PET kinetic analysis —Pitfalls and a solution for the Logan plot. *Annals of Nuclear Medicine* 21(1), pp. 1-8.
- Kirk, R. E. 2007. Experimental design. *The Blackwell Encyclopedia of Sociology*.
- Kosslyn, S. M. et al. 2001. Neural foundations of imagery. *Nature Reviews Neuroscience* 2(9), pp. 635-642.
- Kostakoglu, L. and Valk, P. E. 2006. Assessment of Treatment Response by FDG-PET. *Positron Emission Tomography*. Springer, pp. 387-412.
- Kotasidis, F. A. et al. 2014. Advanced kinetic modelling strategies: towards adoption in clinical PET imaging. *Clinical and Translational Imaging* 2(3), pp. 219-237.

- Kreyszig, E. 2010. *Advanced engineering mathematics*. John Wiley & Sons.
- Kutner, M. H. et al. 2004. *Applied linear regression models*. McGraw-Hill/Irwin.
- Laakso, A. et al. 2002. Sex differences in striatal presynaptic dopamine synthesis capacity in healthy subjects. *Biological psychiatry* 52(7), pp. 759-763.
- Lalchandani, R. R. et al. 2013. Dopamine D2 receptors regulate collateral inhibition between striatal medium spiny neurons. *The Journal of Neuroscience* 33(35), pp. 14075-14086.
- Lammertsma, A. et al. 1996. Comparison of methods for analysis of clinical [¹¹C] raclopride studies. *Journal of Cerebral Blood Flow & Metabolism* 16(1), pp. 42-52.
- Lammertsma, A. A. 2014. Tracer Kinetic Modelling. In: Dierckx, R.A.J.O. et al. eds. *PET and SPECT in Neurology*. Berlin, Heidelberg: Springer Berlin Heidelberg, pp. 59-73.
- Lammertsma, A. A. 2019. Quantification of PET Studies. *Journal of Nuclear Cardiology*.
- Lang, A. E. et al. 2006. Randomized controlled trial of intraputamenal glial cell line-derived neurotrophic factor infusion in Parkinson disease. *Ann Neurol* 59(3), pp. 459-466.
- Leenders, K. et al. 1986. Brain dopamine metabolism in patients with Parkinson's disease measured with positron emission tomography. *Journal of Neurology, Neurosurgery & Psychiatry* 49(8), pp. 853-860.
- Leung, K. 2011. L-3, 4-Dihydroxy-6-[¹⁸F] fluorophenylalanine.
- Lewis-Beck, C. and Lewis-Beck, M. 2015. *Applied regression: An introduction*. Sage publications.
- Logan, J. 2000. Graphical analysis of PET data applied to reversible and irreversible tracers. *Nuclear medicine and biology* 27(7), pp. 661-670.
- Logan, J. 2003. A review of graphical methods for tracer studies and strategies to reduce bias. *Nuclear medicine and biology* 30(8), pp. 833-844.
- Logan, J. et al. 2001. A strategy for removing the bias in the graphical analysis method. *J Cereb Blood Flow Metab* 21(3), pp. 307-320.
- Logan, J. et al. 1990. Graphical analysis of reversible radioligand binding from time-activity measurements applied to [¹¹C-methyl]-(-)-cocaine PET studies in human subjects. *J Cereb Blood Flow Metab* 10(5), pp. 740-747.
- Long, J. S. and Trivedi, P. K. 1992. Some specification tests for the linear regression model. *Sociological Methods & Research* 21(2), pp. 161-204.
- Lu, F. M. and Yuan, Z. 2015. PET/SPECT molecular imaging in clinical neuroscience: recent advances in the investigation of CNS diseases. *Quant Imaging Med Surg* 5(3), pp. 433-447.
- Luurtsema, G. et al. 2017. Improved GMP-compliant multi-dose production and quality control of 6-[¹⁸F] fluoro-L-DOPA. *EJNMMI Radiopharmacy and Chemistry* 1(1), p. 7.

- Mach, R. H. and Luedtke, R. R. 2018. Challenges in the development of dopamine D2 and D3 selective radiotracers for PET imaging studies. *Journal of Labelled Compounds and Radiopharmaceuticals* 61(3), pp. 291-298.
- Markiewicz, P. J. et al. 2018. NiftyPET: a High-throughput Software Platform for High Quantitative Accuracy and Precision PET Imaging and Analysis. *Neuroinformatics* 16(1), pp. 95-115.
- Markovsky, I. and Van Huffel, S. 2007. Overview of total least-squares methods. *Signal processing* 87(10), pp. 2283-2302.
- Martin, W. et al. 1989. Nigrostriatal function in humans studied with positron emission tomography. *Annals of neurology* 26(4), pp. 535-542.
- Martin, W. et al. 1986. Positron emission tomography in Parkinson's disease: glucose and DOPA metabolism. *Advances in neurology* 45, pp. 95-98.
- Meikle, S. R. and Badawi, R. D. 2005. Quantitative techniques in PET. *Positron Emission Tomography*. Springer, pp. 93-126.
- Melega, W. P. et al. 1991. L-6-[18F] fluoro-dopa metabolism in monkeys and humans: biochemical parameters for the formulation of tracer kinetic models with positron emission tomography. *Journal of Cerebral Blood Flow & Metabolism* 11(6), pp. 890-897.
- Méndez-Rial, R. and Martín-Herrero, J. 2018. Separable Anisotropic Diffusion. *International Journal of Computer Vision* 126(6), pp. 651-670.
- Mettler, F. A. and Guiberteau, M. J. 2011. *Essentials of Nuclear Medicine Imaging: (Expert Consult-Online and Print)*. Elsevier Health Sciences.
- Missale, C. et al. 1998. Dopamine receptors: from structure to function. *Physiological reviews* 78(1), pp. 189-225.
- Mitra, S. K. and Kaiser, J. F. 1993. *Handbook for digital signal processing*. John Wiley & Sons, Inc.
- Montgomery, D. C. et al. 2012. *Introduction to linear regression analysis*. John Wiley & Sons.
- Moore, R. Y. et al. 2003. Monoamine neuron innervation of the normal human brain: an 18F-DOPA PET study. *Brain Res* 982(2), pp. 137-145.
- Moré, J. J. 1978. The Levenberg-Marquardt algorithm: implementation and theory. *Numerical analysis*. Springer, pp. 105-116.
- Morgan, T. L. 2012. Quality assurance for PET and PET/CT systems. *Health Physics* 103(6), pp. 810-811.
- Moshnyaga, V. G. and Hashimoto, K. eds. 2009. *An efficient implementation of 1-D median filter*. Circuits and Systems, 2009. MWSCAS'09. 52nd IEEE International Midwest Symposium on. IEEE.

- Müller-Gärtner, H. W. et al. 1992. Measurement of radiotracer concentration in brain gray matter using positron emission tomography: MRI-based correction for partial volume effects. *Journal of Cerebral Blood Flow & Metabolism* 12(4), pp. 571-583.
- Munk, O. L. 2012. Model-independent plot of dynamic PET data facilitates data interpretation and model selection. *Journal of theoretical biology* 295, pp. 1-8.
- Munk, O. L. et al. 2017. Point-spread function reconstructed PET images of sub-centimeter lesions are not quantitative. *EJNMMI Physics* 4(1), p. 5.
- Muzi, M. et al. 2012. Quantitative assessment of dynamic PET imaging data in cancer imaging. *Magnetic resonance imaging* 30(9), pp. 1203-1215.
- Nakamura, T. et al. 2001. Blinded positron emission tomography study of dopamine cell implantation for Parkinson's disease. *Annals of neurology* 50(2), pp. 181-187.
- Nowak, R. D. 1999. Wavelet-based Rician noise removal for magnetic resonance imaging. *IEEE Transactions on Image Processing* 8(10), pp. 1408-1419.
- O'Haver, T. 2016. *A Pragmatic Introduction to Signal Processing*. CreateSpace Independent Publishing Platform, North Charleston.
- Ohira, H. et al. 2014. Quantification of myocardial blood flow using PET to improve the management of patients with stable ischemic coronary artery disease. *Future Cardiology* 10(5), pp. 611-631.
- Ollinger, J. M. and Fessler, J. A. 1997. Positron-emission tomography. *IEEE Signal Processing Magazine* 14(1), pp. 43-55.
- Pafundi, D. H. et al. 2013. Biopsy validation of 18F-DOPA PET and biodistribution in gliomas for neurosurgical planning and radiotherapy target delineation: results of a prospective pilot study. *Neuro-oncology* 15(8), pp. 1058-1067.
- Park, S. et al. 2017. Initial experience with a new PET/CT system using SiPM detectors: image quality comparison with standard PET/CT. *Journal of Nuclear Medicine* 58(supplement 1), pp. 1331-1331.
- Patel, N. H. et al. 2010. Positron emission tomography in schizophrenia: a new perspective. *Journal of Nuclear Medicine* 51(4), pp. 511-520.
- Patlak, C. S. and Blasberg, R. G. 1985. Graphical evaluation of blood-to-brain transfer constants from multiple-time uptake data. Generalizations. *J Cereb Blood Flow Metab* 5(4), pp. 584-590.
- Patlak, C. S. et al. 1983. Graphical evaluation of blood-to-brain transfer constants from multiple-time uptake data. *J Cereb Blood Flow Metab* 3(1), pp. 1-7.
- Paulus, W. and Schomburg, E. D. 2006. Dopamine and the spinal cord in restless legs syndrome: Does spinal cord physiology reveal a basis for augmentation? *Sleep medicine reviews* 10(3), pp. 185-196.

- Perona, P. and Malik, J. 1990. Scale-space and edge detection using anisotropic diffusion. *IEEE Transactions on pattern analysis and machine intelligence* 12(7), pp. 629-639.
- Petráš, I. and Bednářová, D. 2010. Total least squares approach to modeling: a Matlab toolbox. *Acta Montanistica Slovaca* 15(2), p. 158.
- Petras, I. and Podlubny, I. 2010. Least Squares or Least Circles? A comparison of classical regression and orthogonal regression. *Chance* 23(2), pp. 38-42.
- Pinilla, I. et al. 2011. Diagnostic value of CT, PET and combined PET/CT performed with low-dose unenhanced CT and full-dose enhanced CT in the initial staging of lymphoma. *The quarterly journal of nuclear medicine and molecular imaging: official publication of the Italian Association of Nuclear Medicine (AIMN)[and] the International Association of Radiopharmacology (IAR),[and] Section of the Society of...* 55(5), pp. 567-575.
- Pitas, I. and Venetsanopoulos, A. N. 2013. *Nonlinear digital filters: principles and applications*. Springer Science & Business Media.
- Pizurica, A. et al. 2003. A versatile wavelet domain noise filtration technique for medical imaging. *IEEE Trans. Med. Imaging* 22(3), pp. 323-331.
- PMOD, P. T. L. 2017. *PMOD Biomedical Image Quantification* [Online]. Available at: http://www.pmod.com/web/?page_id=476 [Accessed: 09-05-2017]
- Porwik, P. and Lisowska, A. 2004. The Haar-wavelet transform in digital image processing: its status and achievements. *Machine graphics and vision* 13(1/2), pp. 79-98.
- Prante, O. et al. 2013. Radioligands for the dopamine receptor subtypes. *Journal of Labelled Compounds and Radiopharmaceuticals* 56(3-4), pp. 130-148.
- Press, W. H. et al. 2007. *Numerical recipes 3rd edition: The art of scientific computing*. Cambridge university press.
- Rakshi, J. S. et al. 1996. Chapter 17 - Implementation of 3D Acquisition, Reconstruction, and Analysis of Dynamic [18F]Fluorodopa Studies. In: Ralph, M. et al. eds. *Quantification of Brain Function Using PET*. San Diego: Academic Press, pp. 82-87.
- Rousset, O. G. et al. 2008. Design and implementation of an automated partial volume correction in PET: application to dopamine receptor quantification in the normal human striatum. *Journal of Nuclear Medicine* 49(7), pp. 1097-1106.
- Rousset, O. G. et al. 2000. Effect of partial volume correction on estimates of the influx and cerebral metabolism of 6-[18F]fluoro-L-dopa studied with PET in normal control and Parkinson's disease subjects. *Synapse* 37(2), pp. 81-89.
- Rousset, O. G. et al. 1998. Correction for partial volume effects in PET: principle and validation. *Journal of Nuclear Medicine* 39(5), pp. 904-911.
- Ruottinen, H. et al. 1995. Striatal [18F] fluorodopa utilization after COMT inhibition with entacapone studied with PET in advanced Parkinson's disease. *Journal of Neural Transmission-Parkinson's Disease and Dementia Section* 10(2-3), pp. 91-106.

Rutland, M. et al. 2000. "FUR"—one size suits all. *European journal of nuclear medicine* 27(11), pp. 1708-1713.

Salomaki, S. P. et al. 2017. 18F-FDG positron emission tomography/computed tomography in infective endocarditis. *J Nucl Cardiol* 24(1), pp. 195-206.

Sapiro, G. 2006. *Geometric partial differential equations and image analysis*. Cambridge university press.

Savitzky, A. and Golay, M. J. 1964. Smoothing and differentiation of data by simplified least squares procedures. *Analytical chemistry* 36(8), pp. 1627-1639.

Schultz, W. 2007. Multiple dopamine functions at different time courses. *Annu. Rev. Neurosci.* 30, pp. 259-288.

Selivanov, V. V. et al. 2001. Cross-validation stopping rule for ML-EM reconstruction of dynamic PET series: effect on image quality and quantitative accuracy. *Nuclear Science, IEEE Transactions on* 48(3), pp. 883-889.

Shankar, L. K. et al. 2006. Consensus recommendations for the use of 18F-FDG PET as an indicator of therapeutic response in patients in National Cancer Institute Trials. *Journal of Nuclear Medicine* 47(6), pp. 1059-1066.

Simonoff, J. S. 2012. *Smoothing methods in statistics*. Springer Science & Business Media.

Singh, S. P. and Urooj, S. 2015. Wavelets: biomedical applications. *International Journal of Biomedical Engineering and Technology* 19(1), pp. 1-25.

Sioka, C. et al. 2010. Recent advances in PET imaging for evaluation of Parkinson's disease. *European journal of nuclear medicine and molecular imaging* 37(8), pp. 1594-1603.

Slifstein, M. and Laruelle, M. 2000. Effects of statistical noise on graphic analysis of PET neuroreceptor studies. *Journal of Nuclear Medicine* 41(12), pp. 2083-2088.

Stanković, R. S. and Falkowski, B. J. 2003. The Haar wavelet transform: its status and achievements. *Computers & Electrical Engineering* 29(1), pp. 25-44.

Strutz, T. 2010. *Data fitting and uncertainty: A practical introduction to weighted least squares and beyond*. Vieweg and Teubner.

Teymurazyan, A. et al. 2013. Properties of noise in positron emission tomography images reconstructed with filtered-backprojection and row-action maximum likelihood algorithm. *Journal of digital imaging* 26(3), pp. 447-456.

Tong, S. et al. 2010. Image reconstruction for PET/CT scanners: past achievements and future challenges. *Imaging in medicine* 2(5), pp. 529-545.

Turkheimer, F. E. et al. 2014. *Experimental design and practical data analysis in positron emission tomography*. CreateSpace.

Vaidya, M. et al. 2012. Combined PET/CT image characteristics for radiotherapy tumor response in lung cancer. *Radiotherapy and Oncology* 102(2), pp. 239-245.

- van den Bogert, T. 1996. Practical Guide to Data Smoothing and Filtering.
- Vanitha, N. 2011. positron emission tomography in neuroscience research. *Ann Neurosci* 18(2), p. 36.
- Vaquero, J. J. and Kinahan, P. 2015. Positron Emission Tomography: Current Challenges and Opportunities for Technological Advances in Clinical and Preclinical Imaging Systems. *Annual review of biomedical engineering* 17, pp. 385-414.
- Varga, J. and Szabo, Z. 2002. Modified regression model for the Logan plot. *Journal of Cerebral Blood Flow & Metabolism* 22(2), pp. 240-244.
- Veltman, D. and Hutton, C. 2001. Spm99 manual. London, UK: Wellcome.
- Vingerhoets, F. et al. 1996. Reproducibility and discriminating ability of fluorine-18-6-fluoro-L-dopa PET in Parkinson's disease. *Journal of nuclear medicine: official publication, Society of Nuclear Medicine* 37(3), pp. 421-426.
- Vingerhoets, F. et al. 1994. Longitudinal fluorodopa positron emission tomographic studies of the evolution of idiopathic parkinsonism. *Annals of neurology* 36(5), pp. 759-764.
- Wager, T. D. et al. 2005. Increased sensitivity in neuroimaging analyses using robust regression. *NeuroImage* 26(1), pp. 99-113.
- Wahl, L. and Nahmias, C. 1996. Quantification of dopamine metabolism in man: a mathematically justifiable approach. *Phys Med Biol* 41(6), pp. 963-978.
- Wang, J. Z. 2001. Wavelets and imaging informatics: A review of the literature. *Journal of Biomedical Informatics* 34(2), pp. 129-141.
- Wehner, J. et al. 2014. PET/MRI insert using digital SiPMs: Investigation of MR-compatibility. *Nuclear Instruments and Methods in Physics Research Section A: Accelerators, Spectrometers, Detectors and Associated Equipment* 734, pp. 116-121.
- Weisstein, E. W. 2006. Least squares fitting—polynomial. From Mathworld—A Wolfram Web Resource.
- Western, B. 1995. Concepts and suggestions for robust regression analysis. *American Journal of Political Science*, pp. 786-817.
- Whone, A. et al. 2019. Randomized trial of intermittent intraputamenal glial cell line-derived neurotrophic factor in Parkinson's disease. *Brain* 142(3), pp. 512-525.
- Whone, A. L. et al. 2004. A technique for standardized central analysis of 6-18F-fluoro-L-DOPA PET data from a multicenter study. *Journal of Nuclear Medicine* 45(7), pp. 1135-1145.
- Whone, A. L. et al. 2003. Slower progression of Parkinson's disease with ropinirole versus levodopa: The REAL  PET study. *Annals of neurology* 54(1), pp. 93-101.
- Xiao, Y. et al. eds. 2003. *The Generalized Battle-Lemarie Wavelets*. Communications, Circuits and Systems and West Sino Expositions, IEEE 2002 International Conference on. IEEE.

- Xu, C. et al. eds. 2013. *Comparison of digital and analog silicon photomultiplier for positron emission tomography application*. 2013 IEEE Nuclear Science Symposium and Medical Imaging Conference (2013 NSS/MIC). Oct. 27 2013-Nov. 2 2013.
- Xuezhu, Z. et al. 2017. Quantitative image reconstruction for total-body PET imaging using the 2-meter long EXPLORER scanner. *Physics in Medicine & Biology* 62(6), p. 2465.
- Yan, J. et al. 2015. MRI-guided brain PET image filtering and partial volume correction. *Physics in Medicine and Biology* 60(3), pp. 961-976.
- Zaidi, H. 2006. *Quantitative analysis in nuclear medicine imaging*. Springer.
- Zanotti-Fregonara, P. et al. 2011. Image-Derived Input Function for Brain PET Studies: Many Challenges and Few Opportunities. *Journal of Cerebral Blood Flow & Metabolism* 31(10), pp. 1986-1998.
- Zanotti-Fregonara, P. et al. 2014. Application of Calibrated Image Derived Input Function to a Clinical Protocol. *Nuclear medicine communications* 35(11), p. 1188.
- Zhou, Y. et al. 2008. Using a generalized ridge regression with spatial constraint parametric imaging algorithm to improve the quantification of [11C] PIB dynamic PET. *Journal of Nuclear Medicine* 49(supplement 1), pp. 117P-117P.
- Zhou, Y. et al. 2010. Multi-graphical analysis of dynamic PET. *Neuroimage* 49(4), pp. 2947-2957.
- Ziegler, S. I. 2005. Positron emission tomography: principles, technology, and recent developments. *Nuclear Physics A* 752, pp. 679-687.

Glossary

PET:	Positron Emission Tomography
FGLS:	Feasible Generalised Least Squares
BLW:	Battle-Lemarie wavelet
3D:	Three-dimensional
2D:	Two-dimensional
SGF:	Savitzky-Golay Filtering
SE:	Standard Error
SSE:	Sum-Squared error
CT:	Computed Tomography
GDNF:	Glial cell line-Derived Neurotrophic Factor
CED:	Convection-Enhanced Delivery
PD:	Parkinson's Disease
TACs:	Time Activity Curves
ROIs:	Region of Interests
MRI:	Magnetic Resonance Imaging
DA:	Dopamine-system (DA)
¹⁸ F:	Fluorine-18 radioisotope
FDOPA:	Fluorodopa
TKM:	Tracer Kinetic Modelling
QC:	Quality Control
PMTs:	Photomultiplier Tubes
LOR:	Line of Response
SiPMs:	Silicon Photomultipliers
A-SiPM:	Analogue Silicon Photomultipliers
D-SiPM:	Digital Silicon Photomultipliers
FOV:	Field of View
AC:	Attenuation Correction
SNR:	Signal-to-Noise Ratio
FBP:	Filtered Back Projection
MLEM:	Maximum Likelihood Expectation Maximization
OSEM:	Ordered Subset Expectation Maximization
EXPLORER:	EXtreme Performance Long REsearch scanner
FDG:	Fluoro-Deoxy-Glucose
NETs:	Neuroendocrine Tumours
AADC:	Amino Acid Decarboxylase
FDA:	Fluoro-Dopamine
COMT:	Catechol-O-Methyl Transferase
VTA:	Ventral Tegmental Area
VOIs:	Volumes of Interest s
CM:	Compartmental Modelling
SUV:	Standardized Uptake Value
GA:	Graphical Analysis
T/N:	Tissue to Normal reference tissue ratio
FUR:	Fractional Uptake Rate
NEMA:	National Electrical Manufacturers Association

FOV:	Field of View
MTGA:	Multigraphical Analysis
QA:	Quality Assurance
IDIF:	Image-Derived Input Function
PVE:	Partial Volume Effect
PVC:	Partial Volume Correction
PSF:	Point Spread Function
GTM:	Geometric Transfer Matrix
WM:	White Matter
GM:	Grey Matter
ADHD:	Attention Deficit Hyperactivity Disorder
DAT:	Dopaminergic Transporter
3OMFD	3-O-Methyl-6-Fluoro-L-DOPA
SPM:	Statistical Parametric Mapping software
SOR:	Striatal-to-Occipital Ratio
MNI:	Montreal Neurological Institute
DPP:	Diagnostic Predictive Performance
TOF:	Time of Flight
MC:	Monte Carlo
DICOM:	Digital Imaging and Communications in Medicine
OLS:	Ordinary Least Squares
TLS:	Total Least Squares
RFR:	Robust Fitting Regression
PETIC:	Wales Research and Diagnostic PET Imaging Centre
aCSF:	Artificial Cerebral Spinal Fluid
ARSAC:	Administration of Radioactive Substances Advisory Committee
FWHM:	Full Width Half Maximum
CERR:	Computational Environment for Radiological Research
FNRs:	Higher False Negative Rates
FPRs:	Higher False Positive Rates
GLLS:	Generalized Linear Least Squares
WLS:	Weighted Least Squares
RMSE:	Root Mean Squared Error
MSE:	Mean Squared Error
ANOVA:	Analysis of Variance
GADF:	Gradient Anisotropic Diffusion Filter
CADF:	Curvature Anisotropic Diffusion Filter
DW:	Daubechies' Wavelet
BLW:	Battle-Lemarie Wavelet
MAF:	Moving Average Filtering
SGF:	Savitzky-Golay Filtering
PCF:	Polynomial Curve Fitting
MF:	Median Filtering

Software and analysis tools website

GitHub

<https://github.com/explore>

dPETSTEP

<https://github.com/CRossSchmidtlein/dPETSTEP>

MATLAB

<https://ch.mathworks.com/products/matlab.html>

PMOD

<https://www.pmod.com/web/>

TeleHERMES

<http://www.medicaexpo.com/prod/hermes-medical-solutions-inc/product-100595-677508.html>